TECHNISCHE UNIVERSITÄT MÜNCHEN

TUM School of Life Sciences

Quantitative analysis of cellular growth patterns in ovule morphogenesis and curvature in *Arabidopsis thaliana*

Rachele Tofanelli

Vollständiger Abdruck der von der TUM School of Life Sciences der Technischen Universität München zur Erlangung des akademischen Grades einer

Doktorin der Naturwissenschaften (Dr. rer. nat.)

genehmigten Dissertation.

Vorsitzender:	Prof. Dr. Frank Johannes
Prüfer der Dissertation:	1. Prof. Dr. Kay Heinrich Schneitz 2. Prof. Dr. Thomas Greb

Die Dissertation wurde am 17.08.2021 bei der Technischen Universität München eingereicht und durch die School of Life Sciences am 30.11.2021 angenommen

Table of contents

List of figures

List of tables

Summary

How the *Gestalt* of a plant tissue is generated remains an open question in plant developmental biology. The ovule of *Arabidopsis thaliana* represents a model system to investigate tissue morphogenesis since at maturity, the organ exhibits a distinctive curved shape with the micropyle placed to the base of the funiculus, resulting in a 180° bending (anatropy). Thus, ovule curvature represents a unique phenomenon in plant tissue morphogenesis and invites interesting questions regarding the cellular, molecular, and mechanical mechanisms that act at different scales in the formation of this characteristic shape.

The aim of the present study is the generation of a 3D digital atlas of ovule development with cellular resolution, to enable the analysis of the cellular growth pattern shaping the organ and unravelling ovule morphogenesis.

To this end a protocol for rapid and robust confocal microscopy of fixed *Arabidopsis* ovules has been developed. This approach consisted of clearing fixed ovules in ClearSee solution and staining of the cell wall with SCRI Renaissance 2200 and the nuclei with TO-PRO-3 iodide, allowing the deep imaging in 3D of ovule with cellular resolution. The generated raw microscopy data have been employed in the development of PlantSeg, a convolutional neural network able to predict cell boundaries and to segment cells in 3D through graph partitioning based on the neural network predictions. The technical improvement in microscopy and the coupling with PlantSeg for accurate 3D cell segmentation allowed the generation of a complete developmental series of wild-type ovules, enabling a comprehensive quantitative analysis in 3D of cellular features and tissue growth patterns through the application of computational cell type annotation.

The analysis included gene expression, identification of cell division and analysis of cellular growth patterns along an integument specific coordinate system. Additionally, a temporal framework of ovule development has been generated to gain temporal information on ovule morphogenesis.

The quantitative analysis highlighted the differential growth between the integuments, the presence of two morphological distinct subepidermal region composing the central chalaza and the mechanisms of formation of a new layer within the inner integument.

Moreover, findings of the present study suggests that ovule curvature is a multistep process. In a first step, the kink formation is achieved through differential enlargement of subepidermal cells of the posterior chalaza. In a second step, the later bending of the growing integuments results in the final bending. Analysis of *inner no outer* (*ino)* and superman (*sup)* mutant ovule,

characterized by defects in the establishment of the correct curvature, provided genetic evidence for this hypothesis. Additionally, the analysis of *ino* and *sup* mutant indicated that the outer layer of the outer integument is a central regulator of ovule curvature.

The present study demonstrates the power of digital representations of 3D organs and provides an impressive amount of quantitative data that will be employed for the generation of growth model reproducing ovule morphogenesis to investigate the various components contributing to curvature formation in more detail.

Zusammenfassung

Eine ungelöste Frage innerhalb der Entwicklungsbiologie der Pflanzen, ist die Entstehung der Gestalt des Pflanzengewebes. Die Samenanlage der *Arabidopsis thaliana*, dient als Modellsystem zur Untersuchung der Gewebemorphogenese, da das Organ bei der Entwicklung eine charakteristische gekrümmte Form zeigt, bei der die Mikropyle an der Basis des Funiculus platziert ist, was zu einer 180°-Biegung (Anatropie) führt. Diese Krümmung der Samenanlage ist ein einzigartiges Phänomen in der pflanzlichen Gewebemorphogenese und eröffnet interessante Fragen zu den zellulären, molekularen und mechanischen Mechanismen, die auf verschiedenen Ebenen bei der Bildung dieser charakteristischen Form wirken.

Ziel der vorliegenden Studie ist die Erstellung eines digitalen 3D-Atlas der Samenanlagenentwicklung mit zellulärer Auflösung, zur Analyse des zellulären Wachstumsmusters, das das Organ formt, und zur Entschlüsselung der Morphogenese der Samenanlage.

Dazu wurde ein Protokoll entwickelt, für die schnelle und robuste konfokale Mikroskopie von fixierten *Arabidopsis* Samenanlagen. Um eine detaillierte 3D-Abbildung der Samenanlage mit zellulärer Auflösung zu ermöglichen, war eine Klärung der fixierten Samenanlagen in ClearSee-Lösung nötig, sowie die Färbung der Zellwand mit SCRI Renaissance 2200 und der Zellkerne mit TO-PRO-3-Iodid. Die generierten Mikroskopie-Rohdaten wurden für die Entwicklung von PlantSeg genutzt, einem neuronalen Faltungsnetzwerk, das in der Lage ist, Zellgrenzen vorherzusagen und Zellen in 3D durch Graphpartitionierung auf der Grundlage der Vorhersagen des neuronalen Netzwerks zu segmentieren. Die technischen Verbesserungen in der Mikroskopie und die Verbindung mit PlantSeg für eine akkurate 3D-Zellsegmentierung ermöglichten die Erstellung einer vollständigen Entwicklungsreihe von Wild-type Samenanlagen, was eine umfassende quantitative 3D-Analyse von Zellmerkmalen und Gewebewachstumsmustern durch die Anwendung der computergestützten Zelltyp-Annotation ermöglichte. Zusätzlich konnten die zeitlichen Abläufe der Samenanlagenentwicklung erkannt werden, mit deren Hilfe wiederum Informationen über den zeitlichen Ablauf der Morphogenese der Samenanlagen gewonnen werden konnten.

Die quantitativen Analysen zeigten das differentielle Wachstum zwischen den Integumenten, das Vorhandensein von zwei morphologisch unterschiedlichen subepidermalen Regionen, aus denen sich die zentrale Chalaza zusammensetzt, und die Mechanismen der Bildung einer neuen Zellschicht innerhalb des inneren Integuments.

Darüber hinaus deuten die Befunde der vorliegenden Studie darauf hin, dass die Krümmung der Eizelle ein mehrstufiger Prozess ist. In einem ersten Stadium wird die Knickbildung durch eine unterschiedliche Vergrößerung der subepidermalen Zellen der hinteren Chalaza erreicht. In einem zweiten Stadium führt die spätere Biegung der wachsenden Integumente zur endgültigen Biegung. Die Analyse von *inner no outer* (*ino*) und *superman* (*sup*) Mutanten, die durch Defekte bei der Ausbildung der korrekten Krümmung gekennzeichnet sind, lieferte genetische Beweise für diese Hypothese. Darüber hinaus zeigte die Analyse der *ino* und *sup* Mutanten, dass die äußere Schicht des äußeren Integuments ein zentraler Regulator der Samenanlagekrümmung ist.

Die vorliegende Studie demonstriert die Bedeutung der digitalen Darstellung von 3D-Organen und liefert eine beeindruckende Menge an quantitativen Daten zur Erstellung eines Wachstumsmodells, das die Morphogenese der Samenanlage digital reproduziert, um die verschiedenen Komponenten, die zur Krümmungsbildung beitragen, genauer zu untersuchen.

1 Introduction

Morphogenesis is derived from the Greek words that mean the emergence (γεννтση - gennisi) of shape (μορφη - morphi), therefore we refer to morphogenesis as the biological process that leads to a tissue, an organ and an organism to develops its shape.

To achieve its species-specific size and shape, an organism needs to coordinate the cellular behavior within tissues and organs, through complex feedback mechanisms between signals specifying growth. To define the nature of these signals regulating growth, it is necessary to introduce some unique features that characterize plants morphogenesis compared to mammals. Organ formation in animals occurs early during embryogenesis, while in plants growth is mainly established post-embryonically, at structures called meristems. Moreover, in animals, cell migration plays a major role in shaping tissues. In plants, cells are encased by the cell wall preventing cell movement, therefore coordinated differential growth in the tissue assume a central role in plant morphogenesis (Coen et al., 2017; Huang et al., 2018). The physical coupling of cells, due to the presence of cell wall, generates in growth tissues mechanical forces which act, together with molecular mechanisms, as regulatory signals of morphogenesis (Eng & Sampathkumar, 2018; Robinson et al., 2013; Sapala et al., 2019).

1.1 Morphogenesis in plants

Plants can generate an incredible diversity of three-dimensional shaped organs and their development is characterized by a high reproducibility and robustness (Hong et al., 2018).

At the cellular level, one of the most crucial aspect to consider in plants is the presence of a semirigid extracellular matrix composed of polysaccharides called cell wall. The presence of this physical barrier in which cells are encased and bound to each other, influences the growth process, during which cells divide and keep fixed to a certain position within the tissue. For these factors plant morphogenesis relies on the control of cell shape through two main mechanisms: oriented cell division and directionality of growth (Braybrook & Jönsson, 2016; Kirchhelle et al., 2019; Rasmussen & Bellinger, 2018).

The final form of a tissue or organ is the result of a tight coordination within patterns of cell proliferation, expansion, and differentiation (Dupuy et al., 2010). At the cellular level, genetic and molecular mechanisms may be involved in this regulation. For examples, cell expansion occurs through plastic deformation of the cell wall, which is driven by the internal turgor pressure of the cell (Lockhart, 1965).

However, in the last years it became more evident that mechanical clues generated within a growing structure can act as regulator at the tissue level, orchestrating the growth of the tissue and organ, through the integration of different subcellular and cellular processes.

Different cell shapes observed in plant tissue depends on the orientation of cell division plane. It has been proposed by Louveaux et al. that the mechanical stress generated in the shoot apical meristem can control the cell division plane, showing that cells can divide along the maximal tension contributing to the formation of long planes observed in the boundary region (Louveaux et al., 2016). Mechanical clues can also regulate other sub-cellular components that contributes to cell shape and directionality of growth, including microtubule reorganization, oriented cellulose deposition, and auxin transport (Hamant et al., 2008; Hervieux et al., 2016; Nakayama et al., 2012; Sampathkumar et al., 2014; Sapala et al., 2018; Uyttewaal et al., 2012).

1.1.1 Computational morphodynamics

Plant morphogenesis is the results of interactions between gene networks, hormones, and cellular patterning. All these components are tightly regulated and coordinated as a single system and translated in a general process known as growth. In the last decade, computational modelling became a powerful approach for analysing hormonal distribution, genetic networks and mechanical properties, to obtain integrative models, allowing a more comprehensive understanding of plant development (Geitmann & Ortega, 2009; Jönsson & Krupinski, 2010; Prusinkiewicz & Rolland-Lagan, 2006).

Moreover, plant growth is a process that occur in space and time. For a complete understanding of growth it is necessary to study this process in four dimension, while the changes are happening (Bassel & Smith, 2016; Fernandez et al., 2010; Roeder et al., 2011). To understand the changes that occur in space in time during morphogenesis, computational morphodynamics became a successful approach to integrate multi-scale quantitative data (Chickarmane et al., 2010). This approach relay on the application of three technical strategies: high resolution imaging to observe development and cellular patterns, image processing and analysis to extract quantitative information, and computational modelling to analyse and test hypotheses (Bassel, 2015; Boudon et al., 2015; Chickarmane et al., 2010; Roeder et al., 2012; Roeder et al., 2011). The 3D approach in the analysis of entire organs has been a successful approach to gain a better understanding of the mechanisms involved in plant organ morphogenesis (Hong et al., 2018; Kierzkowski et al., 2019; Sapala et al., 2019). Digital 3D atlas of entire plant organs have been successfully obtained for early stage *Arabidopsis* embryo and for larger organs with simple

layered structures like roots and hypocotyls (Bassel et al., 2014; Montenegro-Johnson et al., 2015; Stamm et al., 2017; Yoshida et al., 2014). Three-dimensional dataset of plant organ imaged at multiple time points has also been performed successfully for the shoot apex (Refahi et al., 2021; Willis et al., 2016).

More recent approaches, are focused on the quantitative description of single cell three dimensional properties in order to understand how cell size, cell shape, and cellular topology can dictate tissue architecture (Jackson et al., 2017, 2019). Tissues and organ are viewed as a higher level-structure of interacting cells, therefore analyzing the cellular architecture of the single entities that compose the organ allows the understanding on how multicellular entities are constructed (Bassel, 2019; Bassel, 2018). This approach, conducted in plant hypocotyl, relies on the investigation of the topological properties of the tissue using quantitative network analysis, single cell annotation and digitally analyzing the cellular interactions based on cell geometry and shape (Jackson et al., 2019). The organ-scale cellular network are generated through the application of whole organ 3D imaging with cellular resolution and computational image analysis pipelines in order to perform cell type annotation and extraction of interacting networks of cells (de Reuille et al., 2014; Montenegro-Johnson et al., 2015, 2019). Since development occurs in three spatial dimensions, 2D analysis of cellular patterns are limiting the possibility to perform analysis on cellular shape, division plane control and tissue architecture (Yoshida et al., 2014). This multidimensional approach enables the analysis of the higher-scale cellular organization within the tissue and the local properties of interconnected units, allowing to address the relation between structure and functionality that characterize the tissues and organs (Duran-Nebreda & Bassel, 2017; Jackson et al., 2019).

1.1.2 Modelling curved structure of plant organs

To address the contribution of mechanical forces, gene networks and cellular patterning in the generation of shapes during organ and tissue morphogenesis computational modeling have been employed. The process of formation of curved shapes represents an interesting phenomenon to investigate. Moreover, these modeling approaches attempt to understand how emergent properties of the tissue that are not directly encoded in the genome are integrated during the growth, resulting in the final three-dimensional curved shape (Coen & Rebocho, 2016; Kennaway et al., 2011; Liang & Mahadevan, 2011). On this regard, the modeling proposed by Coen et al. integrates together directionality of growth through polarity cues and mechanical constraints, that are generated during growth of neighboring regions in a simplified

growing tissue template. The formation of curved structure represent the solution of the growing structure as the minimization of mechanical stresses that are generated by differential growth within neighbouring regions (Coen & Rebocho, 2016; Kennaway et al., 2011). This modeling approach has been applied for the understanding of mechanisms leading the curved structure observed in the Snapdragon flower and for the *Utricularia gibba* traps (Coen et al., 2017; Kennaway et al., 2011; Lee et al., 2019).

The complexity of the growing structure can be increased in order to model the growth of multilayered structure and the formation of out-of-plane curvatures. Buckling and curvation arise in situation of surface-conflict when the layers of the growing template show differential growth (Coen & Rebocho, 2016). Other examples of buckling arising through tissue conflict have been proposed in lily petals and *Antirrhinum* flowers (Green et al., 2010; Liang & Mahadevan, 2011).

Another organ in plants characterized by curved structure is the apical hook. Hypocotyls after germination bend into a 180^{o} hook-shaped structures to protect the the apical meristem, while emerging from the soil (Raz & Ecker, 1999). As similarly mentioned, a dynamic computer model that integrates auxin-mediated cell elongation and cell proliferation suggested that differential cell growth enables organ bending. The model showed that asymmetric expression of the PIN-FORMED auxin efflux carrier at the inner compared to the outer side of the hook can induce an auxin maxima at the inner side that is translated into a differential growth between the two sides of the organ (Žádníková et al., 2016). Recent findings suggested the presence of a a positive feedback loop between auxin distribution and cell wall modifications establishing an asymmetry in the cell wall mechanochemical properties in the organ and promoting tissue bending and seedling emergence (Cao et al., 2019; Jonsson et al., 2021).

1.2 Plant sexual reproduction

Within the ovule of *Arabidopsis thaliana* two independent generation coexist: the diploid generation, or sporophyte, which embeds and sustains the haploid generation or the female gametophyte (Schmidt et al., 2015). To understand the relationship between the two generations is important to elucidate the mechanism of sexual reproduction in plants, with a particular focus to life cycle of angiosperm, the clade to which *A. thaliana* belongs (Figure 1 A).

The angiosperm life cycle, defined as haplodiplontic life cycle, alternates between multicellular haploid and diploid generations. The diploid adult, or sporophyte, phase is the main phase in

the life cycle of flowering plants. The haploid generation, produced through meiosis by the diploid sporophyte, gives rise to the gametes, which generate the embryo after fusion. The embryonic development corresponds to the following diploid generation (Figure 1 A).

In contrast to the animal kingdom, among the *Plantae*, gametes are not the direct result of a meiotic division. Diploid cells of the sporophyte produce through meiosis haploid spores, which subsequently undergo mitotic division to yield a multicellular haploid gametophyte. The gametes are formed during the mitotic divisions occurring within the gametophyte. Seed-bearing plants are characterized by gametophytes, which are dependent on autotrophic dominant sporophyte generation, in contrast to mosses where the sporophytes are nutritionally dependent on self-feeding gametophytes.

All spermatophytes are heterosporous, generating two types of spores, the male microspore and the female megaspore, which develop into separate male gametophyte (pollen or microgametophyte) and female gametophyte (embryo sac or megagametophyte). In angiosperm, male and female gametophyte production occurs in the reproductive organs present in the flower, in the stamens and in the carpel, respectively (Figure 1 A).

The stamens are present in the third whorl of the flower and consist of two morphologically distinct structures known as filament and anther (Figure 1 B). The filament serves as stalk-structure and provide structural and nutritional support for the anther, which bears reproductive and non-reproductive tissues. *Arabidopsis* presents four long and two short stamens (tetradynamous) and they are collectively termed androecium. An anther typically presents a four lobed structure containing a microsporangium or pollen sac, giving rise to four chambers called locules in which the pollen is formed (Figure 1 C). The sporogenous cells or pollen mother cells are encased in the tapetum, the inner most wall of the pollen sac, which provides the necessary nourishment for the developing pollen. The pollen mother cells undergo meiosis to produce tetrads of haploid microspores, which remains attached or separate after meiosis (Cardarelli & Cecchetti, 2014; Gómez et al., 2015). Microspores subsequentially divide through asymmetric mitosis to form a highly compact generative nucleus and a diffuse vegetative nucleus. Through a second round of mitosis the generative nucleus, divides to produce two identical sperm cells (Schmidt et al., 2015; Valuchova et al., 2020). At maturity, a pollen grain consists of three cells: two sperm cells formed from a generative cell, and a second cell that will become the pollen tube cell. One of the two sperm fuses with the egg cell to produce the next sporophyte generation, while the second sperm participate in the formation of the endosperm, the structure that provides nourishment for the embryo (Figure 1 A).

The fourth whorl of organs within the flower forms the carpel or gynoecium, in which the female gametophyte is formed (Figure 1 A, B). The carpel consists of three distinct structures the stigma, where the pollen attaches during pollination, the style, and the ovary (Figure 1 A). The ovary wall after fertilization develops into the fruit in angiosperms. One or more ovules are formed within the ovary from the placental tissue attached to the ovary wall and each ovule at maturity harbor the female gametophyte or embryo sac. Ovules of most flowering plants are composed of the nucellus, the chalaza and the funiculus that connect the ovule to placenta. The ovule has one or two outer layers of cells called the integuments, which retain at maturity a small opening called the micropyle, through which the pollen tube will grow. The integuments after fertilization develop into the seed coat. In *Arabidopsis* the female gametophyte originates from a single hypodermal cell, called the archespore, at the tip of the ovule primordium. The archespore directly differentiates into megasporocyte or megaspore mother cell (MMC) that undergoes meiosis to produce a tetrad of megaspores. Typically, only one functional megaspore survives while the others degenerate. The functional megaspore undergoes three rounds of nuclear division to form a syncytial female gametophyte (Schmidt et al., 2015; Kay Schneitz et al., 1995). Subsequently, nuclear migration, polar nuclear fusion, and cellularization take place to yield a seven-celled embryo sac referred to as a *Polygonum* type embryo sac (Figure 1 D). This type of embryo sac is composed of two synergids, important for pollen tube guidance and reception, one egg cell, one central cell, and three antipodals. The *Polygonum* type embryo sac occurs in around 70% of all angiosperms (Figure 1 D).

During pollination and subsequent germination of the pollen on the stigma, the pollen tube extends from the grain and grows down the style. The growing pollen tube access the embryo sac through the micropyle and grows through one of the synergids. The two sperm cells are released, and a double fertilization event occurs. One sperm cell fuse with the egg, producing a diploid zygote that will develop into the sporophyte. The second sperm cell fuses with the central cell forming a triploid cell that originates the endosperm, serving nutrient as storage for the developing embryo. The other accessory cells in the embryo sac degenerate after fertilization. The double fertilization and is unique phenomena happening in angiosperms.

The seed is formed and consists of a layer of integuments forming the coat, the endosperm with food reserves and, at the center, the embryo formed from the diploid zygote (Figure 1 A).

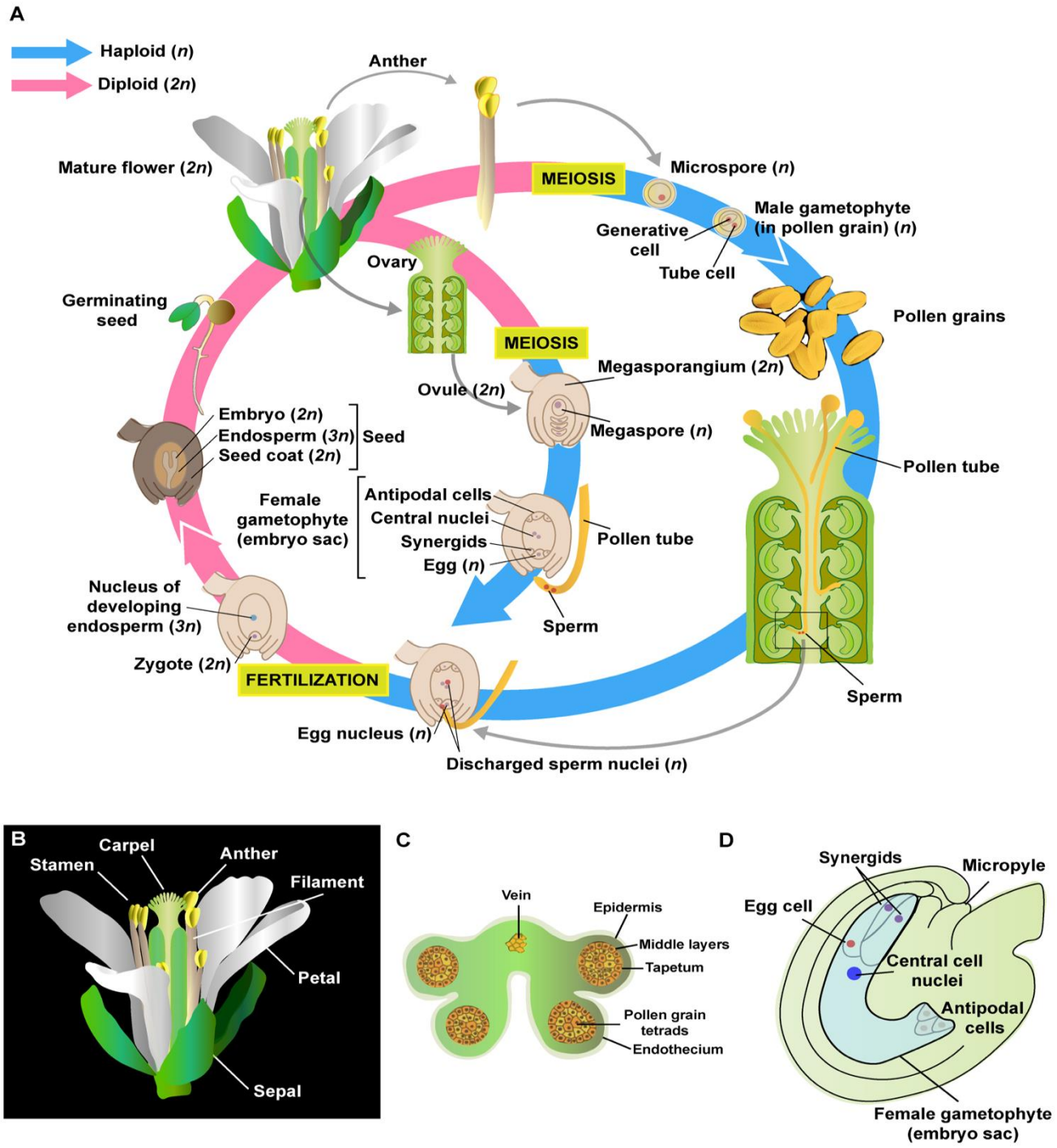

Figure 1 Life cycle of angiosperm and *Arabidopsis* gametophytes.

(A) Life cycle of *Arabidopsis*, showing the alternation of the generation. Image based on Pearson Publishing. (B) Flower of *Arabidopsis thaliana*. (C) Angiosperm anther. (D) Schematic view of the mature seven-celled female gamethophyte (FG) of *Arabidopsis*. The synergids are located at the micropylar pole. The egg cell nucleus is close to the central cell nucleus. Three antipodals are located at the chalazal pole of the embryo sac. Adapted from Sprunck & Groß-Hardt, 2011.

1.3 Ovule development

The ovule is the female reproductive organ of higher plants and represents the seed precursor. Seeds are the primary propagation unit of crop and fruit crops and they have an important role in humans and animal food production. For the centrality in plant reproduction, botanists and plant scientist have been interested in elucidating regulatory mechanisms involved in ovule development.

Arabidopsis thaliana has been used as the major model system for the study of ovule organogenesis and many genes involved in the molecular mechanisms regulating the organ patterning have been investigated (Chaudhary et al., 2018; Cucinotta et al., 2014; Shi & Yang, 2011). Development of wild-type ovule have been qualitatively well described and a comprehensive classification of discrete developmental stages based on morphological landmarks has been proposed for the first time by Schneitz et al. in 1995 (Christensen et al., 1997; Robinson-Beers et al., 1992; Schneitz et al., 1995). According to this staging system, ovule development is divided into four major steps: early ovule development, megasporogenesis, megagametogenesis and post-fertilization development. The detailed description follows the development of the sporophytic tissue and female gametophyte.

Primordium formation initiates stage 1. During stage 2 the megaspore mother cell differentiates within the nucellus and undergoes meiosis followed by cytokinesis. Two integuments initiate from the chalaza concomitantly to meiosis. Both integuments consist of two cell layers which grow to surround the nucellus. Starting with stage 3 the functional megaspore progress in the development and results into the embryo sac, while integument ontogenesis proceeds and the vascular strand becomes visible within the funiculus. At the end of stage 3 pre-fertilization development is completed and the mature ovule is ready to be fertilized. With stage 4 post-fertilization development can proceed. In Supplementary table 1 the stages of the ovule are summarized and the corresponding stages of flower development according to Smyth et al. are additionally reported (Schneitz et al., 1995; Smyth et al., 1990). The staging system will be adopted as a reference throughout this work.

1.3.1 Ovule primordia initiation

Arabidopsis ovules are initiated as small, finger-like primordia from specialized meristematic regions within the gynoecium referred as placenta (Robinson-Beers et al., 1992; Schneitz et al., 1995). The mature gynoecium of Arabidopsis is a Brassicaceae-type syncarpous gynoecium, composed of two congenitally fused carpels separated by a central septum, creating

two distinct compartments called locule. The gynoecium is composed of three distinct regions: the stigma, the style, and the ovary, which houses the ovules. The ovary consists of the valves (seedpod walls), replum (middle ridge), septum, and valve margins (
Figure 2 A). The gynoecium arises as a single cylinder at the center of the flower bud at stage 6 (Smyth et al., 1990). During development, longitudinal middle ridges protrude from opposite sides into the center of the cylinder and fuse to give rise to the septum (Bowman et al., 1999; Roeder & Yanofsky, 2006). The placental tissue differentiates along the length of the septum adjacent to the lateral walls and from this tissue ovule will initiate at stage 8 of flower development (Smyth et al., 1990; Schneitz et al., 1995). One row of ovule is found on opposite placenta in each locule leading to an interdigitated array of ovules within a locule (
Figure 2 B). Ovules are initiated by periclinal division in the subepidermal tissue of the placenta and subsequentially appears in rows as tightly packed, small bulges along the placenta (Schneitz et al., 1995). The ovule is a composite of three clonally distinct radial layers and its organization resemble the general architecture of plant organ into epidermis, first subepidermal layer and innermost layer (Jenik & Irish, 2000; Schneitz et al., 1995). According to the reference staging system, the primordia outgrowth corresponds to the stage 1-I and 1-II of the early phase of ovule development (Supplementary table 1).

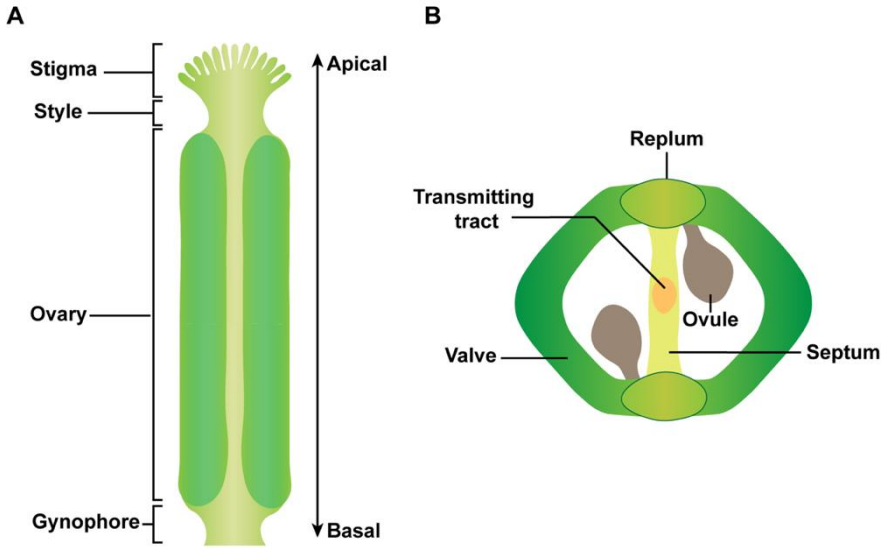

Figure 2 Structure of the *Arabidopsis* gynoecium.

(A) Schematic drawing of the mature gynoecium showing the different functional domain. (B) Drawing of cross section of the ovary at anthesis. Image based on Becker 2020.

The production of a new organ primordium depends on the establishment of a complex network of hormones and regulators that control the proper differentiation of tissues. The phytohormone auxin is central in plant organ formation and its synthesis and transport play an important role also in ovule outgrowth (Benková et al., 2003). Pistils of the double mutant *yucca1 yucca4* (*yuc1 yuc4*), characterized by an impaired auxin biosynthesis, show absence of ovules (Cheng et al., 2006). Additionally, the number of ovules in the partial loss-of-function mutant *pin1-5* is reduced compared to wild-type (Bencivenga et al., 2012). Cytokinin, acting in concert with auxin, is another important plant hormone involved in developmental processes. Plants with reduced cytokinin production or perception show a decreased ovule number and female fertility and additionally it has been showed that cytokinin modulates auxin fluxes during ovule development by regulating *PIN-FORMED 1* (*PIN1*) expression (Bartrina et al., 2011; Bencivenga et al., 2012).

A crucial event in plant lateral organ formation and more in general in plant organogenesis, is the formation of boundary regions. Organ boundaries are groups of specialized cells with restricted growth that separates distinct domains, like organ primordia or adjacent organs, and act as organizing center allowing differentiation of neighboring cell and providing positional clues necessary for the formation of new organ (Caggiano et al., 2017; Dahmann et al., 2011; Žádníková & Simon, 2014). The genes CUP-SHAPED COTYLEDON 1 (*CUC1*), *CUC2* and *CUC3*, encoding NAC-type transcription factors, are specifically expressed in organ and meristem boundaries and share redundant functions in lateral organ development and meristematic activity maintenance (Hasson et al., 2011; Vroemen et al., 2003). It has been reported that *CUC1*, *CUC2* and *CUC3* are also expressed at the ovule boundaries (Cucinotta et al., 2018; Galbiati et al., 2013; Gonçalves et al., 2015; Ishida et al., 2000).

AINTEGUMENTA (*ANT*), a member of the APETALA2-like transcription factors (TF) family has been reported to be important for ovule primordia outgrowth and patterning. The *ant* single mutant shows fewer and more distantly spaced ovule primordia. The remaining ovules are characterized by the lack the two integuments and by the arrest of the embryo sac development, suggesting that *ANT* has multiple functions during ovule development (Schneitz et al., 1998; Schneitz et al., 1997; Elliott et al., 1996). HUELLENLOS (*HLL*), an L14 subunit of mitochondrial ribosomal protein, have overlapping function with *ANT* and redundantly promote ovule primordia formation and patterning (Schneitz et al., 1998).

In recent years, an integrative model has been proposed in which the hormonal network and the aforementioned TFs act together in the initiation of ovule primordia (Figure 3 A) (Cucinotta et al., 2014; Galbiati et al., 2013). In the suggested model, *CUC1* and *CUC2*, in addition with

ANT, are regulated by the auxin response factor (ARF) MONOPTEROS (MP)/AUXIN RESPONSE FACTOR 5 (ARF5). CUC1 and CUC2 localized at the boundaries between emerging ovules control the expression of *PIN1*, which is essential for the formation of the primordia and occurs on the distal-lateral epidermis of the tip of the ovule primordium. Cytokinin may be involved downstream of CUC protein in the promotion of *PIN1* expression, since CUC protein are involved in cytokinin metabolisms (Cucinotta et al., 2018). This mechanism results in the accumulation of an auxin peak at the apex of the forming primordia, as indicated by the activity of the DR5rev::GFP reporter assessing auxin transcriptional response. A computation model has been developed to predict ovule primordia initiation based on the dynamic PIN1 localization and auxin distribution. The simulation showed that in response to PIN1, several localized auxin maxima are formed to promote ovule outgrowth in correspondence to these local maxima, highlighting an asynchrony in the primordia initiation in the gynoecium (Yu et al., 2020). The established auxin maximum may in turn inhibit *CUC1/2*. It has been recently discovered the role of the hormonal brassinosteroid signaling pathway in the positive regulation of the ovule primordia number, partly by the regulation of *ANT* through the BRASSINAZOLE-RESISTANT 1 (BZR1) TF and by strengthening auxin response, extending the model of ovule initiation (Cucinotta et al., 2020; Huang et al., 2013; Yu et al., 2020). Moreover, evidences have shown an additional role of *CUC2* and *CUC3*, acting redundantly in ovule separation, suggesting a differential molecular network regulating the primordia initiation and ovule separation (Gonçalves et al., 2015).

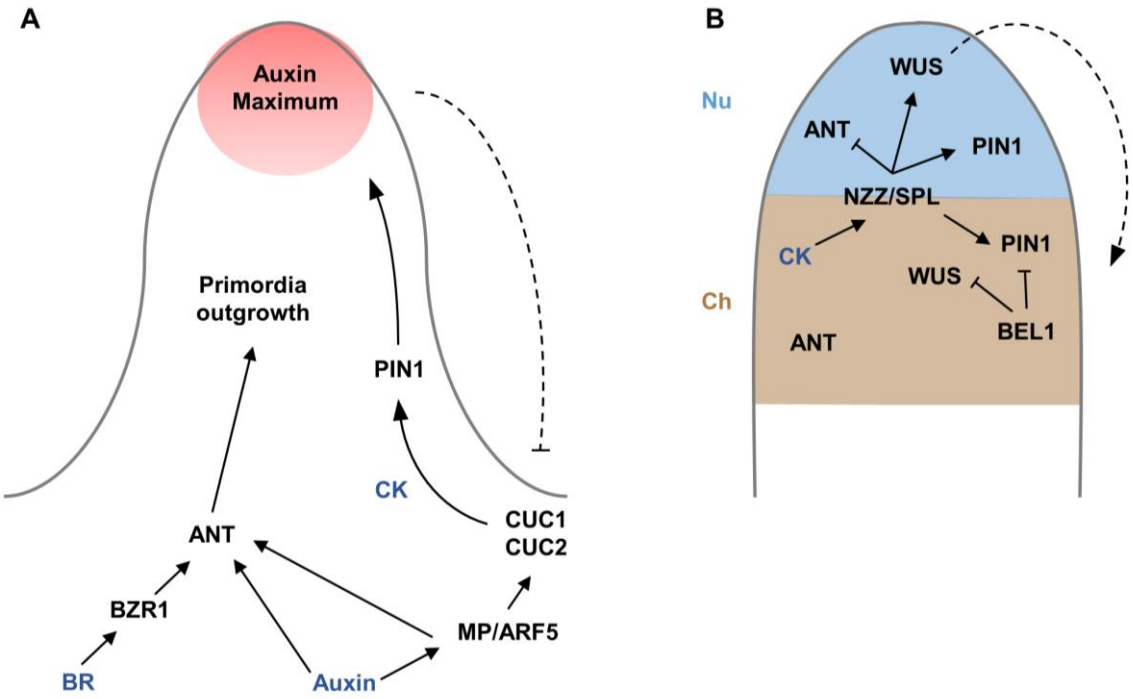

Figure 3 Gene and hormonal network model involved in primorium outgrowth and patterning.

(A) Primordium outgrowth and early outgrowth. (B) Genes involved in early ovule patterning. *NZZ/SPL* and *BEL1* are involved in chalaza specification. *WUS* is involved in nucellus identity. Abbreviations: Nu, nucellus; Ch, chalaza; CK, cytokinin; BR, Brassinosteroid. Adapted from Bencivenga et al., 2013.

1.3.2 Ovule patterning

Following initiation of the ovule primordium the three pattern elements are established along the proximal-distal (PD) axis: the distal nucellus, central chalaza, and proximal funiculus or stalk which harbors the vascular strand and connects the ovule to the placental tissue of the gynoecium (Figure 4). The nucellus is the tissue harboring the sporogenous cells, while the central chalaza is characterized later on by the initiation of two integuments at its flanks (Schneitz, 1999; Schneitz et al., 1998). Although, it remains still unclear how the sequential establishment of PD pattern elements is orchestrated with the simultaneously occurring of the primordia emergence, several of the major patterning genes have been identified.

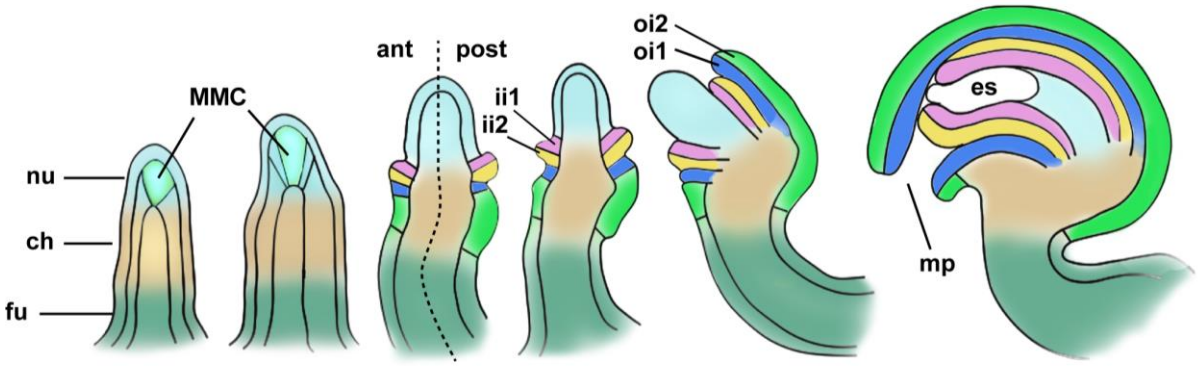

Figure 4 Ovule development.

Schematic representation of ovule development depicting the various functional domain. Abbreviations: nu, nucellus; ch, chalaza; fu, funiculus; ant, anterior; post, posterior; ii2, abaxial inner integument; ii1, adaxial inner integument; oi2, abaxial outer integument; oi1, adaxial outer integument; mp. micropyle; es, embryo sac.

The TF gene *NOZZLE (NZZ)/SPOROCYTELESS (SPL)* is an important regulator of nucellus formation and MMC development (Schiefthaler et al., 1999). In ovules of *nzz/spl* mutants the nucellar region is characterized by a reduction in the length and the MMC frequently fails to be produced. SPL/NZZ also promotes the growth of ovule integuments, showing to be involved in many events of development, with particular relevance in the coordination of ovule patterning (Figure 3 B) (Balasubramanian & Schneitz, 2000; Balasubramanian & Schneitz, 2002).

An important aspect of ovule patterning along the PD axis is the communication between the nucellus and the chalaza. It has been suggested that the distal nucellus is established independently, since it was observed the presence of the nucellus in *hll ant* double mutants characterized by the absence of the chalaza and/or funiculus (Schneitz et al., 1998). However, the development of the chalaza requires instructions provided by the nucellus, speculating that the PD patterning takes place progressively and in a distal–proximal direction (Schneitz et al., 1997).

A clear example of this mechanism is provided by the TF WUSCHEL (WUS). The expression of *WUS* is restricted to the nucellus and not detectable in the chalaza, however WUS is central in the promotion of the development of the latter pattern element (Gross-Hardt et al., 2002; Sieber et al., 2004b). To determine the role of *WUS* during ovule development, Gross-Hardt et al. (2002) generated a *wus* mutants carrying a WUS cDNA under the transcriptional regulation of the CLAVATA1 (pCLV1::WUS). These lines were able to overcome the *wus* meristem and

floral defects to reveal the effects of the mutation on ovules. The ovules produced by *wus* mutants are similar in appearance to *ant* mutant ovules, characterized by the complete lack of integuments (Groß-Hardt et al., 2002). WUS protein is not detected in the chalaza, suggesting that *WUS* controls chalaza development through a non-cell-autonomous mechanism (Groß-Hardt et al., 2002).

An additional example of the communication between the nucellus and the chalaza is the regulation of the *ANT* expression domain exerted by NZZ (Figure 3 B). As already mention, ANT shows a role in promoting the primordium outgrowth and it is required for chalaza identity specification and integument initiation. *ANT* is expressed throughout the young ovule primordia and later on, before integument initiation, its expression becomes restricted to the distal funiculus and chalaza (Balasubramanian & Schneitz, 2000). *NZZ* influences the distal extend of *ANT* in the chalaza through negative regulation of *ANT* in the nucellus. In the *nzz* mutant the length of the nucellar region of the primordium is reduced. This reduction has been associated with the ectopic *ANT* expression causing a distal shift in the position of integument formation along the PD axis, which is consistent with the observed increase in the funicular length (Balasubramanian & Schneitz, 2000; Schiefthaler et al., 1999). Moreover, the *nzz ant* double mutants are *ant*-like, with no obvious reduction of the nucellus, indicating that a major role of *NZZ* is the spatial limitation of *ANT*. The pattern of *ANT* expression is crucial for the establishment of the correct location of integument initiation.

Another gene required for the correct chalazal formation is *BELL1* (*BEL1*), which encodes for a homeodomain putative TF. In *bel1* mutants the chalazal domain undergoes altered development and irregular outgrowths of unknown identity are formed instead of integuments (Reiser et al., 1995). One function of BEL1 is to prevent *WUS* expression from the chalaza (Figure 3 B). In *situ* hybridization analysis of *bel1* have revealed the expression of *WUS* in the chalaza and funiculus in addition to the nucellus, speculating that the enlargement and irregularity in the shape of the integument might be due to *WUS* ectopic expression in these pattern elements (Brambilla et al., 2007). Another function of BEL1 is to control chalaza formation, synergistically interacting with NZZ. It has been observed in *nzz bel1* double mutants that the chalaza is replaced by funiculus-like tissue (Balasubramanian & Schneitz, 2000). Bencivenga et al., (2012), has provided first insights into the molecular mechanism underlying the interplay between BEL1, NZZ/SPL and WUS, showing the involvement of cytokinin and auxin signaling (Figure 3 B). In addition to the function of PIN1 in the ovule primordia outgrowth, PIN1-mediated polar auxin transport is necessary for early gametophyte development and integument initiation (Ceccato et al., 2013). In wild-type ovule the expression

of *PIN1* requires cytokinin signaling and NZZ activity and it is observed in the epidermis of the nucellus as well as in the early inner layer of the inner integument (Bencivenga et al., 2012; Benková et al., 2003). According to the proposed molecular model, in wild-type ovule, *WUS* is activated by cytokinin, which in turn promotes the expression of *NZZ* in the nucellus and *BEL1* in the chalaza (Brambilla et al., 2007; Sieber et al., 2004b). In the nucellus *PIN1* expression is activated in the by NZZ and repressed in the proximal part of the chalaza by BEL1, which in turn represses WUS (Brambilla et al., 2007). In the *bel1* mutant, *PIN1* is ectopically expressed in the chalaza epidermis leading to the outgrowth formation. Therefore, in the *bel1 nzz* double mutant, the ectopic expression of *PIN1* in the chalazal due to the lack of BEL1 function, is not possible as activity of the positive PIN1 regulator NZZ is absent (Bencivenga et al., 2012). As consequence, the central region does not follow a chalaza pathway and the ovule primordium attains funiculus-like identity.

1.3.3 Germline initiation

The formation of the female gametophyte occurs within the developing ovule and is divided into two main steps, megasporogenesis and megagametogenesis (Bajon et al., 1999; Christensen et al., 1997; Schneitz et al., 1995).

Megasporogenesis comprises three major events: MMC formation, meiosis to produce haploid megaspores, and megaspore selection. The development of a single MMC or meiocyte is the first step in germline formation. During early ovule formation, a sub-epidermal diploid somatic cell at the distal end of the ovule primordium forms the archesporial cell. In *Arabidopsis* and most other species, the archesporial cell differentiates directly into the MMC (Drews & Koltunow, 2011). Relative to the surrounding sub-epidermal cells, the MMC is larger and has a denser cytoplasm and a larger nucleus. Just before meiosis, the megaspore mother cell is dramatically enlarged and elongated (Lora et al., 2017). The megaspore mother cell then undergoes meiosis resulting in the formation of four haploid spores, called tetrad. The three most apical megaspores undergo programmed cell death; however, the most proximal one persists forming the functional megaspore, which proceeds into megagametogenesis (Schneitz et al., 1995). Recent reviews have summarized key insight into the pathways involved in the female germline development and thus the transition from somatic to reproductive fate (Hater et al., 2020; Lora et al., 2019; Nakajima, 2018; Pinto et al., 2019).

The increase in the nuclear volume observed in the differentiated MMC may reflect a change in the epigenetic landscape. Indeed, specific chromatin decondensation and re-programming

were observed during MMC differentiation in *Arabidopsis* (Baroux & Autran, 2015; She et al., 2013; She & Baroux, 2015).

Recent studies have highlighted the role of small interfering RNA (siRNA)-dependent suppression of transposable elements (TEs) in MMC specification (Martinez & Köhler, 2017; Martínez & Slotkin, 2012; Nonomura, 2018). Mutations in genes encoding components of siRNA biogenesis and function, including *ARGONAUTE9* (*AGO9*) and other *ARGONAUTE* genes, *RNA-DEPENDENT RNA POLYMERASE6* (*RDR6*), involved in RNA-dependent DNA methylation (RdDM) and *SUPPRESSOR OF GENE SILENCING3* (*SGS3*), result in the formation of multiple MMCs per ovule (Durán-Figueroa & Vielle-Calzada, 2010; Hernández-Lagana et al., 2016; Olmedo-Monfil et al., 2010). Multiple MMC cells per ovule were also reported in mutants of the THO/TREX complex genes (*TEX1*, *HPR1*, and *THO6*). The THO complex is involved in the biogenesis of TAS3-derived *trans*-acting siRNA (ta-siRNA) molecules that spatially restrict the expression of the *AUXIN RESPONSE FACTOR 3* (*ARF3*) gene to the chalazal region of the ovule, while TEX1 is localized in the nuclei of the epidermal cell layer, producing unknown signals that restrict MMC fate (Su et al., 2017). This novel siRNA-dependent mechanism involved in the regulation of *ARF3* functions could represent a possible link between *ARF3* and the local auxin response at the ovule apex (Ceccato et al., 2013; Su et al., 2017). Although, the mechanism through which ARF3 coordinates the local auxin response in the MMC specification is not yet clear.

An early factor in the control of MMC specification and fate is represented by NZZ as *nzz* mutants frequently fail to form an MMC (Balasubramanian & Schneitz, 2000; Schiefthaler et al., 1999). A molecular function for *NZZ* has recently been reported in, suggesting that it may act as a transcriptional co-repressor (Chen et al., 2014). In both male and female sporogenesis, NZZ uses the EAR motif to recruit a TOPLESS/TOPLESS-RELATED (TPL/TPR) and histone deacetylase (HDAC) complex to inhibit CINCINNATA (CIN)-like TEOSINTE BRANCHED1/CYCLOIDEA/PCF (TCP) TFs, thereby promoting meiotic fate in the anther and ovule (Chen et al., 2014; Wei et al., 2015).

Additionally, *NZZ* may in part function through WUS as *WUS* expression was found to be reduced in *nzz* mutants (Sieber et al., 2004b). Furthermore, WUS in turn up-regulates the expression of the small peptides WIH1 (*WINDHOSE1*) and WIH2, which have been linked to megasporogenesis regulation (Lieber et al., 2011) Double mutants of *WIH1/2* genes show defective megasporogenesis in which ~30% of ovules failing to produce an MMC.

It has been reported that the upstream regulation of *NZZ* involves the RdDM pathway, that might be involved in restricting the female germline as mentioned before, suggesting a link

between the different molecular networks involved into the MMC cell fate specification (Mendes et al., 2020). The RdDM pathway silences *NZZ* directly, by degrading its mRNA through AGO9 and/or by methylation of the *NZZ* genomic region through methyltransferases DOMAINS REARRANGED METHYLASE1 and DRM2.

The entry into the germline, namely the MMC specification, appears to be tightly coupled with cell cycle transition from mitosis to meiosis. Zhao et al. (2017) have revealed some of the components involved in the 'meiotic competency' necessary for the entry into meiosis of the committed MMC, including cell cycle regulators cyclin-dependent kinase (CDK) inhibitors belonging to the *KIP-RELATED PROTEIN* (*KRP*) family and *RETINOBLASTOMA-RELATED 1* (*RBR1*) (Zhao et al., 2017). The analysis of loss-of-function *KRP* genes formed supernumerary MMCs, which failed to switch from mitosis to meiosis and differentiating later into functional embryo sacs. Similar phenotype was observed in loss-of-function mutants of RBR1. KRPs and RBR1 mutually promote each other's function via suppression of CDKA;1. In addition to its canonical function in regulating entry into S-phase, RBR1 directly represses WUS, excluding its activity from the developing MMC, enabling MMC differentiation and switch to meiosis (Zhao et al., 2017). This molecular network provides a direct link between the cell cycle machinery and the cell fate regulator *WUS.*

As already mentioned, auxin and cytokinin distribution polarizes ovule primordia development and polarized accumulation of both phytohormones continues during megasporogenesis. Auxin is accumulated at the nucellar epidermis at the distal tip of young ovules via PIN1 and PIN3 (Benková et al., 2003; Ceccato et al., 2013; Pagnussat et al., 2009), while cytokinin has been reported at the proximal part of the ovule, at the chalaza (Bencivenga et al., 2012; Cheng et al., 2013; Zürcher et al., 2013). Moreover, the two hormonal networks are linked through the control of *PIN1* expression carried out by cytokinin (Bencivenga et al., 2012). The female germline in *Arabidopsis* develops while polarized by the auxin and cytokinin present in the maternal tissue. Changes in the hormones distribution affect gametophyte formation, as observed in *nzz* mutant where the auxin maxima was not observed (Bencivenga et al., 2012). Expression of *PIN1* require NZZ and it has been shown that mutation in gene encoding the β-subunit of RGT (*RGTB1*), a component of the RAB-dependent vesicular trafficking, leads to internalization of PIN1 and PIN3 causing a disturbance in auxin homeostasis and affecting the female gametogenesis (Rojek et al., 2021).

1.3.4 Female gametophyte formation

After meiosis four haploid megaspores are formed but only the chalazal-most one survives, the functional megaspore, which proceeds into megagametogenesis. Three steps are involved: a series of mitoses without cytokinesis, followed by cellularization of the nuclei and then cell differentiation. The process has been morphologically well-described, and subdivided into steps from FG1 to FG7 (Christensen et al., 1997). The formation of the functional megaspore marks the FG1 stage of megagametophyte development. Subsequently, the functional megaspore undergoes three consecutive mitotic divisions to form a syncytial female gametophyte (FG1–FG4) that lead to the formation of the mature embryo sac (FG5). During and after cellularization, one nucleus from each pole migrates toward the center of the developing eight-nucleated female gametophyte and they fuse. The mature embryo sac results in a seven-celled mature gametophyte, referred to as a *Polygonum* type embryo sac (Drews & Koltunow, 2011). It harbors one egg cell, one central cell, two female gametes, the synergid cells, which are important for pollen tube guidance and reception, and three antipodal cells which might be involved into in transferring nutrients from the surrounding sporophytic tissues to the embryo sac (Figure 1 D) (Hater et al., 2020). Both the egg cell and the central cell are gametic and are fertilized by the two sperm cells delivered by a single pollen tube, originating the zygote and the triploid endosperm, respectively.

The switch from meiotic phase to the mitotic development of the gametophyte is a vital step in plant reproduction. The two protein RANGTPase ACTIVATING PROTEIN 1 (RanGAP1) and RanGAP2 involve in the nucleocytoplasmic transport, have shown a specific role in the syncytial mitosis in the embryo sac (Rodrigo-Peiris et al., 2011). Recently, the ovule-specific group of RWP-RK domain-containing (RKD) transcription factors were shown to be involved in FM-to-FG transition and regulation of the mitotic growth phase (Tedeschi et al., 2017)

The developing gametophyte shows a distinct polarity between the micropylar and the chalazal pole (Sprunck & Groß-Hardt, 2011). The positional information for this polarity is provided by the maternal polar hormonal pattern: chalazal cytokinin biosynthesis and response and polar auxin transport mediated by PIN1 directed at the tip of the nucellus (Bencivenga et al., 2012; Benková et al., 2003; Cheng et al., 2013; Pagnussat et al., 2009). Knockout or knockdown mutant of PIN1 in the ovule lead to arrested development in the mono- or binuclear embryo sac stage, demonstrating the importance of the maternal hormonal network (Ceccato et al., 2013). However, although the regulating role of auxin in the sporophyte is evident, the role in the patterning of the female gametophyte is still debated. Improved cell biological approaches

did not provide evidence for auxin accumulation within the female gametophyte (Ceccato et al., 2013; Lituiev et al., 2013). Auxin-mediated processes in the sporophytic cells may indirectly regulate cell fate decision in the developing embryo sac. Further evidence suggests a direct role of the cytokinin signaling pathway in the establishment of gametophyte polarity. Around four-nucleate stage, the histidine kinase CYTOKININ INDEPENDENT1 (*CKI1*) is polarly activated at the chalazal pole of the female gametophyte (Yuan et al., 2016). Mutants defective for *CKI1* exhibit micropylar characteristics also in the chalazal half, while ectopic expression of *CKI1* causes expansion of central cell signatures toward the micropylar end (Hejátko et al., 2003; Pischke et al., 2002; Yuan et al., 2016).

Within the mature embryo sac, cellularization-mediated compartmentalization is required for the establishment and specification of cell fate. Many factors that control cell fate decisions have been identified either through forward genetics or transcriptome analysis (Hater et al., 2020; Nakajima, 2018; Schmidt et al., 2011; Sprunck & Groß-Hardt, 2011; Steffen et al., 2007; Susaki et al., 2021). The transcription factors MYB64 and MYB119 are essential for the cell specification. *MYB119* expression becomes restricted to antipodal and central cell nuclei, and MYB119 protein is detected only in the central cell nucleus. By contrast, MYB64 is found in the central and egg cell nuclei (Rabiger & Drews, 2013). Additionally, many genes such as *LACHESIS*, *CLOTHO*, *ATROPOS*, *BEL1-LIKE HOMEODOMAIN* (*BLH1*), *AGAMOUS-LIKE80* (*AGLO80*) and *AGL61* have been reported to control egg cell fate (Bemer et al., 2008; Groß-Hardt et al., 2007; Moll et al., 2008; Pagnussat et al., 2007; Steffen et al., 2008).

The embryo sac development is highly synchronized with the development of the maternal sporophyte surrounding the gametophyte. During megagametogenesis the outer and inner integument grow to surround the embryo sac providing sustainment. It has been observed that in most of the known sporophytic ovule development mutants the embryo sac development is severely affected (Baker et al., 1997; Gaiser et al., 1995; Klucher et al., 1996; Ray et al., 1996; Reiser et al., 1995; Schneitz et al., 1997). Interesting, many of the gametophytic mutants described to date are characterized by a normal development of the ovule sporophytic tissues. Therefore, it has been proposed that a hierarchy exists in the communication between the two generations, attributing a higher order to the sporophytic maternal tissues (Bencivenga et al., 2011).

1.3.5 Integument initiation

Slightly after the first appearance of the MMC in the ovule primordia at stage 2-I, the initiation of the inner and the outer integument become apparent at the flanks of the chalaza (Figure 4) (Robinson-Beers et al., 1992; Schneitz et al., 1995). The ovule of *Arabidopsis* is a bitegmic ovule, consisting of two distinct integuments, which grow in a coordinated manner over the nucellus and enclose the embryo sac, leaving the micropyle at the apex of the mature ovule (Figure 5 A). Both the integuments consists of a two-layered structure, formed by an abaxial (or dorsal) and an adaxial (or ventral) layer (Figure 5 B) (Schneitz et al., 1995; Truernit & Haseloff, 2008). At maturity the ovule shows its characteristic anatropous shape, meaning that the ovule is curved toward the placenta and the micropyle results oriented toward the apex of the gynoecium (anterior or gyn-apical), from which the pollen tube will reach for the fertilization of the female gametophyte (Figure 5 C, D). Moreover, integuments show additional axes including the proximal-distal (PD) axis and a medio-lateral (ML) axis for the outer integument, which derives from the hood-like shape (Figure 5 E). The ML axis encounter on the lateral side a frontal region (Figure 5 E).

The earliest diverging angiosperm lineages are largely bitegmic and anatropous and these two characters are likely to be intimately connected (Doyle & Endress, 2000; Endress & Igersheim, 2000; Endress, 2011; Shi et al., 2021).

The inner integument (ii) initiates earlier than the outer integument, around stage 2-II, and become apparent as a bulging ring of cells in the region of the chalaza proximal to the nucellus. Around stage 2-IV, the inner integument appears as a two-layered radially symmetric structure surrounding the base of the nucellus. At later stage of ovule development, when the integuments have eventually surrounded the nucellus, the adaxial inner integument (ii1) differentiates into an endothelium characterized by cells with cube-like shape and very little or absent vacuolization. Before fertilization, the adaxial inner integument gives rise to an additional cell layer called parenchymatic inner integument (ii1') (Schneitz et al., 1995). The outer integument (oi) become evident later than the inner integument, as a semi-annular bulging at the side of the chalaza that faces the basal end of the carpel (posterior or gyn-basal) (Figure 5 D). In contrast to the inner integument, the outer integument is characterized by asymmetric growth, which mostly occurs at the posterior side of the organ (Figure 5 D, E) (Robinson-Beers et al., 1992; Schneitz et al., 1995). Both integuments are solely of epidermal origin (L1) and are the only lateral organs produced by the ovule (Jenik & Irish, 2000).

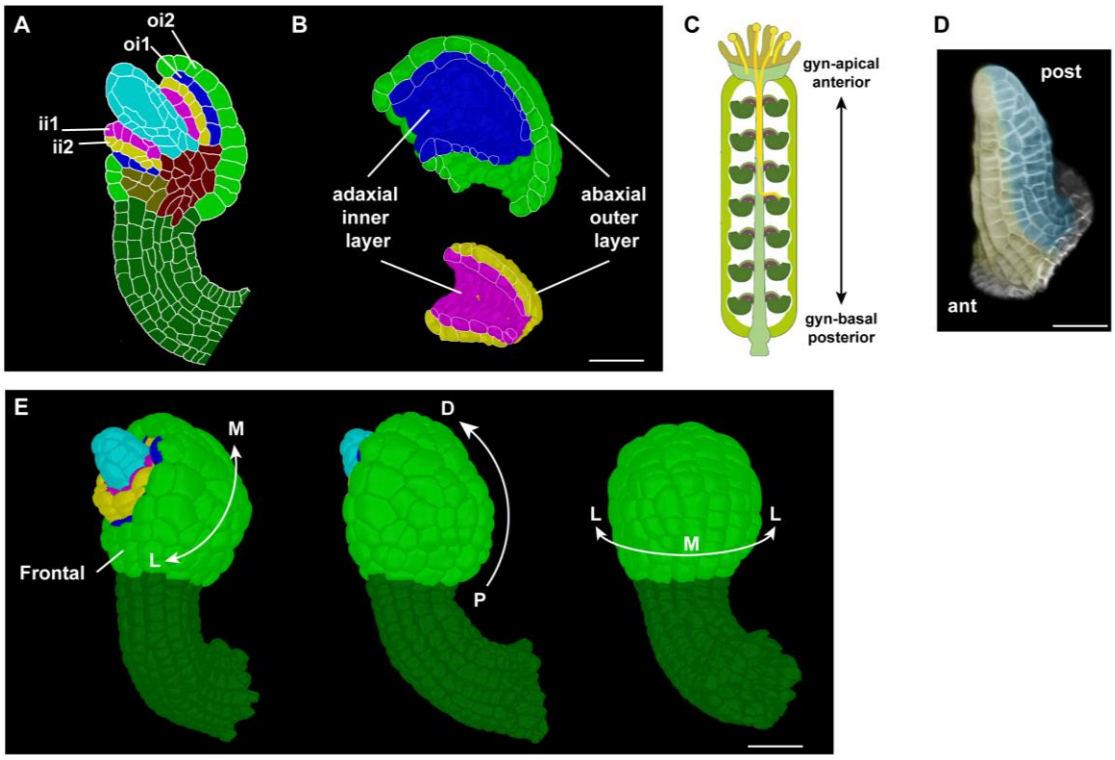

Figure 5 Integument polarity and ovule axes.

(A) Mid-sagittal section of 3D cell mesh showing the cell type annotation of an ovule stage 2-V. (B) Section view of the 3D cell meshes of the outer (top) and inner (bottom) integument showing the abaxial (or dorsal) and an adaxial (or ventral) layer. (C) Drawing showing the ovule orientation within the carpel. Image adapted from Vijayan & Tofanelli et al., 2021. (D) Ovule anterior-posterior axis. (E) Integument ML and PD axis. Abbreviation: oi2, abaxial outer integument; oi1, adaxial outer integument; ii2, abaxial inner integument; ii1, adaxial inner integument; ant, anterior; post, posterior; M, medio; L, lateral; P, proximal; D, distal. Scale bar: 20 µm.

The evolutionary origin of the integuments is still not clear and matter of debate. According to the telome theory, the integuments originated from the fusion of sterile or fertile branches (telomes) (Herr, 1995; Zimmermann, 1952). It is generally believed that the inner and outer integument derived independently. While the inner integument most likely originated directly from the fusion of telomes or sporangiophores, the outer integument is believed to have developed later from a cupule, a leaf-like structure surrounding one or more ovules (Stebbins, 1974). Recent development in technology allowed the analysis of several groups of Mesozoic ancient fossil plants, giving confirmation to this hypothesis, that the second integument of angiosperms derives from recurved cupules (Shi et al., 2021).

Some genes have been reported to be required for the formation of the integuments. As mentioned before, *ANT* and *WUS* are essential for their formation, as it is observed in *ant* and *wus* single mutant lacking both the integuments (Elliott et al., 1996; Gross-Hardt et al., 2002;

Schneitz et al., 1998). In plants ectopically expressing *WUS* in the chalazal region under the control of the *ANT* promoter, it has been observed the formation of ectopic integuments toward the base of the ovule, indicating that WUS is required for the formation of the integuments. Nevertheless, these ectopic structures are highly unorganized and irregular, suggesting that more factors are involved in the correct initiation and growth of the integuments (Groß-Hardt et al., 2002). In wild-type plants, the spatial relationship between *WUS* expression in the nucellus and *ANT* expression in the chalaza seems to determine the site of inner integument growth. Another gene required for the correct initiation and growth of the integument is *BEL1*. As already mentioned, *bel1* mutants show abnormal outgrowths in place of integuments, indicating that the correct patterning of the central chalaza is required for the lateral organ outgrowth (Brambilla et al., 2007; Reiser et al., 1995).

In addition to those genes involved in the PD patterning of the ovule, other genes are required for the integument identity. *INNER NO OUTER* (*INO*) is a central known factor involved in the early formation of the outer integument. Loss of *INO* function, results in the absence of the outer integument and alteration in the development of the female gametophyte (Baker et al., 1997; Schneitz et al., 1997). *INO* encodes a YABBY putative TF and it is the only YABBY gene expressed in the ovule (Meister et al., 2002; Villanueva et al., 1999). The YABBY gene family in Arabidopsis includes *CRABS CLAW* (*CRC*) and *INO* expressed exclusively in reproductive organs and *FILAMENTOUS FLOWER* (*FIL*), *YAB2*, *YAB3* and *YAB5* which exhibit both vegetative and reproductive expression (Simon et al., 2017; Villanueva et al., 1999). Evidences suggested that proteins of the YABBY family members promotes abaxial cell fate specification and regulate laminar growth expansion in lateral organ formation (Bowman, 2000). In *situ* hybridization showed the spatial distribution of *INO* transcript accumulation. The expression of *INO* is firstly detected in a group of epidermal cells on the posterior half of each ovule primordium, before the emergence of the integuments (Villanueva et al., 1999). Those cells expressing *INO* correspond to the site of outer integument initiation. Later, *INO* is expressed on the abaxial outer integument (oi2). Analysis of *INO* expression in the context of ovule mutants background revealed that in *SUPERMAN* (*SUP*) ovule, characterized by symmetric growth of the outer integument resulting in long tubular structure, the area of *INO* transcript accumulation extends on both side of the ovule (Villanueva et al., 1999). The ectopic expression of *INO* in *sup* mutants results in the growth of the outer integument on both sides of the ovule forming a radially symmetrical structure, indicating that *INO* in the context of the chalaza is sufficient for outer integument initiation and growth (Gaiser et al., 1995; Meister et al., 2002). The gene *SUP*, encoding a zinc-finger TF, was initially

identified for its involvement in the determination of carpel identity and from the observation of the phenotype in the flowers, characterized by the presence of supernumerary stamens and defects in the carpel formation (Coen & Meyerowitz, 1991). In addition to the flower abnormalities, ovules show alteration in the shape and polarity development (Gaiser et al., 1995). *SUP* is involved in the asymmetric expression of *INO* in the ovule, repressing *INO* expression in the anterior side of the ovule (Meister et al., 2002). It has been shown that the expression of *SUP* under the control of the *INO* promoter is sufficient to reduce the integument growth and mimic the *ino* mutant phenotype (Meister et al., 2002). The identification of a transcription repression domain in *SUP* support its role as suppressor of *INO* (Hiratsu et al., 2002). However, the mRNA accumulation of *SUP* has only be reported in the funiculus, in area adjacent to the chalazal region where *SUP* appears to suppress *INO* expression, showing a non-cell autonomous activity (Sakai et al., 1995).

The first axis of symmetry of the organ to be established is the PD axis within the ovule primordia. Before the appearance of the integuments, the primordia are radially symmetric structures. The initiation of the outer integument marks the first sign of the polarity along the anterior-posterior (AP or gynapical-gynbasal) axis in a developing ovule (Figure 4 and 5 D). Ovule at stage 2-III shows polarity in two axes of symmetry and this event correspond to the switch from a radially symmetrical structure to a bilateral symmetric organ (Schneitz et al., 1995). As previously mentioned, the outer integument shows differential growth along the AP axis, initiating and elongating only on the anterior side of the organ. A crucial molecular factor involved in the orchestration growth patterns along the axes of polarity was identified in *NZZ*, which integrates the pattern formation along the PD axis with its interaction with *BEL1* and *ANT* and the establishment of the AP axis regulating the timing of the outer integument initiation through the regulation of *INO* (Balasubramanian & Schneitz, 2000; Balasubramanian & Schneitz, 2002). *NZZ* acts redundantly with *BEL1* in restricting *WUS* expression to the nucellus for the proper chalaza formation (Balasubramanian & Schneitz, 2000; Brambilla et al., 2007; Sieber et al., 2004b). For the correct establishment of the PD patterning *NZZ* negatively regulates *ANT* in the nucellus and delimits the distal extent of *ANT* expression (Balasubramanian & Schneitz, 2000). In *nzz* mutant is observed a shift, more distally, in the spatial distribution of *ANT* causing a distal shift of the position of integument formation along the PD axis (Balasubramanian & Schneitz, 2000; Schiefthaler et al., 1999). In addition to the defect in the PD patterning causing positional defects, *nzz* mutant shows alteration in the temporal arrangement of integument initiation. The outer integument in *nzz* mutant usually initiate before the inner integument and often both integuments show a reduced growth at later

stages (Balasubramanian & Schneitz, 2000). It has been shown that *NZZ* is a positional and temporal regulator of *INO* expression, coordinating *INO* regulation with other genes and showing its central role in the ovule patterning along different axes (Balasubramanian & Schneitz, 2002). The analysis of the expression pattern in *ant* and *nzz* mutants revealed that for the proper temporal expression of *INO*, *ANT* and *NZZ* needs to coordinate their activities. An early and a later onset of *INO* expression has been observed for *nzz* and *ant* mutants respectively, indicating their roles as negative and positive temporal regulators. The negative temporal regulation of *INO* performed by NZZ has been identified as the molecular link for the coupling of the PD patterning with AP patterning (Balasubramanian & Schneitz, 2002).

1.3.6 Integument polarity

A central factor involved in the early formation of the outer integument is INO, which encodes a YABBY- family putative TF. YABBY genes are known regulators of the abaxial identity in lateral organs, indicating that abaxial-adaxial (ab-ad or dorso-ventral) polarity establishment can play a role in the in the integument initiation and growth (Figure 5 B) (Bowman, 2000; Siegfried et al., 1999). During the development of later organ such as leaves, sepals, petals and carpels it has been observed that the juxtaposition of adaxial and abaxial signals is required for the correct outgrowth (Bowman et al., 2002; Du et al., 2018; Eshed et al., 2001, 2004). Few key gene families have been identified in the establishment ab-ad polarity in lateral organ, including HD-ZIPIII transcription factor genes for the control of adaxial identity and the KAN gene family in the regulation of abaxial identity (Emery et al., 2003; Eshed et al., 2004, 2001; Kerstetter et al., 2001; McConnell et al., 2001). Members of these gene families also affect the growth and shape of the integuments, and mutation in these genes have shown to also affect integument development (Bowman et al., 1999; McAbee et al., 2006; Villanueva et al., 1999b). *ABERRANT TESTA SHAPE/KANADI4* (*ATS*/*KAN4*) is a member of the KANADI gene family expressed in the abaxial inner integument (ii2) and is involved in the laminar extension of the inner integument and in the maintenance of integument separation (McAbee et al., 2006). In *ats* mutant ovules, the two integuments fail to form separate structures, giving rise to a single ‘fused’ integument, leading to an aberrant heart-shaped seeds (Leon-Kloosterziel et al., 1994; McAbee et al., 2006).

It has been shown that *ATS* acts as temporal repressor together with *NZZ* in the regulation of *INO* expression (Balasubramanian & Schneitz, 2002). In the double mutant *nzz ats* ovule phenotype was reported to be like *sup* mutant. The analysis of *INO* expression, showed a

similar pattern of expression reported for *sup* mutant, with the expression detectable on both the side of the ovule (Balasubramanian & Schneitz, 2002; Villanueva et al., 1999).

Other abaxial polarity determinants belonging to the KANADI gene family, *KAN1* and *KAN2*, are involved in the specification and laminar outgrowth of the outer integument in conjunction with the YABBY TF INO. Loss of function of *KAN1* and *KAN2* causes alteration in the outer integument outgrowth, which results in an amorphous structure (Eshed et al., 2004; Kelley et al., 2009; McAbee et al., 2006).

The HD-ZIPIII genes *PHABULOSA* (*PHB*), *PHAVOLUTA* (*PHV*), and *CORONA* (*CNA*) are expressed adaxially in both leaf and inner integument primordia (Kelley et al., 2009; Sieber et al., 2004a). Triple mutants *cna phb phv* ovules show a variable phenotype in addition to other developmental defects, including defects in the integuments length and planar outgrowth (Kelley et al., 2009b; Prigge et al., 2005). MicroRNA resistant forms of HD-ZIPIII genes produce effects on both leaf and integument (Hashimoto et al., 2018; Kelley et al., 2009; McConnell et al., 2001; Sieber et al., 2004a). Although the effect is not restricted to the inner integument, as expected form the pattern of expression, the combined loss of *CNA*, *PHB* and *PHV* function leads to abnormal integument development. Only the HD-ZIPIII gene REVOLUTA (REV) has been shown to be expressed in the both the integuments (Sieber et al., 2004a). Although it appears that *REV* contributes to integument growth from the analysis of HD-ZIPIII multiple mutants, its role in the network of ab-ad polarity determinants involved in integument morphogenesis is not yet clear (Kelley et al., 2009).

It has been suggested that juxtaposition of adaxial and abaxial signals is needed for the outgrowth of lateral organs (Bowman et al., 2002). According to the reported studies, it appears evident that these genes act together to positively regulate integument formation as they do in leaves to promote blade growth (Enugutti et al., 2012; Kelley et al., 2009; McAbee et al., 2006; Sieber et al., 2004a; Villanueva et al., 1999). Although, some differences are reported in the interactions between these genes family for integument morphogenesis compared to the genetic model proposed in leaves. The expression of HD-ZIPIII in leaves expands abaxially in *kan* mutants, showing that *KAN* genes negatively regulate HD-ZIPIII expression (Emery et al., 2003; McConnell et al., 2001). Such agonistic interaction has not been observed in integument (Kelley et al., 2009). The only YABBY member expressed during ovule development is *INO*, required for the abaxial outer integument formation (Villanueva et al., 1999). In leaves in *KAN* genes are positive regulators for YABBY expression , however in ovules loss of *KAN1* and *KAN2* results in alteration in the structure of the outer integument, suggesting that they are not

directly required for *INO* expression (Eshed et al., 2004). Additionally, *REV* is uniformly expressed in both the integuments and not restriction to the adaxial region (Kelley et al., 2009). It has been hypothesized a model in which integument growth depends on a proper balance between abaxial and adaxial factors, with some differences compared to the model in leaves. According to the model, *ATS* and *CNA/PHB/PHV* are required for the inner integument growth, while *INO* and *KAN1/2* regulate outer integument growth, and *REV* is contributing as an additional participant in both cases. The model for integument morphogenesis would not rely on the absolute levels of activities of abaxial and adaxial polarity determinants and the two functions would not act as mutually suppressive (Kelley et al., 2009). Although some conflicting evidence suggest that the interaction and regulatory network within these genes family in the integument morphogenesis has not yet been completely elucidated and that the observed difference between integument and leaf development might be the result of a distinct evolutionary origin. The observation of *INO* mutant phenotype seems to suggest that the absence of abaxial signals within the outer integument leads to the lack of the outer integument observed in this mutant, suggesting that the absolute presence of these polarity signal is required in the outer integument formation (Balasubramanian & Schneitz, 2002).
Moreover, the difference in terms of polarity determinants expression observed between the outer integument and inner integument could reflect the different hypnotized evolutionary origins of the two integument (Kelley & Gasser, 2009; McAbee et al., 2006).

1.3.7 Integument outgrowth

After their initiation, both integuments grow as bilayer laminar structure, and eventually they surround the nucellus. A large number of mutant showing defects in the organization of integument have been identified (Kelley & Gasser, 2009; Schneitz, 1999; Schneitz et al., 1997). Receptor-like kinases (RLKs) ARABIDOPSIS CRINKLY 4 (ACR4) is an epidermal-specific protein that mediates several aspects of epidermal patterning and additionally is involve in integument development in ovules (Gifford et al., 2003, 2005). In mutant *acr4* ovules are characterized by epidermal irregularities, including abnormal cell size and shape, callus-like outgrowths, and failure of the integument to outgrowth and cover the nucellus (Gifford et al., 2003). Another RLK, STRUBBELIG (SUB), is also involved in integument outgrowth (Chevalier et al., 2005). In *sub* mutant the outer integument sometimes fails to spread around the circumference of the ovule, resulting in a scoop-like incomplete outer integument and the

bilayer organization is not maintained, probably due to aberration in the orientation of the planes of cell division (Chevalier et al., 2005).

The gene *UNICORN* (*UCN*) has been involved in the regulation of laminar growth, which characterize integument outgrowth. *UCN* encodes for a protein kinase of the AGC VIII class (Enugutti et al., 2012). Plants with a defect in *UCN* produce ovules with integuments exhibiting localized disorganization of growth and frequently exhibiting single or multiple distinct protrusions (Enugutti et al., 2012; Enugutti & Schneitz, 2013; Schneitz et al., 1997; Scholz et al., 2019). Molecular and genetic evidence suggests that UCN suppresses ectopic growth in integuments by phosphorylating ATS thereby attenuating ATS activity. Thus, ectopic growth in integuments of *ucn* mutants would be the consequence of an ectopic transcriptional program initiated by hyperactive ATS (Scholz et al., 2019).

Although many genes are likely to be involved in the control of integument outgrowth, also identified through transcriptomics analysis approaches, a coherent molecular network is not yet present (Chaudhary et al., 2018; Skinner & Gasser, 2009).

1.3.8 Roles of hormones in integument development

Compared to the evidence that suggest the role of auxin in ovule initiation and patterning, much less is known regarding its role in integument morphogenesis.

A link to the role of auxin in integument morphogenesis has been suggested from the analysis of AUXIN RESPONSE FACTOR3/ETTIN (ARF3/ETT) mutant, in which ovules are characterized by the fusion of outer and inner integument, similarly to what is reported in *ats* mutant ovules (Kelley et al., 2012; McAbee et al., 2006). Both *ETT* and *ATS* are expressed at the border between the inner integument and outer integument, and in the abaxial inner integument (Kelley et al., 2012; McAbee et al., 2006). Analysis of proteins interaction have revealed that ATS and ARF3/ETT can physically interact in the plant cell nucleus (Kelley et al., 2012). These observations suggest that auxin could be regulating the spacing between integuments and ab-ad polarity via an ATS-ARF3/ETT complex. As reported in leaves, KAN function depends on interaction with the ARF proteins ETT and ARF4 and this mode of action could be similar to the one observed in ovule between ATS-ARF3/ETT (Arnault et al., 2018; Kelley et al., 2012; Pekker et al., 2005). Moreover, KAN proteins have been reported to act as repressors of growth (Eshed et al., 2001). ETT has also been shown to be able to directly respond to auxin, promoting the disruption of interaction with its interacting TF upon auxin presence (Simonini et al., 2016, 2017). Auxin might control the spatial activity of ATS-

ARF3/ETT complex, confining the complex at the border between the integument, promoting the separation of the two integuments and the laminar growth of the inner integument. The suggested model of ATS-ARF3/ETT interaction might imply a formation of two auxin maxima at the growing points of the two integuments (Kelley et al., 2012). Although it has been suggested the presence of PIN1 protein in the emerging inner integument and genes involved in auxin biosynthesis to be expressed during ovule development, a clear picture of auxin role and distribution during integument morphogenesis is not yet being extensively elucidated (Barro-Trastoy et al., 2020; Benkova et al., 2003; Larsson et al., 2017). Further evidence support a role of auxin in integument morphogenesis, as the weak *pin1–5* mutant produces ovules, with about 10% completely lacking integuments, but its mode of action remains elusive (Bencivenga et al., 2012).

It has been shown a link between PIN1 and the cytokinin regulatory pathway. Plants mutant for three cytokinin receptors encoding genes, *ARABIDOPSIS HISTIDINE KINASE2* (*AHK2*), *AHK3* and *AHK4*, produce defective ovules with similar characteristics to those of the *pin1–5* mutant and fail to accumulate PIN1 protein in ovules (Bencivenga et al., 2012).

Ectopic accumulation of PIN1 in the chalaza region is observed upon treatment with synthetic cytokinin, leading the formation of a single irregular structure in place of the integuments (Bencivenga et al., 2012). This evidence suggests that cytokinin pathway is an indirect regulator of auxin gradient formation during ovule development and control the correct integument formation (Bencivenga et al., 2012).

A role of gibberellin in integument morphogenesis has been reported. Several DELLA proteins are localized in the integument primordia and funiculus (Gomez et al., 2016, 2018, 2020). Moreover, defects in the function of multiple DELLA gibberellin-sensing proteins results in plants harboring mature ovules with an irregular shape (Gomez et al., 2016). The irregular ovules are resembling the *ats* mutant ovules, characterized by the fusion of the outer integument and inner integument (McAbee et al., 2006). Interestingly, *ats* mutant shows GA-related phenotype, including the earlier germination rate and altered flowering time and an upregulation of GA biosynthesis genes have been reported (Gomez et al., 2016). Yeast two-hybrid analyses showed that both DELLA protein GIBBERELLIC ACID INSENSITIVE (GAI) and REPRESSOR OF GA (RGA) can physically interact with ATS (Gomez et al., 2016). A model that links ATS and GA signaling pathway in the regulation of proper integument growth has been suggested. Thus, ATS and DELLA form a complex, allowing ATS to repress GA biosynthesis, promoting the stabilization of DELLAs and strengthening the protein complex (Gomez et al., 2016).

It has been recently reported a possible role of the brassinosteroid in the regulation of integument development. In null mutant of brassinosteroid receptor BRASSINOSTEROID INSENSITIVE 1 (BRI1) the outer integument growth and embryo sac development were impaired. Moreover, *INO* expression was significantly reduced in the null mutant background. An increase in *INO* expression was observed due to overexpression or increased transcriptional activity of BRASSINAZOLE-RESISTANT 1 (BZR1) in the mutant, rescuing the outer integument growth defect. These evidences suggest that brassinosteroid are possibly involved in the regulation of the outer integument growth partially via BZR1-mediated transcriptional regulation of *INO* (Jia et al., 2020).

1.3.9 Ovule curvature

Ovule curvature is a predominant feature in angiosperms, in contrast to the commonly uncurved ovules in gymnosperms. Curvature ensures a position of the micropyle close to the attachment site of the ovule and thus close to the placenta (Endress, 2011). Evolutionary studies on the structural diversity of angiosperms ovules suggest that the presence of an outer integument is fundamental for anatropy in bitegmic ovules (Endress, 2011; Gasser & Skinner, 2019; Rudall, 2021; Shi et al., 2021).

Moreover, genetic evidence suggests a central role of the outer integument in the establishment of ovule curvature. In *ino* mutant, ovules lacking the outer integument develops as orthotropous ovules as the inner integument is characterized by a straight growth (Schneitz et al., 1997; Villanueva et al., 1999). In *sup* mutant, ovules are characterized by polarity defects in the outer integument resulting in trumpet-shape ovules rather than hood-like structure (Balasubramanian & Schneitz, 2002; Gaiser et al., 1995; Sakai et al., 1995). Thus, the outer integument seems to play a crucial role for the observed curvature or *Arabidopsis* ovules.

Morphological analysis has hypothesized that the control of ovule curvature in *Arabidopsis* involves several steps with a major involvement by the proximal chalaza and the integuments (Schneitz et al., 1997, 1995). It has been suggested that two temporal distinct processes contribute to ovule curvature: kink formation at early stage of ovule morphogenesis and the later bending of the developing integuments (Vijayan & Tofanelli et al., 2021). The kink formation seems to involve subepidermal chalazal cells next to the initiating outer integument, which divide periclinal originating the precocious kink in the developing ovule. In a second phase, the outer integument outgrowth and develops into a hood-like structure that surround

the inner integument and the nucellus harboring the embryo sac and forms the bend observed at ovule maturity.

However, despite the mentioned observations, a comprehensive mechanism of curvature formation is not yet been completely proposed. Although some of the genetic player involved in this mechanism have been identified, their integration in the morphogenesis process in 3D organ-specific context has not been yet proposed.

1.4 Objectives

How an organ reproduces its three-dimensional architecture is a crucial a question in developmental biology. The ovule of *Arabidopsis thaliana* represents an excellent model for the study of the morphogenetic process in plants. At maturity, the ovule presents a strong curvature, therefore this organ offers the possibility to explore and understand how tissue deforms to form complex 3D shapes.

The aim of the study is to understand the mechanisms and the cellular growth patterns of the different tissues constituting the ovule of *Arabidopsis thaliana* and their contributions to curvature formation, through the generation of 3D digital ovule models with cellular resolution encompassing all developmental stages of wild-type ovules. The present work will resume some of the findings already published in Vijayan & Tofanelli et al., 2021. However, the data will be re-elaborated and analysed, in addition to some new findings, in the context of curvature morphogenesis to propose an innovative perspective and interpretation of growth patterns shaping the ovule of *Arabidopsis thaliana*.

The study will also include quantitative analysis of ovule mutant characterized by defective establishment of the final curvature to gain genetic knowledge and insight into the cellular behaviours that contribute to the bending process.

2 Material and Methods

2.1 Plant work and plant transformation

Arabidopsis thaliana (L.) Heynh. var. Columbia (Col-0) and var. Landsberg (erecta mutant) (Ler) were used as wild-type strains. Plants were grown as described earlier (Fulton et al., 2009). The Col-0 line carrying the WUSCHEL (WUS) promoter construct pWUS (pWUS::2xVENUS:NLS::tWUS) is similar to a previously described reporter line (Zhao et al., 2017).

The *ino-5* mutation (Col-0) was generated using a CRISPR/Cas9 system in which the egg cell-specific promoter pEC1.2 controls Cas9 expression (Wang et al., 2015). This mutant line was already described in Vijayan & Tofanelli et al., 2021, but will be described briefly in the next paragraph. The single guide RNA (sgRNA) 5'-ACCATCTATTTGATCTGCCG-3' binds to the region +34 to +55 of the *INO* coding sequence (AT1G23420). The sgRNA was designed according to the guidelines outlined in Xie et al., 2014. The mutant carries a frameshift mutation at position 51 relative to the *INO* start AUG, which was verified by sequencing. The resulting predicted short INO protein comprises 78 amino acids. The first 17 amino acids correspond to INO, while amino acids 18–78 represent an aberrant amino acid sequence.

The *sup-7* mutation (Col-0) was as well generated using the CRISPR/Cas9 system (Wang et al., 2015). Two sgRNA 5'- GCCGTGCAAGAACTTCACCA -3' (sgRNA1) and 5'-TCCTCACCAAGATATAGGGC -3' (sgRNA2) were employed. The sgRNA1 binds to the region +44 to +64, while the sgRNA2 binds to the region +367 to +387 of the SUP coding sequence (AT3G23130). The mutant carries a frameshift mutation at position 385 relative to the SUP start AUG, which was verified by sequencing. The resulting predicted SUP protein comprises 130 amino acids. The first 128 amino acids correspond to SUP, while amino acids 129-130 represent an aberrant amino acid sequence.

Wild-type and mutant plants were transformed with different constructs using Agrobacterium strain GV3101/pMP90 (Koncz & Schell, 1986; Sambrook et al., 1989) and the floral dip method (Clough & Bent, 1998). Transgenic T1 plants were selected on Kanamycin (50 μg/ml), Hygromycin (20 μg/ml) or Glufosinate (Basta) (10 μg/ml) plates and around 10 DAG, viable seedlings were transferred to soil for further inspection. Seedlings were grown on half-strength Murashige and Skook (1/2 MS) agar plates (Murashige & Skoog, 1962). Before sowing seeds on 1/2 MS, they were surface sterilized in 3.5% (V/V) sodium hypochlorite (NaOCl) plus 0.1% (V/V) Triton X-100 for 10 min on a rotator to prevent bacterial and fungal growth on plates. Seeds were washed three times with ddH2O and stratified for 4 days at 4°C prior to incubation.

Dry seeds were sown on soil (Patzer Einheitserde, extra-gesiebt, Typ T, Patzer GmbH & Co. KG, Sinntal-Jossa, Germany) situated above a layer of perlite, stratified for 4 days at 4°C and then placed in a long day cycle (16 hrs light) using Philips SON-T Plus 400 Watt fluorescent bulbs. The light intensity was 120-150 µmol/m^2sec. The plants were kept under a lid for 7-8 days to increase humidity (50-60%) and support equal germination.

2.2 Recombinant DNA work

For DNA work standard molecular biology techniques were used. DNA used for cloning was extracted from *Arabidopsis thaliana* using the NucleoSpin Plant II kit (Macherey-Nagel GmbH und Co. KG). Cloning was performed using standard methods described in (Sambrook et al., 1989). PCR-fragments used for cloning were obtained using Q5 high-fidelity DNA polymerase (New England Biolabs, Frankfurt, Germany). Restriction enzymes and T4 DNA Ligase used for cloning were also received from NEB GmbH and used according to the manufacturer's protocols. PCR products were purified using the NucleoSpin Gel and PCR clean-up kit (Macherey-Nagel GmbH und Co. KG) according to the manufacturer's protocol. Plasmids were isolated with the NucleoSpin Plasmid kit (Macherey-Nagel GmbH und Co. KG) according to the manufacturer's protocol. *Escherichia coli* strain DH10β was used for amplification of the plasmids. Bacteria were grown on corresponding selection media (Lysogeny broth). Antibiotics for bacterial selection were used at final concentrations as follows: Kanamycin 50 µg/mL; Ampicillin 100 µg/mL; Gentamycin 25 µg/mL; Spectinomycin 100 µg/mL; Tetracyclin 12.5 µg/mL; and Rifampicin 10 µg/mL. All PCR-based constructs were sequenced by Eurofins Genomics GmbH following the company's standards. Sequencing results were aligned with Geneious software to reference sequences received from The Arabidopsis Information Resource (TAIR, www.arabidopsis.org). Details of the PCR reaction mix and steps involved in PCR using Q5 high-fidelity DNA polymerase have been summarized in Table 1. Vectors used in this work are listed in Table 2. Detailed information for all oligonucleotides used in this study are listed in Supplementary table 2.

Table 1 PCR reaction mix and cycler program.

Reaction mix for Q5® High-Fidelity DNA polymerase based PCR amplification.

Components/reaction	**Volume (µl)**	
5x Q5 Reaction buffer	10	
2 mM dNTPs	5	
10 µM Forward primer	2.5	
10 µM Reverse primer	2.5	
Q5 High-Fidelity DNA polymerase (2 U/µl)	0.5	
Template DNA (100 ng made up to 2.5 µl)	2.5	
Sterile double distilled water	To 50	
PCR Cycler program for Q5 polymerase		
Temperature	**Time**	**Cycle**
98 °C	30 sec	1 cycle
98 °C	15 sec	25 - 35 cycles
X °C	10 sec	
72 °C	30 sec/kb	
72 °C	3 min	1 cycle

Table 2 Plasmid vectors used in this work.

Name	**Purpose**	**Description**
pGGA000	GreenGate (GG) entry vector	Entry vector for cloning promoter region of interest
pGGA-pINO	GG entry with pINO	Entry vector carrying INO promoter
pGGB005	GG entry with SV40 NLS	Entry vector carrying N-tag nuclear localization signal
pGGC014	GG entry with CDS of GFP	Entry vector carrying GFP
pGGD002	GG entry with D-dummy	Entry vector carrying D-dummy in case no C-tag is needed
pGGE000	GG entry vector	Entry vector for cloning terminator region of interest
pGGE-tINO	GG entry with tINO	Entry vector carrying INO terminator

pGGF007	GG entry with Kanamycin-R	Entry vector carrying Kanamycin resistance for plant selection
pGGZ001	GG destination vector	Destination vector, binary vector for plant transformation
pCBC-DT1T2	CRISPR/Cas9 gRNA assembly	Cloning multiple gRNA target sites
pHEE401E	CRISPR/Cas9 plant expression vector	Egg cell-specific promoter-controlled expression of 3×FLAG-NLS-zCas9-NLS containing gRNA scaffold

2.3 Fluorescent reporter construct

The pINO::NLS-GFP::tINO construct was assembled using the GreenGate system (Lampropoulos et al., 2013). Previous work indicated that 2kb of upstream sequence is sufficient for a correct spatial *INO* expression pattern (Meister et al., 2002). 2079 bp of *INO* (AT1G23420) upstream control region was amplified from genomic Col-0 DNA using primers pINO_F1 and pINO_R1. In addition, 2.8 kb of downstream sequence of *INO*, up to the next gene, was amplified from genomic Col-0 DNA using primers tINO_F1 and tINO_R1. Other sequences, including GFP and the plant resistance module were available from the GreenGate vectors stocks (Lampropoulos et al., 2013). The pINO::NLS-GFP::tINO was assembled into the intermediate vectors and then combined into the pGGZ0001 destination vector with a standard GreenGate reaction.

2.4 Clearing and staining of ovules

A detailed protocol is described in Tofanelli & Vijayan et al. 2019. Briefly, fixing and clearing of dissected ovules in ClearSee was done as described (Kurihara et al., 2015). Slightly opened pistils were fixed in 4% paraformaldehyde in PBS and followed by two washes in PBS before transfer into the ClearSee solution (xylitol (10%, w/v), sodium deoxycholate (15%, w/v), urea (25%, w/v), in H2O). Clearing was done at least overnight or for up to 2–3 days. Staining with SR2200 (Renaissance Chemicals, Selby, UK) was performed as described in Musielak et al. (Musielak et al., 2015). Cleared samples were washed in PBS and then stained in PBS solution containing 0.1% SR2200 and a 1/1000 dilution of TO-PRO-3 iodide (Thermo Fisher Scientific) for 20 min (Bink et al., 2001; Van Hooijdonk et al., 1994). Samples were washed in PBS for

one minute, transferred again to ClearSee for 20 min before mounting in Vectashield antifade agent (Vectashield Laboratories, Burlingame, CA, USA) (Florijn et al., 1995).

2.5 Microscopy and image acquisition

Microscopy and image acquisition settings have been already published and discussed in Tofanelli & Vijayan et al. 2019 and Vijayan & Tofanelli et al., 2021. Confocal laser scanning microscopy of ovules stained with SR2200 and TO-PRO-3 iodide was performed on an upright Leica TCS SP8 X WLL2 HyVolution 2 (Leica Microsystems) equipped with GaAsP (HyD) detectors and a 63x glycerol objective (HC PL APO CS2 63x/1.30 GLYC, CORR CS2). Scan speed was set at 400 Hz, the pinhole at 0.8 Airy units, line average between 1 and 3, and the digital zoom between 1 and 2. Laser power or gain was adjusted for z compensation to obtain an optimal z-stack. SR2200 fluorescence was excited with a 405 nm diode laser (50 mW) with a laser power ranging from 0.1% to 1.5% intensity and detected at 420–500 nm with the gain of the HyD detector set to 10. TO-PRO-3 iodide fluorescence excitation was done at 642 nm with the white-light laser, with a laser power ranging from 2% to 3.5% and detected at 655 to 720 nm, with the gain of the HyD detector set to 100. For high-quality z-stacks, 12-bit images were captured at a slice interval of 0.24 mm with optimized system resolution of 0.063 µm x 0.063 µm x 0.240 µm as final pixel size according to the Nyquist criterion. Some of the z-stacks were captured with 2x down sampled voxel size of 0.125 µm x 0.125 µm x 0.30 µm where the PlantSeg-trained model was used to generate equal standard cell segmentation as for images with fine voxels. This was possible because the PlantSeg model 'generic_confocal_3d_unet' was trained on down sampled original images and ground truths segmentation. The model required raw images with scaled voxels to match the trained dataset to generate high quality cell boundary predictions. Overall, raw images captured with 2x down sampled voxels were helpful to simplify the rescaling step in PlantSeg and allowed faster generation of raw images and with accurate segmentation.

Image acquisition parameters for pWUS reporter line were the following: SR2200; 405 diode laser 0.10%, HyD 420–480 nm, detector gain 10. 2xVenus; 514 nm Argon laser 2%, HyD 525–550 nm, detector gain 100. TO-PRO-3; 642 nm White Laser 2%, HyD 660–720 nm, detector gain 100. Image acquisition parameters for pINO, reporter line were the following: SR2200; 405 diode laser 0.10%, HyD 420–480 nm, detector gain 10. GFP; 488 nm Argon laser between 1 and 3% for and GFP respectively, HyD 500–540 nm, detector gain 100. TO-PRO-3; 642 nm

White Laser 2%, HyD 660–720 nm, detector gain 100. In each case, sequential scanning was performed to avoid crosstalk between the spectra.

Image acquisition of mature ovules takes about 15 min for both channels (SR2200/cell contours; TO-PRO-3/nuclei). If sequential scanning is performed, the imaging time can be up to 20 min for mature ovule.

Images were adjusted for color and contrast using Adobe Photoshop CC (Adobe, San Jose, USA) or MorphographX software (MGX) (Barbier de Reuille et al., 2015).

2.6 Segmentation

2.6.1 3D Cell segmentation

3D cell segmentation settings have been already published and discussed in Vijayan & Tofanelli et al., 2021. Cells were segmented in 3D using PlantSeg (Wolny et al., 2020). The generation of boundary predictions in PlantSeg was performed as a preparatory step for cell segmentation and allowed the processing of microscopic image z-stacks captured with voxel size 0.125 µm x 0.125 µm x 0.30 µm, with minimize segmentation errors, and reduction of the imaging time and laser exposure and phototoxicity to samples.

The batch of raw images in tiff format depicting the cell walls stained by SR2200 were processed through the PlantSeq pipeline and a cell boundary prediction files were created as output U-Net-based convolutional neural network (CNN) together with 3D cell segmentation performed through the partitioning of the boundary predictions (Ronneberger et al., 2015).

The PlantSeg pipeline consisted of four steps listed in Table 3.

Table 3 PlantSeg pipeline steps.

Input (format)	Step name	Description	Output (format)
Raw image depicting cell wall (Tiff)	Pre-processing	The raw image is pre-processed. When necessary, the raw image is rescaled with the semi-automatically guided rescaling tool.	Pre-processed image, eventually rescaled (HDF5)
Pre-processed image (HDF5)	Cell boundary prediction	CNNs pre-trained can be chosen to better fit the raw data.	Cell boundary prediction file (HDF5)

Cell boundary prediction file (HDF5)	Segmentation	Different segmentation partitioning based strategy can be chosen (Multicut, GASP etc.)	Segmented image (HDF5)
Cell boundary prediction file and segmented image (HDF5)	Post-processing	Conversion to the original voxel resolution when rescaling was applied and to Tiff file format	Cell boundary prediction file and segmented image (Tiff)

In the processing of ovule dataset rescaling the raw images to match the U-Net training data was essential to achieve the best performances. Optimal result were obtained by using voxel size 0.15 x 0.15 x 0.25 (mm, xyz) for the guided rescaling. The 'generic_confocal_3D_unet' CNN was employed for the boundary prediction, which has been previously trained on the *Arabidopsis* ovules dataset **(**https://osf.io/w38uf). The partitioning strategy adopted for image segmentation was the GASP average (Bailoni et al., 2019). These settings allowed for a highly accurate 3D cell segmentation as only a small number of errors, like over-segmented cells, were corrected in MGX during a visual inspection and manual correction step. In critical cases, this included cross-checking the TO-PRO-3 channel which showed the cell nuclei.

Running the PlantSeg pipeline required about 25 min on the following computer hardware (1x Nvidia Quadro P5000 GPU), and manual correction of segmentation errors toke around 5 to 10 minutes. An alternative 3D segmentation (PlantSeg-MGX hybrid) was performed on some wild-type samples from stages 3-I, 3-II, 3-III, and 3-V. The z-stacks of raw cell wall images and PlantSeg cell boundary predictions were combined in MGX using the process "Stack/Multistack/Combine Stack/Max" to generate a merged image stack, which was further blurred twice with a radius of 0.3 x 0.3 x 0.3 using the process "Stack/Filter/Gaussian Blur Stack". The processed image was further segmented in MGX by auto-seeded ITK watershed with the default threshold of 1500 using "Stack/ITK/Segmentation/ITK Watershed Auto Seeded". PlantSeg-MGX hybrid segmentation was time consuming, but the results were comparable to the graph-partitioning-based 3D segmentation of PlantSeg.

2.6.2 Quantification of pWUS nuclei in Col-0 ovule

Quantification of pWUS nuclei method has been already published and discussed in Vijayan & Tofanelli et al., 2021. The nuclei labeled by pWUS signal (blobs) were counted using the

Local Maxima process in MGX. The raw z-stacks were processed with "Stack/Filter/Brighten Darken" with a value ranging from 2 to 4, depending on image quality. Further Gaussian blur was applied twice with a low sigma of 0.2 x 0.2 x 0.2 μm^3 using "Stack/Filter/Gaussian Blur Stack". The processed stack was used to generate local signal maxima of radius 1.5 μm in xyz and with a threshold of 8000 using process "Stack/Segmentation/Local Maxima". The blobs were visualized by creating 3D blob meshes using the process "Mesh/Creation/Mesh from Local Maxima". Blob size were adjusted only if required. A blob radius of size 1.2 μm that fits inside the nuclei was used. The blob meshes were further linked to their parent 3D cell meshes using the MGX process "Mesh/Nucleus/Label Nuclei". This requires the 3D cell meshes to be loaded into the Mesh 1 workspace and the blob meshes into the Mesh 2 workspace of MGX. This process sets the cell identities of the 3D cell meshes as parents to the blob meshes. Blob numbers were determined in exported csv files that contained the Blob IDs associated with their parent cell IDs.

2.7 Image processing in MGX

2.7.1 Generation of 3D cell meshes and cell type annotation

Generation of 3D cell meshes and cell type annotation were performed as described in Vijayan & Tofanelli et al., 2021. 3D cell meshes were generated in MGX using the segmented image stacks using the process "Mesh/Creation/Marching Cube 3D" with a cube size of 1. All the cell annotations were performed on the 3D cell meshes in MGX. A tissue surface mesh is required for the method of semi-automatic cell type labeling. The tissue surface mesh is generated from the segmented stack. The segmented stack was first blurred using the process "Stack/Filter/Gaussian Blur Stack" with a radius of 0.3 in xyz. The blurred stack was used to generate tissue surface mesh using "Mesh/Creation/Marching Cube Surface" with a cube size of 1 and threshold 1. The generated surface mesh was then smoothed several times using the process "Mesh/Structure/Smooth Mesh" with 10 passes. For mature ovules cell type annotation, the MGX process "Mesh/Cell Atlas 3D/Ovule/Detect Cell Layer" was used, a modified 3DCellAtlas Meristem tool, with the 3D cell meshes in the Mesh 1 workspace and the tissue surface mesh in the Mesh 2 workspace using a cone angle parameter of 1.2 (Montenegro-Johnson et al., 2019). This process correctly classified about 60% of cells based on the tissue they belong to. Incorrect annotations were manually corrected using the mesh tools in MGX. The "Select Connected Area" tool was used to select individual cells of different layers in 3D and proofread the cell type labeling with "Mesh/Cell Types/Set Cell Type". Each

cell layer of the integuments was consecutively shaved off and proofreading was performed using 3D surface view. The process "Mesh/Cell Types/Save Cell Type" was used to save all labels, load labels and select cell types as required. The saved cell type csv file was reloaded onto the original 3D cell mesh and final proofreading was performed in the section view. For primordia, the cells were manually labeled using the tools in "Mesh/Cell Types/Set Cell Type". The cell type annotations were exported to the attribute map of the 3D Cell Mesh. In the attribute map all the cell parameters measured, including annotation and fluorescent intensity are saved within the 3D Cell Mesh and can be exported as csv file with the command "Mesh/Attributes/Advanced/Save to CSV Extended". Additional information can be added to the csv file including Filename, Genotype, Sample Name, Time Point and Stage. All the cell type annotated, some of which already discussed in Vijayan & Tofanelli et al., 2021, are reported in the Supplementary table 3.

2.7.2 Annotation of dividing cells and *INO* expressing cells

Annotation of dividing cells was performed as described in Vijayan & Tofanelli et al., 2021. Annotation of *INO* expressing cells has been adapted from the same procedure. Annotation of dividing cells and INO expressing cells was performed on the 3D cell meshes. For the annotation of dividing cells, the raw z-stacks of TO-PRO-3 Iodide channel were processed with the process "Stack/Filter/Brighten Darken" with a value ranging from 2 to 4 depending on image quality. Further Gaussian blur was applied twice with a low sigma of 0.2 x 0.2 x 0.2 μm^3 using "Stack/Filter/Gaussian Blur Stack". Through the visual inspection of the nuclei, stained with TO-PRO-3 Iodide, was possible to recognize mitotic figure, which appear as rod-shape nuclei with a brighter intensity of the signal. The cells showing this nuclei pattern were classified as dividing cells. With the help of the clipping plane tool in the view menu in MGX, the dividing cells were selected in the 3D cell meshes present in the Mesh 1 workspace and annotated using the tool in "Mesh/Lineage Tracking/Set Parent". The mitotic annotations were exported as csv file and exported to the attribute map using the command "Mesh/Lineage Tracking/Parent Export Attr Map".

The same processes were carried out for the annotation of *INO* expressing cells. The raw z-stacks of pINO::NLS-GFP::tINO nuclei channel were processed as mentioned before. Through the visual inspection was possible to recognize the nuclei signal of the cells expressing *INO*. Cells were selected in the 3D cell meshes present in the Mesh 1 workspace and annotated using the tools in "Mesh/Lineage Tracking/Set Parent".

The annotations were saved as csv file and exported to attributes using the command "Mesh/Lineage Tracking/Parent Export Attr Map".

2.7.3 Cell 3D geometric properties

Basic geometric properties in 3D of cells are calculated from the 3D cell mesh present in the Mesh 1 workspace using the tools in "Mesh/Heat Map/Analysis/Cell Analysis 3D". The cellular geometric properties were automatically saved in the attribute map and included cell volume, cell area and cell centroids.

2.7.4 Medio-lateral and anterior-posterior cell annotation

Additional cell type labels have been added to the tissue type annotation for the integuments of the 3D cell mesh present in the Mesh 1. With the tool "Add Label to Selection" cells of the medio, lateral and frontal region of the abaxial outer integument were selected and differentially labeled with the tool "Mesh/Cell Types/Set Cell Type". With the same processes the anterior and posterior half of the adaxial outer integument, abaxial inner integument and adaxial inner integument are annotated. The addition of these cell type annotations will be necessary to increase the accuracy of the distance measurement along the PD axis through the application of the ring coordinated system (see below). Annotations were saved as csv file and exported to attributes using the command "Mesh/Lineage Tracking/Parent Export Attr Map".

2.7.5 Coordinate system measurements

The method to obtain coordinate system measurements for ovule integuments has been develop by Vijayan and Strauss (unpublished method). The method has been applied to a cohort of wild-type ovules already employed in the publication from Vijayan & Tofanelli et al., 2021. Application of the methods, collection of data and interpretation of the results has been performed by me.

After removing the abaxial outer integument using the "Add Label to Selection" tool, the cells at the base of the adaxial outer integument are selected with "Select Connected Area" of the 3D cell mesh present in the Mesh 1. A Bezier ring, which passes through the cell centroid of the connected cells selected in the adaxial outer integument, was generate with the tool "Misc/Bezier/New Bezier Ring from Selected Cells" with a xy radius of 15. The Bezier ring is inspected, and the positioning is adjusted for an optimal measurement of the cells distance. The 3D cell mesh is loaded again in the Mesh 1 to have the abaxial outer integument present. To

measure the distance of the cell centroid within each layer of the integument from the Bezier ring, the process “Heat map/Measure 3D/Location/Cell distance Bezier ring” is used. The parameter chosen were: Wall Weight Euclidian, Direct Distance Limit 15 and Select Direct Cells Yes. The other parameters were left as default. The cell distances were automatically exported in the attribute map. The PD distance values have been normalized to relative PD distance with the following formula: $x_{rel\ PD\ dist} = x_{\ dist\ \mu m} / x_{\ max\ dist\ \mu m} \times 100$. After normalizing the distance values, it is possible to relatively compare different ovule from different stages.

2.7.6 Exporting attributes map

All the quantitative cellular features measured and generated were exported as attributes from MGX. The attributes included genotype, stage, cell IDs (segmentation label of individual cells), cell type IDs (tissue annotation), cell cycle IDs (mitotic cells annotation), cell volume and cell distance generated with the ring coordinate system for the integument cells. The attributes from individual ovules were exported as csv files and merged to create long-format Excel sheets listing all the scored attributes of all the cells from the analyzed ovules.

2.7.7 Dataset

The analyzed dataset and the relative information are reported in Supplementary table 4. The following dataset have been already published in Vijayan & Tofanelli et al., 2021 and include dataset 1, 2 and 4 listed in Supplementary table 4.

2.8 Temporal progression of ovule development

The temporal progression experiment has been previously described and published in Vijayan & Tofanelli et al., 2021. Gynoecium lengths of partially dissected flowers were measured from images taken by a stereo microscope (Leica Microsystems S Apo StereoZoom 1.0 x - 8.0 x equipped with a Leica MC170 HD camera). Except for the gynoecium, most other floral organs were carefully removed with forceps. Carpels that showed any signs of degeneration or stress (anthocyanin production) during the measured growth period were omitted from the analysis. Gynoecium length was measured from the upper end of the gynophore to the top edge of the style (bottom of the stigma) using Fiji/ImageJ (Schindelin et al., 2012). Gynoecium length measurements were performed on six individual live gynoecia, each from a different plant and still connected to the gynophore and pedicel, using images captured every 24 hours for a maximum of 192 hours. To establish the timeline of ovule development 64 individual

pistils of different lengths and from several plants were collected, the pistil length determined, and the stages of the ovules present within a pistil were assessed. The analyzed dataset is reported in Supplementary table 5. The number of ovules per stage for a given pistil was counted. The stage with the largest number of ovules was defined as reference, since asynchrony of ovule development was observed within an individual carpel. Subsequently, the pistils with the shortest and longest lengths that harbored a given stage were identified. The corresponding time interval spanning the difference in pistil length was derived from the pistil growth curve. The calculation gave an estimate of the duration of ovule stage.

2.9 Imaging ovules at two time points

To image ovules from the same gynoecium at two time points (T0 and T1, after 24 hours), the top half of a pistil was cut under the stereomicroscope and ovules imaged according the already mentioned pipeline consisting of 3D z-stacks acquisition with confocal microscopy and image processing steps. The other half of the pistil was kept attached to the stele and ovules were collected for imaging and processing after 24 hours. Only tissues that did not show any evident damage (tissue shrinkage, dehydration, or anthocyanin accumulation) were included in the analysis. Overall, the analysis has been performed on a total of 8 pistils of each half a minimum of 5 ovules was imaged and analyzed.

2.10 Growth analysis

Growth analysis has been performed as previously described in Vijayan & Tofanelli et al., 2021. Ovule growth rates were estimated as the ratio of the mean cell number or volume calculated between two consecutive stages and divided by the time interval required to progress between the two stages. $(A=ln((x(n+1)/x(n))/t(n\rightarrow n+1)))$. The time interval was calculated by dividing the sum of the respective stage-specific time intervals by two. To obtain the relative growth rate, the growth rates of the different stage transitions were normalized against the growth rate calculated for the transition from stage 1-I to stage 1-II. Stage-specific relative growth was estimated by taking the ratio between a given mean parameter of two consecutive stages $(x(n+1)/x(n))$. Relative growth of the integuments was estimated by taking the ratio of the respective mean parameter of two consecutive stages divided by the relative ovule growth $(y(n+1)/y(n))/(x(n+1)/x(n))$.

2.11 Statistical analysis

Statistical analysis was performed using a combination of R (R Development Core Team, 2019) with RStudio (R Studio Team, 2019) and PRISM8 software (Graph-Pad Software, San Diego, USA).

3 Results

3.1 Generation of stage-specific 3D digital atlas of wild-type ovule

The following section will discuss the findings published in Vijayan & Tofanelli et al., 2021.
For a complete understanding of ovule morphogenesis in *Arabidopsis thaliana*, a 3D cellular level description and quantification of the whole organ is required. A full developmental series of 3D digital wild-type (WT) ovule at cellular resolution has been obtained as described in Vijayan & Tofanelli et al., 2021. Since ovules of *Arabidopsis* are buried within the gynoecium, live imaging of samples is not feasible with standard confocal set up (Tofanelli & Vijayan et al., 2019; Valuchova et al., 2020). Therefore, the full developmental series consisted of fixed specimens. The digital ovules have been obtained from z-stack microscopic images, including cell wall-stained and nuclei-stained channels (Figure 6 A). Segmentation has been performed with PlantSeg, while quantitative analysis has been carried out on the open access software for 3D biological image analysis MorphographX (MGX) (de Reuille et al., 2014; Wolny et al., 2020) (Figure 6 B, C). The atlas covers all stages from early primordium outgrowth to the mature pre-fertilization ovule. Only ovules without drastic segmentation errors for stages 1 to 2-II and 3-I to 3-IV were selected. For stages 2-III to 2-V, ovules containing no more than five under-segmented (uncorrected) cells in the region occupied by the MMC and its lateral neighboring cells (ca 10% of nucellar cells) were included. Mature ovules (stages 3-V and 3-VI) without apparent segmentation errors in the sporophytic tissue have been included in the dataset. Each developmental stage included a minimum of 10 digital ovules.
A more precise definition of the subdivision of stage 1 into stage 1-I and 1-II has been introduced as described in Vijayan & Tofanelli et al., 2021. The subdivision was based on the first appearance of the signal of a reporter for *WUS* expression that became apparent when ovule primordia consisted of 50 cells. The build-up of *WUS* expression domain will be explained more in detail later in this work.
The average number of cells per ovule at each stage was determined and an increase in cell number for every consecutive stage of development was found, until ovules at stage 3-VI which exhibited an average of about 1900 cells (1897 ± 179.9 (mean ± SD)) (Figure 6 D) (Table 4). The mean organ volume was assessed for each stage by summing up the cell volumes of all cells in each ovule. Mean total volume was measured for ovules at stage 3-VI of about 5×10^5 μm^3 (4.9×10^5 $\mu m^3 \pm 0.7 \times 10^5$ μm^3) (Figure 6 E) (Table 4). The analysis of the data point

distribution in the two graphs suggests that cell number and cell volume both contribute similarly to the overall size of the ovule.

Staining with TO-PRO-3 also allowed the identification of cells undergoing mitosis. Two additional parameters have been quantified: the number of mitotic cells per ovule and the percentage of mitotic cells per ovule (Figure 6 F, G) (Table 4). In stage 1 ovules, 0-2 mitotic cells per ovule were found, indicating that either only few cells show mitosis or that progression through M-phase is a rapid process. At later stages, the number of mitotic cells per ovule increased. Starting with stages 2-II/2-III the value of percentage of mitotic cells tended to distribute around a mean percentage of 0.87 percent ± 0.4 percent. This value for the ovule is smaller than the percentage of mitotic cells found in *Arabidopsis* root tip, where about 1 - 3 percent of cells were found to be in the M phase of the cell cycle (Malamy and Benfey 1997). The results suggest there is a constant increase in cell number across the different stages, indicating that cell proliferation occurs in a steady and continuous fashion throughout much of ovule development.

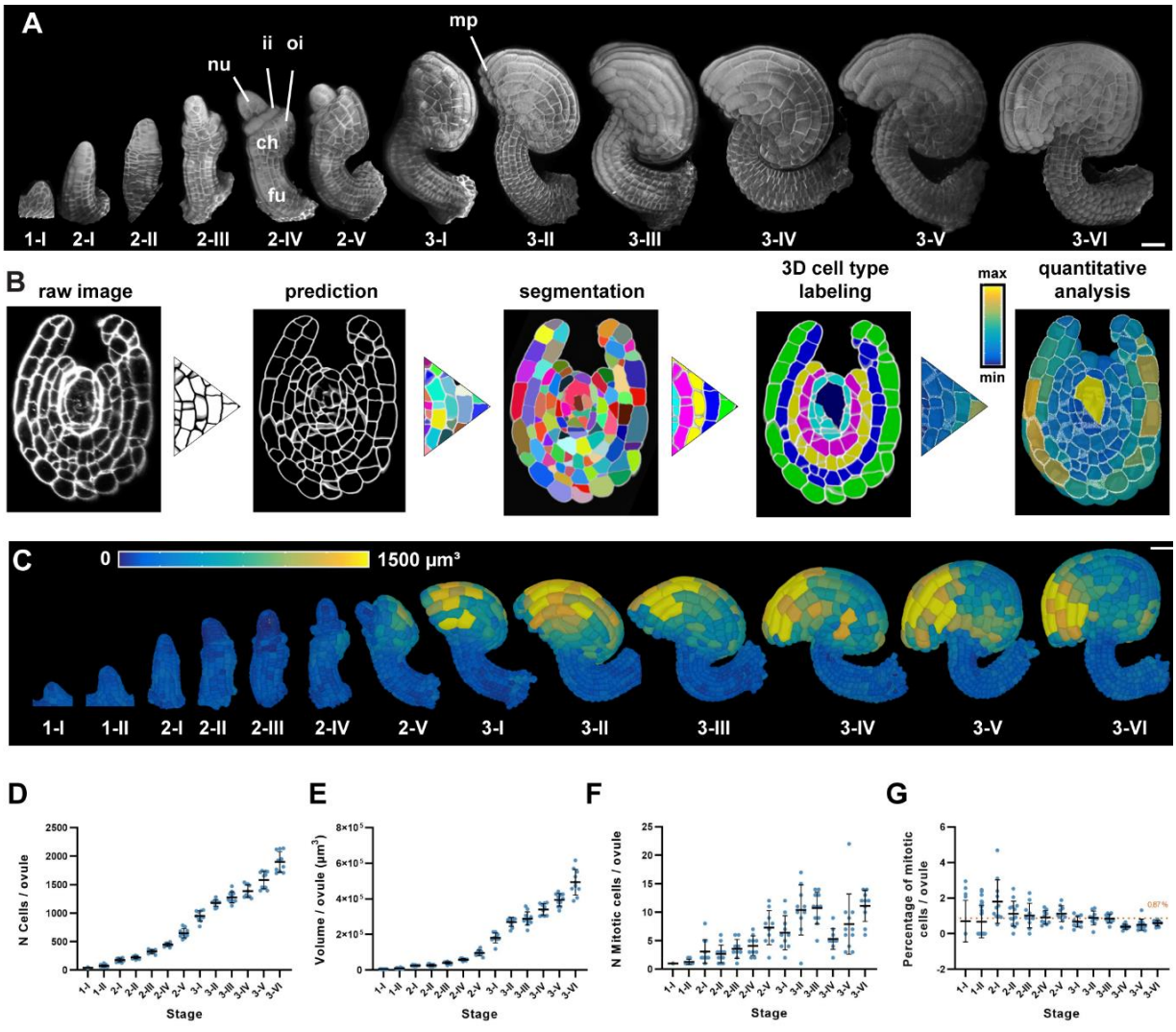

Figure 6 3D digital atlas of ovule development and growth patterns.

(A) 3D rendering of confocal z-stacks of SR2200-stained cell walls of ovule showing organ development from initiation at stage 1-I to maturity at stage 3-VI. (B) Pipeline for the generation of 3D digital ovules showing the raw data, PlantSeg cell contour prediction, 3D GASP segmentation, cell type annotation and quantitative analysis. (C) 3D cell mesh view of wild-type ovules at different stages displaying heat maps of cell volume ranging from 0 to 1200 μm^3. (D, E) Plots showing the total number of cells and total volume of individual ovules from early to late stages of development, respectively. (F, G) Plots showing the number of mitotic cells and the percentage of mitotic cells per ovule from early to late stages of development, respectively. Data points indicate individual ovules. Number of 3D digital ovules scored: 10 (stages 2-III, 2-IV, 2-V, 3-I, 3-II, 3-IV, 3-VI), 11 (stages 2-I, 3-III, 3-V), 13 (stage 2-II), 14 (stage 1-I), 28 (stage 1-II). Mean ± SD is shown. Abbreviations: oi, outer integument; ii, inner integument; nu, nucellus; ch, chalaza; fu, funiculus; mp, micropyle. Scale bar: 20 µm. Image from Vijayan & Tofanelli et al., 2021.

Table 4 Cell numbers, total volumes of ovules and mitotic counting during ovule development.

Stage[a]	N Cells	Volume (x 10^4 μm^3)	N Mitotic cells	% mitotic cells
1-I	39.6 ± 5.3	0.5 ± 0.09	1.0 ± 0.0	0.7 ± 1.2
1-II	74.0 ± 17.1	1.0 ± 0.2	1.3 ± 0.5	0.7 ± 0.9
2-I	176.9 ± 31.5	2.5 ± 0.4	3.1 ± 2.1	1.8 ± 1.2
2-II	220.6 ± 24.9	2.7 ± 0.6	2.7 ± 1.6	1.1 ± 0.7
2-III	324.1 ± 32.9	4.1 ± 0.7	3.6 ± 1.7	1.0 ± 0.7
2-IV	447.1 ± 30.7	5.9 ± 0.6	4.1 ± 1.7	0.9 ± 0.4
2-V	648.7 ± 81.5	9.7 ± 1.6	7.3 ± 3.0	1.1 ± 0.5
3-I	948.1 ± 92.5	18.1 ± 2.7	6.4 ± 3.0	0.7 ± 0.3
3-II	1178.0 ± 58.0	27.0 ± 2.5	10.4 ± 4.4	0.9 ± 0.4
3-III	1276.0 ± 97.7	28.9 ± 3.8	10.7 ± 2.8	0.9 ± 0.2
3-IV	1387 ± 111.9	34.0 ± 3.3	5.36 ± 1.8	0.4 ± 0.1
3-V	1580.0 ± 150.7	39.4 ± 3.5	7.9 ± 5.3	0.5± 0.3
3-VI	1897.0 ± 179.9	49.4 ± 7.2	11.1 ± 2.7	0.6 ± 0.2

[a]Number of 3D digital ovules scored: 10 (stages 2-III, 2-IV, 2-V, 3-I 3-II, 3-IV, 3-VI), 11 (stages 2-I, 3-III, 3-V), 13 (stage 2-II), 14 (stage 1-I), 28 (stage 1-II).
Values represent mean ± SD.
Data published in Vijayan & Tofanelli et al., 2021.

3.1.1 Analysis of tissue growth patterns of wild-type ovule

The following section will discuss the findings published in Vijayan & Tofanelli et al., 2021. Following the generation of 3D cell meshes, specific labels to individual cells were added, to describe the different tissue types, such as radial cell layers (L1, L2, L3), nucellus, internal tissue of the chalaza, inner or outer integument, or the funiculus (Figure 7) (see Supplementary table 3 for cell types). To get insights into tissue-specific growth patterns in wild-type ovule, a stage-specific quantitative cellular analysis of different tissues in early-stage ovule was performed. The analysis included stages from 1-I to 2-II and following primordium formation from stage 2-III to stage 3-VI.

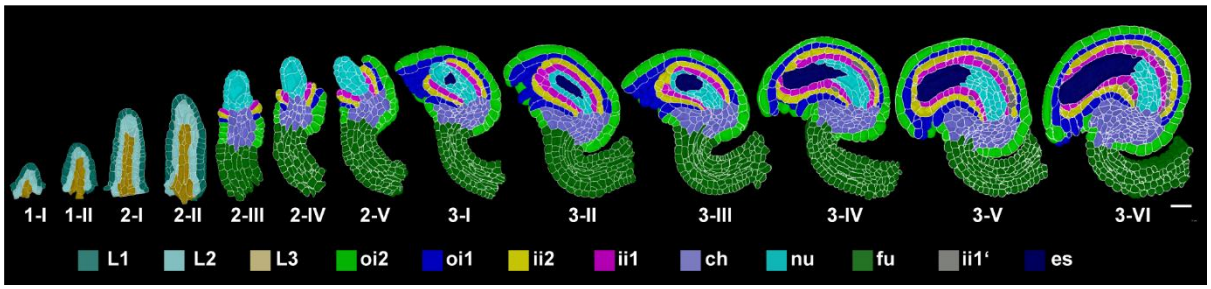

Figure 7 Stage-specific 3D digital ovules with cell type annotation.

Mid-sagittal section of ovules from stages 1-I to 3-VI showing the cell type organization in wild-type ovules. Stages 1-I to 2-II includes radial L1, L2, L3 labeling. From stage 2-III, individual cell type labels are assigned according to the specific tissue. Abbreviations: oi2, abaxial outer integument; oi1, adaxial outer integument; ii2, abaxial inner integument; ii1, adaxial inner integument; ii1', parenchymatic inner integument; nu, nucellus; ch, chalaza; es, embryo sac; fu, funiculus. Scale bars: 20 µm. Image from Vijayan & Tofanelli et al., 2021.

3.1.1.1 Tissue growth patterns from stage 1-I to 2-II

The following section will discuss some of the findings published in Vijayan & Tofanelli et al., 2021.

Previous studies indicated that the ovule is a composite of three clonally distinct radial layers (Jenik & Irish, 2000; Schneitz et al., 1995). Thus, the general principle of plant organ architecture into L1 (epidermis), L2 (first subepidermal layer) and L3 (innermost layer) has been adopted for the ovule (Satina et al., 1940). The radial organization was evident already in the early stage 1 of ovule outgrowth from the inspection of the 3D digital ovule primordia (Figure 8 A). The cellular growth patterns of the three radial layers constituting the primordium were investigated in a dataset of 63 ovules, including stages 1-I, 1-II and 2-I. The analysis

included the correlation between cell number and cell number per tissue for each primordium, the cell number per tissue and the distribution of cell volumes per tissue across the stages. The total number of cells of each primordium has been correlated with its total number of L1, L2, and L3 cells, respectively (Figure 8 B-D). A regular correlation was observed for L1 and L2. However, L3 showed scattering of the data points, suggesting that the cellular behavior is more stereotypic in L1 and L2 compared to L3 during outgrowth. Next, the number of cells in the L1, L2, and L3 layers has been analyzed for each primordium stage (Figure 8 E-G) (Table 5). The cell number of each layer increase in a linear fashion, suggesting a tight coordination in cell proliferation during primordium outgrowth. The number of cells differed across the layers within the same stage. The average cell volume was analyzed between cells of the three layers and stages (Figure 8 H-J) (Table 5). The average cell volume of L1 cells was significantly smaller than the average cell volume of L2 and L3 cells and ranged from 115.6 $\mu m^3 \pm 35.7$ μm^3 at stage 1-I to 129.9 $\mu m^3 \pm 44.5$ μm^3 at stage 2-I. The average volumes of L2 and L3 cells differed only slightly, with a mean volume of L2 cells ranging from 152.8 $\mu m^3 \pm 50.3$ μm^3 at stage 1-I to 158.5 $\mu m^3 \pm 74.2$ μm^3 at stage 2-I (Figure 8 H-J) (Table 5).

As already mentioned the presence of the L2-derived MMC at the distal tip of the ovule primordium defines stage 2-I (Schneitz et al., 1995). Therefore, the cell volume of the L2 cells at stage 2-I was analyzed and the largest cell for each ovule was identified and checked by visual inspection on the 3D digital ovule if the cell was at the distal tip of the primordium. The MMC can be identified based on its presence in the L2 and its large cell volume (Figure 8 L). At stage 2-I, an average MMC volume of 543 μm^3 was measured (543.3 ± 120.6, n = 11). The smallest MMC at stage 2-I showed a volume of 339.2 μm^3.While it can not be excluded that MMC development starts already earlier than stage 2-I according to the MMC analysis performed the minimal cell volume observed at stage 2-I correspond to 335 μm^3.

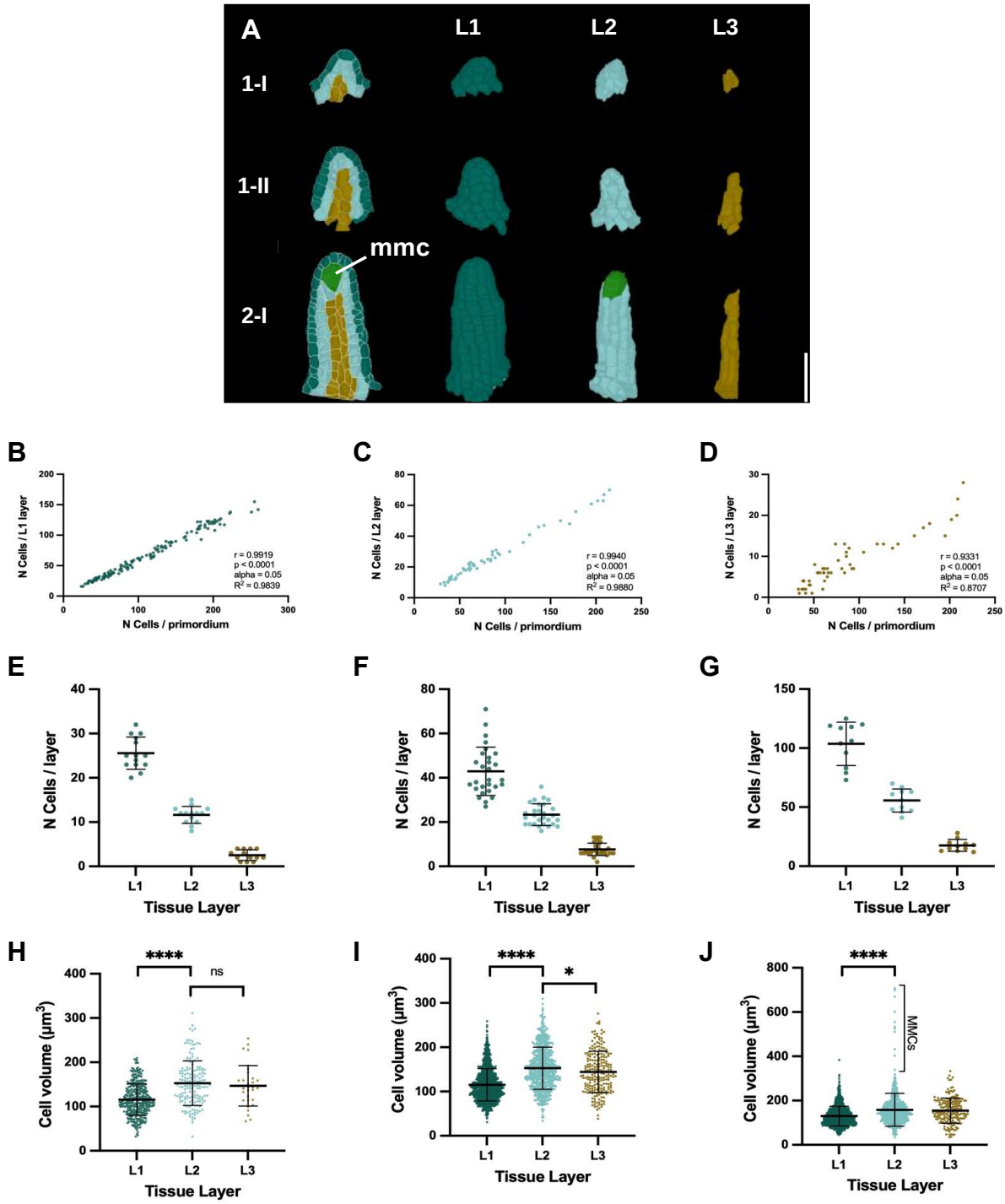

Figure 8 Quantitative analysis of cellular patterns in ovule primordium.

(A) Mid-sagittal section of ovules from stages 1-I to 2-I showing the L1, L2, L3 radial cell type organization. The layers have been removed to show the internal organization of the tissues. (B-D) Plots showing the correlation between the cell number per primordium and cell number of L1, L2 and L3, respectively. (E-G) Plots showing the cell number per layer for stage 1-I, 1-II and 2-I, respectively. (H-J) Plots showing distribution of cell volume per layer for stage 1-I, 1-II and 2-I, respectively. Data points indicate individual ovules and cell volumes in cell volume distribution graphs. Asterisks represent statistical significance (ns, $p \geq 0.5$; *, $p < 0.05$; **, $p < 0.01$; ***,

p<0.001; ****, p<0.0001; Student's t-test). Number of 3D digital ovules scored: 11 (stage 2-I), 14 (stage 1-I), 28 (stage 1-II). Mean ± SD is shown. Abbreviations: mmc, megaspore mother cell. Scale bar: 20 µm. Image adapted from Vijayan & Tofanelli et al., 2021.

Table 5 Cell numbers and cell volume of L1, L2 and L3 at early ovule stages.

Stage[a]	Layer	N Cells	Cell volume (µm^3)	N cells scored
1-I	L1	25.1 ± 3.5	114.6 ± 35.8	351
	L2	11.0 ± 2.67	150.4 ± 50.22	154
	L3	2.3 ± 1.29	148.7 ± 52.66	27
2-I	L1	40.38 ± 10.20	121.2 ± 39.03	969
	L2	21.63 ± 4.91	155.9 ± 48.08	519
	L3	7.21 ± 2.84	148.9 ± 49.73	173
2-III	L1	100.4 ± 20.50	130.0 ± 44.52	1205
	L2	53.67 ± 11.09	158.8 ± 77.33	644
	L3	17.17 ± 5.15	152.8 ± 56.96	206

[a]Number of 3D digital ovules scored: 11 (stage 2-I), 14 (stage 1-I), 28 (stage 1-II).
Values represent mean ± SD.
Data published in Vijayan & Tofanelli et al., 2021.

3.1.1.2 Tissue growth patterns from stage 2-III to 3-VI

The following section will discuss some of the findings published in Vijayan & Tofanelli et al., 2021.

The tissue-specific growth patterns have been analyzed in later stage of ovule development. To this end the counted cell numbers and total volumes in the nucellus, embryo sac, chalaza, funiculus and two integuments of stage 2-III to 3-VI digital ovules have been analyzed (Figure 9 A) (Table 6).

The cell number in the nucellus stayed roughly constant from stage 2-III up to 3-III (Figure 9 B). At stage 3-I the average cell number per nucellus was 66.9 ± 13.4 (Table 6). The results suggest that there is a low cell proliferation in the nucellus during ovule development. Nevertheless, the number of cells increase from stage 3-IV, with an average number of 85.0 ± 16.5 at stage 3-VI, suggesting an increase in the cell proliferation at later stage of development. This pattern was correlated to a 2.2-fold increase in the average volume of the nucellus across different stages (excluding the developing embryo sac) (Figure 9 C) (Table 6). Starting from stage 3-IV, no nucellus cells were detected at the micropyle (distal) end of the developing embryo sac (Figure 7 and Figure 9 A). This remark confirmed previous observations and suggested that nucellus cells undergo degeneration to allow the growing embryo sac to position

in proximity of the micropyle (Schneitz et al., 1995). However, as the average cell number per nucellus keeps constant and slightly increase, suggesting that the growing embryo sac possibly displacing some distal nucellar cells.

Following the formation of the functional megaspore, coenocytic embryo sac development starts at stage 3-I. Three rounds of mitoses followed by cellularization eventually result in the typical eight-nuclear, seven-celled *Polygonum*-type of embryo sac found at stage 3-VI (Figure 9 D). The mono-nuclear embryo sac features a volume of 0.2×10^4 $\mu m^3 \pm 0.1 \times 10^4$ μm^3. At stage 3-VI observed a total volume of 1.8×10^4 $\mu m^3 \pm 0.7 \times 10^4$ μm^3 was observed, corresponding to a nine-fold increase (Figure 9 E).

The central region of the ovule, classically known as chalaza, is of complex composition (see below). A steady increase of the cell number has been observed in the central region from stage 2-III (35.0 ± 5.7) up to stage 3-VI (268.5 ± 31.4) (Figure 9 F) (Table 6). Additionally, a steady increase in volume of the internal central region was observed from stage 2-III (0.4×10^4 $\mu m^3 \pm 0.1 \times 10^4$ μm^3) up to stage 3-VI (5.3×10^4 $\mu m^3 \pm 0.8 \times 10^4$ μm^3) (Figure 9 E) (Table 6). Thus, cell numbers increased 7.7-fold while tissue volume increased 13.3 fold over the stages.

In the funiculus a steady increase in the average cell number was observed from stage 2-III (153.7 ± 28.5) until the average cell number per funiculus reached 477.1 ± 54.2 at stage 3-II, a 3.1-fold increase (Figure 9 F) (Table 6). At later stage, the value kept constant although a minor increase to 533.0 ± 68.6 at stage 3-VI. The funiculus volume showed a 4.1-fold increase with an average volume at stage 2-III of 1.9×10^4 $\mu m^3 \pm 0.5 \times 10^4$ μm^3 and at stage 3-VI of 7.7×10^4 $\mu m^3 \pm 1.1 \times 10^4$ μm^3 (Figure 9 G) (Table 6). The data suggest that there is very little if any growth in the funiculus after stage 3-II.

The analysis of the integuments has been carried out initially analyzing the abaxial and adaxial layer together. The inner integument at stage 2-III featured an average cell number of 23.5 ± 5.5 and at stage 3-VI of 453.9 ± 69.8 (Figure 9 J) (Table 6). Regarding the volume increase, a 35.3-fold increase in the volume of the inner integument was observed, with an average volume of 0.3×10^4 $\mu m^3 \pm 0.07 \times 10^4$ μm^3 at stage 2-III and 10.6×10^4 $\mu m^3 \pm 1.9 \times 10^4$ μm^3 at stage 3-VI (Figure 9 K) (Table 6). The outer integument showed a 10.3-fold increase in cell number with an average number of cells of 53.8 ± 12.1 at stage 2-III and of 551.6 ± 62.7 at stage 3-VI (Figure 9 L) (Table 6). Regarding the volume increase, the outer integument underwent a 28.4-fold increase in volume with an average volume of 0.8×10^4 $\mu m^3 \pm 0.02 \times 10^4$ μm^3 at stage 2-III and 22.7×10^4 $\mu m^3 \pm 3.7 \times 10^4$ μm^3 at stage 3-VI (Figure 9 M) (Table 6).

Taken together, the results indicate that starting with stage 2-III development of the central region and the two integuments drives most of ovule growth. By contrast, there is only minimal growth of the nucellus (disregarding the embryo sac) and the funiculus grows only up to stage 3-II.

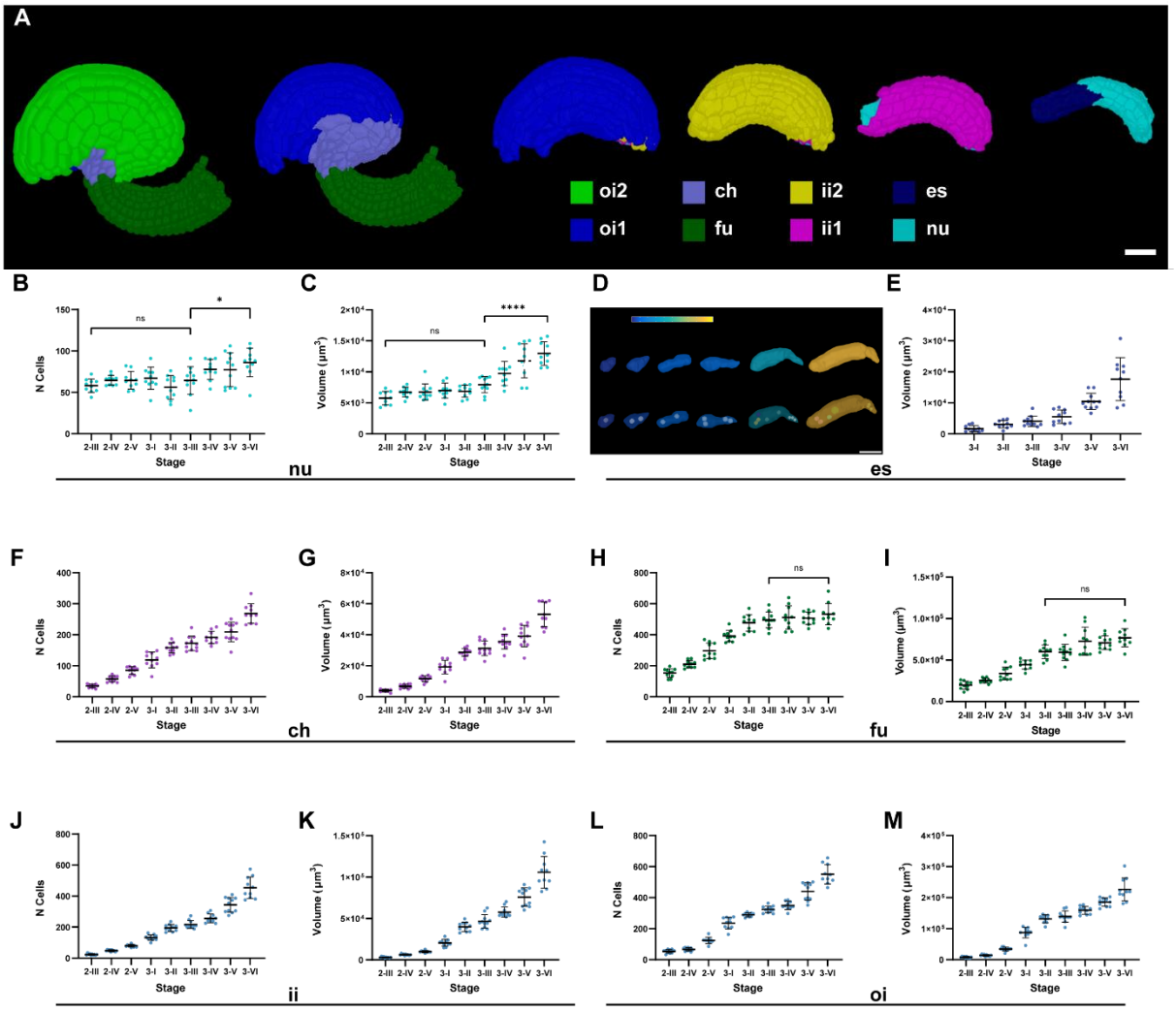

Figure 9 Quantitative analysis of tissue growth patterns in mature ovules.

(A) Digital 3D ovule showing the different annotated tissue. The layers have been removed to show the internal architecture of the ovule. (B, C) Plots showing the nucellus cell number and tissue volume at different stages, respectively. (D) 3D cell mesh view of the embryo sac at different stages displaying the volume ranging from 0 to 2.5 x 10^4 µm^3. (E) Plot showing the embryo sac volume at different stages. (F, G) Plots showing the chalaza cell number and tissue volume at different stages, respectively. (H, I) Plots showing the funiculus cell number and tissue volume at different stages, respectively. (J, K) Plots showing the inner integument cell number and tissue volume at different stages, respectively. (L, M) Plots showing the outer integument cell number and tissue volume at different stages, respectively. Data points indicate individual ovules. Asterisks represent statistical significance (ns, p≥0.5; *, p<0.05; **, p<0.01; ***, p<0.001; ****, p<0.0001; Student's t-test). Number of 3D digital ovules scored: 10 (stages 2-III, 2-IV, 2-V, 3-I, 3-II, 3-IV, 3-VI), 11 (stages 3-

III, 3-V). Mean ± SD is shown. Abbreviations: oi, outer integument; oi2, abaxial outer integument; oi1, adaxial outer integument; ii, inner integument; ii2, abaxial inner integument; ii1, abaxial inner integument; nu, nucellus; ch, chalaza; fu, funiculus; es, embryo sac. Scale bar: 20 µm. Image adapted from Vijayan & Tofanelli et al., 2021.

Table 6 Cell numbers and total volumes of the major ovule tissues.

	Tissue									
Stage[a]	**Nucellus**		**Chalaza**		**Funiculus**		**Inner Integument**		**Outer Integument**	
	N cells	Volume ($\times 10^4$ µm^3)	N cells	Volume ($\times 10^4$ µm^3)	N cells	Volume ($\times 10^4$ µm^3)	N cells	Volume ($\times 10^4$ µm^3)	N cells	Volume ($\times 10^4$ µm^3)
2-III	58.1 ± 8.1	0.6 ± 0.1	35.0 ± 5.7	0.4 ± 0.08	23.5 ± 5.5	0.30 ± 0.07	53.8 ± 12.1	0.8 ± 0.2	153.7 ± 28.5	2.0 ± 0.5
2-IV	64.6 ± 5.9	0.7 ± 0.1	57.6 ± 9.7	0.7 ± 0.01	48.1 ± 5.9	0.62 ± 0.08	66.6 ± 10.6	1.4 ± 0.3	210.2 ± 23.6	2.5 ± 0.3
2-V	64.5 ± 10.5	0.7 ± 0.1	85.0 ± 12.2	1.2 ± 0.2	79.3 ± 8.4	1.0 ± 0.1	124.0 ± 20.2	3.4 ± 0.6	295.9 ± 50.0	3.4 ± 0.8
3-I	66.9 ± 13.4	0.7 ± 0.1	118.9 ± 25.4	1.9 ± 0.4	132.6 ± 18.2	2.04 ± 0.4	235.9 ± 37.6	8.8 ± 1.7	392.4 ± 36.4	4.5 ± 0.6
3-II	56.0 ± 14.4	0.7 ± 0.1	158.1 ± 16.6	2.9 ± 0.3	194.7 ± 22.9	4.0 ± 0.6	289.1 ± 12.6	13.2 ± 1.3	477.1 ± 54.2	6.0 ± 0.8
3-III	64.4 ± 16.6	0.8 ± 0.1	172.2 ± 23.4	3.1 ± 0.5	216.8 ± 25.4	4.7 ± 0.8	324.5 ± 21.4	13.9 ± 1.8	496.2 ± 50.6	6.0 ± 1.0
3-IV	77.7 ± 12.2	1.0 ± 0.2	191.3 ± 20.1	3.6 ± 0.5	255.8 ± 28.4	5.8 ± 0.6	349.6 ± 26.6	15.9 ± 1.3	511.1 ± 75.8	7.3 ± 1.7
3-V	77.4 ± 20.4	1.2 ± 0.3	209.2 ± 31.7	3.9 ± 0.7	343.5 ± 48.3	7.6 ± 1.1	439.8 ± 57.0	18.6 ± 1.3	506.8 ± 40.1	7.1 ± 0.8
3-VI	85.9 ± 17.2	1.3 ± 0.2	268.5 ± 31.4	5.3 ± 0.8	453.9 ± 69.8	10.6 ± 1.9	551.6 ± 62.7	22.7 ± 3.7	533.0 ± 68.6	7.7 ± 1.1

[a]Number of 3D digital ovules scored: 10 (stages 2-III, 2-IV, 2-V, 3-I, 3-II, 3-IV, 3-VI), 11 (stages 3-III, 3-V). Values represent mean ± SD.
Data published in Vijayan & Tofanelli et al., 2021.

3.1.2 Characterization of *WUSCHEL* expression domain shows the establishment of ovule patterning

The following section will discuss some of the findings published in Vijayan & Tofanelli et al., 2021.

To analyze in detail, the patterning of ovule during early stage of ovule development, the expression of *WUSCHEL* (WUS, AT2G17950) in young ovule was analyzed. *WUS* is involved in the control of stem cell development in the shoot apical meristem and in ovule, is expressed in the nucellus and controls germ line development and the organization of the central region (Gaillochet et al., 2015; Groß-Hardt et al., 2002; Sieber et al., 2004b). The analysis of *WUS* expression was carried out through a Col-0 reporter line for *WUS* promoter activity (pWUS::2xVenus-NLS(tWUS)) (Figure 10 C). The analysis was performed on 67 3D digital ovules from the pWUS reporter line including stages 1-I to 2-III ($9 \leq n \leq 21$ per stage).

The pWUS signal was detected starting from ovule composed of 50 or more cells (Figure 10 D). Only two over 38 ovules with fewer than 50 cells (32 and 48 cells) showed either one or two cells expressing pWUS signal, respectively. The expression pattern of WUS was used in this work to discriminate between stage 1-I and 1-II, since the morphological distinction between stages 1-I and 1-II was not previously clearly defined (Schneitz et al. 1995). Therefore, the value of 50 cell was used as a threshold for the distinction between the two stages.

The pWUS reporter signal in the nucellar epidermis at early stage 2 was consistent with previous reports, with the signal detected in the epidermis of the distal tip of the primordium in individual cells or in small irregular patches (Figure 10 D-F) (Tucker et al., 2012; Zhao et al., 2017). Additionally, starting with stage 2-I about half of the ovules exhibited reporter signal in a few cells of the first subepidermal layer (L2) (Figure 10 B, D-F). The L2 cells expressing pWUS were the bottom neighboring of the MMC. By stage 2-III, most of the epidermal cells of the nucellus exhibited pWUS signal (Figure 10 G). The signal has not been detected in the MMC, in the central region or in the integuments. Thus, pWUS expression was strictly restricted to the nucellus.

The analysis of the elaboration of the spatial pWUS expression gave insight into the process of ovule patterning. Three elements are distinguishable along the PD axis in the ovule primordia: nucellus, chalaza and funiculus. Previous *in situ* hybridization analysis already gave insight into the establishment of the patterning in terms of gene expression pattern and the molecular network involved (Balasubramanian & Schneitz, 2000; Sieber et al., 2004b). Nevertheless, a correlation between quantitative data on ovule composition and the establishment of ovule

patterning was never proposed. The results from the pWUS analysis of expression suggests that the ovule patterning start to be established when the ovule is composed of 50 cells. The initiation of pWUS expression would then correspond to the establishment of the nucellus domain and to the progression of the ovule developmental stage from 1-I to 1-II.

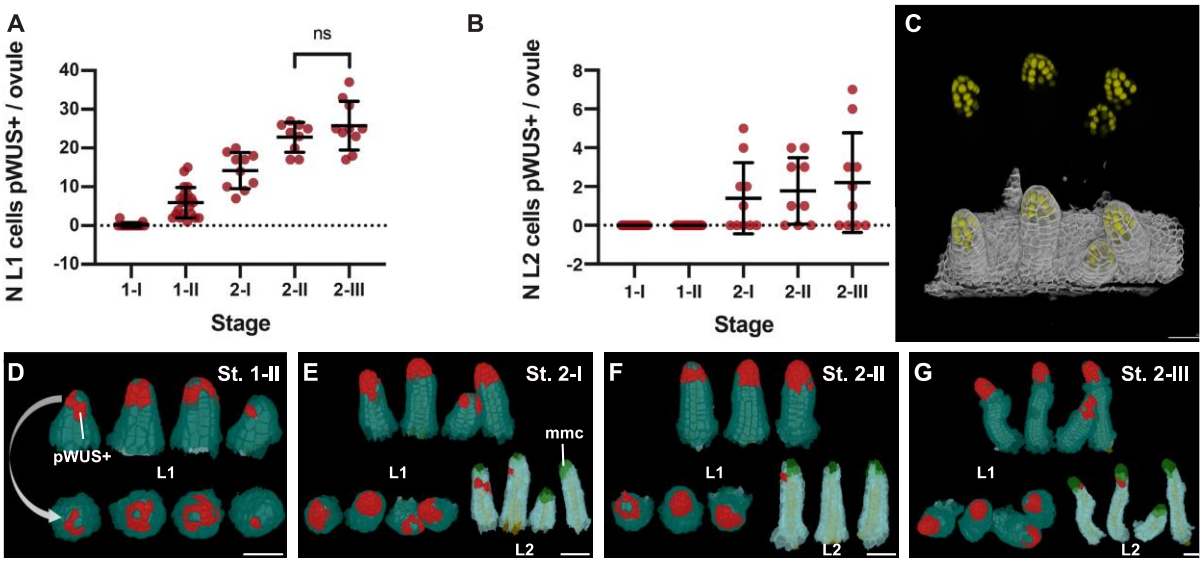

Figure 10 Expression pattern of the pWUS reporter.

(A) Plot showing the number of L1 cells per ovule expressing pWUS across stage 1-I to 2-III. (B) Plot showing the number of L2 cells per ovule expressing pWUS across stages 1-I to 2-III. (C) Raw 3D z-stack of multiple ovules at stage 1-II/2-I of pWUS reported line. On the top, the nuclei channel in yellow of pWUS. On the bottom, the overlap of the cell wall signal in white and the pWUS nuclei signal in yellow. The signal is present in the nucellar epidermal cells. (D–G) 3D cell meshes showing L1 and L2 cells expressing pWUS in red from stage 1-II to stage 2-III. Data points indicate individual ovules. Number of 3D pWUS digital ovules scored: 17 (stage 1-I), 21 (stage 1-II), 10 (stage 2-I), 9 (stage 2-II), 10 (stage 2-III). Mean ± SD are represented as bars. Abbreviations: mmc, megaspore mother cell. Scale bars: 20 µm. Image from Vijayan & Tofanelli et al., 2021.

3.1.3 The chalaza is composed of two morphologically different regions

The following section will discuss some of the findings published in Vijayan & Tofanelli et al., 2021.

Previous genetic results suggested that the chalaza can be divided into distal and proximal region which are flanked by the inner and outer integuments, respectively (Baker et al., 1997; Gasser & Skinner, 2019; Sieber et al., 2004b). The architecture of the central chalaza was analyzed more in detail with the use of the 3D digital atlas of ovule development. The distal chalaza could not be detected based on morphological characteristic of the cellular population. A reporter line where cells of the distal chalaza are selectively labeled could be employed for further analysis. However, two groups of subepidermal cells in the proximal chalaza has been

identified (Figure 11 A). The proximal chalaza is flanked by the outer integument and constitutes a major part of the central region. The two groups of cells were termed anterior and posterior chalaza, respectively. The two groups of cells contribute to ovule development differentially (Figure 11 A). The anterior chalaza showed to contribute as subepidermally to the formation of the outer integument, intercalating between the two layers of the outer integument in the frontal region (Figure 11 C). Posterior chalazal cells are found to not intercalate between the two epidermis-derived cell layers of the outer integument, suggesting that cells of the posterior chalaza do not contribute to the outer integument.

At stage 2-III cells of the proximal chalaza appear relatively homogeneous in size and shape and no evident differences between the two group of cells is observed (Figure 11 A). By stage 2-IV cells of the anterior and posterior chalaza become distinguishable based on cellular features, such as cell size and cell number (Figure 11 A, B) (Table 7). At stage 2-V, 13 ± 6 cells in the anterior chalaza are observed, with an average cell volume of 226.4 μm^3 ± 77.3 μm^3. By stage 3-VI cell number increased to 59 ± 6 cells (a 4.5-fold increase) and the average cell volume to 428.7 μm^3 ± 284.4 μm^3 (a 1.9-fold increase). The volume of the anterior chalaza increased from 0.31 x 10^4 μm^3 ± 0.1 x 10^4 μm^3 at stage 2-V to 2.5 x 10^4 μm^3 ± 0.4 x 10^4 μm^3 at stage 3-VI (Figure 11 E-G) (Table 7). The increase in cell volume of the cells in the anterior chalaza majorly contributes to the overall volume of the anterior chalaza (Figure 11 D). Regarding the posterior chalaza, 71.2 ± 10 cells were scored in this domain at stage 2-V. At stage 3-VI a 3-fold increase in cell number was measured, with 209 ± 31.5 cells. Average cell volume was 120 μm^3 ± 52.7 μm^3 at stage 2-V. The cell volume observed at stage 3-IV did not deviate from the values measured at stage 2-V. Tissue volume increased from 0.85 x 10^4 μm^3 ± 0.1 x 10^4 μm^3 at stage 2-V to 2.7 x 10^4 μm^3 ± 0.4 x 10^4 μm^3 at stage 3-VI (Figure 11 D) (Table 7). Therefore, cell proliferation appears to be largely contributing to the increase in the volume of the posterior chalaza (Figure 11 D).

The results indicate that the central region is a complex structure. The data suggest that two groups of cells are morphologically recognizable and contribute to its interior architecture. The anterior and posterior chalaza constitute the subepidermal central region and they eventually reach comparable volumes (Table 7). Nevertheless, they show distinguishable characteristics with fewer but bigger cells contributing to the anterior chalaza and more, but smaller cells making the posterior chalaza. Moreover, the two tissues show different shapes with the anterior chalaza exhibiting two “wing-like” lateral extensions and the posterior chalaza characterized by a radially symmetric, rod-like shape (Figure 11 D). Cells of the anterior chalaza provide a

subepidermal contribution to the outer integument. The combined activity of cells of the anterior and posterior chalaza eventually leads to a widening of the proximal chalaza and the repositioning of the nucellus and inner integument on top of the posterior half of the proximal chalaza.

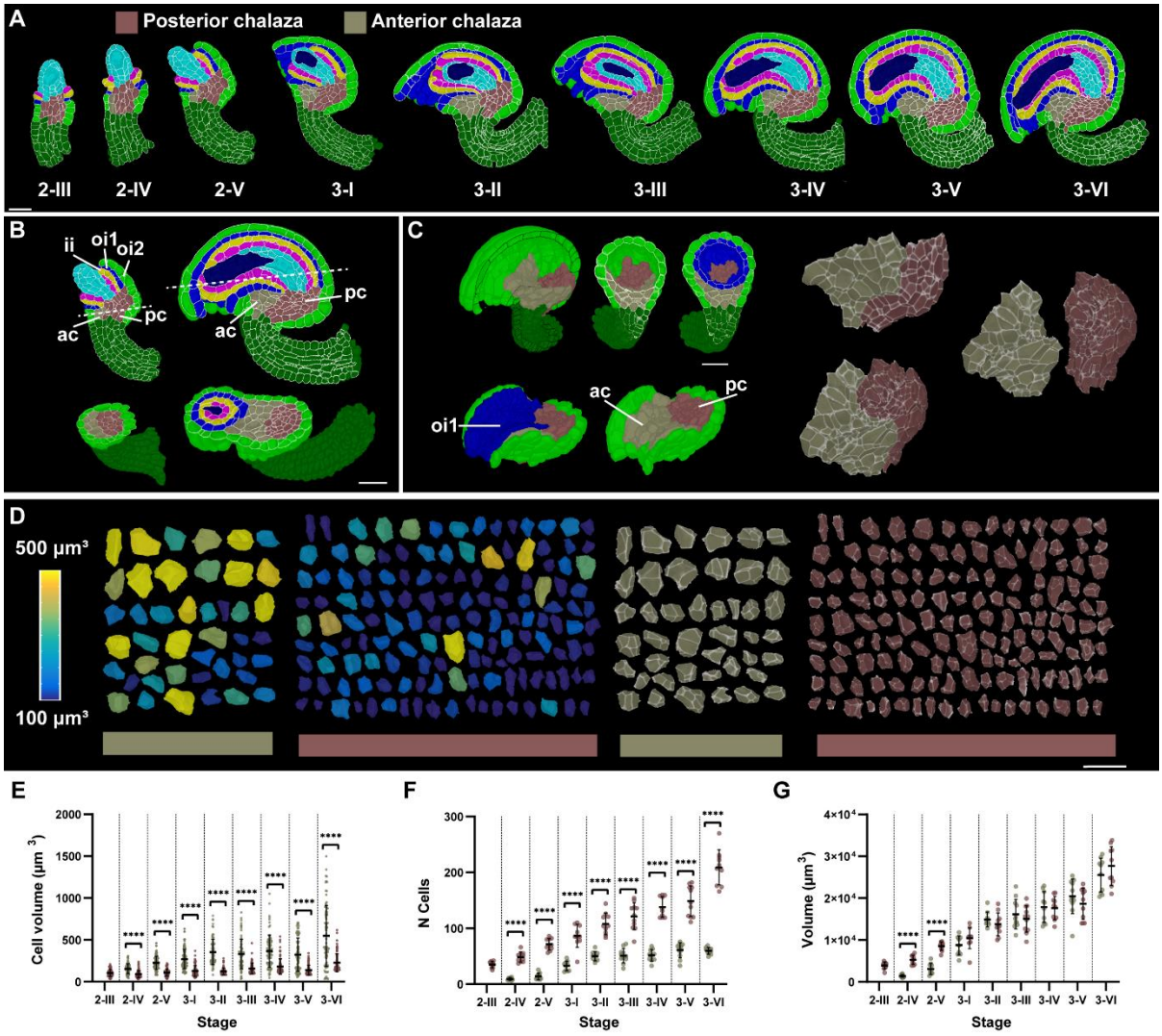

Figure 11 Tissue architecture of the proximal chalaza.

(A) Sagittal section of digital 3D ovule showing the different annotated tissue. Tissues are colored as before, and the anterior and posterior chalaza differently labeled are included. (B) Left: sagittal (top) and transverse (bottom) sections through a stage 3D digital wild-type ovule. The anterior and posterior chalaza are highlighted. The dotted lines in the upper ovule indicate the plane of the transverse section shown in the bottom ovule. Right: sagittal (top) and oblique-transverse (bottom) sections through a stage 3-IV 3D digital ovule. The dotted lines in the upper ovule indicate the plane of the oblique-transverse section shown in the bottom ovule. The inner integument and the nucellus are located on top of the posterior chalaza while the anterior chalaza forms a prominent bulge. (C) Sequential removal of various tissues of the stage 3-IV ovule shown in to reveal the anterior and posterior chalaza. On the bottom left only the

anterior part of the integuments are left. When the adaxial outer integument is removed, it is possible to observe the portion of the anterior chalaza that is intercalating between the two layers, forming the wing-like structure. On the right only the anterior and posterior chalaza are left, and their shape can be appreciated. (D) Comparisons of cell shapes and cell volumes of individual cells of the anterior and posterior chalaza, respectively. Cells are from the stage 3-IV ovule depicted in (B). (E–G) Comparison of different parameters between the anterior and posterior chalaza at different stages. (E) Comparison of anterior and posterior chalaza cell volumes. (F) Comparison of anterior and posterior chalaza cell numbers. (G) Comparison of anterior chalaza and posterior chalaza tissue volumes. Data points indicate individual ovules and cell volumes in cell volume distribution graphs. Number of 3D digital ovules scored: 10 (stages 2-III, 2-IV, 2-V, 3-I, 3-II, 3-IV, 3-VI), 11 (stages 3-III, 3-V). Mean ± SD is shown. Abbreviations: ac, anterior chalaza; ii, inner integument; oi1, adaxial outer integument; oi2, abaxial outer integument; pc, posterior chalaza. Scale bars: 20 μm. Image from Vijayan & Tofanelli et al., 2021.

Table 7 Cellular characterization of the chalaza.

	Tissue					
Stage[a]	**Anterior chalaza**			**Posterior chalaza**		
	N Cells	Cell volume (μm^3)	Tissue volume (x 10^4 μm^3)	N Cells	Cell volume (μm^3)	Tissue volume (x 10^4 μm^3)
2-III	-	-	-	35 ± 5	113 ± 41.2	0.4 ± 0.08
2-IV	9 ± 2	160 ± 59.6	0.14 ± 0.03	48 ± 9	109 ± 45.6	0.52 ± 0.1
2-V	13 ± 6	226.4 ± 77.3	0.31 ± 0.1	71.2 ± 10	120 ± 52.7	0.85 ± 0.1
3-I	32 ± 8	270.4 ± 121.3	0.87 ± 0.2	86 ± 20	120 ± 59.5	1 ± 0.2
3-II	50 ± 8	298 ± 156	1.5 ± 0.2	108 ± 19	127 ± 70	1.3 ± 0.2
3-III	51 ± 13	318.1 ± 192	1.6 ± 0.35	121 ± 32	124 ± 68	1.5 ± 0.3
3-IV	52 ± 11	347.5 ± 198.2	1.8 ± 0.36	138 ± 18	128 ± 73	1.7 ± 0.2
3-V	60 ± 14	336.8 ± 227.4	2 ± 0.4	148 ± 27	126 ± 70.5	1.8 ± 0.4
3-VI	59 ± 6	428.7 ± 284.4	2.5 ± 0.4	209 ± 31	132 ± 90.7	2.7 ± 0.4

[a]Number of 3D digital ovules scored: 10 (stages 2-III, 2-IV, 2-V, 3-I, 3-II, 3-IV, 3-VI), 11 (stages 3-III, 3-V). Values represent mean ± SD.
Data published in Vijayan & Tofanelli et al., 2021.

3.1.4 The integuments show differential growth between the layers

The ovule of *Arabidopsis* is a bitegmic ovule, consisting of two distinct integuments, which grow enclosing the nucellus and embryo sac and leaving the micropyle at the apex of the mature ovule. Both the integuments consists of a two-layered structure, formed by an abaxial (or

dorsal) and an adaxial (or ventral) layer (Figure 5 A) (Schneitz et al., 1995; Truernit & Haseloff, 2008).

To have a more detailed analysis on the growth of the integument, which represent the tissues majorly contributing to the ovule growth, each layer within the outer and inner integument has been analyzed separately in terms of number of cells and volume of the tissue. Subsequently, the growth of the abaxial and adaxial layer have been compared within the same layer.

The adaxial outer integument (oi1) at stage 2-III featured an average cell number of 12.0 ± 2.4 and at stage 3-VI of 294.6 ± 36.0 (Figure 12 E) (Table 8). In terms of volume of the tissue, an average volume of 0.1×10^4 μm^3 ± 0.05×10^4 μm^3 at stage 2-III and 7.9×10^4 μm^3 ± 1.6×10^4 μm^3 at stage 3-VI (Figure 12 F) (Table 8). The abaxial outer integument (oi2) at stage 2-III featured an average cell number of 41.8 ± 10.5 and at stage 3-VI of 257.0 ± 28.2 (Figure 12 E) (Table 8). In terms of volume of the tissue, an average volume of 0.7×10^4 μm^3 ± 0.2×10^4 μm^3 at stage 2-III and 14.8×10^4 μm^3 ± 2.1×10^4 μm^3 at stage 3-VI (Figure 12 F) (Table 8). Between stage 2-III and 3-III the abaxial outer integument showed a higher number of cells compared to the adaxial outer integument. However, at stage 3-VI the number of cells in the adaxial outer integument is significantly higher compared to the abaxial layer, indicating that at late stage the proliferation in the adaxial outer integument is higher compared to the abaxial layer (Figure 12 E). When the tissue volume was analyzed, the abaxial outer integument always showed a higher tissue volume compared to the adaxial layer (Figure 12 F). The analysis of the cell volume distribution across the layer, suggested that the higher volume in the abaxial outer integument is due to the presence of cells with a higher cell volume, which can be observed as well in the heat-map of cell volume of the abaxial outer integument (Figure 12 A, B, G). These differences in terms of growth between the two layers were analyzed more in detail calculating the ratio in terms of cells and volume between the abaxial and adaxial layers of the outer integument. In terms of cell number, the abaxial outer integument at stage 2-III to 2-V is roughly 3.5, 2.5-fold bigger than the adaxial outer integument. However, how already mentioned, starting from 3-I to later stage the ratio is close to 1, meaning that the two layers have comparable number of cells (Figure 13 A). In terms of tissue volume, the abaxial outer integument at stage 2-III to 2-V is roughly 4-fold bigger than the adaxial layer. Starting from 3-I to later stage the ratio is decreasing and the abaxial outer integument is 2-fold bigger than the adaxial layer (Figure 13 B). These results suggest that the two layers show differential growth. In the abaxial outer integument, major of the contribution in terms of growth derives from the extensive enlargement of cells, while for the adaxial outer integument the major

contribution to growth derives from cell proliferation. Moreover, the growth of the two layers showed differential dynamics across the different stages, with the early stages showing a bigger contribution of the abaxial outer integument in terms of growth compared to the adaxial layer. Although, at later stage the two layers are contributing equally to the growth in terms of cell proliferation, the abaxial outer integument is the major driver of the growth of the outer integument.

The adaxial inner integument (ii1) at stage 2-III featured an average cell number of 9.4 ± 15 and at stage 3-VI of 199.0 ± 36.9 (Figure 12 H) (Table 8). In terms of volume of the tissue, an average volume of 0.1 x 10^4 μm^3 ± 0.03 x 10^4 μm^3 at stage 2-III and 4.8 x 10^4 μm^3 ± 0.9 x 10^4 μm^3 at stage 3-VI (Figure 12 I) (Table 8). The abaxial inner integument (ii2) at stage 2-III featured an average cell number of 14.1 ± 5.8 and at stage 3-VI of 254.9 ± 33.3 (Figure 12 H) (Table 8). In terms of volume of the tissue, an average volume of 0.2 x 10^4 μm^3 ± 0.07 x 10^4 μm^3 at stage 2-III and 5.7 x 10^4 μm^3 ± 1.0 x 10^4 μm^3 at stage 3-VI (Figure 12 I) (Table 8). Throughout the development, the abaxial inner integument showed a higher number of cells compared to the adaxial layer, as well as in terms of tissue volume (Figure 12 H, I). The distribution of the cell volume across the layers does not highlight any highly significant differences between the abaxial and adaxial inner integument, except at stage 3-VI (Figure 12 J). These differences in terms of growth between the two layers were analyzed more in detail calculating the ratio in terms of cells and volume between abaxial and adaxial inner integument. In terms of cell number, the abaxial inner integument during development is roughly 1.5, 2-fold bigger than the adaxial layer, confirming the observed higher number of cells in the abaxial inner integument (Figure 13 C). In terms of tissue volume, the abaxial inner integument is roughly 1.5-fold bigger than the adaxial layer, with a very similar data point distribution as observed for the cell number (Figure 13 D). These results suggest that the two layers show differential growth, with the abaxial inner integument contributing at larger extent to the overall growth of the inner integument.

In summary, the two integuments show differential growth. Difference in the growth of the layers within the same integument are also observed. The outer integument always shows more cells than the inner integument, although the difference was relatively small throughout the various stages with stage 3-VI showing a ratio of 1.2. By contrast, the volume of the outer integument was always more than twice the volume of the inner integument. At stage 3-I, a 4.3-fold larger volume of the outer integument is observed. Within the outer integument the abaxial outer integument contributes majorly to the growth of the integument through cell

enlargement, since in later stage the two layers seems to contribute equally in terms of cell proliferation. Within the inner integument, the abaxial inner integument contributes majorly to the growth of the inner integument compared to the adaxial layer proliferation.

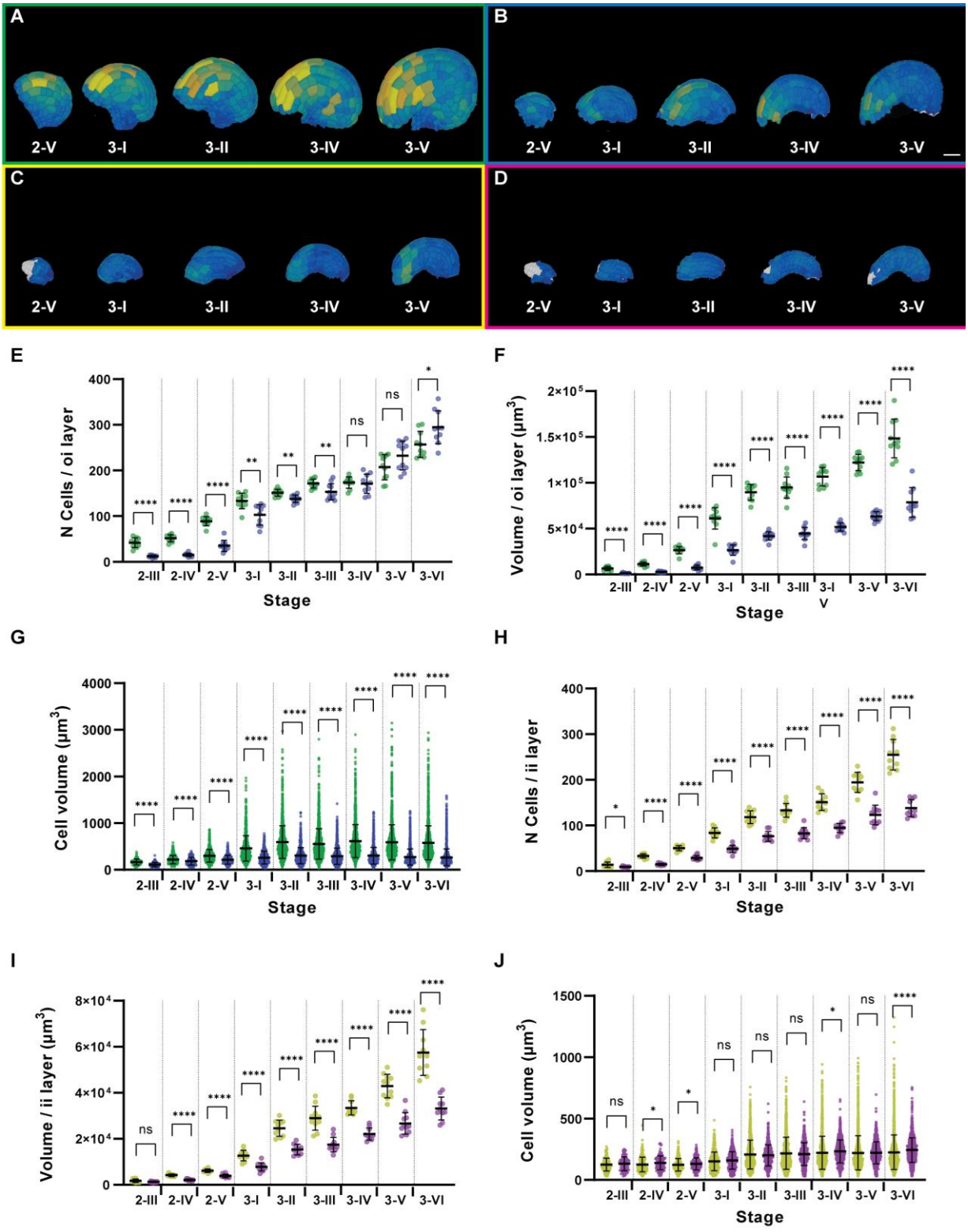

Figure 12 Growth patterns within the integument layers.

(A, D) Sequential removal of various layer of the integument to show the distribution of cell volume depicted in the 3D cell mesh showing the heat map of cell volume and the architecture of the tissue. Different stages are showed. The cell volume ranges from 0 to 1500 µm^3. (A) Abaxial outer integument, oi2. (B) Adaxial outer integument, oi1. (C) Abaxial inner integument, ii2. (D) Adaxial inner integument, ii1. (E–G) Comparison of different parameters between the adaxial and abaxial outer integument at different stages. Data points indicate individual ovules or individual cells for the cell volume graph. In green the abaxial outer integument and in blue the adaxial outer integument. (E) Comparison of abaxial and adaxial layers cell numbers. (F) Comparison of abaxial and adaxial layers volume. (F) Comparison of abaxial and adaxial layers cell volume. (H–J) Comparison of different parameters between the adaxial and abaxial inner integument at different stages. Data points indicate individual ovules or individual cells for the cell volume graph. In yellow the abaxial inner integument and in pink the adaxial inner integument. (H) Comparison of abaxial and adaxial layers cell numbers. (I) Comparison of abaxial and adaxial layers volume. (J) Comparison of abaxial and adaxial layers cell volume. Data points indicate individual ovules or individual cells in the cell volume distribution graph. Asterisks represent statistical significance (ns, p≥0.5; *, p<0.05; **, p<0.01; ***, p<0.001; ****, p<0.0001; Student's t-test). Number of 3D digital ovules scored: 10 (stages 2-III, 2-IV, 2-V, 3-I, 3-II, 3-IV, 3-VI), 11 (stages 3-III, 3-V). Mean ± SD is shown. Scale bar: 20 µm.

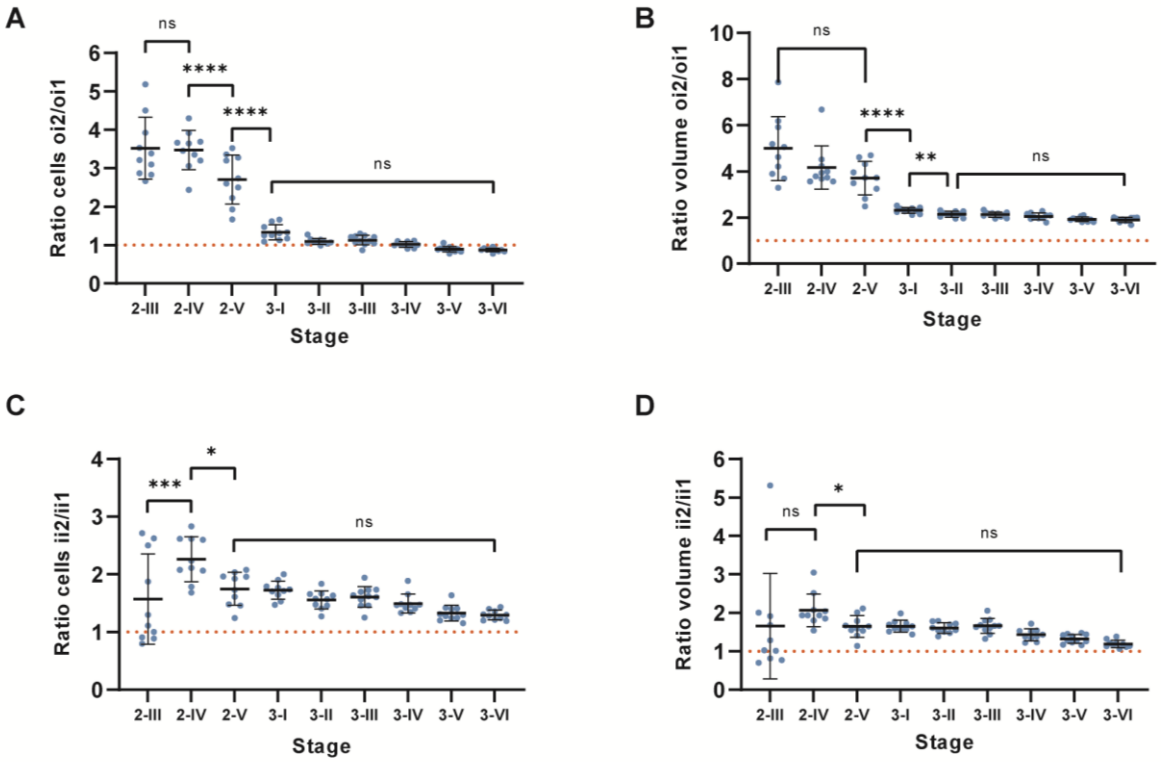

Figure 13 Ratio of cell number and volume between the integument layers

(A) Ratio of the cell number between the abaxial and adaxial outer integument. (B) Ratio of the volume between the abaxial and adaxial outer integument. (C) Ratio of the cell number between the abaxial and adaxial inner integument. (D) Ratio of the volume

between the abaxial and adaxial inner integument. The orange line indicates one. Data points indicate individual ovules. Asterisks represent statistical significance (ns, $p \geq 0.5$; *, $p < 0.05$; **, $p < 0.01$; ***, $p < 0.001$; ****, $p < 0.0001$; Student's t-test). Number of 3D digital ovules scored: 10 (stages 2-III, 2-IV, 2-V, 3-I, 3-II, 3-IV, 3-VI), 11 (stages 3-III, 3-V). Mean ± SD is shown.

Table 8 Cell numbers and total volume of the different integument layers.

	Inner integument						**Outer integument**			
Stage[a]	**ii1**		**ii1'**		**ii2**		**oi1**		**oi2**	
	N cells	Volume (x 10^4 μm^3)	N cells	Volume (x 10^4 μm^3)	N cells	Volume (x 10^4 μm^3)	N cells	Volume (x 10^4 μm^3)	N cells	Volume (x 10^4 μm^3)
2-III	9.4 ± 15	0.1 ± 0.03	-	-	14.1 ± 5.8	0.2 ± 0.07	12.0 ± 2.4	0.1 ± 0.05	41.8 ± 10.5	0.7 ± 0.2
2-IV	14.9 ± 2.4	0.2 ± 0.04	-	-	33.2 ± 4.6	0.4 ± 0.05	15.2 ± 3.7	0.3 ± 0.07	51.4 ± 7.6	1.1 ± 0.2
2-V	29.2 ± 5.0	0.4 ± 0.08	-	-	50.1 ± 5.6	0.6 ± 0.07	35.2 ± 12.0	0.8 ± 0.2	88.8 ± 10.1	2.7 ± 0.4
3-I	48.9 ± 8.1	0.8 ± 0.2	-	-	83.7 ± 10.8	1.3 ± 0.2	102.7 ± 22.4	2.7 ± 0.6	133.2 ± 17.1	6.18 ± 1.2
3-II	76.5 ± 11.0	1.5 ± 0.2	1.0 ± 0.0	1.5 ± 0.2	118.2 ± 14.1	2.5 ± 0.4	138.0 ± 8.2	4.2 ± 0.5	151.1 ± 7.8	9.0 ± 0.9
3-III	83.6 ± 12.6	1.8 ± 0.3	2.3 ± 1.9	1.8 ± 0.3	133.2 ± 15.0	2.9 ± 0.5	153.2 ± 17.6	4.5 ± 0.7	171.4 ± 9.6	9.5 ± 1.2
3-IV	102.8 ± 12.4	2.4 ± 0.4	7.8 ± 6.5	2.4 ± 0.4	153.0 ± 18.6	3.4 ± 0.3	173.8 ± 18.5	5.2 ± 0.4	175.8 ± 9.3	10.7 ± 1.0
3-V	148.8 ± 27.4	3.3 ± 0.6	26.3 ± 15.6	3.3 ± 0.6	194.7 ± 21.9	4.3 ± 0.5	232.5 ± 31.6	6.4 ± 0.5	207.4 ± 27.7	12.2 ± 0.9
3-VI	199.0 ± 36.9	4.8 ± 0.9	60.8 ± 19.5	4.8 ± 0.9	254.9 ± 33.3	5.7 ± 1.0	294.6 ± 36.0	7.9 ± 1.6	257.0 ± 28.2	14.8 ± 2.1

[a]Number of 3D digital ovules scored: 10 (stages 2-III, 2-IV, 2-V, 3-I, 3-II, 3-IV, 3-VI), 11 (stages 3-III, 3-V). Values represent mean ± SD.

3.1.5 Few spatially scattered asymmetric cell divisions initiate the parenchymatic inner integument layer

The following section will discuss some of the findings published in Vijayan & Tofanelli et al., 2021.

It is long been observed that a third cell layer is formed within the inner integument shortly before fertilization (Debeaujon et al., 2003; Schneitz et al., 1995). The adaxial inner integument or endothelial layer eventually generates an additional cell layer (ii1') by periclinal oriented asymmetric cell divisions (Figure 14 A). Cells of the parenchymatic inner integument are immediately distinguishable from adaxial inner integument cells by their altered shape and staining characteristics (Schneitz et al. 1995). During early seed development, adaxial inner integument cells will produce tannins while parenchymatic inner integument cells will contribute to parenchymatic ground tissue. Thus, cambium-like activity of the inner integument layer results in asymmetric cell divisions, thickening of the inner integument, and formation of distinct tissues with separate functions.

The formation of the parenchymatic inner integument layer was monitored through all of stage 3 and was analyzed with the help the 3D digital ovules (Figure 14). The outer integument and abaxial inner integument were removed and the internal tissues analyzed. The parenchymatic inner integument was analyzed at various stages of development in 36 digital ovules. In contrast to what was previously described, first signs of parenchymatic inner integument formation were observed at stage 3-II, with 2 / 10 of the digital ovules showing one cell of this layer (Figure 14 A, B). At stage 3-III 4 / 11 and at stage 3-VI 9 / 10 digital ovules showed at least one parenchymatic layer cell, respectively. By stages 3-V and 3-VI, all digital ovules exhibited this layer. The number of parenchymatic layer cells increased from 0.2 ± 0.4 cells per layer at stage 3-II to 7.0 ± 6.6 at stage 3-IV to 60.8 ± 19.5 at stage 3-VI. Thus, at this stage the average the parenchymatic inner integument consisted of 13.4 percent of the total cells of the inner integument (453.9 ± 69.8) and with a volume of 1.53×10^4 μm^3 ± 0.5×10^4 μm^3 contributing to 14.4 percent of its total volume (10.6×10^4 μm^3 ± 1.9×10^4 μm^3). Regarding the spatial organization of the parenchymatic inner integument, single cells or patches of cells are observed on both lateral sides of the posterior half of the inner integument at stages 3-II and 3-III (Figure 14 C). A patch of connected cells became visible at later stages, probably because of subsequently cell divisions. Proximal-distal and lateral extension of the parenchymatic layer took place until a ring-like structure enveloping the proximal half of the inner integument at

stage 3-VI was visible (Figure 14 D-F). The parenchymatic layer showed an irregular appearance at the border region (Figure 14 E, F).

To analyze, which kind of oriented cell division originated this tissue (periclinal or anticlinal), 978 cells of the parenchymatic inner integument were scored across the 36 ovules and 14 cells in were identified in M-Phase as indicated by the presence of mitotic figures in the TO-PRO-3 channel (Figure 14 G). Only one of the 14 cells was interested by a periclinal cell division that generated a cell of the parenchymatic inner integument layer. Interestingly, the other 13 mitotic cells were undergoing anticlinal cell divisions. This finding indicates that only a few scattered cells of the adaxial inner integument undergo periclinal cell divisions. The most part of the parenchymatic inner integument is formed by anticlinal cell divisions. The results suggest that initiation of the parenchymatic inner integument layer does not involve only asymmetric cell divisions of adaxial inner integument cells to form parenchymatic tissue. The results suggest that periclinal cell divisions occur only in a few spatially scattered cells present within the adaxial inner integument. Further anticlinal cell divisions of the founder cells and their progeny in the parenchymatic inner integument will form a continuous parenchymatic inner integument layer with irregular edges.

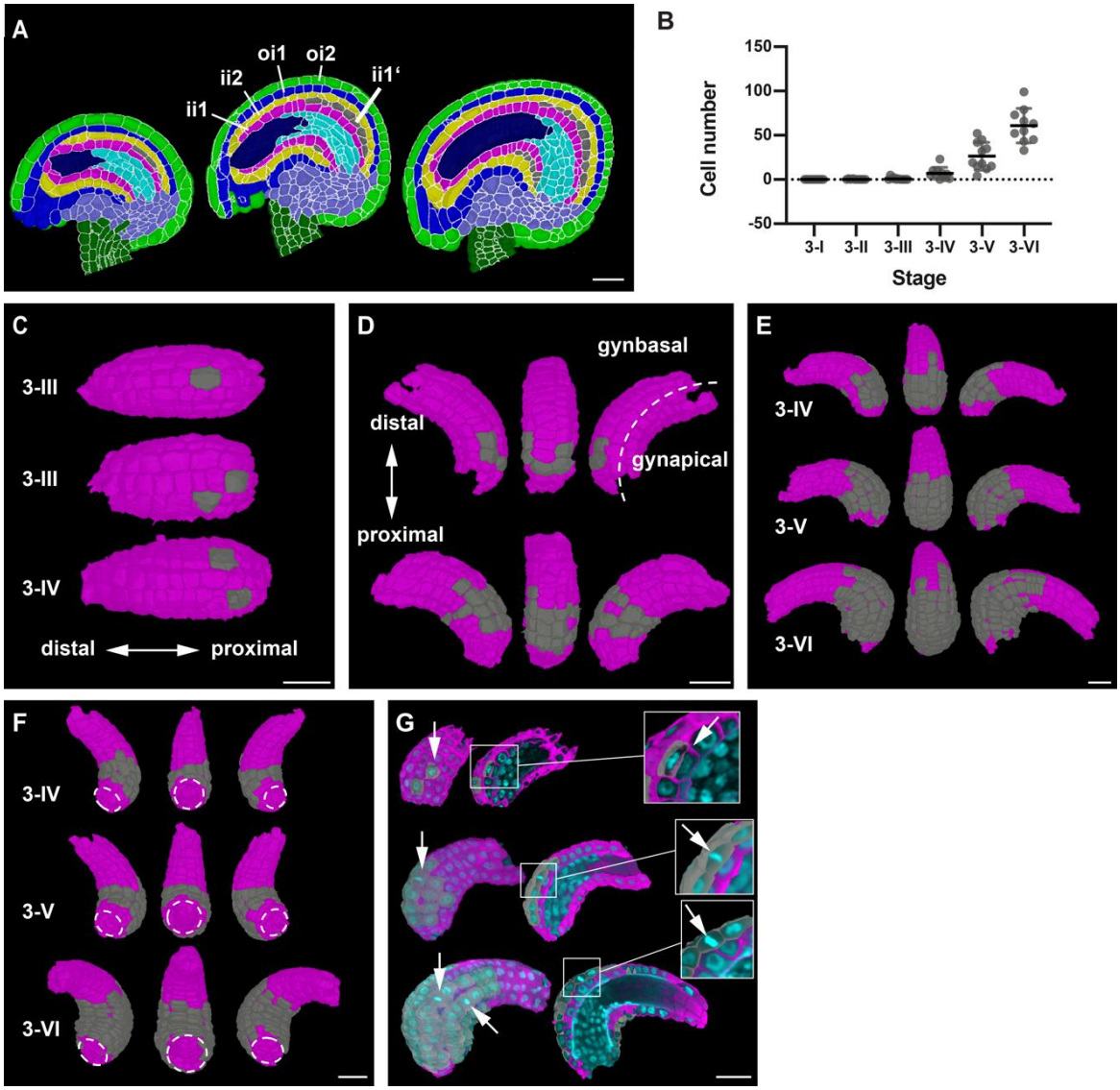

Figure 14 Formation of the parenchymatic inner integument layer (ii1').

(A) Mid-sagittal section of wild-type ovule at stages 3-IV, 3-V, and 3-VI, showing the initiation of a new cell layer (ii1') in the adaxial inner integument. (B) Plot depicting the number of cells of the developing parenchymatic layer. (C) 3D top surface view of the adaxial inner integument at stages 3-III and 3- IV showing the occurrence of the first few founder cells of the parenchymatic layer. (D) 3D side surface view of adaxial inner integument showing presence of parenchymatic cells. (E) 3D side surface view of adaxial inner integument at later stages of 3-IV, 3-V, and 3-VI where the newly formed tissue layer is observed as a patch of connected cells present at the proximal region of the inner integument. (F) 3D bottom surface view of the parenchymatic inner integument at different stages showing a ring-like structure of connected cells covering the proximal half of the inner integument. (G) Section view of the 3D cell meshes of adaxial inner integument with the overlaid nuclei z-stack displaying a periclinal division (top) and anticlinal divisions (center, bottom) in the parenchymatic inner integument layer. Data points indicate individual ovules. Number of 3D digital ovules scored: 10 (stages 3-I, 3-II, 3-IV, 3-VI), 11 (stages 3-III, 3-V). Mean ± SD are represented as bars. Abbreviations: ii1, adaxial inner integument; ii1', parenchymatic inner integument layer; ii2, abaxial inner integument; oi1, adaxial outer integument; oi2, abaxial outer integument. Scale bars: 20 µm. Image from Vijayan & Tofanelli et al., 2021.

3.2 Establishment of the temporal progression of wild-type ovule development

3.2.1 Estimation of the duration of ovule developmental stages

The following section will discuss some of the findings published in Vijayan & Tofanelli et al., 2021.

To gain more insight into the growth dynamics during ovule development, through a two-step procedure the temporal progression of ovule development was assessed. First, pistil growth during ovule development, was registered by measuring pistil length of 6 individual live pistils attached to the plant at different times, including floral stages 8 – 12 (stages according to Smyth et al., 1990) (Figure 15 A) (Table 9). The measurements of pistil length over time were employed to generate a pistil growth curve by fitting a curve to the data points (Figure 15 B).

Next, ovules from 64 pistils of different lengths were dissected out and the stages of the ovules for each pistil was determined. The pistil growth curve generated in the first steps was used to estimate of the duration of the different ovule stages. As previously noticed, ovules do not develop synchronously within a pistil (Schneitz et al., 1995; Wolny et al., 2020; Yu et al., 2020). In line with these results, ovules of different stages within a given pistil were observed (Supplementary table 5). Asynchrony was reported for all stages and ovules within a pistil were usually found to be distributed across two to four consecutive stages. To counteract this factor, the number of ovules for each stage was determined and the stage used as reference was the one with the largest number of counted ovules. Stages 3-II and 3-III were grouped together since an equal number of ovules of the two stages were contained within the same pistils. The pistil growth curve was employed to derive the time duration between the minimal and maximal pistil lengths covering a given stage and used to estimate the duration of the stages (Figure 15 C).

Under our growth conditions, ovules emerge from placental tissue in pistils with a corresponding length of about 0.33 mm and undergo anthesis when the pistil reach 2.3 mm of length. Ovules developed from early stage 1 to the end of stage 3 within a period of 146.2 hours or 6.1 days. The three main stages differed in their durations. Stage 1 required about 31.7 hours (1.32 days), while stage 2 was 58.9 hours (2.45 days) and stage 3 was 55.6 hours (2.32 days), roughly 1.9 or 1.8 times longer, respectively. These results provide a refined timeline for ovule development and are comparable to previously estimated durations (Schneitz et al., 1995).

Table 9 Pistil length of individual live pistils monitored up to 192 hours.

	Pistil Nr							
Hours	**1[a]**	**2[a]**	**3[a]**	**4[a]**	**5[a]**	**6[a]**	**Mean**	**SD**
0	0.31	0.32					0.315	0.007
24	0.54	0.49	0.45	0.47			0.488	0.039
48	0.74	0.78	0.66	0.64	0.77	0.63	0.703	0.068
72	0.97	1	1	1	1		0.994	0.013
96	1.31	1.33	1.29	1.22	1.38		1.306	0.059
120	1.81	1.8	1.85	1.73	1.73		1.784	0.053
144	2.3	2.28	2.54	2.15	2.3		2.314	0.141
168	2.75	3.26	3				3.003	0.255
192	3.7	4	4				3.900	0.173

[a]Pistil length in mm
Data published in Vijayan & Tofanelli et al., 2021.

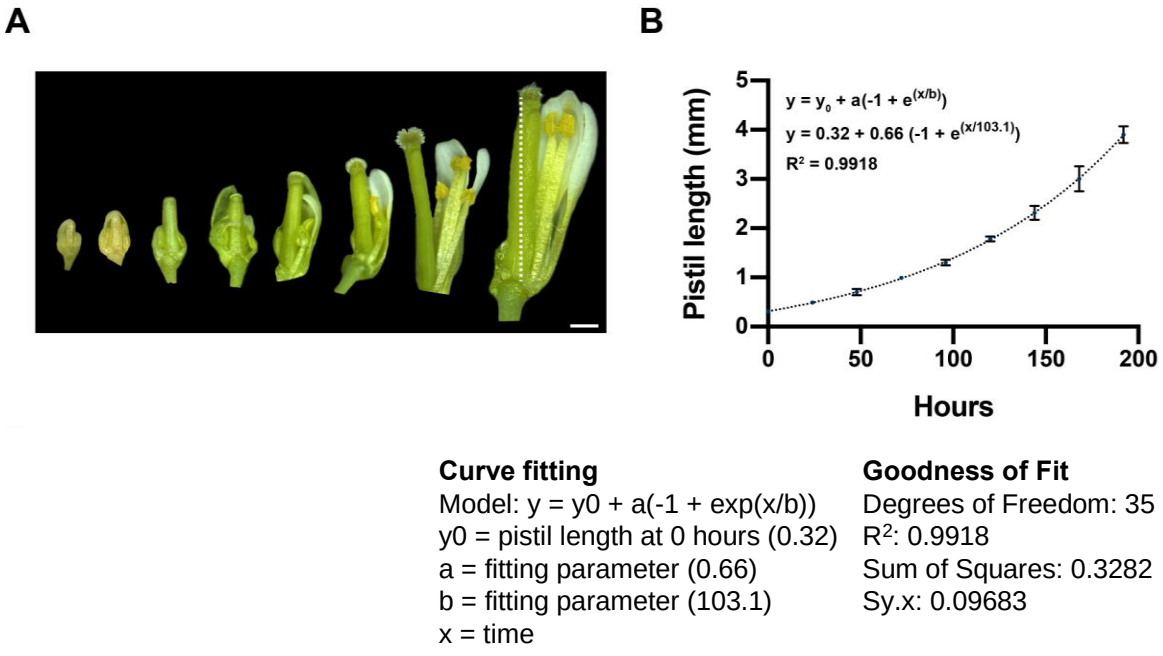

Figure 15 Temporal progression of ovule development.

(A) Micrograph depicting gynoecia (pistils) at different time points (day 0 to day 7). Number of pistils scored: 6. (B) Graph showing the increase in pistil length (mm) over

time. The fitted curve is indicated by the dotted line. The curve fitting model and the goodness of fit are reported. (C) Correlation between pistil length and duration of ovule stages. The values at the top represent the range of pistil lengths spanning the given ovule stage indicated beneath. The respective time values were deduced from the fitted curve in (B). The values within the green arrow indicate the deduced durations of the respective ovule stages. Mean ± SD are represented as bars. Number of pistils scored: 64. Scale bar: 0.5 mm. Image from Vijayan & Tofanelli et al., 2021.

3.2.2 Analysis of ovule growth at two time points

To confirm the established temporal progression of ovule development, ovules from the same pistil were imaged at two time points T0 and T1 (after 24h). The analysis has been performed on a total of 8 pistils, including a total of 94 ovule imaged and processed according to the mentioned pipeline. For each of the half of the pistil a minimum of 4 to 9 ovules has been analyzed in terms of cell number and total volume (Table 10). The indicated reference ovule stage corresponds to the stage with the highest number of analyzed ovule, as was already applied for the duration of ovule stages. To check if the growth was not affected because of the removal of the first carpel half, the values of cell number and volume were compared to those observed from the 3D digital atlas of wild-type ovule of the corresponding stage. Overall, similar values were observed per stage between the two datasets (Table 10 and Table 4).

As previously observed, approximately 24 hours are required to pass through stage 2-II to reach stage 2-IV. This remark has been confirmed from pistil 4, where ovules passed from stage 2-II to stage 2-IV after 24 hours (Figure 16). Pistil 5, 6 and 7 confirmed that approximately an interval of 24 hours is required to pass from stage 2-III/2-IV to stage 3-I (Figure 16). Pistil 12 took approximately 24 hours to pass form stage 3-I to stages 3-IV (Figure 16). Although, the duration did not match exactly with the timeframe experiment (around 30 hours), the values are similar. According to the timeframe of ovule stages, around 30 hours are required to pass from stage 2-V to stage 3-II. Although, the values did not match exactly, pistils 11 and 3 confirm the time interval observed for the corresponding stages (Figure 16). Pistil 2 confirmed that approximately 24 hours are required to pass from stage 3-II/3-III to stage 3-V (Figure 16). The time interval observed did not match exactly to those annotated during the establishment of the staging duration. The asynchronicity observed among ovules within the same pistil, might account for a complexity that needs to be considered for the interpretation of the results. Therefore, these results have been only employed as control for the previous established framework for stage duration.

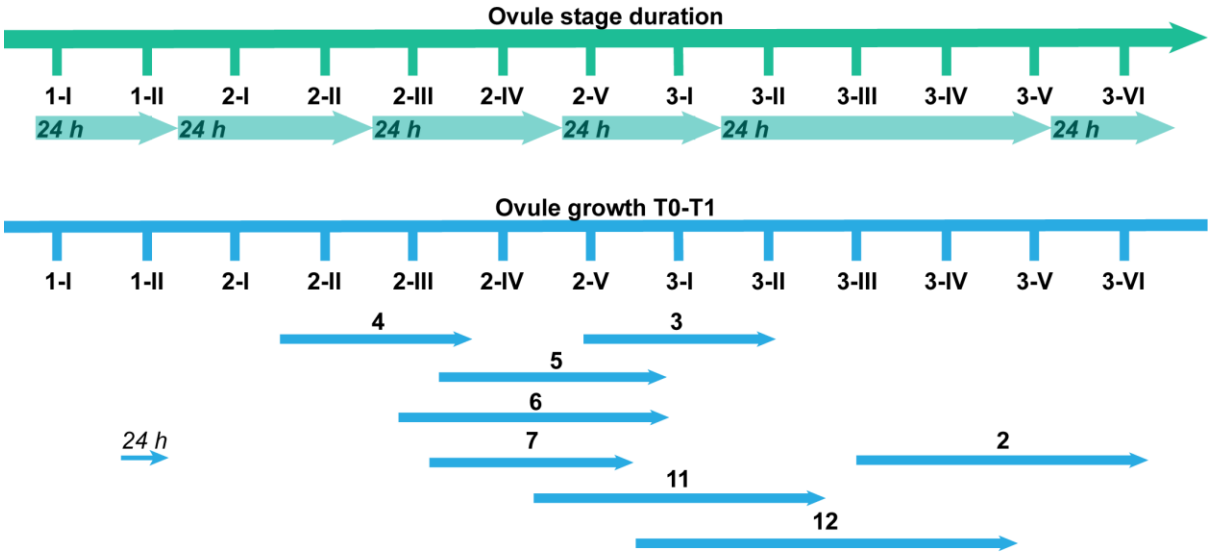

Figure 16 Ovule growth at two time points.

Correlation between ovule stage duration and ovule growth at two-time points. The values on the top represent ovule stages and different 24 h time interval. The values on the bottom the arrows represent the various pistil analyzed with the corresponding number. Each arrow has a duration of 24 hours. It is possible to observe the ovule stages covered within the pistil analyzed. Number of pistils scored: 8. Number of ovules scored: 94.

Table 10 Ovules analyzed at two time points.

Pistil Nr	Timepoint	Ovule scored	Stage	N Cells	Tissue volume (x 10^4 µm^3)
2	T0	5	3-III	1226.6 ± 49.32	28.11 ± 3.71
	T1	5	3-V	1988.6 ± 121.87	51.56 ± 4.85
3	T0	5	2-V	543.2 ± 35.27	7.38 ± 0.72
	T1	5	3-II	1042.6 ± 190.68	24.11 ± 4.30
4	T0	7	2-II	247.14 ± 47.53	2.77 ± 0.37
	T1	9	2-IV	388.22 ± 77.13	5.96 ± 1.29
5	T0	7	2-IV	432.28 ± 48.17	6.43 ± 0.85
	T1	5	3-I	772 ± 109.81	16.03 ± 1.77
6	T0	4	2-III	386.25 ± 47.85	5.28 ± 0.43
	T1	7	3-I	932.14 ± 152.95	21.01 ± 3.05
7	T0	5	2-IV	417.8 ± 41.63	5.74 ± 0.52
	T1	5	3-II	732.6 ± 170.07	14.45 ± 3.67

11	T0	7	2-V	514.57 ± 23.97	7.29 ± 0.28
	T1	6	3-II	902 ± 78.65	20.27 ± 2.31
12	T0	5	3-I	738.6 ± 78.34	13.67 ± 2.22
	T1	7	3-IV	1344.85 ± 131.65	33.49 ± 4.06

Values represent mean ± SD.

3.3 Relative growth dynamics during wild-type ovule development

The following section will discuss some of the findings published in Vijayan & Tofanelli et al., 2021.

The development of an organ occurs through two different processes: increase in the cell number through cell division and change in size through growth including increase in the volume of single cells. To get initial insight into the general growth dynamics of *Arabidopsis* ovule development, the quantitative data on the stage-specific variations in cell numbers and growth were related with the temporal information of the duration of ovules stages.

The average growth rates for certain time intervals have been estimated, evaluating the mean ovule volume increase of each stage (Table 4). Up to the end of stage 1-II, the average growth rate calculated was 0.3×10^3 µm^3/hr, of 1.5×10^3 µm^3/hr for the interval including stages 2-I to 2-V and 7.2×10^3 µm^3/hr for the interval including stages 3-I to 3-IV. The growth rate decreased to 2.9×10^3 µm^3/hr for stage 3-V.

To analyze the relative growth, the global volume increase and cell proliferation rates during two consecutive stages were normalized by the respective rate of the stage 1-I/1-II interval (Figure 17 A). Both relative growth rate curves highlighted a dynamic behavior across the development and for many stage intervals, similar relative growth rates were observed. However, the relative cell proliferation rate from stages 2-I to 2-II showed to be higher compared to the relative growth rate, suggesting that for this stage interval growth is achieved mainly through cell proliferation rather than increase in volume. The opposite was observed for stages 2-IV to 3-IV, indicating that ovule growth occurs through these stages by cell enlargement. Additionally, the relative growth of the ovule was analyzed by plotting the ratio between the mean total volume and mean total number of cells for two consecutive stages (Figure 17 B). The curves in Figure 17 A and B qualitatively resemble each other. This is presumably due to the relatively minor variations in the duration of the individual ovule stages.

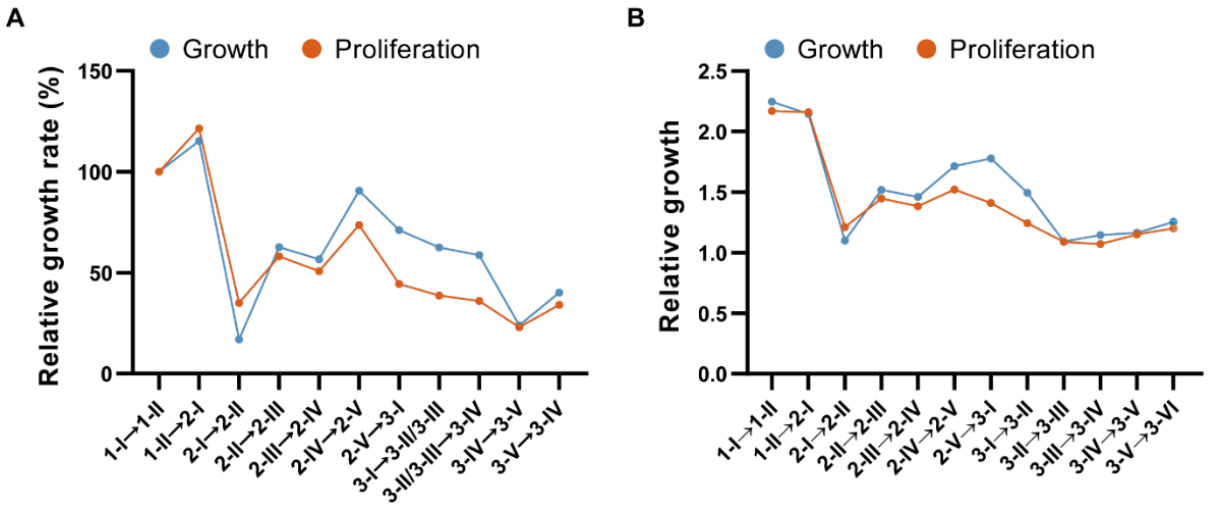

Figure 17 Growth dynamics of ovule development.

(A, B) Plots showing the ovule volume or cell number increases. (A) Plot showing the growth rate normalized to the growth rate of the transition from stage 1-I to 1-II. (B) Plot depicts relative growth between two consecutive stages. Image from Vijayan & Tofanelli et al., 2021.

3.3.1 Relative growth of the integuments in wild-type ovule

The relative growth of the integuments has been analyzed according to the principles already applied in Vijayan & Tofanelli et al., 2021 for the analysis of other tissues (Figure 18 A–D). To calculate the relative growth, the ratio of the mean volume or mean cell number of the tissue for two consecutive stages was divided by the corresponding relative ovule growth. The calculated ratio relates the integument growth rate to the overall ovule growth. When the values are above one the tissue is growing at a higher rate than the general ovule growth.

The analysis showed that the integuments are characterized by dynamic changes during development (Figure 18 A–D). Up to stage 3-I the outer integument exhibited a higher relative growth compared to the inner integument, while from stage 3-I on the relative growth pattern was reversed.

The main contribution to the growth, up to stage 3-I, of the abaxial outer integument occurs mainly through cell expansion rather than cell proliferation, with relative rate of 1.44 and 1.14 in the transition from 2-IV to 2-V, respectively. These developmental stages correspond to the initiation of the outer integument, which is characterized by cell enlargement on the posterior half of the ovule. Up to stage 3-I the adaxial outer integument showed relative higher rate in terms of cell proliferation and cell enlargement. Interestingly, the growth rate of the adaxial outer integument showed a higher growth than the abaxial outer integument.

Regarding the abaxial inner integument, up to stage 3-I, the growth resulted to be lower compared to the outer integument, except during the transition from stage 2-III to 2-IV where the growth and proliferation rate were 1.62 and 1.70, respectively. This stage is characterized by the initiation of the inner integument, which is morphological described as a ring-like cell bulging located at the upper part chalaza at the interphase with the nucellus. The adaxial inner integument is characterized by a high proliferation rate during transition from 2-IV to 2-V and by a low growth rate up to stage 3-I. As it was morphologically described, up to stage 3-I the outer integument initiates after the inner integument and grows to encase the inner integument and the nucellus, therefore the higher rate observed would describe this behavior.

From stage 3-I the abaxial and adaxial outer integument showed a steady growth throughout the development. On the contrary the abaxial and adaxial inner integument, showed a slightly higher growth, with a particular higher rate a stage 3-I which correspond to the stage in which the inner integument grows to enclose the nucellus.

In summary, the results reveal ovule growth a dynamic process, in terms of both cell enlargement and cell proliferation and the respective relative contributions of individual integument layer during development. The analysis of growth rates seems to quantitatively describe the integuments growth that was previously described only in morphological terms (Schneitz et al., 1995).

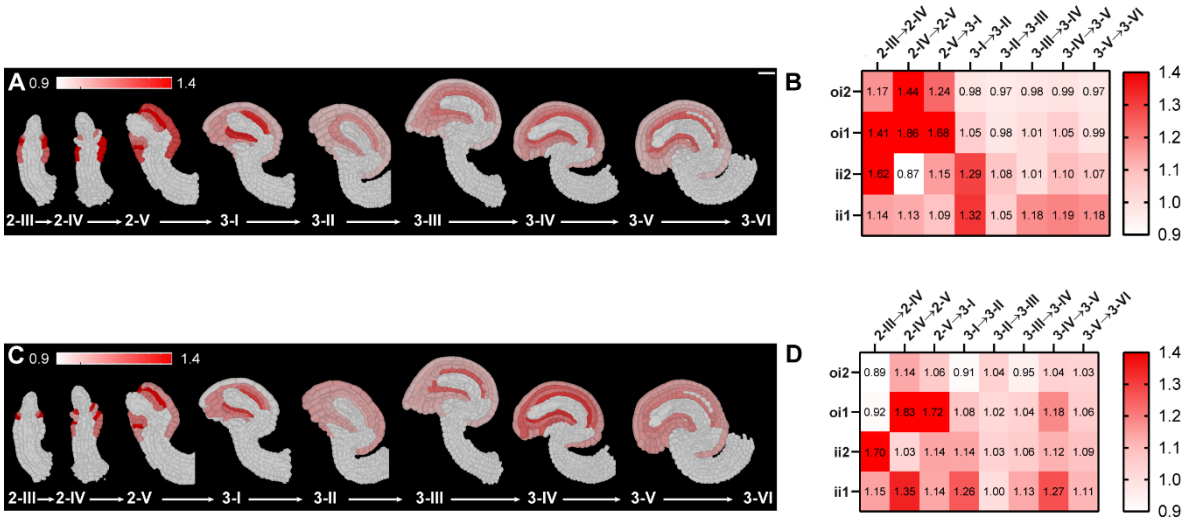

Figure 18 Growth dynamics of integuments development.

(A-D) Mid-sections and heat maps depicting relative tissue growth across the different ovule stages of the integuments. Stages are indicated. Heat map values indicate ratios. Plots showing the ovule volume or cell number increases. (A, B) Integument-specific growth rate. (C, D) Integument-specific proliferation rate. Number of 3D digital ovules scored: 10 (stages 2-III, 2-IV, 2-V, 3-I, 3-II, 3-IV, 3-VI), 11 (stages 2-I, 3-III, 3-V). Abbreviations: oi2, abaxial outer integument; oi1, adaxial outer integument; ii2, abaxial inner integument; ii1, adaxial inner integument.

3.3.2 Spatial regulation of growth in the integuments of wild-type ovule

As previously mentioned, the development of an organ occurs through cell increase and change in size through growth. These processes are tightly coordinated in time and space. The analysis of growth dynamics in the integuments during different stages of ovule development already provided information on the temporal regulation of growth in these specific tissues. However, this analysis did not provide additional information on how integuments growth patterns are regulated in space. Therefore, a coordinate system in 3D has been applied to the integuments to gain spatial information on growth pattern with cellular resolution within the tissue. The integument coordinate system allowed to identify cellular position along the PD axis and to track cellular features with spatial resolution.

A similar approach has been applied for the spatiotemporal characterization of growth dynamics in leaf of *Arabidopsis* tracking cell shape and cell division along measured organ distances. It has been shown the presence of a proximal-distal gradient of growth, decreasing towards the distal leaf tip and a higher medio-lateral growth towards the lateral lamina corresponding to the marginal meristem (Fox et al., 2018; Kierzkowski et al., 2019).

The assignment of position to individual cells along the length the integuments is achieved by the application of a Bezier ring through the most proximal cell centroid of the adaxial outer integument in MGX (Figure 19 A) (Vijayan and Strauss, unpublished). The use of a Bezier was implemented originally in MGX in the 3DCellAtlas tool, which combines a central Bezier line and a surface mesh to align the principal axes of cells and generate an organ specific coordinate system (Barbier de Reuille et al., 2015; Montenegro-Johnson et al., 2015). One of the advantage of this tool is its wide applicability and flexibility to generate coordinate system in various organs, as applied to the shoot apical meristem for semi-automatic cell annotation (Montenegro-Johnson et al., 2019).

In ovule, when the measurements of the distance of cell centroid from the generated Bezier is carried out, the identification of cell position along the PD axis of the tissue is performed. To facilitate and increase the accuracy of distance measurements, additional cell type annotations are applied to differentially label the anterior and posterior sides of the integuments layer (Figure 19 B). The application of the Bezier ring at the most proximal circle of cells of the adaxial outer integument, the site of attachment to the chalaza, has shown to allow measurements of cell position along the PD axis in one single step for the 4 layers of the integuments (Figure 19 D) (Vijayan and Strauss, unpublished). Within the abaxial outer integument, the most proximal part of the layer, cells interfacing sub epidermally the posterior

chalaza assumes negative values, because placed spatially behind the Bezier ring for distance measurements (Figure 19 A, C). The PD distance values have been normalized to relative PD distance with the following formula: $x_{rel\ PD\ dist} = x_{dist\ \mu m} / x_{max\ dist\ \mu m} \times 100$. After normalizing the distance values, it was possible to relatively compare different ovule from different stages.

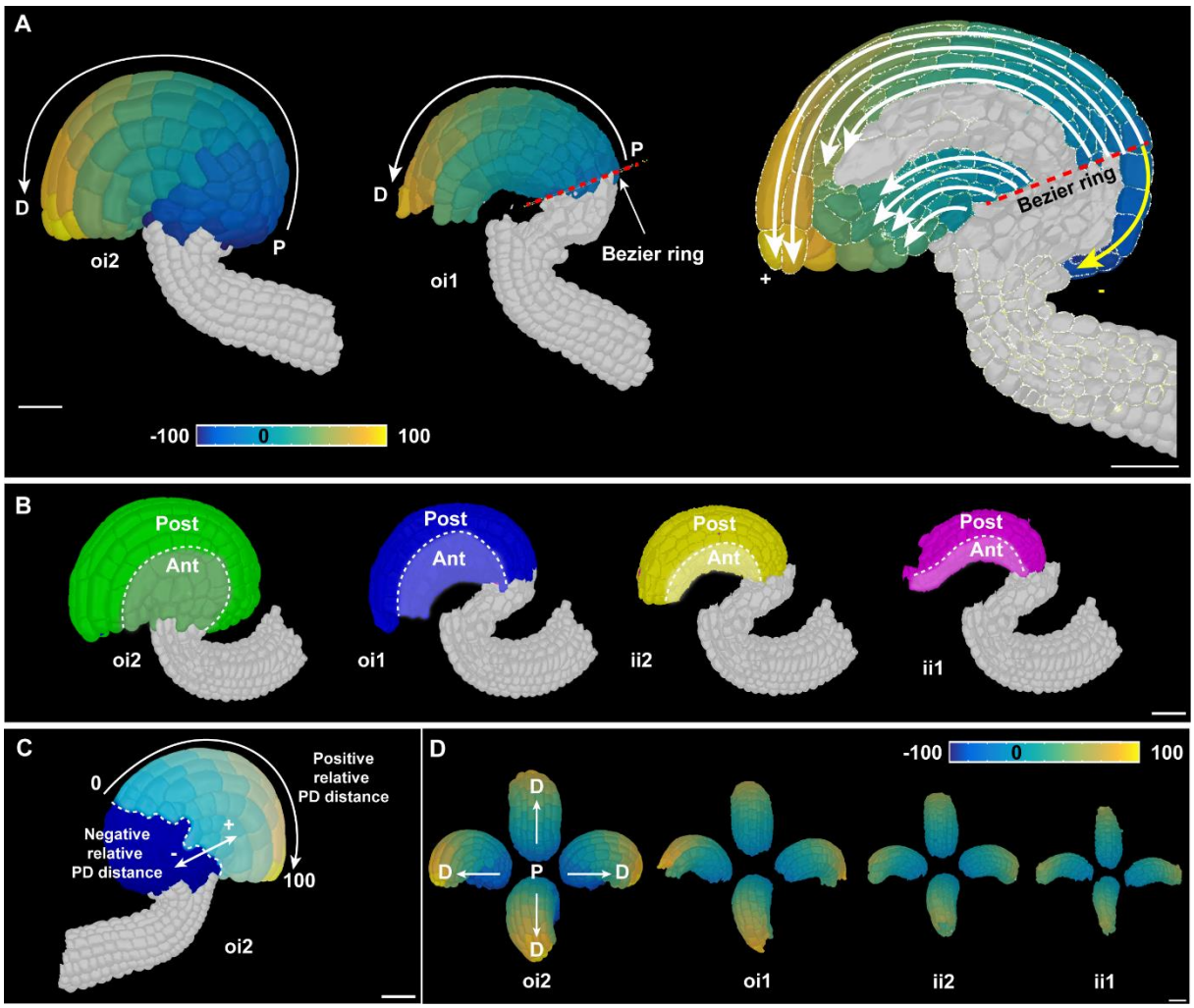

Figure 19 Integuments coordinate system.

(A) 3D cell mesh of ovule at stage 3-IV showing heap map of relative PD distance and schematic view of the coordinate system applied to the integuments. On the left, the 3D cell mesh of the abaxial and adaxial outer integument. The dotted red line highlights the position of the Bezier ring applied for cell distance measurements. The proximal-distal axis is reported. On the right, the coordinated system is displayed on the mid-section heat map of the same ovule. The dotted red line highlights the position of the Bezier ring. The white arrows show the measurement of the cell distances within each layer of the integuments. The values of the relative PD distances are positive. The yellow arrow shows the portion of the abaxial outer integuments facing the posterior chalaza and characterized by negative relative PD distances values. (B) 3D cell mesh of ovule at stage 3-IV showing the anterior and posterior cell type labelling. The layers are sequentially removed to show the internal layers. Additional cell type annotations

applied to differentially label the anterior and posterior sides of the integuments layer. (C) 3D cell mesh of ovule at stage 3-IV showing in detail the coordinate system for the abaxial outer integument. Negative PD distance values are generated within the proximal region of the layer colored in blue, while positive values are generated within the light-colored region. (D) 3D cell mesh of ovule showing heap map of relative PD distance of different integuments layers at different angle view. The first layer reported (oi2) show the reference of the PD axis with white arrows. Abbreviations: oi2, abaxial outer integument; oi1, adaxial outer integument; ii2, abaxial inner integument; ii1, adaxial inner integument; P, proximal; D, distal; Post, posterior; Ant, anterior. Scale bar: 20 μm.

3.3.2.1 Spatial regulation of proliferation in the integuments of wild-type ovule

To identify within the integuments regions of preferential cell proliferation, the coordinate system has been employed to track the position of mitotic cells (Figure 20 A). The TO-PRO-3 Iodide channel allowed the labeling of dividing cells, through the identification of mitotic figure characterized by a rod-shape nucleus and a brighter intensity of signal (Table 11).

Through the generation of relative PD distance, the ovule analyzed for each stage were plotted to identify the region with preferential cell proliferation (Figure 20 B, D, F, G).

Within the abaxial outer integument, the most proximal region showed throughout the analyzed stages few or absent cell division (Figure 20 B). The most proximal abaxial outer integument, represent the region with negative distance values in the layer, in which the cells do not face the adaxial layer of the outer integument but are neighboring the posterior chalaza (Figure 11). The result and the structural composition of the region support the hypothesis that this region presents some morphological differences compared to the most proximal region of the abaxial outer integument laying above the other integument layer. Overall, within the abaxial outer integument throughout development the cell divisions appear to be more proximal distributed, with most of the dividing cells located in the proximal half of the tissue ($0 \leq$ relative PD distance ≤ 50). Exceptions are observed at early stages 2-V and 3-I, in which 8 mitoses are observed in the distal half, and at later stage 8 mitoses are placed in the mid-region, where relative PD distance is close but over 50 (Figure 20 B). The region of higher proliferation is highlighted throughout the developmental stages in Figure 20 D.

Within the adaxial outer integument, the most proximal region shows throughout the analyzed stages most of the cell division (Figure 20 C). Overall, within the abaxial outer integument throughout development the cell divisions appear to be more proximal distributed, with most of the mitotic figures located in the proximal half of the tissue (relative PD distance ≤ 50). Exceptions are observed for 8 mitotic figures, which are occasionally present in different

stages, after relative PD distance value of 50. (Figure 20 C). The region of higher proliferation is highlighted throughout the developmental stages in Figure 20 E.

Within the abaxial inner integument, at stage 2-V and 3-I dividing cells are broadly distributed throughout the whole integument length (Figure 20 F). Starting from stage 3-I, the mitotic cells resulted to be distributed mostly proximally compared to earlier stages (relative PD distance ≤ 50) (Figure 20 F). Overall, within the abaxial inner integument throughout development the cell divisions appear to be more proximal distributed only at later stages of the development. The region of higher proliferation is highlighted throughout the developmental stages in Figure 20.

Within the adaxial inner integument, form stage 2-V to 3-II dividing cells are broadly distributed throughout the whole integument length (Figure 20 G). Starting from stage 3-IV, the mitotic cells are distributed more proximally compared to earlier stages (relative PD distance ≤ 50) (Figure 20 G). Overall, within the abaxial inner integument throughout development the cell divisions appear to be more proximal distribute only at later stages of the development. The region of higher proliferation is highlighted throughout the developmental stages in Figure 20 I.

To summarize, within the integuments the analysis showed the presence of a region of preferential distribution of cell proliferation. Within these regions, growth most likely occur through cell division. These regions are localized in the most proximal half of the integuments, except the abaxial outer integument, where the mid-region represent the highly proliferative area and showing a proximal portion with absent cell division. These results suggest the presence of spatial regulation of cell proliferation within the integuments.

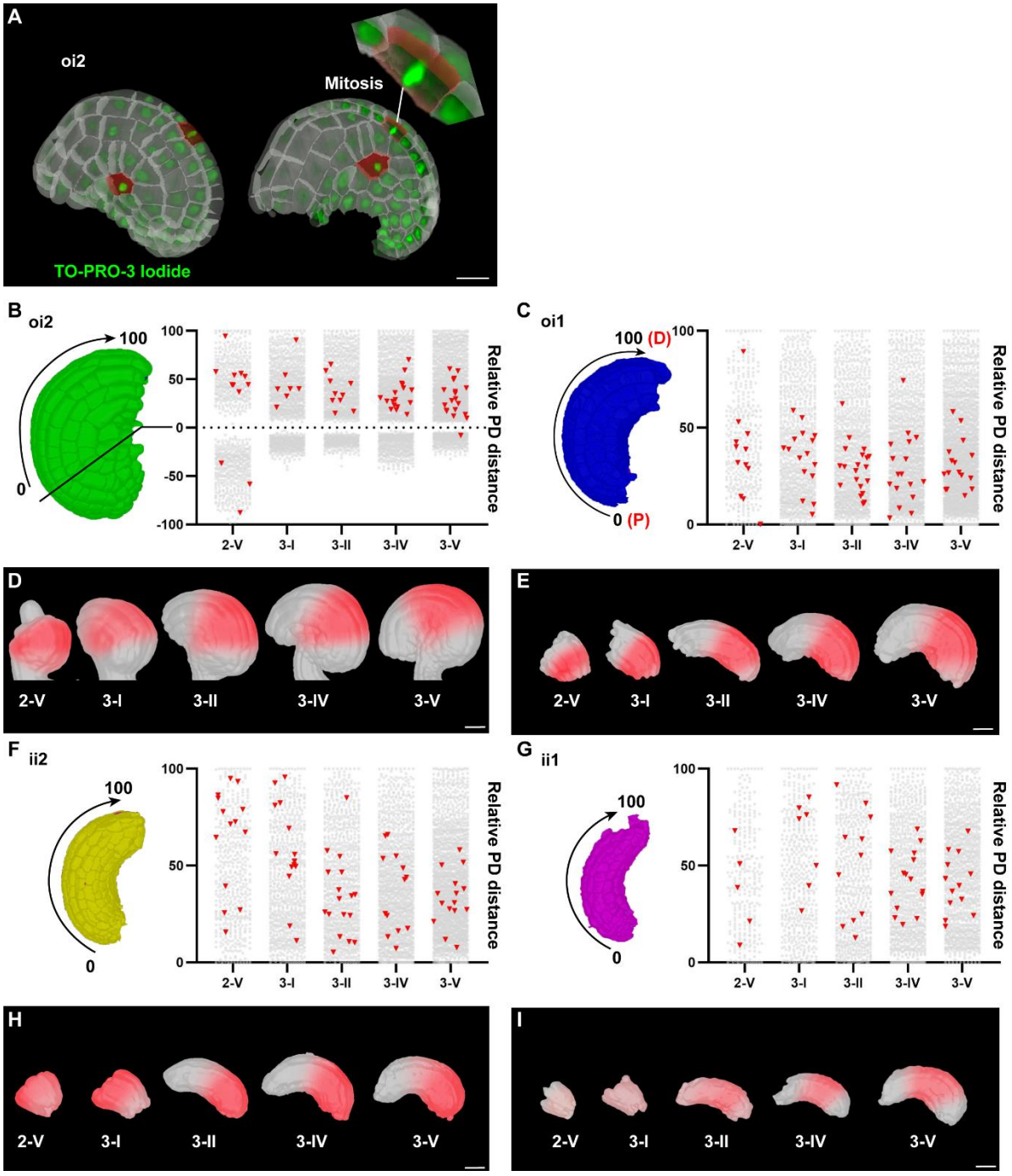

Figure 20 Spatial localization of cell proliferation in the integuments.

(A) 3D cell mesh of abaxial outer integument showing the tracking of cell proliferation. The TO-PRO-3 Iodide channel is visible in green and allow the identification of cells undergoing mitosis. Cells dividing are differentially labeled and are visible in red. White cells are in interphase, not dividing. (B, C, F, G) Column graph showing the distribution of dividing cells in different integuments layers along the PD axis, across different stage of development. The stages are reported on the x-axis. The relative PD distance is reported on the y-axis and ranges between 0 and 100. For the abaxial outer integument, the negative values are showed on the 3D cell mesh. Each gray point is a cell in interphase. Each red triangle is a dividing cell. On the left part the 3D cell mesh of the specific layer is reported. The arrows show the relative PD distance and the

delimiting values. (D, E, H, I) Surface mesh of the specific layer of the integuments at different developmental stages, showing highlights in red the region of highest proliferation. (B, D) Spatial distribution of cell proliferation in the abaxial outer integument. (C, E) Spatial distribution of cell proliferation in the adaxial outer integument. (F, H) Spatial distribution of cell proliferation in the abaxial inner integument. (G, I) Spatial distribution of cell proliferation in the adaxial inner integument. Data points indicate individual cells. Number of 3D digital wild-type ovules scored: 10 (stages 2-V, 3-I, 3-II, 3-IV), 11 (stage 3-V). Abbreviations: oi2, abaxial outer integument; oi1, adaxial outer integument; ii2, abaxial inner integument; ii1, adaxial inner integument; P, proximal; D, distal. Scale bar: 20 μm.

Table 11 Cell division analysis in the integuments.

Sample[a]	**Tissue**	**N mitotic cells**	**% of mitotic cells**	**N cells scored**
2-V	oi2	1.2 ± 1.03	1.44 ± 1.40	906
	oi1	1.2 ± 1.13	3.15 ± 3.31	396
	ii2	1.4 ± 0.96	2.84 ± 1.86	500
	ii1	0.5 ± 0.70	1.93 ± 2.65	289
3-I	oi2	0.7 ± 0.82	0.49 ± 0.57	1331
	oi1	1.6 ± 1.17	1.68 ± 1.23	1021
	ii2	1.5 ± 1.35	1.83 ± 1.69	835
	ii1	0.7 ± 0.82	1.35 ± 1.65	487
3-II	oi2	1.11 ± 0.92	0.70 ± 0.52	1403
	oi1	2.33 ± 1.73	1.68 ± 1.20	1229
	ii2	1.88 ± 1.05	1.68 ± 0.96	1044
	ii1	1.22 ± 0.97	1.55 ± 1.17	690
3-IV	oi2	1.7 ± 0.82	0.98 ± 0.47	1733
	oi1	1.7 ± 1.33	0.96 ± 0.76	1730
	ii2	1.3 ± 1.88	0.91 ± 1.42	1524
	ii1	1.5 ± 1.35	1.55 ± 1.43	948
3-V	oi2	1.72 ± 1.10	0.85 ± 0.59	2270
	oi1	1.45 ± 1.57	0.61 ± 0.63	2554
	ii2	1.36 ± 1.36	0.66 ± 0.65	2133
	ii1	1.18 ± 1.08	0.95 ± 0.80	1300

[a]Number of 3D digital ovules scored: 10 (stages 2-V, 3-I, 3-II, 3-IV), 11 (stage 3-V). Values represent mean ± SD

3.3.2.2 Spatial control of cell enlargement in the integuments of wild-type ovule

To analyze growth patterns within the integument regions, the distribution of cell volumes has been analyzed along the relative PD distance.

Within the abaxial outer integument, a progressive increase in the cell volume is observed in the distal half throughout development (Figure 21 A-E). At stage 2-V, the cell volume is constant along the PD axes, and with stage 3-I a progressive increase in the cell volume is observed (Figure 21 A, B). Up to stage 3-II, the increase of cell volume is more evident and results to be localized within the distal half of the integument (relative PD distance $\geq$ 50) (Figure 21 C-E). Interesting the most proximal part of the integument, characterized by negative relative PD distance values, at stages 3-V showed a higher cell volume compared to those cells located most proximally (0 $\leq$ relative PD distance $\leq$ 50) (Figure 21 E). These results suggest the hypothesis of a differential regional composition within the abaxial outer integument, with a difference between the proximal outer integument interfacing the posterior chalaza and the outer integument portion facing the adaxial layer of the outer integument. In summary, the abaxial outer integument show a preferential cell enlargement localized at the distal half at later stage of ovule development (relative PD distance $\geq$ 50). These results suggest that the growth of this region is characterized by volume increase through cell enlargement rather than by increase in cell number.

Within the adaxial outer integument, cell volumes are distributed uniformly throughout the development (Figure 21 F-J). In contrast with the abaxial layer of the outer integument, no enlarged cells with cell volume higher than 1500 μm^3 are observed at the distal half of the adaxial layer of the outer integument. Overall, the results confirm the differential growth of the abaxial and adaxial layer of the outer integument, as it was already mentioned in paragraph 3.1.4.

Within the abaxial inner integument, a progressive increase in the cell volume is observed in the distal half throughout development (Figure 21 K-O). In contrast with the abaxial layer of the outer integument, the extend of the cell enlargement localized at the distal pole do not reach the same extent.

Within the adaxial inner integument, a slight increase in the cell volume is observed progressively along the PD axis throughout development (Figure 21 P-T). Interestingly, a slow decrease in the cell volume is observed at stage 3-V at the distal side compared to stage 3-II and 3-IV, which is possibly due to the enlargement of the embryo sac that squeeze cells of the

integument to relocate in proximity of the micropyle (Figure 21 R-T). Overall, the results confirm a differential growth of the abaxial and adaxial layer of the inner integument, as it was already mentioned in paragraph 3.1.4.

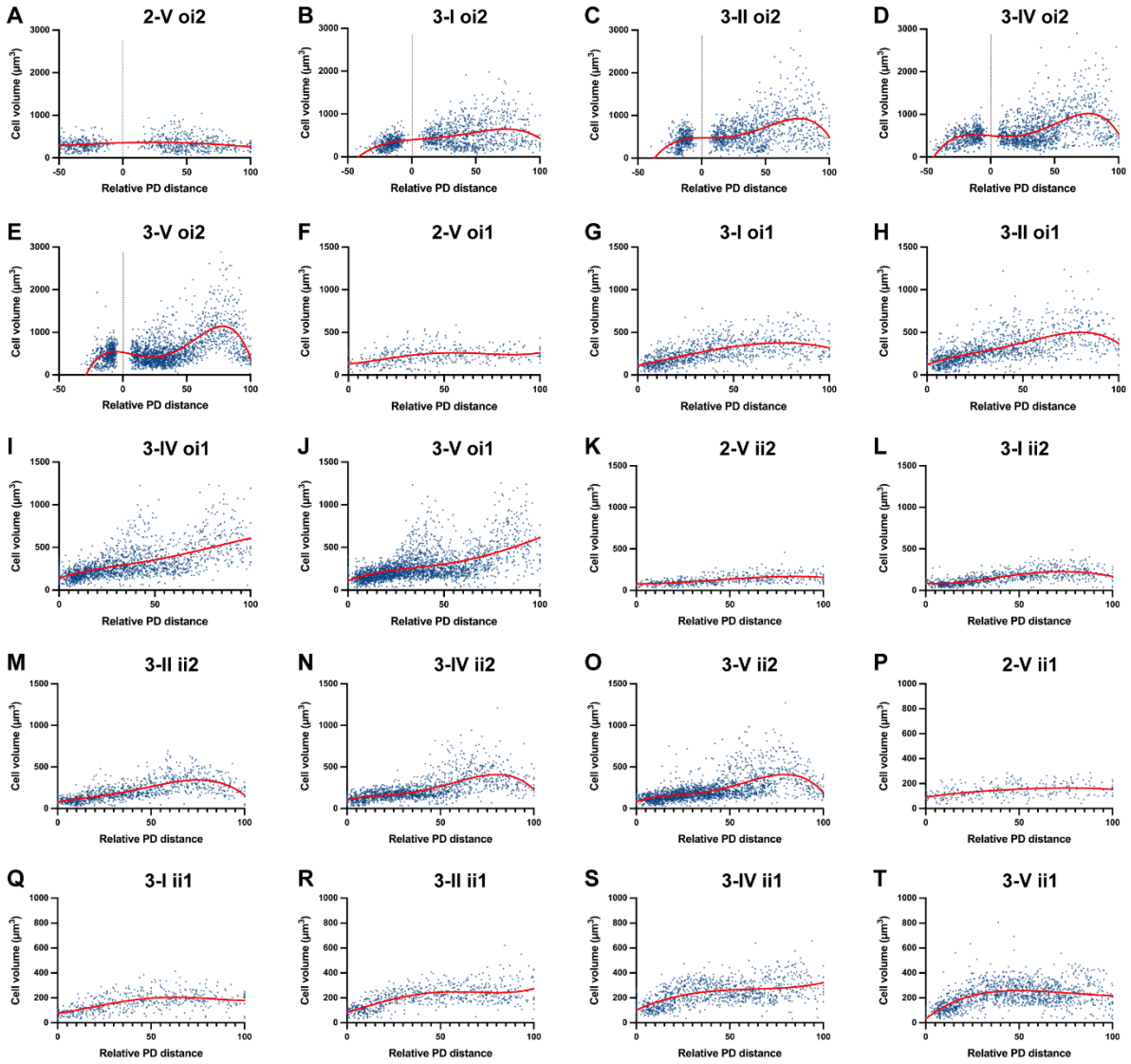

Figure 21 Spatial distribution of cell volumes in the integuments along the PD axis.

(A-T) Plots depicting the distribution of cell volumes along the PD axis in the different layers of the integument throughout the development. Each point represents a single cell. In red, fitting curve of fourth order polynomial. Cell volume is reported on the y-axis. Relative PD distance is reported in the x-axis. (A, B, C, D, E) Distribution of cell volumes along the PD axis of abaxial outer integument for stages 2-V, 3-I, 3-II, 3-IV and 3-V, respectively. (F, G, H, I, J) Distribution of cell volumes along the PD axis of adaxial outer integument for stages 2-V, 3-I, 3-II, 3-IV and 3-V, respectively. (K, L, M, N, O) Distribution of cell volumes along the PD axis of abaxial inner integument for stages 2-V, 3-I, 3-II, 3-IV and 3-V, respectively. (P, Q, R, S, T) Distribution of cell volumes along the PD axis of adaxial inner integument for stages 2-V, 3-I, 3-II, 3-IV and 3-V, respectively. Number of 3D digital ovules scored: 10 (stages 2-V, 3-I, 3-II,

3-IV), 11 (stage 3-V). Abbreviations: oi2, abaxial outer integument; oi1, adaxial outer integument; ii2, abaxial inner integument; ii1, adaxial inner integument.

To summarize, the outer integument showed a higher extent of cell volume increase at the distal half of the integuments compared to the inner integument at later stages of the development. Within the integuments, the abaxial layers showed an increase in cell volume of distally localized cells at later stage of development compared to the adaxial layers. Within these regions, growth most likely occur through increase in the cell volume. These results and the analysis of cell proliferation distribution, suggest the presence of regional growth patterns along the PD axis within the integuments.

3.3.2.3 Regional growth pattern within the abaxial layer of the outer integument

Genetic studies suggest that the outer integument has a central role in ovule morphogenesis. In *ino* mutant ovules are characterized by lack the characteristic curvature (Schneitz et al., 1997; Villanueva et al., 1999). Due to its central role in ovule morphogenesis, the regional growth pattern along the PD axis within the abaxial outer integument has been analyzed more in detail. From the previous analysis, three main regions have been highlighted: a most proximal part characterized by negative relative PD distance obtained through the application of coordinate tissue system and facing sub-epidermally the posterior chalaza, a mid-region of cells between relative PD distance values of 0 and 50 and a most distal region characterized by relative PD distance above 50 (Figure 22 A, D, G). Growth and proliferation have been analyzed for the three distinct regions of the abaxial outer integument across different developmental stages.
At stage 2-V, 46.4 ± 5.5 cells are found in most proximal part of the outer integument (Figure 22 B) (Table 12). In terms of tissue volume, the region is 1.37×10^4 μm^3 ± 0.17×10^4 μm^3 (Figure 22 C) (Table 12). At stage 3-V, 46.36 ± 4.84 cells are found in most proximal part of the outer integument (Figure 22 B) (Table 12). In terms of tissue volume, the region is 2.22×10^4 μm^3 ± 0.28×10^4 μm^3 (Figure 22 C) (Table 12). Within the most proximal part of the outer integument, the number of cells across ovule development remains constant and no significant difference has been reported across the stages (Figure 22 B) (Table 12). The volume of the region increases steadily across the stages (Figure 22 C) (Table 12). As previously reported in the analysis of the spatial localization of cell division in the integuments, this region is characterized by minimal growth in terms of cell proliferation and accompanied only by a slight increase in volume (Figure 22 B, C) (Table 12).

Within the proximal part of the outer integument, at stage 2-V, 22.5 ± 14.49 cells are found in this region of the outer integument (Figure 22 E) (Table 12). In terms of tissue volume, the region is 0.82 x 10^4 μm^3 ± 0.5 x 10^4 μm^3 (Figure 22 F) (Table 12). At stage 3-V, 111.9 ± 19.6 cells are found proximal part of the outer integument (Figure 22 E) (Table 12). In terms of tissue volume, the region is 5.38 x 10^4 μm^3 ± 0.6 x 10^4 μm^3 (Figure 22 F) (Table 12). During growth of this region, between stage 3-II to 3-IV no significant difference is calculated (Figure 22 E) (Table 12). The volume of the region followed similar increase as observed for the cell numbers (Figure 22 F) (Table 12). Overall, the proximal abaxial outer integument at stage 3-V the region is 5-fold time bigger in terms of cell number, while it is 6.7-fold bigger in terms of tissue volume (Table 12).

Within the distal part of the outer integument, at stage 2-V, 21.7 ± 5.92 cells are found in this region of the outer integument (Figure 22 H) (Table 12). In terms of tissue volume, the region is 0.69 x 10^4 μm^3 ± 0.19 x 10^4 μm^3 (Figure 22 I) (Table 12). At stage 3-V, 48.09 ± 8.13 cells are found proximal part of the outer integument (Figure 22 H) (Table 12). In terms of tissue volume, the region is 4.46 x 10^4 μm^3 ± 0.54 x 10^4 μm^3 (Figure 22 I) (Table 12). Within the distal part of the outer integument, the number of cell across ovule development increase significantly only between stage 2-V to 3-I and no significant difference is observed at later stages in term of cell increase (Figure 22 H) (Table 12). The volume of the region significantly increase between the stages, however no significant increase is reported between the stage 3-II to 3-IV (Figure 22 I) (Table 12). Overall, the distal abaxial outer integument at stage 3-V the region is 2.2-fold time bigger in terms of cell number, while it is 6.4-fold bigger in terms of tissue volume (Table 12).

As previously reported in the analysis of the spatial localization of cell division in the integuments, the proximal abaxial outer integument is characterized by growth mainly through the increase of cell number due to the preferential localization of cell division (Figure 22 F, E) (Table 12). The distal region of the abaxial outer integument is characterized by reduced cell proliferation and it is mainly interested by volume increase due to cell elongation (Figure 22 H, I) (Table 12).

To summarized, the abaxial layer of the outer integument is interested by complex spatial and temporal regulation of growth pattern. The most proximal region of the layer did no show growth throughout the development. The mid-region of the layer showed a preferential localization of cell proliferation, and it is characterized by reduced cell volume. The distal region of the layer showed the opposite composition compared to proximal region, showing no

increase in cell number through the different stages and being interested mostly by growth through cell enlargement.

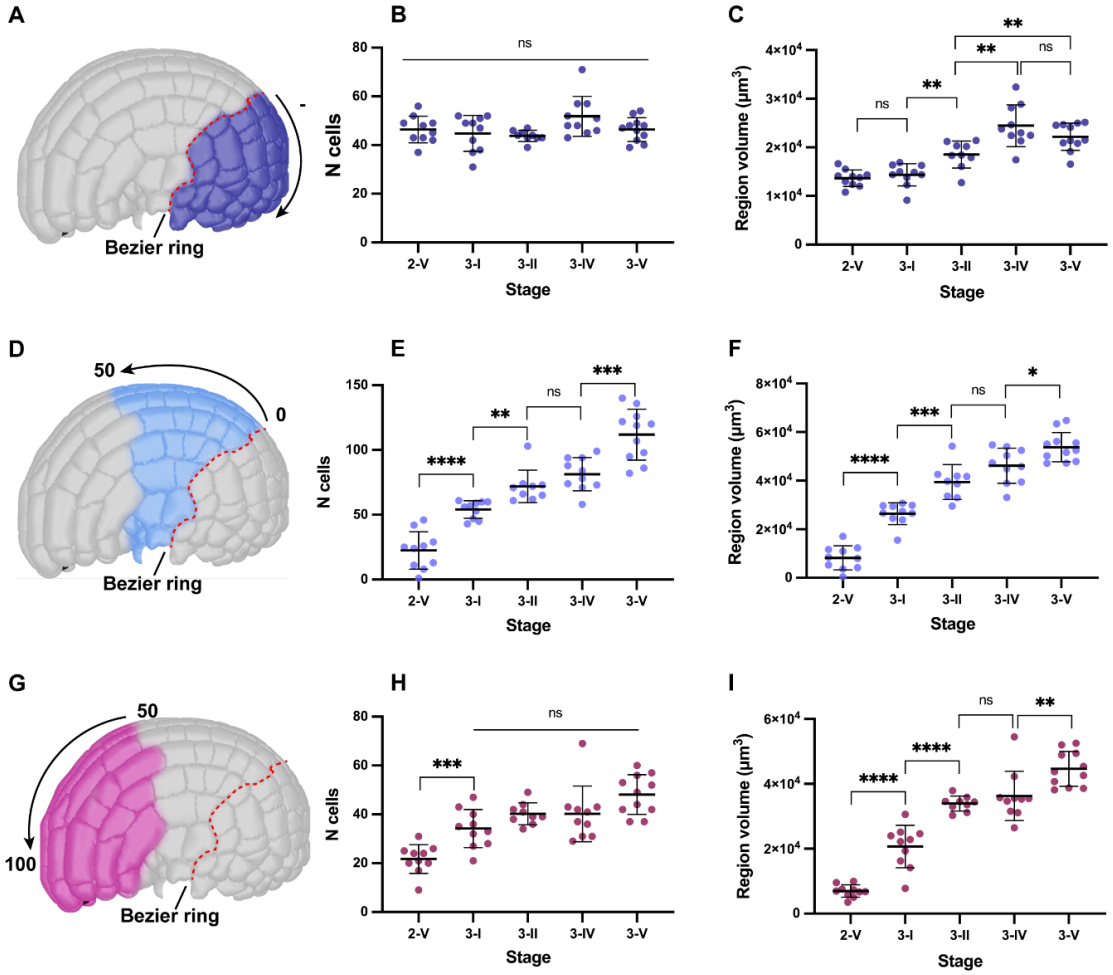

Figure 22 Growth pattern within the abaxial outer integument.

(A, D, G) 3D cell mesh of abaxial outer integument showing the region analyzed with different colors. Purple, light blue and pink indicate the most proximal (negative relative PD distance values), proximal (relative PD distance values between 0 and 50) and distal (relative PD distance values between 50 and 100) region, respectively. (B, E, H) Plot showing the number of cells within the different regions of the abaxial outer integument across development. (C, F, I) Plot showing the volume of different regions of the abaxial outer integument across development. (A, B, C) Growth pattern within the most proximal region of the abaxial outer integument during ovule development. (D, E, F) Growth pattern within the proximal region of the abaxial outer integument during ovule development. (G, H, I) Growth pattern within the distal region of the abaxial outer integument during ovule development. Data points indicate individual ovules. Asterisks represent statistical significance (ns, $p \geq 0.5$; *, $p < 0.05$; **, $p < 0.01$; ***, $p < 0.001$; ****, $p < 0.0001$; Student's t-test). Number of 3D digital ovules scored: 10 (stages 2-V, 3-I, 3-II, 3-IV), 11 (stage 3-V). Mean ± SD is shown.

Table 12 Cell numbers and total volume of the different integument layers.

	Abaxial outer integument region					
Stage[a]	**Most proximal**		**Proximal**		**Distal**	
	N cells	Volume (x 10^4 μm^3)	N cells	Volume (x 10^4 μm^3)	N cells	Volume (x 10^4 μm^3)
2-V	46,4 ± 5,502	1.37 ± 0.17	22,5 ± 14,49	0.82 ± 0.5	21,7 ± 5,926	0.69 ± 0.19
3-I	44,8 ± 7,361	1.43 ± 0.23	54,1 ± 6,757	2.64 ± 0.45	34,2 ± 7,815	2.07 ± 0.65
3-II	43,78 ± 2,28	1.85 ± 0.28	71,9 ± 12,61	3.95 ± 0.72	40,22 ± 4,46	3.39 ± 0.23
3-IV	51,8 ± 8,23	2.45 ± 0.43	81,3 ± 12,78	4.61 ± 0.72	40,2 ± 11,41	3.63 ± 0.76
3-V	46,36 ± 4,84	2.22 ± 0.28	111,9 ± 19,6	5.38 ± 0.6	48,09 ± 8,13	4.46 ± 0.54

[a]Number of 3D digital ovules scored: 10 (stages 2-V, 3-I, 3-II, 3-IV), 11 (stage 3-V). Values represent mean ± SD.

3.4 Establishment of stage-specific 3D digital atlas of mutant ovule

For a more complete understanding of ovule curvature formation in *Arabidopsis thaliana*, a 3D cellular level description and quantification of the whole organ has been obtained for ovule mutants that show defect in curvature formation. In *ino* mutant, ovules lacking the outer integument develops as orthotropous ovules as the inner integument is characterized by a straight growth (Schneitz et al., 1997; Villanueva et al., 1999). In *sup* mutant, ovules are characterized by polarity defects in the outer integument resulting in trumpet-shape ovules rather than hood-like structure (Balasubramanian & Schneitz, 2002; Gaiser et al., 1995; Sakai et al., 1995). A developmental series of 3D digital *ino* and *sup* mutant ovule at cellular resolution has been obtained.

3.4.1 Stage-specific 3D digital atlas of *ino* ovule

The following section will discuss some of the findings published in Vijayan & Tofanelli et al., 2021.

The ovule phenotype of *ino* mutants has been well characterized, however, a quantitative phenotypic analysis of *ino* ovules has not been performed (Figure 23 A). As proof-of-concept, *ino-5*, a putative null allele of *INO* in Col-0, has been generated by a CRISPR/Cas9-based approach. A dataset of 119 3D digital *ino-5* ovules covering stages 1-II to 3-VI ($3 \leq n \leq 20$ per stage) has been generated similarly to the WT dataset. Ovules lacking *INO* activity are difficult to stage during much of stage 2 and stage 3 as they lack many of the distinct criteria that define different stages of wild-type ovule development. To overcome this issue, *ino-5* ovules were staged by comparing the total number of cells and the total volume of *ino* mutant ovules to the corresponding stage-specific values of wild-type 3D digital ovules for which the outer integument had been removed in MGX (Table 13).

First, the total cell number per primordium and the total volume per primordium for *ino-5* ovules of stages 1-II to 2-II were analyzed. Any significant differences between *ino-5* and wild-type for the two parameters have been observed (Figure 23 B, C). These results are in line with *INO* expression which became first detectable only around stage 2-II/III (Figure 29) (Balasubramanian & Schneitz, 2000; Meister et al., 2002; Villanueva et al., 1999). Similarly, only minor differences were detected when examining the funiculus at later stages (Figure 23 G, H) (Table 14). In *ino-5* mutants the embryo sac development is severely affected and did not extend beyond the mono-nuclear embryo sac stage although up to four-nuclear embryo sacs could be detected as well (Figure 23 D). The nucellar development has been investigated. Wild-

type stage 3-I ovules featured 66.9 ± 13.4 cells per nucellus while *ino-5* carried 81.41 ± 9.6 cells per nucellus (Figure 23 E) (Table 14). The nucellar volume of *ino-5* (0.9×10^4 μm^3 ± 0.1×10^4 μm^3) was also increased relative to wild-type (0.7×10^4 μm^3 ± 0.1×10^4 μm^3) (Figure 23 F) (Table 14). The results indicate that *INO* affects ontogenesis of the embryo sac and of the outer integument but additionally of the nucellus. The failure in the formation of the embryo sac might influence the correct development of the nucellus, which results abnormal. However, nucellar cell number and volume are also higher than normal in stage 3-IV *ino-5* ovules that exhibit a four-nuclear embryo sac (Figure 23 I, J). Therefore, abnormalities in the nucellus might be controlled by other tissue, most likely by the outer integuments. The absence of the outer integument might cause a lack of signaling pathways and/or a mechanism involving mechanical stress, required for proper nucellus development.

The inner integument and central region of the *ino-5* mutant have been analyzed and compared to wild-type dataset more in detail later in this work in the contest of ovule curvature mechanisms formation.

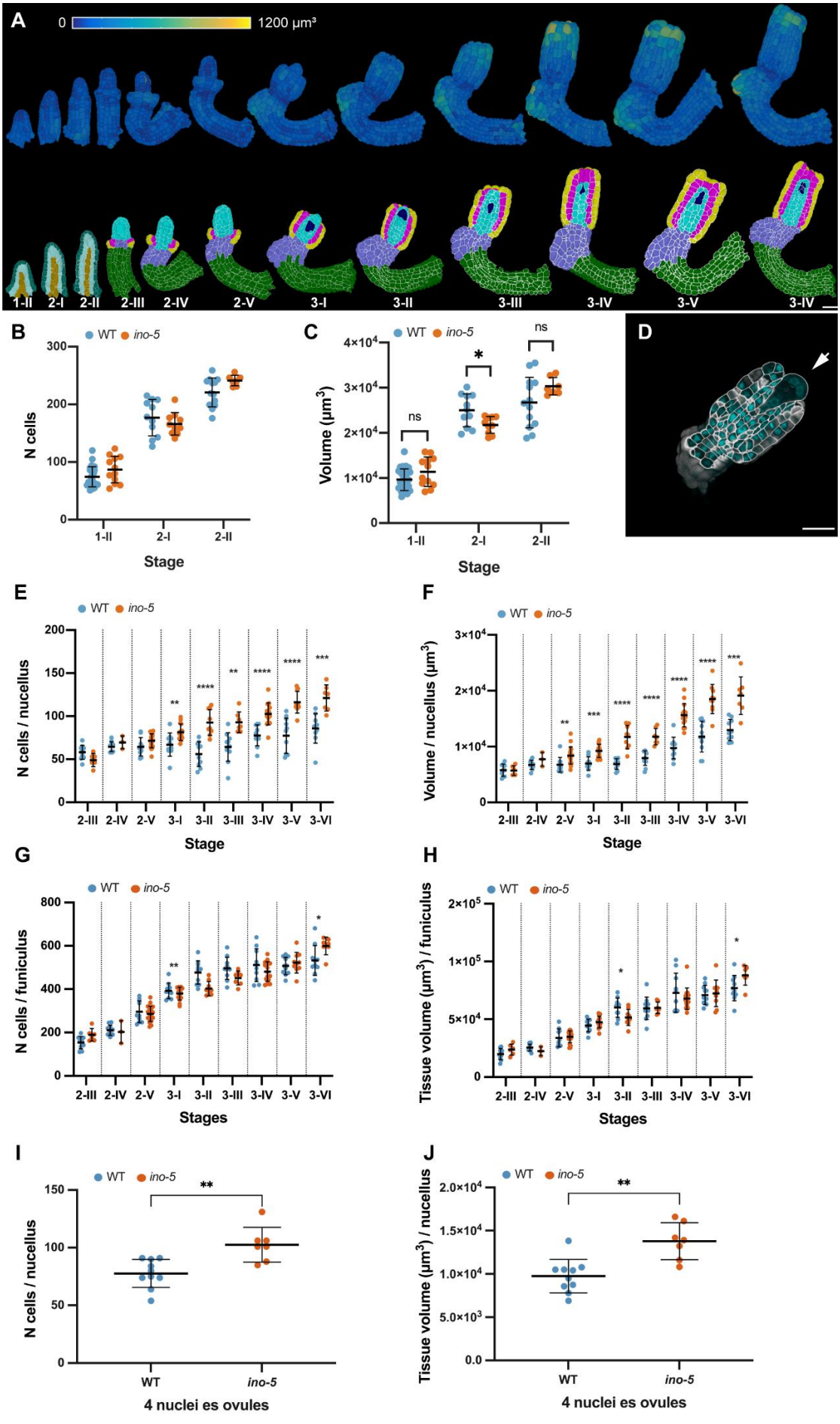
A
0
1200 µm³
1-II
2-I
2-II
2-III
2-IV
2-V
3-I
3-II
3-III
3-IV
3-V
3-IV
B
WT
ino-5
N cells
Stage
C
Volume (µm³)
ns
*
ns
D
E
N cells / nucellus
F
Volume / nucellus (µm³)
G
N cells / funiculus
Stages
H
Tissue volume (µm³) / funiculus
I
N cells / nucellus
4 nuclei es ovules
J
Tissue volume (µm³) / nucellus

Figure 23 Quantitative analysis of cellular patterns in *ino-5* ovule.

(A) On top, 3D cell mesh view of *ino-5* ovules at different stages displaying heat maps of cell volume ranging from 0 to 1200 µm^3. On bottom, mid-sagittal section of 3D cell mesh of *ino-5* ovules showing the cell type organization and cell type annotation. The color code is the same used for WT ovules. (B) Plot showing the total number of cells in wild-type and *ino-5* at early stages of ovule development. (C) Plot showing the total volume of wild-type and *ino-5* ovules at early stages of ovule development. (D) Section view of the cell boundary z-stack (white) overlaid with the z-stack of stained nuclei showing a four-nuclear embryo sac in an *ino-5* ovule. (E, F) Plots comparing total cell number and tissue volume of the nucellus between wild-type and *ino-5* at different stages. (G, H) Plots comparing total cell number and tissue volume of the funiculus between wild-type and *ino-5* at different stages. (I, J) Plots comparing total cells and tissue volume of nucellus of ovules with 4 nuclei embryo sac between wild-type and *ino-5* at different stages. Data points indicate individual ovules. Mean ± SD are represented as bars. Asterisks represent statistical significance (ns, p≥0.5; *, p<0.05; **, p<0.01, ***, p<0.001; ****, p<0.0001; Student's t-test). Number of 3D digital *ino-5* ovules scored: 3 (stage 2-IV), 6 (stage 2-III), 7 (stages 2-II, 3-III, 3-VI), 9 (stage 3-II), 10 (stages 2-I, 3-V), 12 (stage 1-II), 14 (stage 3-I), 15 (stage 3-IV), 20 (stage 2-V). Scale bars: 20 µm. Extended version of the image from Vijayan & Tofanelli et al., 2021.

Table 13 Cell numbers and total volumes of *ino-5* ovules staged according to the wild-type cohort with removed outer integument.

Stage[a,b]	**N Cells wild-type (-oi)**	**Volume (x 10^4 µm^3) wild-type (-oi)**	**N Cells *ino-5***	**Volume (x 10^4 µm^3) *ino-5***
1-II	74.0 ± 17.1	1.0 ± 0.2	87 ± 23.1	1.1 ± 0.3
2-I	176.9 ± 31.5	2.5 ± 0.4	166.2 ± 19.5	2.1 ± 0.1
2-II	220.6 ± 24.9	2.7 ± 0.6	241.1 ± 9.1	3.0 ± 0.2
2-III	270.3 ± 32.4	3.2 ± 0.6	305.5 ± 34.6	3.7 ± 0.3
2-IV	380.5 ± 26.5	4.5 ± 0.4	382.3 ± 45.7	4.1 ± 0.5
2-V	524.7 ± 66.3	6.2 ± 1.0	536.7 ± 60.8	6.4 ± 0.9
3-I	712.2 ± 61.2	9.2 ± 1.1	716.9 ± 58.8	9.4 ± 0.9
3-II	888.4 ± 52.9	13.8 ± 1.3	858.0 ± 28.7	12.7 ± 0.9
3-III	951.2 ± 90.1	14.9 ± 2.1	956.7 ± 28.9	15.5 ± 0.6
3-IV	1037 ± 103.7	18.1 ± 2.2	1102 ± 49.5	19.6 ± 2.1
3-V	1140 ± 96.8	20.8 ± 2.3	1241 ± 32.2	23.5 ± 17.7

3-VI	1345 ± 131.9	26.6 ± 3.7	1383 ± 61.1	25.7 ± 16.8

[a]Number of 3D digital ovules scored for WT dataset: 10 (stages 2-III, 2-IV, 2-V, 3-I, 3-II, 3-IV, 3-VI), 11 (stages 2-I, 3-III, 3-V), 13 (stage 2-II), 14 (stage 1-I), 28 (stage 1-II).
[b]Number of 3D digital ovules scored for *ino-5* dataset: 3 (stage 2-IV), 6 (stage 2-III), 7 (stages 2-II, 3-III, 3-VI), 9 (stage 3-II), 10 (stages 2-I, 3-V), 12 (stage 1-II), 14 (stages 3-I, 3-IV), 20 (stage 2-V). Values represent mean ± SD.
Data published in Vijayan & Tofanelli et al., 2021.

Table 14 Cell numbers and total volumes of different tissues in *ino-5*.

	Tissue							
Stage [a]	**Nucellus**		**Inner Integument**		**Funiculus**		**Central region**	
	N cells	Volume (x 10^4 μm^3)	N cells	Volume (x 10^4 μm^3)	N cells	Volume (x 10^4 μm^3)	N cells	Volume (x 10^4 μm^3)
2-III	49 ± 7.6	0.5 ± 0.08	31.3 ± 3.2	0.4 ± 0.03	189.0 ± 29	2.4 ± 0.4	35.8 ± 37.1	0.3 ± 0.3
2-IV	69.7 ± 7.5	0.7 ± 0.1	41.6 ± 8.3	0.5 ± 0.1	202.7 ± 25	2.2 ± 0.4	68.3 ± 6.6	0.6 ± 0.2
2-V	71.4 ± 8.1	0.8 ± 0.1	70.7 ± 17.7	0.9 ± 0.2	286.4 ± 35.2	3.4 ± 0.5	108.1 ± 19.3	1.2 ± 0.3
3-I	81.4 ± 9.5	0.9 ± 0.1	122.0 ± 27.3	1.8 ± 0.5	379.0 ± 29.7	4.7 ± 0.5	134.0 ± 23.1	1.8 ± 0.4
3-II	92.6 ± 15.0	1.1 ± 0.2	185.1 ± 21.9	3.9 ± 0.7	402.9 ± 32.6	5.1 ± 0.7	176.9 ± 24.6	2.6 ± 0.4
3-III	93.0 ± 12.0	1.1 ± 0.1	208.4 ± 14.6	4.8 ± 0.5	451.6 ± 32.7	5.9 ± 0.7	202.9 ± 24.1	3.2 ± 0.5
3-IV	102.7 ± 12.8	1.5 ± 0.2	296.9 ± 43.5	7.3 ± 1.3	481.3 ± 45.7	6.7 ± 0.5	215.4 ± 30.7	3.6 ± 0.7
3-V	116.3 ± 12.5	1.8 ± 0.2	360.8 ± 35.2	9.6 ± 1.0	522.6 ± 47.4	7.2 ± 1.1	239.6 ± 31.2	4.2 ± 0.7
3-VI	121.1 ± 15.2	1.9 ± 0.3	406.1 ± 61.3	10.0 ± 1.6	599.6 ± 40.6	8.8 ± 0.8	254.4 ± 48.5	4.5 ± 0.9

[a]Number of 3D digital ovules scored: 3 (stage 2-IV), 6 (stage 2-III), 7 (stages 3-III, 3-VI), 9 (stage 3-II), 10 (stage 3-V), 14 (stages 3-I, 3-IV), 20 (stage 2-V). Values represent mean ± SD.
Data published in Vijayan & Tofanelli et al., 2021.

3.4.2 Stage specific 3D digital atlas of *sup* ovule

Analogous to the *ino-5* analysis, a quantitative phenotypic analysis of *sup* ovules has been carried out (Figure 24 A).

A putative null allele of *SUP* in Col-0 called *sup-7*, has been generated by a CRISPR/Cas9-based approach. A dataset of 55 3D digital *sup-7* ovules covering stages 2-III to 3-VI ($2 \leq n \leq 15$ per stage) has been generated. Ovules lacking *SUP* activity are difficult to stage as the embryo sac development does not occur as in wild-type, resulting often in a block of the embryo sac at mono-nuclear stage. For this reason, the ovules included in the *sup* dataset have been selected by a normal development of the embryo sac, resulting in a reduced dataset in numbers compared to wild-type, particularly at late stages.

Ovules of *sup* mutant are characterized by polarity defects in the outer integument resulting in trumpet-shape ovules rather than hood-like structure (Balasubramanian & Schneitz, 2002; Gaiser et al., 1995; Sakai et al., 1995). Therefore, the quantitative analysis has been concentrated on ovule stages up to 2-III, corresponding to the initiation of the outer integument (Table 15). The nucellar development has been investigated. Wild-type stage 3-I ovules featured 66.9 ± 13.4 cells per nucellus while *sup-7* carried 57.5 ± 24.54 cells per nucellus (Figure 24 B) (Table 15). The nucellar volume of *sup-7* (0.88×10^4 $\mu m^3 \pm 0.31 \times 10^4$ μm^3) was similar relative to wild-type (0.7×10^4 $\mu m^3 \pm 0.1 \times 10^4$ μm^3) (Figure 24 C) (Table 15). The results indicate that *SUP* do not dramatically affects ontogenesis of the nucellus. However up to stage 3-II a slight increase in the nucellus volume is observed for *sup-7*, which is not accompanied by a significant increase in terms of number of cells. Up to 3-V no difference is observed between WT and *sup-7* in terms of nucellus volume.

Similarly, only minor differences were detected in the funiculus (Figure 24 D, E) (Table 15). However, not all the sample present the funiculus attached to the placenta due to the difficulties in the dissection of the ovule from the carpel structure, which also results affected.

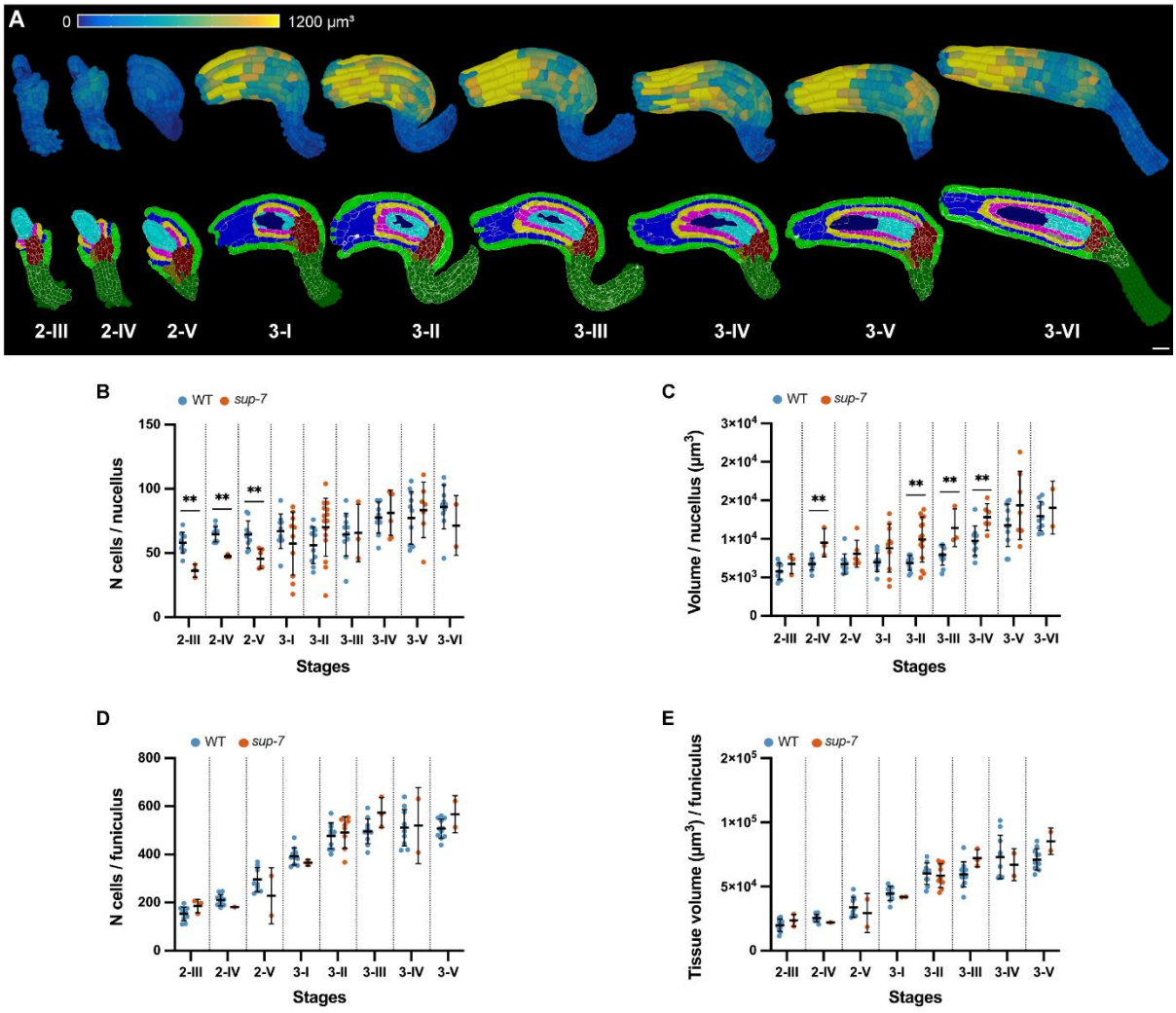

Figure 24 Quantitative analysis of cellular patterns in *sup-7* ovule.

(A) On top, 3D cell mesh view of *sup-7* ovules at different stages displaying heat maps of cell volume ranging from 0 to 1200 µm^3. On bottom, mid-sagittal section of 3D cell mesh of *sup-7* ovules showing the cell type organization and cell type annotation. The color code is the same used for WT ovules. (B, C) Plots comparing total cell number and tissue volume of the nucellus between wild-type and *sup-7* at different stages. (D, E) Plots comparing total cell number and tissue volume of the funiculus between wild-type and *sup-7* at different stages. Data points indicate individual ovules. Mean ± SD are represented as bars. Asterisks represent statistical significance (ns, $p \geq 0.5$; *, $p < 0.05$; **, $p < 0.01$, ***, $p < 0.001$; ****, $p < 0.0001$; Student's t-test). Number of 3D digital WT ovules: 10 (stages 2-III, 2-IV, 2-V, 3-I, 3-II, 3-IV, 3-VI), 11 (stages 3-III, 3-V). Number of 3D digital *sup-7* ovules scored: 2 (stage 3-VI), 3 (stages 2-III, 2-IV, 3-III), 6 (stages 2-V, 3-IV), 10 (stage 3-I), 15 (stage 3-II). Number of 3D digital *sup-7* ovules scored for the funiculus: 1 (stage 2-IV), 2 (stages 2-V, 3-IV, 3-V), 3 (stages 2-III, 3-III), 9 (stage 3-II). Scale bars: 20 µm.

Table 15 Cell numbers and total volumes of different tissues in *sup-7*.

	Tissue									
Stage [a,b]	**Nucellus**		**Inner Integument**		**Outer Integument**		**Funiculus**		**Central region**	
	N cells	Volume ($\times 10^4$ μm^3)	N cells	Volume ($\times 10^4$ μm^3)	N cells	Volume ($\times 10^4$ μm^3)	N cells	Volume ($\times 10^4$ μm^3)	N cells	Volume ($\times 10^4$ μm^3)
2-III	36.33 ± 5.03	0.67 ± 0.12	36 ± 10	0.52 ± 0.14	55.33 ± 13.6	1.08 ± 0.4	186 ± 28	2.36 ± 0.47	60 ± 23.64	0.79 ± 0.36
2-IV	47.66 ± 1.15	0.95 ± 0.18	63.66 ± 10.2	1.03 ± 0.18	116 ± 27.18	3.73 ± 1.4	182	2.19	89.33 ± 8.50	1.34 ± 0.36
2-V	45.5 ± 7.6	0.8 ± 0.17	83.83 ± 11.2	1.4 ± 0.15	186.5 ± 19.1	7.46 ± 0.9	228.5 ± 116	2.92 ± 1.52	91 ± 12.05	1.38 ± 0.18
3-I	57.5 ± 24.54	0.88 ± 0.31	125.7 ± 27.2	2.45 ± 0.64	263.6 ± 35.8	12.57 ± 2.77	365.5 ± 13.4	4.18 ± 0.02	129.5 ± 24.8	2.21 ± 0.49
3-II	70.13 ± 22.6	0.99 ± 0.29	213.06 ± 44	5.16 ± 1.11	359 ± 46.78	19.53 ± 3.04	491.5 ± 66	5.85 ± 0.9	161.06 ± 34.4	2.88 ± 0.67
3-III	65.66 ± 22.3	1.14 ± 0.24	253.33 ± 48.6	6.68 ± 1.85	389.66 ± 60.6	21.39 ± 1.6	573.66 ± 62.2	7.2 ± 0.68	170 ± 6.24	3.1 ± 0.09
3-IV	81.33 ± 17.5	1.28 ± 0.17	284.16 ± 51.9	7.41 ± 0.9	451.83 ± 50.2	23.78 ± 2.11	519.5 ± 157	6.7 ± 1.24	188.8 ± 47.3	3.03 ± 1.06
3-V	83.57 ± 21.5	1.43 ± 0.44	367.28 ± 106	9.9 ± 2.31	516.4 ± 105	25.99 ± 3.47	567.5 ± 77.0	8.52 ± 1.03	203.42 ± 47	3.59 ± 1.11
3-VI	71.5 ± 23.33	1.4 ± 0.34	408.5 ± 62.9	10.22 ± 3.46	540 ± 141.42	25.53 ± 2.47	-	-	209.5 ± 29	4.02 ± 1.04

[a]Number of 3D digital ovules scored: 2 (stage 3-VI), 3 (stages 2-III, 2-IV, 3-III), 6 (stages 2-V, 3-IV), 10 (stage 3-I), 15 (stage 3-II).

[b]Number of 3D digital ovules scored for the funiculus: 1 (stage 2-IV), 2 (stages 2-V, 3-IV, 3-V), 3 (stages 2-III, 3-III), 9 (stage 3-II). Values represent mean ± SD.

3.5 Ovule curvature is a multi-step process

The curvature of the *Arabidopsis* ovule is a unique morphogenetic process. During investigation of this work, the curvature process appeared to be subdivided into distinct, genetically controlled steps. During stages 2-III to 2-V of wild-type ovule development the central region of the ovule primordium forms a prominent kink resulting in the nucellus pointing toward the anterior side of the ovule (Figure 25 A). Following kink formation, integuments grow and result in the bending and curved shape of the ovule (Figure 7).

3.5.1 *INO* is required for correct kink formation

The following section will discuss some of the findings published in Vijayan & Tofanelli et al., 2021.

INO seems to be required for regular kink formation as this characteristic is not maintained in *ino-5* ovules (Figure 25 A). An aberrant growth of the anterior chalaza was found at later stage of *ino-5* development, resulting in the pointing of the nucellus toward the posterior side of the ovule (Figure 25 A). In addition to the absence of a regularly oriented kink, in *ino-5* ovules there is an evident effect on the bending of the ovule since the nucellus and inner integument develop into a straight structure. This observation suggests that *INO* is required for the correct growth of the of outer integument and it is required for the normal growth of the central region. The cellular architecture in the subepidermal central region of wild-type and *ino-5* has been investigated to understand the cellular basis of early kink formation. At stage 2-III, 6.7 ± 2.3 periclinal cell division planes in the subepidermal proximal chalaza were found (Figure 25 H, I). This number increased to 12.6 ± 3.3 by stage 2-IV. A small number of division planes oriented in a longitudinal-anticlinal fashion were observed (3.2. ± 2.2 at stage 2-III and 1.8. ± 2.1 at stage 2-IV) (Figure 25 H, J). These division planes were observed in the subepidermal region of the proximal chalaza. Interestingly, also a few oblique division planes were spotted (1.3 ± 1.5 at stage 2-III and 1.4 ± 0.9 at stage 2-IV) (Figure 25 H, K). These oriented cell divisions were preferentially found at the posterior chalaza underlying the initiating outer integument. Moreover, the progeny of the posterior oblique cell divisions showed asymmetric enlargement of the cells placed adjacent to the epidermal cells of the initiating outer integument (Figure 25 B, H). By stage 2-IV, a few oblique division planes were also observed at the anterior chalaza. In *ino-5* ovules, fewer periclinal division planes at stage 2-III/IV were found (Figure 25 H, I). Furthermore, no oblique division planes were observed (Figure 25 B, E). Interestingly, the number of longitudinal-anticlinal division planes was increased (Figure 25

H, J). Therefore, in the absence of *INO* function, fewer periclinal cell divisions are observed. Symmetric longitudinal-anticlinal cell divisions occur instead of the asymmetric oblique cell divisions in the subepidermal proximal chalaza, resulting in the absence of the enlarged cells which cause the bulging of the posterior epidermis and the failure of kink formation (Figure 25 B, C). These results indicate that differential cellular growth patterns in the chalaza contributes to kink formation. By stage 2-III oblique cell divisions, originate asymmetric cell enlargement, preferentially at the posterior chalaza, contributing to early kink formation. The periclinal and longitudinal anticlinal cell division observed might contribute to the widening of the chalaza. The control of these cellular patterns requires *INO* activity, since in *ino-5* these characteristic growth patterns within the central region are not preserved and results in the absence of nucellus reorientation, which is the visible effect of the kink.

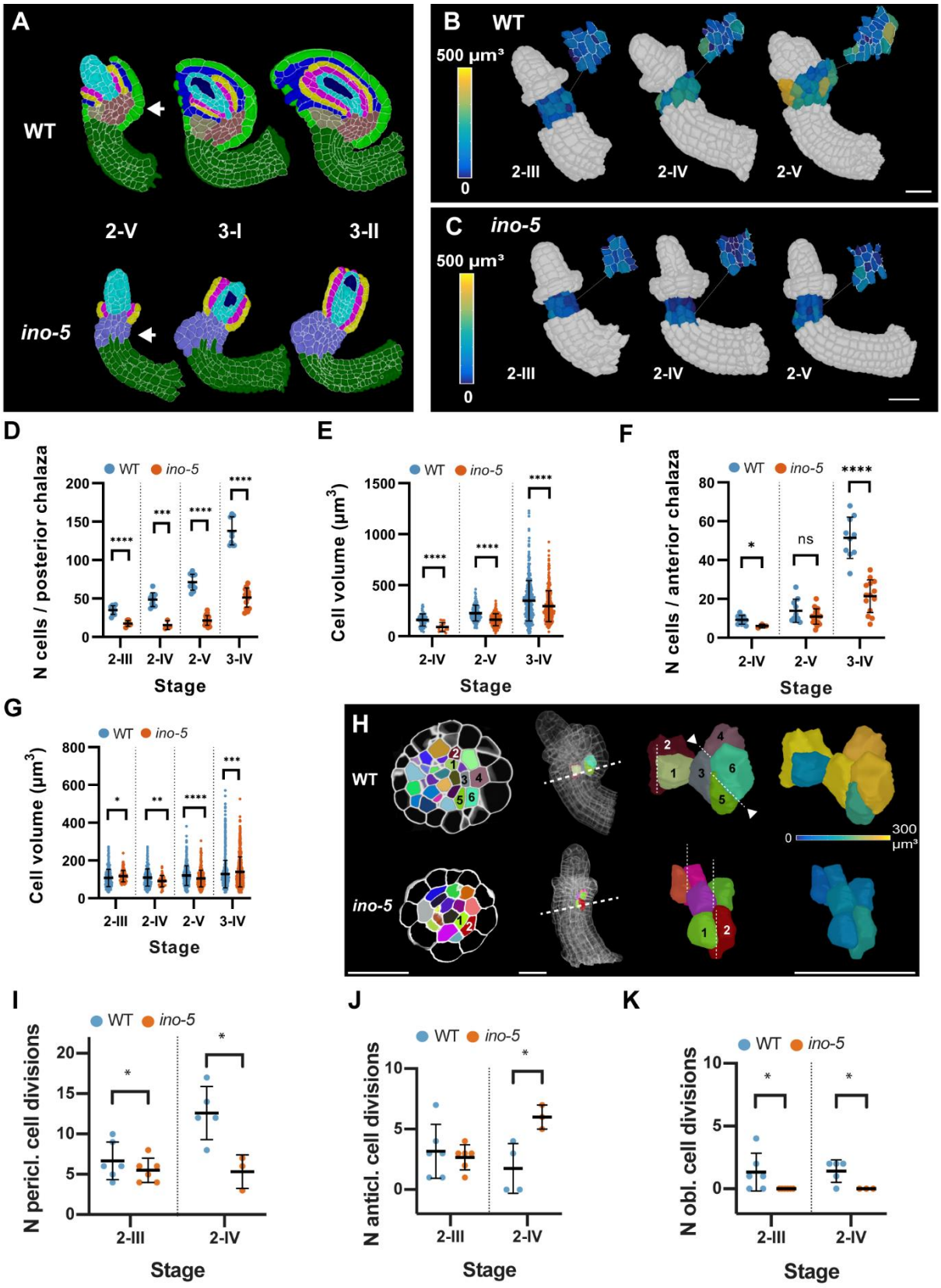
A
WT
2-V
3-I
3-II
ino-5
B WT
500 µm³
0
2-III
2-IV
2-V
C ino-5
500 µm³
0
2-III
2-IV
2-V
D
N cells / posterior chalaza
WT
ino-5
Stage
2-III
2-IV
2-V
3-IV
E
Cell volume (µm³)
WT
ino-5
Stage
2-IV
2-V
3-IV
F
N cells / anterior chalaza
WT
ino-5
ns
Stage
2-IV
2-V
3-IV
G
Cell volume (µm³)
WT
ino-5
Stage
2-III
2-IV
2-V
3-IV
H
WT
ino-5
0
300 µm³
I
N pericl. cell divisions
WT
ino-5
Stage
2-III
2-IV
J
N anticl. cell divisions
WT
ino-5
Stage
2-III
2-IV
K
N obl. cell divisions
WT
ino-5
Stage
2-III
2-IV

Figure 25 Growth patterns within the subepidermal central region in wild-type and *ino-5* ovules contributing to kink formation.

(A) Mid-sagittal section view of the cell-type labeled 3D cell meshes of wild-type and *ino-5* showing the differences in tissue organization across stages 2-V to 3-II. The arrow indicates the posterior kink in wild-type and its absence in *ino-5*. (B, C) 3D cell mesh showing the heat map of volume of the sub-epidermal central region in wild-type and *ino-5* after the removal of epidermal cells, at different stages. The sub-epidermal central region is also showed in the mid-sagittal section. The cell volume ranges from 0 to 500 μm^3. (D) Plot comparing the number of cells in the posterior chalaza in WT and *ino-5* ovules. (E) Plot comparing the number of cells in the posterior chalaza in WT and *ino-5* ovules. (F) Plot comparing the number of cells in the anterior chalaza in WT and *ino-5* ovules. Data points indicate individual ovules or individual cells in the cell volume distribution graph. (H) Plot comparing the number of cells in the posterior chalaza in WT and *ino-5* ovules. (H) Top row: transverse section view depicting the division patterns observed in the chalaza region in wild-type and *ino-5* ovules. The two arrows indicate enlarged epidermal cells participating in outer integument formation. The dashed line in the ovule indicates the section plane shown on the left. Bottom row: Oblique 3D view of the cells numbered in the transverse section view. Dashed lines indicate the cell division plane. Arrowheads highlight oblique periclinal cell division planes. The heat map indicates the cell volumes of the pair of posterior oblique dividing cells resulting in asymmetric enlargement in wild-type and symmetric longitudinal anticlinal dividing cells in *ino-5*. (I) Plot comparing the number of periclinal divisions in wild-type and *ino-5* ovules. (J) Plot comparing the number of longitudinal-anticlinal cell divisions in wild-type and *ino-5*. (K) Plot comparing the number of oblique divisions in wild-type and *ino-5*. Data points indicate individual cell division. Mean ± SD are represented as bars. Asterisks represent statistical significance (ns, $p \geq 0.5$; *, $p < 0.05$; **, $p < 0.01$; ***, $p < 0.001$; ****, $p < 0.0001$; Student's t-test). Number of 3D WT digital ovules scored: 6 (stage 2-III), 5 (stage 2-IV). Number of 3D *ino-5* digital ovules scored: 3 (stage 2-IV), 6 (stage 2-III). Scale bars: 20 μm. Extended version of the image from Vijayan & Tofanelli et al., 2021.

3.5.2 *SUP* controls chalaza polarity

To clarify the role of *SUP* in the kink formation, the composition of the central region in the mutant dataset was analyzed and compared to wild-type ovules. The results showed that, *SUP* is not required for kink formation as this feature is conserved in stage 2-V *sup-7* ovule (Figure 26 A, B). However, an aberrant growth within the chalaza is found (Figure 26 C-H).

From the analysis of the cellular growth pattern within the central region, the growth of the anterior chalaza resulted to be decreased in the *sup-7* mutant ovule (Figure 26 F, G). The number of cells and the volume of the anterior chalaza results reduced in *sup-7* ovules compared to wild-type up to stage 3-I. At stage 3-I, 60.73 ± 13.48 cells are found in wild-type anterior chalaza, while in *sup-7* 16 ± 9.4 cells are found (Figure 26 F) (Table 16 and Table 7). In terms of tissue volume, at stage 3-I the anterior chalaza in wild-type the volume is around 0.8×10^4 $\mu m^3 \pm 0.2 \times 10^4$ μm^3, while in *sup-7* the tissue volume is equal 0.4×10^4 $\mu m^3 \pm 0.12 \times 10^4$ μm^3 (Figure 26 G) (Table 16 and Table 7). The higher values of the anterior chalaza in

wild-type compared to *sup-7* remain constant throughout ovule development, suggesting a role of *SUP* as positive regulator of the anterior chalaza growth.

Additionally, to the role of *SUP* in the control of the anterior chalaza growth, findings suggest a role of *SUP* also in the regulation of the posterior chalaza. More in detail, when comparing the number of cells in the posterior chalaza slight differences are found between WT and *sup-7*, particularly at stage 2-III and 2-IV. Differences are also found at later stage with less significance, or no differences are observed up to stage 3-I. At stage 3-I, 86.40 ± 20.42 cells are found in wild-type posterior chalaza, while in *sup-7* 113.6 ± 26.88 cells are found (Figure 26 F) (Table 16 and Table 7). A difference of approximately 20 cells is observed between wild-type and *sup-7* ovule throughout the stages. In terms of tissue volume, the difference between wild-type and *sup-7* become more consistent. At stage 3-I the posterior chalaza in wild-type the volume is around 1×10^4 $\mu m^3 \pm 0.2 \times 10^4$ μm^3, while in *sup-7* the tissue volume is equal 1.7×10^4 $\mu m^3 \pm 0.5 \times 10^4$ μm^3 (Figure 26 G) (Table 16 and Table 7). When comparing the distribution of cells volume at different stages between wild-type and *sup-7*, it became evident the presence of cells of higher volume in *sup-7*, which accounts for the increase in volume of the tissue in mutant ovules (Figure 26 E) (Table 16 and Table 7).

Ovules of *sup* mutant are characterized by polarity defects in the outer integument resulting in trumpet-shape ovules rather than hood-like structure (Balasubramanian & Schneitz, 2002; Gaiser et al., 1995; Sakai et al., 1995). From the analysis performed on the central region composition between wild-type and *sup-7*, it appears the *SUP* is required to establish the correct polarity also in the central region, since in the mutant ovule the anterior chalaza resulted to be reduced and the posterior chalaza increased in terms of volumes. However, *SUP* is not strictly required for the kink formation, since mutant ovules present the correct reorientation of the nucellus towards the apex of the gynoecium around stage 2-IV, opposite to what previously reported in *ino* mutant. The abnormal shape observed in the *sup* mutant, might not be directly caused from the abnormalities observed in the central region, although they could be indirectly contributing to the defective establishment of the curvature in *sup*. The abnormal growth of the outer integument in *sup* seems to be the responsible factor for the abnormal shape observed in this mutant, corroborating the proposed model of a multi-step process for ovule curvature formation, in which integuments growth and bending lead the final steps in the curvature process.

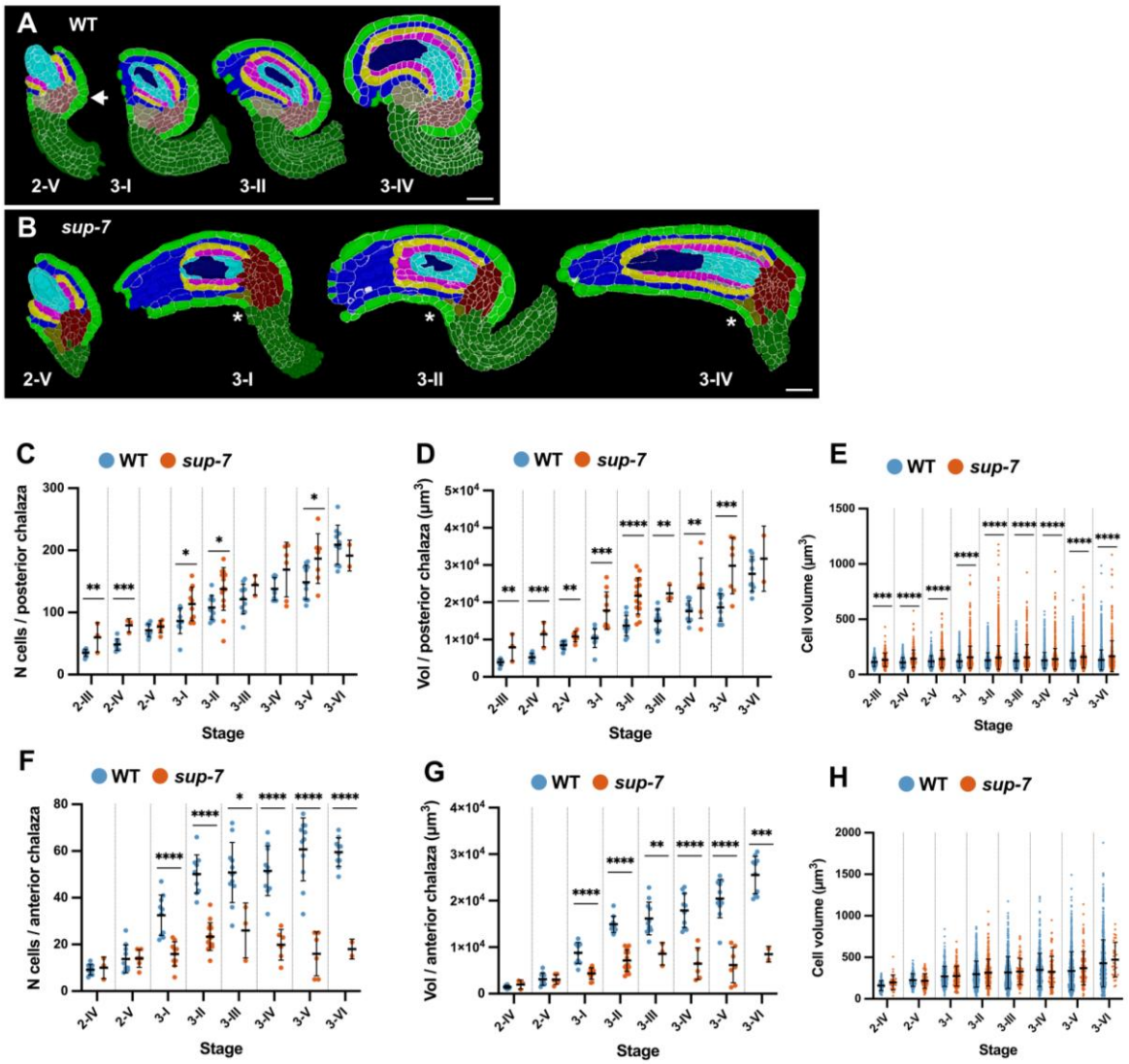

Figure 26 Growth patterns within the central region in wild-type and *sup-7* ovules.

(A) Mid-sagittal section view of the cell-type-labeled 3D cell meshes of wild-type showing tissue organization across stages 2-V to 3-II and 3-IV. The arrow indicates the posterior kink in wild-type. (A) Mid-sagittal section view of the cell-type-labeled 3D cell meshes of *sup-7* showing tissue organization across stages 2-V to 3-II and 3-IV. (C) Plot comparing the number of cells in the posterior chalaza in wild-type and *sup-7* ovules. (D) Plot comparing the number of cells in the posterior chalaza in wild-type and *sup-7* ovules. (E) Plot comparing the cell volume distribution in the posterior chalaza in WT and *sup-7* ovules. (F) Plot comparing the number of cells in the anterior chalaza in WT and *sup-7* ovules. (G) Plot comparing the number of cells in the anterior chalaza in WT and *sup-7* ovules. (H) Plot comparing the cell volume distribution in the anterior chalaza in WT and *sup-7* ovules. Data points indicate individual ovules or individual cells in the cell volume distribution graph. Mean ± SD are represented as bars. Asterisks represent statistical significance (ns, $p \geq 0.5$; *, $p < 0.05$; **, $p < 0.01$; ***, $p < 0.001$; ****, $p < 0.0001$; Student's t-test). Number of 3D digital ovules scored: 10 (stages 2-III, 2-IV, 2-V, 3-I, 3-II, 3-IV, 3-VI), 11 (stages 2-I, 3-III, 3-V). Number of 3D digital *sup-7* ovules scored: 2 (stage 3-VI), 3 (stages 2-III, 2-IV, 3-III), 6 (stages 2-V, 3-IV), 10 (stage 3-I), 15 (stage 3-II). Scale bars: 20 µm.

Table 16 Cell parameters of central region of *sup-7*.

	Tissue					
Stage[a]	**Anterior chalaza**			**Posterior chalaza**		
	N cells	Volume (x 10^4 μm^3)	Cell volume (μm^3)	N cells	Volume (x 10^4 μm^3)	Cell volume (μm^3)
2-III	-	-	-	60 ± 23.64	0.8 ± 0.37	132.6 ± 60.3
2-IV	10 ± 4.58	0.2 ± 0.1	198.1 ± 91.09	79.33 ± 10.79	1.15 ± 0.34	144.4 ± 79.5
2-V	14 ± 3.79	0.3 ± 0.1	216.5 ± 88.04	77 ± 9.818	1.08 ± 0.14	140.8 ± 80.1
3-I	15.9 ± 5.21	0.43 ± 0.12	273.4 ± 119.7	113.6 ± 26.88	1.78 ± 0.5	156.7 ± 99.4
3-II	23.3 ± 5.94	0.71 ± 0.23	316.9 ± 161.9	137.7 ± 34.37	2.18 ± 0.48	153 ± 106.7
3-III	26 ± 11.79	0.86 ± 0.24	330.3 ± 154.9	144 ± 16.09	2.24 ± 0.22	155.7 ± 115
3-IV	19.83 ± 6.5	0.65 ± 0.34	325.9 ± 184.6	169 ± 43.87	2.39 ± 0.81	141.2 ± 94.0
3-V	16 ± 9.42	0.62 ± 0.38	368.7 ± 200.8	186.7 ± 40.05	2.98 ± 0.75	159.8 ± 98.4
3-VI	18 ± 4.24	0.85 ± 0.17	471.1 ± 207.1	191.5 ± 24.75	3.17 ± 0.88	165.7 ± 140

[a]Number of 3D digital *sup-7* ovules scored: 2 (stage 3-VI), 3 (stages 2-III, 2-IV, 3-III), 6 (stages 2-V, 3-IV), 10 (stage 3-I), 15 (stage 3-II).

3.5.3 The outer integument controls the inner integument bending

The later step in the establishment of the curvature is represented by the final bending that result in the positioning of the micropyle close to the funiculus. This process is associated with the integuments growth (Figure 6). After the analysis of the cellular growth pattern within the integuments in wild-type, a comparison in respect to the mutant ovule was performed to investigate the role of the integuments in the curvature formation.

From the analysis of *ino-5* dataset, it appears evident that the inner integument in this mutant, grows straight. The growth patterns within the inner integument have been compared between wild-type and *ino-5*, to identify the factors that lead to the straight growth of the inner integument.

Firstly, the cell number, tissue volume and cellular volume for the different layers of the inner integument of wild-type and *ino-5* were compared (Figure 27 A-I). For the different layers, the three parameters did not deviate noticeably between wild-type and *ino-5* except for stages 3-IV and 3-V where a small but perceivable increase in tissue volume and cell volume was observed (Figure 27 B, C, E, F, H, I) (Table 17and Table 12). However, this increase appeared to be transient as both parameters were normal in *ino-5* ovules of stage 3-VI. These findings indicate that *INO* does not exert a major influence on the monitored cellular characteristics of the inner integument.

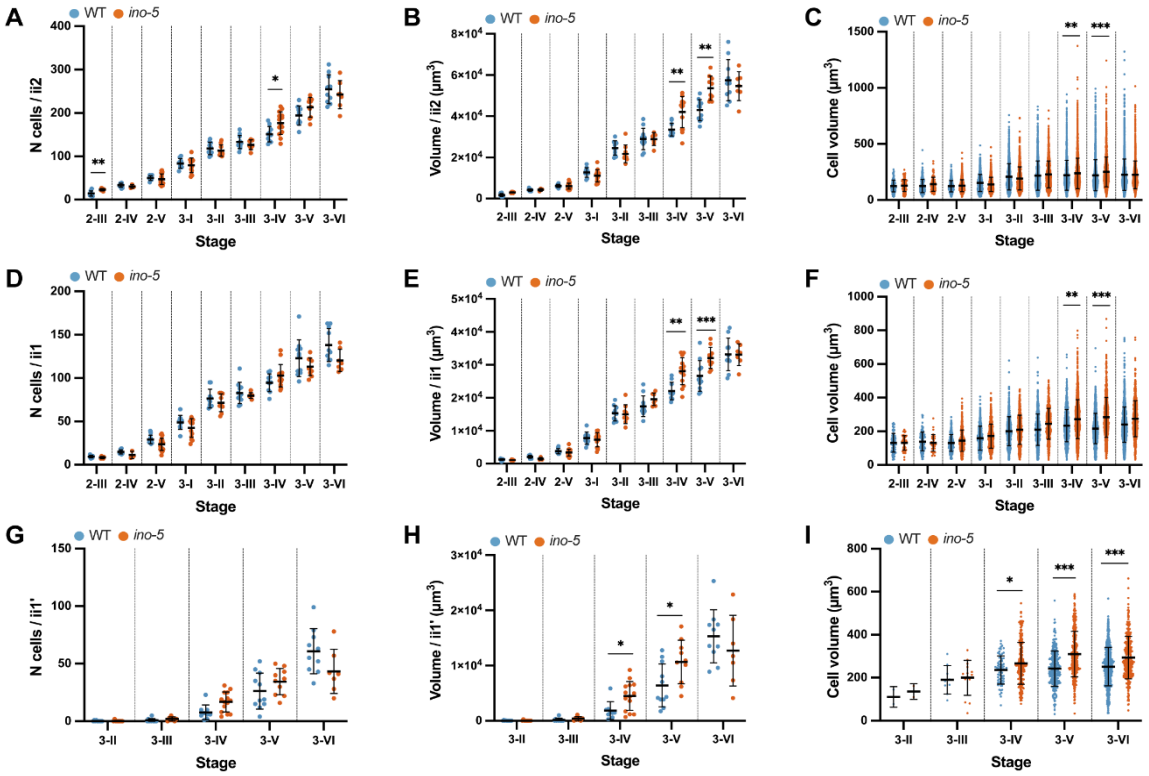

Figure 27 Comparison of cellular patterns in the inner integument between WT and *ino-5*.

(A, B, C) Plot showing the comparison of total number of cells, total volume and cell volume between the abaxial inner integument of wild-type and *ino-5* during ovule development, respectively. (D, E, F) Plot showing the comparison of total number of cells, total volume, and cell volume between the adaxial inner integument of wild-type and *ino-5* during ovule development, respectively. (G, H, I) Plot showing the comparison of total number of cells, total volume, and cell volume between the parenchymatic inner integument of wild-type and *ino-5* during ovule development, respectively. Data points indicate individual ovules or individual cells in the cell volume distribution graph. Mean ± SD are represented as bars. Asterisks represent statistical significance (ns, $p \geq 0.5$; *, $p < 0.05$; **, $p < 0.01$, ***, $p < 0.001$; ****, $p < 0.0001$; Student's t-test). Number of 3D digital WT ovules scored: 10 (stages 2-III, 2-IV, 2-V, 3-I, 3-II, 3-IV, 3-VI), 11 (stages 2-I, 3-III, 3-V). Number of 3D digital *ino-5* ovules scored: 3 (stage 2-IV), 6 (stage 2-III), 7 (stages 3-III, 3-VI), 9 (stage 3-II), 10 (stage 3-V), 14 (stage 3-I), 15 (stage 3-IV), 20 (stage 2-V).

Table 17 Cell number and tissue volume of *ino-5* inner integument.

	Tissue					
Stage[a]	**Abaxial inner integument**		**Adaxial inner integument**		**Parenchymatic inner integument**	
	N cells	Volume (x 10^4 μm^3)	N cells	Volume (x 10^4 μm^3)	N cells	Volume (x 10^4 μm^3)
2-III	23 ± 2.68	0.29 ± 0.03	8.33 ± 1.21	0.11 ± 0.01	-	-
2-IV	30.33 ± 4.16	0.42 ± 0.06	11.33 ± 4.16	0.15 ± 0.04	-	-
2-V	47.25 ± 12.2	0.6 ± 0.14	23.55 ± 7.02	0.34 ± 0.1	-	-
3-I	79.5 ± 16.98	1.1 ± 0.29	42.5 ± 10.76	0.73 ± 0.21	-	-
3-II	113.3 ± 13.2	2.17 ± 0.43	71.7 ± 10.18	1.5 ± 0.28	0.22 ± 0.66	0.01 ± 0.01
3-III	126.5 ± 11.2	2.88 ± 0.3	81.85 ± 4.41	1.99 ± 0.21	2 ± 1.82	0.04 ± 0.04
3-IV	176.7 ± 26.1	4.19 ± 0.75	119.7 ± 18.3	3.25 ± 0.62	16.86 ± 8.62	0.44 ± 0.26
3-V	213.3 ± 22.6	5.36 ± 0.58	147.5 ± 14.1	4.27 ± 0.54	34.4 ± 11.46	1.06 ± 0.39
3-VI	242.4 ± 32.5	5.46 ± 0.69	163.7 ± 29.5	4.58 ± 0.94	43.3 ± 19.22	1.27 ± 0.64

[a]Number of 3D digital ovules scored for *ino-5* dataset: 3 (stage 2-IV), 6 (stage 2-III), 7 (stage 3-III, 3-VI), 9 (stage 3-II), 10 (stage 3-V), 14 (stages 3-I, 3-IV), 20 (stage 2-V). Values represent mean ± SD.

To gain more insight into the regional growth pattern of the inner integument in *ino-5* mutant, the coordinate system has been applied on *ino-5* mutant ovule to stage 2-V, 3-I and 3-IV (Figure 28 A). The results have been compared to wild-type dataset for the same stages.

Firstly, the spatial distribution of cell proliferation has been analyzed (Table 18). Within the abaxial inner integument, at stage 2-V and 3-I dividing cells are broadly distributed throughout the whole integument length in both wild-type and *ino-5* dataset (Figure 28 B, C). At later

stage, the mitotic cells resulted to be distributed mostly proximally compared to earlier stages in both wild-type and *ino-5* (Figure 28 B, C). Overall, within the abaxial inner integument in both wild-type and *ino-5* throughout development the cell divisions appear to be more proximal distribute only at later stages of the development.

Within the adaxial inner integument, form stage 2-V to 3-I, only few cell divisions are observed in wild-type and *ino-5* and these dividing cells are broadly distributed throughout the whole integument length (Figure 28 D, E). Starting from stage 3-IV, the mitotic cells are distributed more proximally compared to earlier stages in both wild-type and *ino-5* (Figure 28 D, E). Overall, within the adaxial inner integument in both wild-type and *ino-5* throughout development the cell divisions appear to be more proximally distributed only at later stages.

To summarize, within the inner integuments the comparison between wild-type and *ino-5* didn't show any evident difference in the spatial distribution of cell proliferation These results corroborate the hypothesis that *INO* does not exert a major influence on the growth characteristics of the inner integument.

Secondly, the spatial distribution of cell volumes has been analyzed. Within the abaxial inner integument, a comparable progressive increase in the cell volume is observed in the distal half throughout development in both wild-type and *ino-5* (Figure 21 K, L, N and Figure 28 F-H).

Within the adaxial inner integument, a slight comparable increase in the cell volume is observed progressively along the PD axis throughout development in both wild-type and *ino-5* (Figure 21 P, Q, S and Figure 28 I-K). Overall, the results confirm a differential growth of the abaxial and adaxial layer of the inner integument in both wild-type and *ino-5*.

These findings indicate that *INO* does not exert a major influence on the monitored cellular characteristics of the inner integument. However, there is an obvious effect on the curvature of the ovule since the nucellus and inner integument develop into straight rather than curved structures. As the cellular characteristics and growth pattern of the inner integument appear largely unaffected in *ino-5*, suggesting that the developing outer integument imposes the curvature onto the interior tissues.

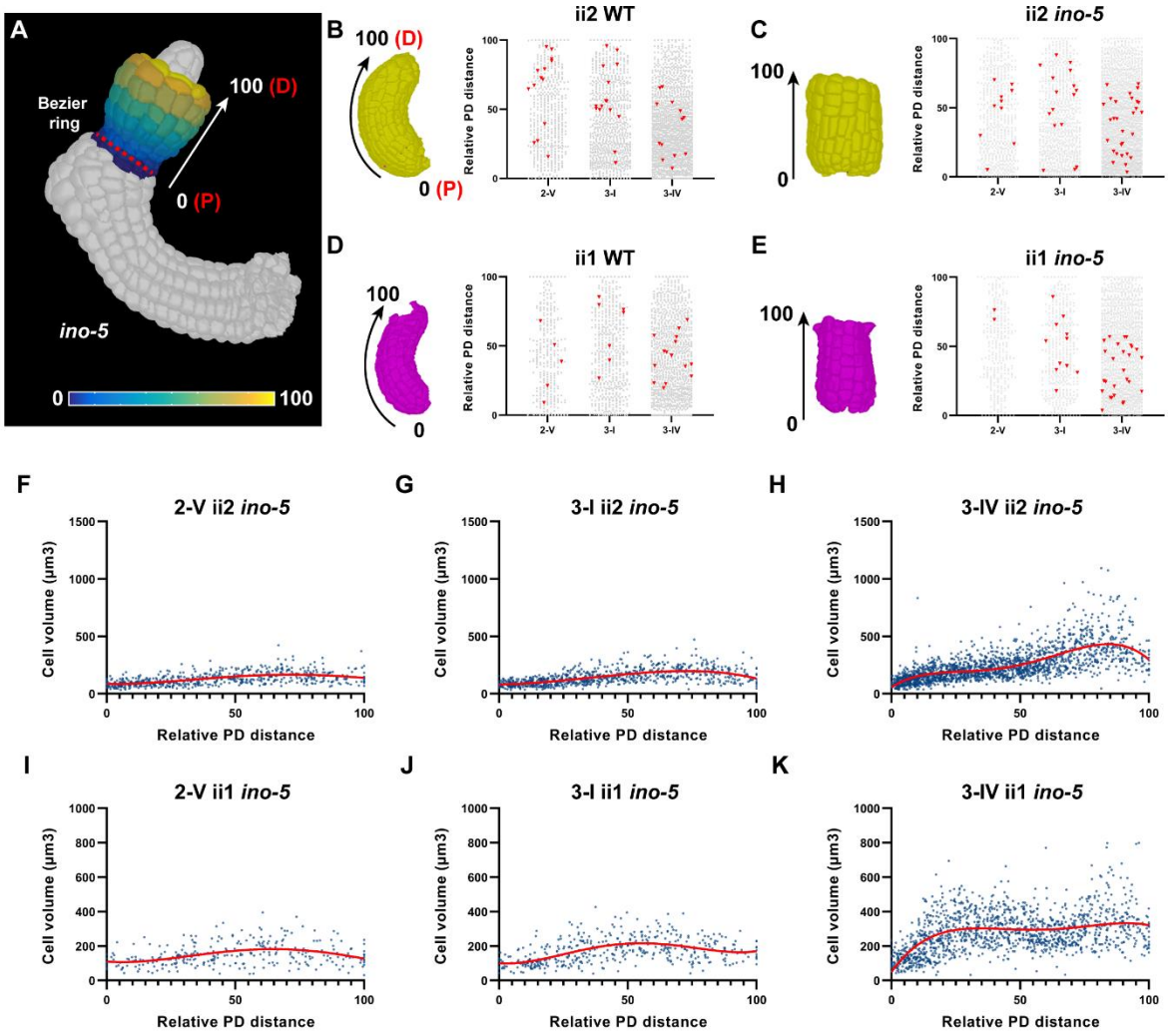

Figure 28 Spatial distribution of cell proliferation and volumes in the integuments along the PD axis in wild-type and *ino-5*.

(A) 3D cell mesh of *ino-5* ovule at stage 3-I showing heap map of relative PD distance and schematic view of the coordinate system applied to the inner integument of *ino-5* mutant ovule. The dotted red line highlights the position of the Bezier ring applied for cell distance measurements. The relative proximal-distal axis values are reported. (B, C, D, E) Column graph showing the distribution of dividing cells in different integuments layers along the PD axis, across different stage of development in wild-type and *ino-5* ovules. The stages are reported on the x-axis. The relative PD distance is reported on the y-axis and ranges between 0 and 100. Each gray point is a cell in interphase. Each red triangle is a dividing cell. On the left part, the 3D cell mesh of the specific layer is reported. The arrows show the relative PD distance and the delimiting values. (F-K) Plots depicting the distribution of cell volumes along the PD axis in the different layers of the inner integument of *ino-5* throughout the development. Each point represents a single cell. In red, fitting curve of fourth order polynomial. Cell volume is reported on the y-axis. Relative PD distance is reported in the x-axis. (F, G, H) Distribution of cell volumes along the PD axis of *ino-5* abaxial inner integument for stages 2-V, 3-I and 3-IV, respectively. (I, J, K) Distribution of cell volumes along the PD axis of *ino-5* adaxial inner integument for stages 2-V, 3-I, and 3-IV, respectively. Number of 3D digital ovules scored for wild-type: 10 (stages 2-V, 3-I, 3-IV). Number of 3D digital ovules scored for *ino-5* dataset: 10 (stages 2-V, 3-I), 11

(stage 3-IV). Abbreviations: ii2, abaxial inner integument; ii1, adaxial inner integument, P; proximal, D; distal.

Table 18 Cell division analysis in the inner integument of *ino-5*.

Sample[a]	Tissue	N mitotic cells	% of mitotic cells	N cells scored
2-V	ii2	1.09 ± 0.83	2.25 ± 1.98	595
	ii1	0.18 ± 0.40	0.82 ± 1.83	293
3-I	ii2	1.6 ± 1.43	1.83 ± 1.52	800
	ii1	1 ± 0.82	2.67 ± 2.56	424
3-IV	ii2	2.45 ± 1.86	1.32 ± 0.94	1943
	ii1	2.27 ± 1.68	1.94 ± 1.59	1340

[a]Number of 3D digital *ino-5* ovules scored: 10 (stages 2-V, 3-I), 11 (stage 3-IV). Values represent mean ± SD

3.5.4 Analysis of *INO* expression pattern reveals the presence of a frontal region of the abaxial outer integument characterized by absent growth

From the analysis of the cellular characteristics and growth pattern of *ino* mutant ovules, it appeared evident that the outer integument has a central role for the formation of the final bending and correct establishment of ovule curvature. Therefore, the gene expression pattern of *INO* has been analysed in the ovule. As previously mentioned, *INO* encodes a YABBY putative TF and it is the only YABBY gene expressed in the ovule (Meister et al., 2002; Villanueva et al., 1999). Expression pattern analysis was already performed through *in situ* hybridization, showing *INO* to be expressed on the abaxial outer integument. However, *in situ* analysis do not provide 3D information on the expression patterns. Therefore, the reported line pINO::NLS-GFP in Col-0 background has been employed to perform the analysis.

The expression of *INO* is firstly detected in a group of epidermal cells on the posterior half of ovule primordium, before the emergence of the integuments (Villanueva et al., 1999) (Figure 29 A). Those cells expressing *INO* correspond to the site of outer integument initiation. Later, *INO* is expressed on the abaxial outer integument. However, 3D analysis of expression pattern highlighted the presence of a frontal part characterized by the absence of INO signal (Figure 5 E and Figure 29 B, C). Therefore, *INO* expression results to be confined to the medio-lateral region of abaxial outer integument, which forms the hood-like structure enveloping the inner structures (Figure 5 E and Figure 29 B, C).

A differential cell labeling has been performed on the dataset of pINO::NLS-GFP reported line, in order to determine during development the growth, in terms of cell proliferation, of the two regions (Figure 29 D, E). The hood-like structure characterized by *INO* expression showed a similar growth in terms of cell number as observed in the wild-type dataset (Figure 29 D and Figure 12 E). Therefore, this region of the abaxial outer integument is mainly contributing to overall growth of the layer. On the other hand, the frontal region characterized by absence of *INO* expression, showed a constant number of cells throughout development (Figure 29 E). Therefore, the frontal region is characterized by absent growth.

The results confirm that *INO* is a promoting growth factor within the outer integument and positively regulate the growth of the outer integument. Additionally, it appears evident that the abaxial outer integument is a complex structure characterized by regions with different gene expression and growth patterns. The frontal region, characterized by absence of *INO* expression and absence of growth, remaining constant in terms of number of cells throughout development.

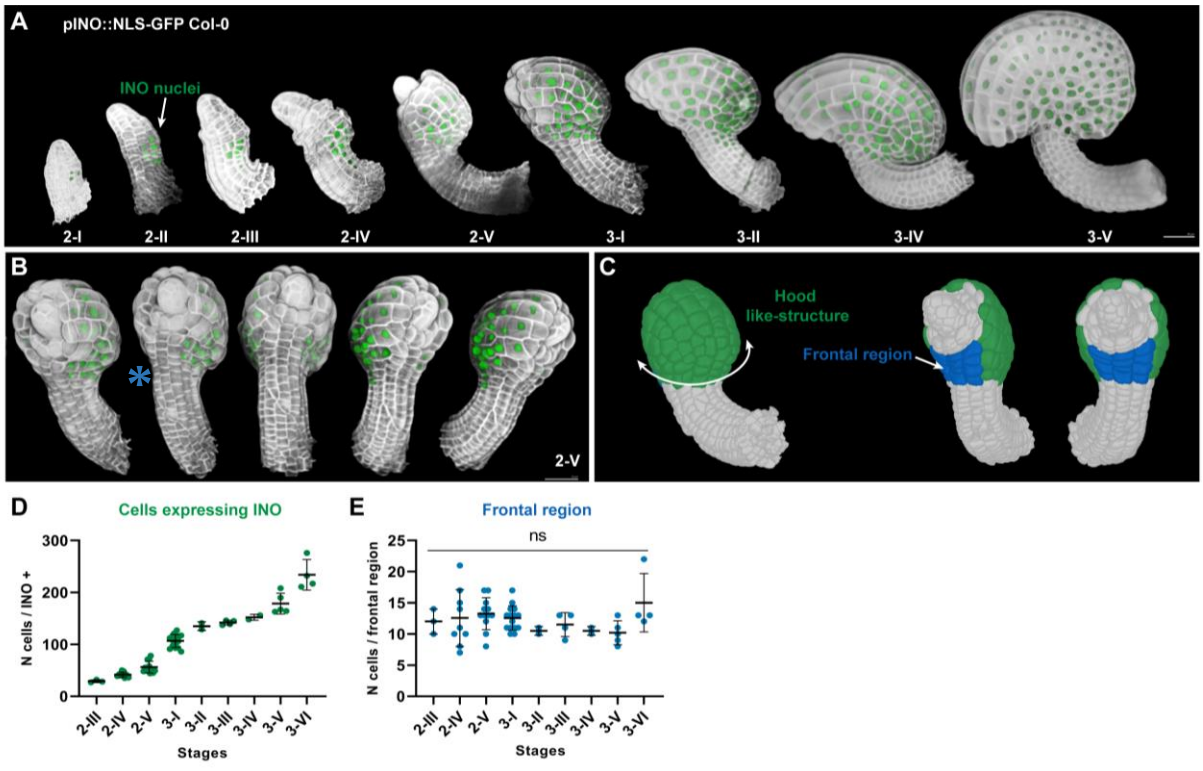

Figure 29 Expression pattern of *INO* during ovule development.

(A) 3D rendering of confocal z-stacks of SR2200-stained cell walls of ovule showing *INO* expressing nuclei in green during the development, from stage 2-I to maturity. Reporter line pINO::NLS-GFP in Col-0 background. (B) 3D rendering of confocal z-stacks of SR2200-stained cell walls and *INO* expressing nuclei in green of one ovule

at stage 2-V from different angle, showing the frontal region without *INO* labeled nuclei highlighted with one blue asterisk. (C) 3D cell mesh of ovule at stage 2-V, with cells of the abaxial outer integument differentially labeled. The green cells correspond to those expressing *INO* and in blue those that do not show *INO* expression. (D) Plot depicting the number of cells of the abaxial outer integument expressing *INO* during ovule development. (E) Plot depicting the number of cells of the abaxial outer integument that do not express *INO* during ovule development. Each point represents a single ovule. Mean ± SD are represented as bars. Student's t-test; ns, $p \geq 0.5$. Number of 3D digital ovules scored for pINO::NLS-GFP dataset: 2 (stages 3-II, 3-IV), 3 (stage 2-III), 4 (stages 3-III, 3-IV), 5 (stage 3-V), 9 (stage 2-IV), 12 (stage 2-V), 15 (stage 3-I). Scale bars: 20 μm.

3.5.5 The abaxial outer integument shows asymmetric growth

The analysis of pINO::NLS-GFP expression pattern highlighted the presence of a frontal region within the ovule characterized by the absence of pINO signal and absence of growth (Figure 29 B, C). Moreover, the analysis showed that the growth is confined to the hood-like structure of the outer integument characterize by a medio-lateral extension.

To characterize the regional growth pattern within the abaxial outer integument, along with PD coordinate system, differential cell annotation for the medio-lateral and frontal region are added to include further spatial components to the organ coordinate. Three labels, including medio, lateral and frontal annotations are added to the dataset previously analyzed with the PD coordinate system (Figure 30 A and Figure 5 E).

The analysis of mitosis distribution along the PD and medio-lateral axes showed the presence of a gradient of distribution of mitosis along the medio-later axis (Figure 30 B). The analysis confirmed the presence of a frontal region without growth (Figure 30 B) (Table 19 and Table 20). The analysis of cell number, tissue volume and cell volume of the frontal region throughout different stages confirmed the absence of growth within this region as could be visualized in the 3D cell mesh of ovule at different stages (Figure 30 C-F) (Table 19).

The analysis showed most of the mitosis distributed in the medial region of the abaxial outer integument (Figure 30 B) (Table 20). The region showed constant growth with a stop in growth between stage 3-II and 3-IV (Figure 30 G, H) (Table 19). The lateral region showed a reduced number of dividing cells compare to the medial region (Figure 30 B). The region showed an increased growth between stage 3-I and 3-IV (Figure 30 J, K). As previously mentioned, most of the mitosis occured in the proximal half of the abaxial integument.

To summarize, the analysis showed the presence differential growth within the regions of the abaxial outer integument. With the addition of spatial information along the medio-lateral axis to the PD axis, the region of higher proliferation has been restricted to the proximal and medial region of the abaxial outer integument during development. The analysis confirmed the

presence of a frontal region characterized by absent growth. Taken together these results, suggest that the abaxial outer integument is characterized by asymmetric growth.

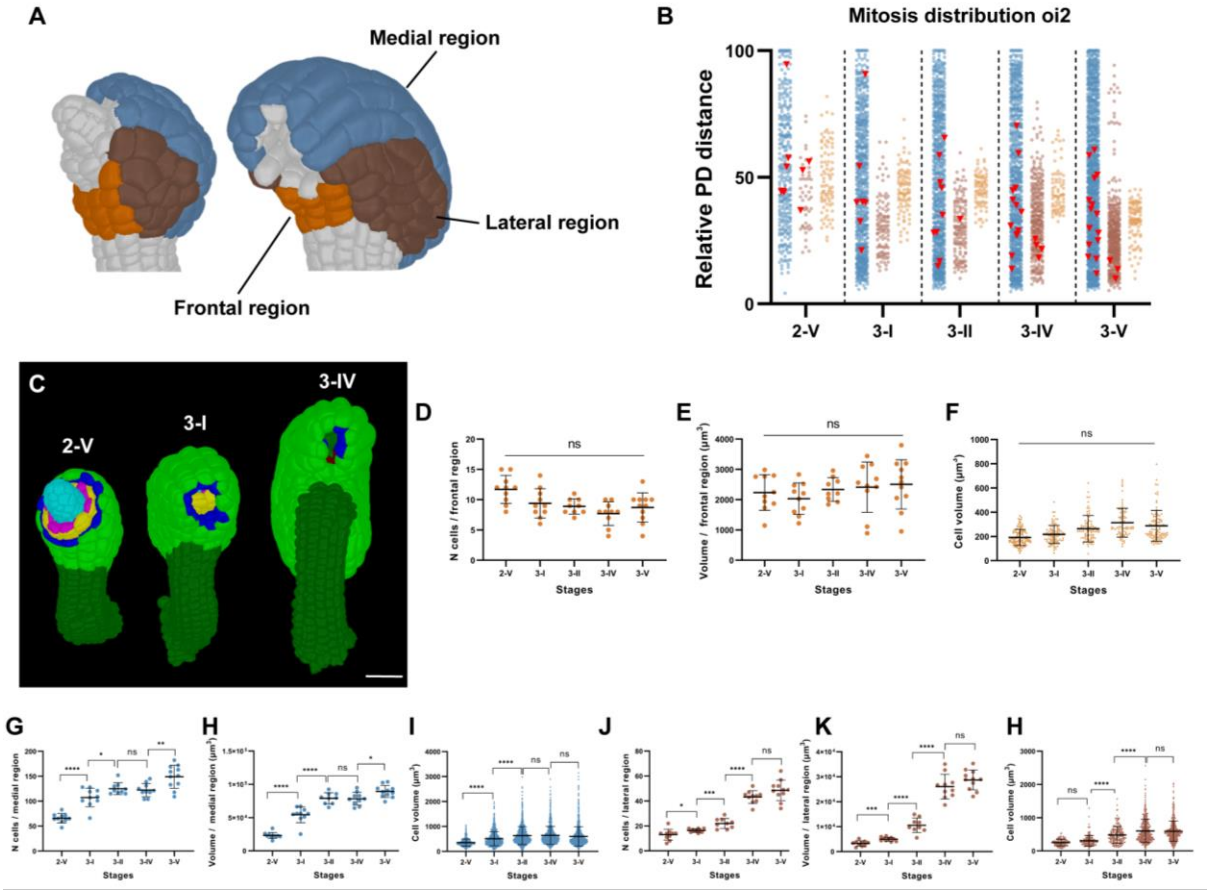

Figure 30 Growth patterns along the medio-lateral axis of the abaxial outer integument.

(A) 3D cell mesh of ovule at stage 2-V and 3-I showing the cell labeling of the medial, lateral, and frontal region of the abaxial outer integument. (B) Column graph showing the distribution of dividing cells in different abaxial outer integument regions along the PD and ML axese during ovule development. The stages are reported on the x-axis. The relative PD distance is reported on the y-axis and ranges between 0 and 100. Each blue, brown and orange point is a cell in interphase of the medial, lateral and frontal region, respectively. Each red triangle is a dividing cell. (C) 3D cell mesh of ovule at different stages showing the tissue cell labeling from a frontal view. (D, E, F) Plot depicting the cell number, tissue volume and cell volume of the frontal region of the abaxial outer integument, respectively. (G, H, I) Plot depicting the cell number, tissue volume and cell volume of the medial region of the abaxial outer integument, respectively. (J, K, H) Plot depicting the cell number, tissue volume and cell volume of the lateral region of the abaxial outer integument, respectively. Data points indicate individual ovules or cells in case of cell volumes plots. Asterisks represent statistical significance (ns, $p \geq 0.5$; *, $p < 0.05$; **, $p < 0.01$; ***, $p < 0.001$; ****, $p < 0.0001$; Student's t-test). Number of 3D digital ovules scored: 10 (stages 2-V, 3-I, 3-II, 3-IV), 11 (stage 3-V). Mean ± SD is shown.

Table 19 Cell parameters along the medio-lateral axis of the abaxial outer integument.

	Abaxial outer integument regions								
Stage[a]	**Medio**			**Lateral**			**Frontal**		
	N cells	Volume (x 10^4 μm^3)	Cell volume (μm^3)	N cells	Volume (x 10^4 μm^3)	Cell volume (μm^3)	N cells	Volume (x 10^4 μm^3)	Cell volume (μm^3)
2-V	65.8 ± 9.41	2.32 ± 0.46	353.2 ± 145.3	13 ± 4.32	0.33 ± 0.11	252.3 ± 97.1	11.7 ± 2.31	0.22 ± 0.06	11.7 ± 2.312
3-I	107.4 ± 18.7	5.44 ± 1.19	506.6 ± 278.5	16.3 ± 1.418	0.5 ± 0.08	307.3 ± 158.4	9.4 ± 2.41	0.2 ± 0.05	9.4 ± 2.413
3-II	125 ± 11.83	7.9 ± 0.85	632 ± 359.9	22 ± 4	1.06 ± 0.29	481 ± 247	8.889 ± 1.269	0.23 ± 0.04	8.889 ± 1.269
3-IV	122.4 ± 13.32	7.84 ± 0.96	640.2 ± 360.7	43.2 ± 5.073	2.61 ± 0.49	603.6 ± 346.9	7.7 ± 1.947	0.24 ± 0.08	7.7 ± 1.947
3-V	149.1 ± 23.09	8.93 ± 0.9	599.3 ± 385	48.55 ± 8.226	2.87 ± 0.4	591.8 ± 305.5	8.727 ± 2.412	0.25 ± 0.08	8.727 ± 2.412

[a]Number of 3D digital ovules scored: 10 (stages 2-V, 3-I, 3-II, 3-IV), 11 (stage 3-V). Values represent mean ± SD.

Table 20 Cell division analysis along the medio-lateral axis of the abaxial outer integument.

Sample[a]	**Region**	**N mitotic cells**	**% of mitotic cells**	**N cells scored**
2-V	Medio	0.8 ± 0.92	1.35 ± 1.66	658
	Lateral	0.3 ± 0.48	2.84 ± 5.47	130
	Frontal	0 ± 0	0 ± 0	117
3-I	Medio	0.7 ± 0.82	0.59 ± 0.69	1074
	Lateral	0 ± 0	0 ± 0	163
	Frontal	0 ± 0	0 ± 0	94
3-II	Medio	1 ± 1	0.78 ± 0.71	1125
	Lateral	0.11 ± 0.33	0.38 ± 1.15	198
	Frontal	0 ± 0	0 ± 0	80
3-IV	Medio	1.3 ± 0.67	1.08 ± 0.54	1224
	Lateral	0.4 ± 0.52	0.94 ± 1.21	432
	Frontal	0 ± 0	0 ± 0	77
	Medio	1.45 ± 0.82	1 ± 0.6	1640

	Lateral	0.27 ± 0.47	0.58 ± 1.05	534
	Frontal	0 ± 0	0 ± 0	96

[a]Number of 3D digital ovules scored: 10 (stages 2-V, 3-I, 3-II, 3-IV), 11 (stage 3-V). Values represent mean ± SD.

3.5.6 *SUP* is required for the asymmetric growth of the abaxial outer integument

To further understand the mechanisms of asymmetric growth characterizing the abaxial outer integument, wild-type ovules have been visually compared to ovule of the *sup* mutant. The *sup* ovule mutant is characterized by defects in the growth polarity, as already mention, and they grow as tubular structure (Meister et al., 2002; Villanueva et al., 1999).

The quantitative analysis showed that the abaxial outer integument in *sup-7* has a significant higher number of cells and higher tissue volume compared to wild-type throughout development (Figure 31 A, B) (Table 12 and Table 22).

At stage 2-IV, 51.4 ± 7.6 cells are found in wild-type abaxial outer integument, while in *sup-7* 87 ± 14.93 cells are found (Figure 31 A) (Table 12 and Table 22). In terms of tissue volume, at stage 2-IV in wild-type the volume is around 1.1×10^4 $\mu m^3 \pm 0.2 \times 10^4$ μm^3, while in *sup-7* the tissue volume is equal 3.05×10^4 $\mu m^3 \pm 1.06 \times 10^4$ μm^3 (Figure 31 B) (Table 12 and Table 22). The abaxial outer integument of *sup-7* at stage 2-IV is roughly 1.7-fold bigger than wild-type in terms of cell number, while it is 3-fold bigger in terms of tissue volume. On the other hand at stage 3-II, 151.1 ± 7.8 cells are found in wild-type abaxial outer integument, while in *sup-7* 186.07 ± 26.67 cells are found (Figure 31 B) (Table 12 and Table 22). In terms of tissue volume, at stage 3-II the abaxial outer integument in wild-type the volume is around 9.0×10^4 $\mu m^3 \pm 0.9 \times 10^4$ μm^3, while in *sup-7* the tissue volume is equal 13.26×10^4 $\mu m^3 \pm 2.07 \times 10^4$ μm^3 (Figure 31 B) (Table 12 and Table 22). The abaxial outer integument of *sup-7* at stage 3-II is roughly 1.2-fold bigger than wild-type in terms of cell number, while it is 1.4-fold bigger in terms of tissue volume. Exception is made for stage 2-III and later stages, suggesting that the outer integument initiation occur similarly to wild-type in *sup-7* (Figure 31 A, B) (Table 12 and Table 22). At maturity, the cellular parameters reach similar value in wild-type and *sup-7*, although differences in the overall ovule shape are observed (Figure 31 A, B) (Table 12 and Table 22).

When analyzing the frontal region of the abaxial outer integument it appeared evident an over proliferation and growth within this region in *sup-7* compared to wild-type. The number of cells and the volume of the frontal region of the abaxial outer integument results increased in *sup-7* ovules compared to wild-type up to stage 2-V. At stage 3-I, 9.4 ± 2.41 cells are found in

wild-type frontal abaxial outer integument, while in *sup-7* 16.6 ± 3.95 cells are found (Figure 31 D) (Table 22). In terms of tissue volume, at stage 3-I the frontal region in wild-type has volume around 0.2 ± 0.05 μm^3, while in *sup-7* the tissue volume is equal 0.84 x 10^4 μm^3 ± 0.32 x 10^4 μm^3 (Figure 31 E) (Table 22). The frontal abaxial outer integument of *sup-7* at stage 3-I is roughly 1.7-fold bigger than wild-type in terms of cell number, while it is 4.2-fold bigger in terms of tissue volume. The lower values of the frontal region in wild-type compared to *sup-7* remain constant throughout ovule development. At stage 3-V, 9.09 ± 1.87 cells are found in wild-type frontal abaxial outer integument, while in *sup-7* 26.14 ± 11.2 cells are found (Figure 31 D) (Table 22). In terms of tissue volume, at stage 3-I the frontal abaxial outer integument in wild-type the volume is around 0.25 x 10^4 μm^3 ± 0.08 x 10^4 μm^3, while in *sup-7* the tissue volume is equal 1.93 x 10^4 μm^3 ± 0.63 x 10^4 μm^3 (Figure 31 E) (Table 22). The frontal abaxial outer integument of *sup-7* at stage 3-V is roughly 2.8-fold bigger than wild-type in terms of cell number, while it is 7.7-fold bigger in terms of tissue volume.

These results suggest a role of *SUP* in maintaining the asymmetric growth of the abaxial outer integument in wild-type ovule. As previously showed, *SUP* is required to negatively regulate *INO* expression in the frontal region of the outer integument (Balasubramanian & Schneitz, 2002; Meister et al., 2002).

Moreover, the asymmetric growth of the abaxial outer integument seems to be a necessary factor for the formation of a hood-like structure and therefore allowing the bending of the integuments during growth, resulting in the curved shape of the ovule at maturity.

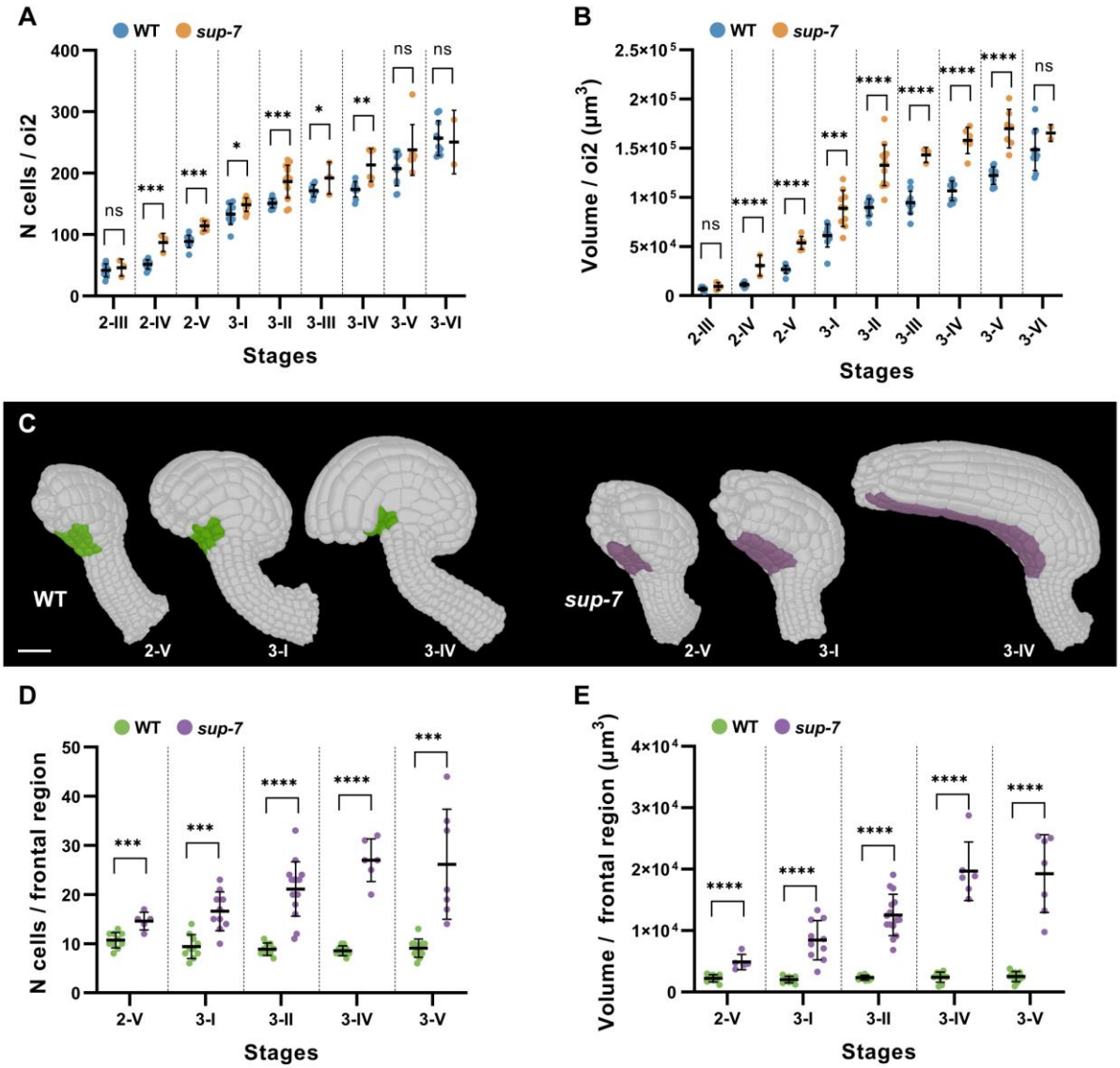

Figure 31 Comparison of cellular parameter of abaxial outer integument between WT and *sup-7*.

(A) Plot comparing the cell number of the abaxial outer integument between wild-type and *sup-7* during ovule development. (B) Plot comparing the tissue volume of the abaxial outer integument between wild-type and *sup-7* during ovule development. (C) 3D cell mesh of ovule of wild-type and *sup-7* at stage 2-V, 3-I and 3-IV showing the cell labeling of the frontal region of the abaxial outer integument. (D) Plot comparing the cell number of the frontal abaxial outer integument between wild-type and *sup-7* during ovule development. (E) Plot comparing the tissue volume of the frontal abaxial outer integument between wild-type and *sup-7* during ovule development. Data points indicate individual ovules. Asterisks represent statistical significance (ns, $p \geq 0.5$; *, $p < 0.05$; **, $p < 0.01$; ***, $p < 0.001$; ****, $p < 0.0001$; Student's t-test). Number of 3D digital ovules scored for WT dataset: 10 (stages 2-V, 3-I, 3-II, 3-IV), 11 (stage 3-V). Number of 3D digital ovules scored for *sup-7* dataset: 6 (stages 2-V, 3-IV), 7 (stage 3-V), 10 (stage 3-I), 15 (stage 3-II). Mean ± SD is shown.

Table 21 Cell number and tissue volume of *sup-7* integuments.

	Tissue									
Stage[a]	**Abaxial outer integument**		**Adaxial outer integument**		**Abaxial inner integument**		**Adaxial inner integument**		**Parenchymatic inner integument**	
	N cells	Volume (x 10^4 μm^3)	N cells	Volume (x 10^4 μm^3)	N cells	Volume (x 10^4 μm^3)	N cells	Volume (x 10^4 μm^3)	N cells	Volume (x 10^4 μm^3)
2-III	46 ± 13.75	0.95 ± 0.34	9.33 ± 1.53	0.14 ± 0.02	23 ± 6.24	0.32 ± 0.07	13 ± 4.36	0.2 ± 0.08	-	-
2-IV	87 ± 14.93	3.05 ± 1.06	29 ± 12.53	0.68 ± 0.34	39 ± 7.21	0.68 ± 0.11	24.67 ± 4.73	0.36 ± 0.08	-	-
2-V	114.1 ± 8.13	5.37 ± 0.67	72.3 ± 12.1	2.1 ± 0.32	54 ± 6.1	0.95 ± 0.11	29.83 ± 7.65	0.45 ± 0.12	-	-
3-I	148.5 ± 11.2	8.87 ± 1.83	115.1 ± 27.1	3.7 ± 0.98	82.2 ± 15.52	1.63 ± 0.43	43.3 ± 12.18	0.82 ± 0.28	-	-
3-II	186.1 ± 26.6	13.27 ± 2.08	172.9 ± 26.7	6.27 ± 1.1	128.9 ± 24.5	3.17 ± 0.6	81.27 ± 19.6	1.99 ± 0.54	2 ± 0	0.04 ± 0
3-III	192 ± 26.06	14.32 ± 0.77	197.6 ± 34.8	7.07 ± 1.05	154 ± 31.32	4.24 ± 1.37	99.33 ± 17.4	2.45 ± 0.5	14.67 ± 22.8	0.04 ± 0.01
3-IV	213.2 ± 26.8	15.79 ± 1.33	238.6 ± 31.1	8 ± 0.87	172.7 ± 32.9	4.47 ± 0.37	106.5 ± 17.4	2.82 ± 0.52	6 ± 3.94	0.15 ± 0.12
3-V	237.7 ± 41.1	16.99 ± 1.95	278.7 ± 68.1	9.01 ± 1.58	204.7 ± 50.5	5.44 ± 0.99	129.3 ± 30.7	3.55 ± 0.7	38.8 ± 24.54	1.07 ± 0.67
3-VI	250.5 ± 51.6	16.55 ± 0.86	289.5 ± 89.8	8.99 ± 1.61	235.5 ± 36.1	5.75 ± 1.69	158.5 ± 47.4	4.19 ± 2.18	29 ± 0	0.58 ± 0

[a]Number of 3D digital ovules scored for *sup-7* dataset: 2 (stage 3-VI), 3 (stages 2-III, 2-IV, 3-III), 6 (stages 2-V, 3-IV), 7 (stage 3-V), 10 (stage 3-I), 15 (stage 3-II). Values represent mean ± SD.

Table 22 Cell number and tissue volume of WT and *sup-7* frontal region.

	Frontal region abaxial outer integument			
Stage[a]	**Wild-type**		***sup-7***	
	N cells	Volume (x 10^4 μm^3)	N cells	Volume (x 10^4 μm^3)
2-V	10.7 ± 1.57	0.22 ± 0.06	14.6 ± 1.82	0.49 ± 0.13
3-I	9.4 ± 2.41	0.2 ± 0.05	16.6 ± 3.95	0.84 ± 0.32

3-II	8.89 ± 1.27	0.23 ± 0.04	21.13 ± 5.55	1.25 ± 0.34
3-IV	8.56 ± 1.01	0.24 ± 0.08	27 ± 4.34	1.97 ± 0.48
3-V	9.09 ± 1.87	0.25 ± 0.08	26.14 ± 11.2	1.93 ± 0.63

[a]Number of 3D digital ovules scored for WT dataset: 10 (stages 2-V, 3-I, 3-II, 3-IV), 11 (stage 3-V). Number of 3D digital ovules scored for *sup-7* dataset: 6 (stages 2-V, 3-IV), 7 (stage 3-V), 10 (stage 3-I), 15 (stage 3-II). Values represent mean ± SD.

4 Discussion

4.1 Stage-specific 3D digital atlas of wild-type ovule

The 3D digital organ generated has demonstrated to be a powerful tool for the analysis of tissue morphogenesis in *Arabidopsis thaliana* ovule. The improvements obtained with the combination of segmentation pipeline PlantSeg (Wolny et al., 2020) and ClearSee-based clearing and staining of fixed tissue (Kurihara et al., 2015; Tofanelli et al., 2019) allowed the analysis of organ architecture through the obtainment of 3D digital organ with increased accuracy and in reasonable time compared to the past.

The analysis of 3D digital atlas of ovules with cellular resolution gave new insight into ovule morphogenesis, highlighting a complex 3D architecture of the organ. The analysis of the cell number and organ volume of ovules during the development showed that both increase in cells and overall increase in volume contribute similarly to the ovule growth. Moreover, the analysis highlighted a steady and continuous growth of the organ, during development.

The possibility to combine the ClearSee-based staining of fixed tissue methods with TO-PRO-3 allowed the analysis of cell division in the organ. The percentage of mitotic cells tend to cluster around values of 0.90 % up to stage 2-II/2-III, showing lower values compared to what observed in *Arabidopsis* root (Malamy and Benfey 1997).

4.1.1 Early-stage ovules show an even growth

The ovule of *Arabidopsis* is a relatively small organ, measuring around 100 µm on the major axis at maturity. Although its small dimensions, the 3D digital atlas of ovule with cellular resolution showed a complex organization in terms of tissue architecture.

The global analysis in terms of number of cells and tissue volume showed some limitations in the possibility to appreciate and unravel the complexity of the organ organization. Therefore, a more powerful tool was applied to the 3D digital atlas to monitor tissue growth and composition. Specific tissue labels were applied to individual cells to describe the different tissue types.

Previous studies reported that ovule is a composite of three distinct radial layer (Jenik & Irish, 2000; Schneitz et al., 1995). Therefore, this general principle of radial tissue organization (L1, L2, L3) has been adopted for early-stage ovules. The analysis of the cellular growth pattern of the tissue layers highlighted the appropriateness of the adopted labeling. The correlation of the total number of cells with the number of cells per each tissue was positive for the L1 and L2,

showing a stereotypic behavior of the tissue between different samples. However, the L3 tissue showed more scattering, meaning a less organized development of this tissue between different samples. Moreover, the early-stage tissue analysis highlighted an even growth of ovule primordia since distinct subclasses of primordia were not detected, rather a steady and continuous rise in primordium volume and cell number was observed. Taken together the data support the notion that from the youngest detectable primordia to late stage 2-I primordia outgrowth does not undergo major fluctuations.

The proposed quantitative approach gives the possibility to identify according to the position and cell volume the developing MMC cells which become firstly detectable at stage 2-I, proposing the applicability of a quantitative and unambiguous criteria for the correct staging of ovule development.

4.1.2 Late-stage ovule of *Arabidopsis* shows a complex tissue organization

Specific tissue labels were applied to individual cells to describe the different tissue types and multiple labels were used for late-stage ovules. The labeled applied included: funiculus, nucellus, embryo sac, central region, and integuments. The analysis highlighted a complexity within the ovule in terms of tissue organization and the analysis of cell number and tissue volume across development showed different and unique tissue growth dynamics.

The analysis highlighted a steady growth of the funiculus up to stage 3-I. On the other hand, the nucellus showed a opposite behavior with most of the growth occurring at later stage of the development up to 3-III. The embryo sac showed a dramatic increase in volume, constituting the major tissue undergoing growth during early stage, indicating its central role as the structure harboring the next generation. Additionally, the integuments showed to drive most of the ovule growth together with the central region. There is a certain degree of correlation between the growth of the female gametophyte and the sporophytic tissues that has to surround, protect and nourish the embryo sac, suggesting the important role of the growth coordination between these different structures to guarantee the success in the production of the reproductive structure.

4.1.3 Ovule patterning occurs early in ovule development

The analysis of gene expression with the help of the 3D digital ovule in pWUS::2xVenus-NLS reporter line provided new information regarding the temporal and spatial control of WUS expression and its role in ovule development.

The pWUS signal was detectable starting from 50 cells and was employed as a marker to distinguish the transition between stage 1-I and 1-II. The analysis of pWUS, gave insight into the process of ovule patterning and its temporal establishment, correlating it for the first time with quantitative information. The results showed that ovule patterning it's established very early in ovule development, earlier compared to the visual appearance of the three elements in the ovule primordia. Nucellus become first apparent at stage 2-I when it possible to notice the presence of a larger subepidermal cells, the MMC. Moreover, it is possible to distinguish the distal nucellus from the other pattern elements because the ovule primordia at the bottom region appears more wide compared to the proximal nucellus. Therefore, the analysis of pWUS revealed that the ovule pattering occurs already at stage 1-II, before the visible elements become detectable at stage 2-I.

Further studies of genes expression pattern of recognized genes involved in the patterning of ovule, will allow further clarification on the buildup of ovule patterning and the correlation with quantitative information.

4.1.4 The central chalaza is composed of two distinct regions

With the employment of the 3D digital atlas of ovule development it has been possible to quantitatively describe two distinct tissues composing the proximal central region, which were not characterized before. The two tissues were named anterior and posterior proximal chalaza and they showed different cellular parameters, allowing the classification into distinct regions based on these cellular characteristics. The posterior chalaza showed a higher number of smaller cells, while the anterior chalaza is composed of less but bigger cells. Overall, at later stages of development the two regions show different shapes. Moreover, these regions seem to contribute differentially to ovule development, with the cells of the anterior chalaza intercalating between the abaxial and adaxial outer integument on the frontal region of the ovule and the proximal chalaza being buried deeply into the central region of the ovule and sustaining the inner integument and nucellus, which are placed on the upper part of the tissue.

4.1.5 The differential growth between the integument layers might contribute to ovule curvature

The ovule of *Arabidopsis* is a bitegmic ovule, consisting of two bi-layered integuments (Schneitz et al., 1995; Tuernitt & Haseloff 2008). From the comparison of the growth of the abaxial and adaxial layers within the same integument, it appeared evident that the layers are interested by differential growth. At maturity the adaxial outer integument showed a higher number of cells compared to the abaxial outer integument. Interestingly, the abaxial outer integument still showed a higher tissue volume (around 2-fold bigger) compared to the adaxial layer. The results suggested that the abaxial outer integument is the major driver of the growth of the outer integument. Similarly, throughout the development, the abaxial inner integument showed a higher number of cells and tissue volume compared to the adaxial inner integument. Therefore, the inner integument as well showed a differential growth between the two layers.

Deformation in space of tissue sheets is an important phenomenon involved in morphogenesis to create complex 3D shapes in plants but also in mammals. Several models have been proposed to explain the mechanisms behind these tissue deformations, including differential surface contractions, oriented tissue tensions and differential growth (Brodland, 2015; X. Chen & Brodland, 2008; Rebocho et al., 2017; Savin et al., 2011; Tallinen et al., 2016; Wyczalkowski et al., 2012). Included into out-of-plane deformations, is the generation of curvature that can be explained as local rotations out of the plane. One of the discussed mechanisms that can account for the generation of curved structures, is that regions within the tissue sheet are specified to grow at different rates and/or directions. Local rotations can arise as consequence of reduction of potential conflicts within the tissue lead by such differential growth (Coen and Rebocho, 2016), to reduce the mechanical stress generated. Therefore curvature or rotations are generated to minimized the stress exerted on the growing structure (Coen & Rebocho, 2016). The model, called tissue conflict resolution, predicts the formation of a bulged 3D structure starting form a 2-layered sheet structure, in which the abaxial and adaxial layer show differential growth, in particular with the abaxial interested by a higher level of growth compared to the adaxial layer (Rebocho et al., 2017).

Considering these proposed models describing morphogenetic processes, that leads to the curvature of a biological structure, it become interesting to adapt them in the contest of a curved structure such as the ovule of *Arabidopsis*. Particularly, the elucidation and analysis of the growth pattern characterizing the integuments showed that the integument are interest by a differential growth. Into this context, it is possible to speculate that the differential growth

observed between the adaxial and abaxial layer of the integument it might contribute as an important factor involved in the curvature formation. However, additional analysis and possibly the generation of a growing model of ovule growth can investigate the role of integuments layer differential growth in the overall curvature formation.

4.1.6 Generation of a new layer within the ovule

The mode of formation of the parenchymatic inner integument broadened the repertoire of modes of how a new cell layer can be formed in plants. Cambium-like activity of the innermost layer of the inner integument resulted in the formation of the parenchymatic inner integument layer (Debeaujon et al., 2003; Schneitz et al., 1995). Early morphological analysis in 2D led to the hypothesis that all cells located in the proximal half of the ii1 layer undergo periclinal divisions resulting in the formation of the ii1' cell layer. This model assimilates to the supported notion that periclinal asymmetric cell divisions is the basis of the formation of new cell layers in plants. Similarly, periclinal asymmetric cell divisions in all the radially arranged cortex/endodermis initials contribute to the formation of the cortex and endodermis cell layers of the main root (Di Laurenzio et al., 1996; Dolan et al., 1993). By contrast, the employed 3D digital ovules revealed a distinct mode for the formation of the parenchymatic inner integument layer. The analysis indicated that only a small number of the adaxial inner integument undergo asymmetric cell divisions to produce the first parenchymatic precursor cells. Much of the subsequent layer formation seems to rely on symmetric cell divisions that originate in the daughters of those few parenchymatic founder cells. Thus, formation of the parenchymatic layer depends on lateral extension starting from a few scattered pioneer cells, a process that may be called as layer invasion (Vijayan & Tofanelli et al., 2021).

4.2 Temporal framework of wild-type ovule development

The present study investigated the temporal progression of ovule development, estimating the duration of each developmental stage. The estimation was performed on a two-step procedure. Ovules were staged from 64 pistils of various length and the ovule stage duration was estimated from the pistil growth curve that was previously generated.

The findings confirmed the asynchrony in ovule development that was previously observed (Schneitz et al., 1995; Wolny et al., 2020; Yu et al., 2020). The stage duration estimated accounted for about 31.7 hours for stage 1, while stage 2 was 58.9 hours. The stage 3 was estimated with 55.6 hours of duration.

To confirm the measured time intervals for ovule stage, a two-time points imaging strategy was performed, and the results showed to be similar in term of stage duration compared to the established framework of stage duration.

Recently, great improvements have been achieved in performing live-cell imaging of the female gametophyte to visualize the living dynamics of embryo sac development and to assess cell type specification (Susaki et al., 2021). The present study showed the different temporal dynamics in the embryo sac development and estimated a duration of 11.8 ± 3.3 hours for stage 3-II and 3-III, 8.1 ± 1.2 hours for stage 3-IV and around 14.6 ± 3.9 hours for stage 3-V (Susaki et al., 2021). According to our established framework the duration of stage 3-II/3-III is around 6.3 hours, as well as for stage 3-IV and of 18.6 hours for stage 3-V. Considering the reported standard deviation in the study from Susaki et al., 2021, the duration reported by our study appeared to not withdraw from the values measured through life-imaging approach. However, the slight differences observed could be accounted for the different growth conditions of the conducted experimental settings.

4.3 Ovule growth is a dynamic process

The analysis of the general growth dynamics of *Arabidopsis* ovule highlighted a dynamic behavior across the development, with similar relative growth and proliferation rates were observed for different stages. Some exceptions are observed, from stage 2-I to 2-II where the proliferation rate is higher compared to growth and for stage 2-IV to 3-IV where the growth is predominately occurring through volume increase achieved through cell elongation. These results suggests that the development of *Arabidopsis* ovule is a dynamic process.

Additionally, to the overall relative growth rates of ovule development, the relative growth of the integuments has been analyzed. The integuments growth was well characterized already since 1995, however with the present study a quantitative approach has been applied to describe their growth (Schneitz et al., 1995). The inner integument (ii) initiates earlier than the outer integument, around stage 2-II, and become apparent as a bulging ring of cells in the region of the chalaza proximal to the nucellus. The analysis showed that the inner integument is interested by high cell proliferation at early stage of ovule development and up to stage 3-I the growth re-started after a short interval of lower growth. Up to stage 3-I, the inner integument starts to grow to finally envelop completely the nucellus. The nucellar structure is firstly envelop by the outer integument and only after is surrounded by the inner integument. The different growth dynamics observed for the tissues are well described by the proposed analysis.

The outer integument become evident later than the inner integument, as a semi-annular bulging at the side of the chalaza that faces the basal end of the carpel. Up to stage 3-I the main contribution to the outer integument growth is mainly achieved through cell expansion rather than through cell proliferation, which is only higher at early stage when the outer integument is emerging and surrounding the nucellus.

4.3.1 Analysis of regional growth pattern in the integuments

A coordinate organ system has been applied to the integument to gain spatial information on the regional growth pattern within the tissues. The analysis provided therefore a detailed description of growth throughout development along the PD axis. The assignment of positional descriptor to each cell in the tissue was possible through the application and adaptation of the 3DCellAltas tool in MGX to ovule integuments (Barbier de Ruille et al., 2015; Montenegro-Johnson et al., 2015; Vijayan and Strauss, unpublished).

The analysis of the distribution of cell proliferation highlighted the presence of preferential distribution of proliferating regions within the integuments. More in detail, the adaxial outer integument, abaxial and adaxial inner integument showed the presence of a region in the proximal half of the tissue characterized by the preferential presence of dividing cells. The distal half of the tissue on the contrary did not show any cell division. Regarding the abaxial outer integument, the analysis of the cell division distribution highlighted the presence of a region interacting subepidermally directly with the posterior chalaza that did not show any cell division throughout the development. The cell division resulted to be mainly concentrated at the middle region of the tissue, that would interact subepidermally with the proximal half of the adaxial outer integument. As observed for the internal layers of the integuments, also the abaxial outer integument did not show cell division. Similarly, to what is observed in the present work, also in leaves the presence of regions with differential growth has been extensively documented (Fox et al., 2018; Kierzkowski et al., 2019). Leaves show the presence of a proximal-distal gradient of growth, with a higher growth towards the lateral lamina and lower growth towards the distal tip.

The same spatial analysis has been performed to analyse the distribution along the PD axis of the single cell volumes. Throughout the development appeared evident the presence of a preferential distribution of cells with higher cell volumes at the distal half of the different layers of the inner and outer integument. More specifically, the extent of cell volumes tended to

decrease gradually from outside to inside. The abaxial outer integument represent the layer that presents more obviously large cells at the distal side, that reach values up to 1200 μm^3.

The analysis suggests the presence of differential regional growth patterns within the integuments. The distal half is characterized by cell enlargement and exclude any cell proliferation, while in the proximal half, where cells are smaller compared the distal pole, most of the cell proliferation is concentrated. Therefore, the growth of the distal half is mainly archived in the increase of single cells dimension that summed up leads to the increase in the region volume, while the proximal half grows through the increase of cell number within the region. The outer integument seems to be composed by three different regions, characterized by different cellular behaviours. As for the internal layers, the distal and proximal half showed opposite behaviour, but additionally there is a most proximal region which did not show any growth during ovule development.

As previously mentioned, the integuments showed differential growth between the abaxial and adaxial layers. These results illustrate that there are also differential growth patterns between regions within the same layer but also confirms the differential growth patterns characterizing the four layers that constitute the integumental apparatus.

The quantitative characterization carried out in this section will be employed in further studies for the build-up of growth models to understand the single contribution of the differential pattern of growth within the integuments in shaping ovule curvature.

4.4 Phenotypic characterization of ovule mutants

To gain insight in the mechanisms of ovule curvature formation, ovule of *Arabidopsis* mutant characterized by defect in the overall shape have been analyzed. Therefore, a developmental series of 3D digital *ino* and *sup* mutant ovule at cellular resolution has been obtained and a phenotypic analysis has been conducted.

The phenotypic characterization of ovule mutant was carefully conducted through traditional techniques including, tissue sections of paraffin-embedded specimens, optical sections through whole-mount ovules, and scanning electron microscopy (Baker et al., 1997; Balasubramanian and Schneitz, 2002; Balasubramanian and Schneitz, 2000; Meister et al., 2002; Schneitz et al., 1997; Sieber et al., 2004; Villanueva et al., 1999). Therefore, a 3D analysis results to be necessary for elucidating additional gene functions and to understand the contribution of *INO* and *SUP* to the curvature formation.

Regarding *ino* mutant, the ovules show not only a missing outer integument and defective embryo sac development but also exhibit cellular aberrations in the nucellus and chalaza. Concerning *sup* mutant, the ovules show defect in the outer integument polarity resulting in a "trumpet-shaped" ovule. Similarly, ovules of *sup* also show defects in the embryo sac, which results with high frequency blocked to the mono-nuclear stage, and light abnormalities are detected in the nucellar tissue. It has long been recognized that ontogenesis of the embryo sac correlates with proper integument development although the molecular mechanism remains unclear (Bencivenga et al., 2011, Gasser et al., 1998; Grossniklaus & Schneitz, 1998). Therefore, the observed abnormalities might be consequence of an impaired growth of the integuments that is required for the control of the correct embryo sac formation and nucellus patterning, through molecular or mechanical mechanisms. However, the involvement of the chalaza might offer an alternative interpretation, speculating a role of this tissue in the control of hormones distribution through the other tissues of the organ. Cytokinin is known to affect ovule patterning through the control of the expression of the auxin efflux carrier gene PIN-FORMED 1 (PIN1) and a chalaza-localized cytokinin signal is required for early gametophyte development (Bencivenga et al., 2012; Ceccato et al., 2013; Cheng et al., 2013). Thus, the defects in the development of the nucellus and embryo sac may relate to the cellular mis-organization of the chalaza and thus altered cytokinin and in turn auxin signaling. These hypotheses might be explored through the generation of a 3D ovule atlas of phytohormones distribution in future studies.

4.5 Ovule curvature is a multistep process

The present work provided new insight into the genetic and cellular processes regulating ovule curvature. Previous studies hypothesized ovule curvature to be a multi-step process with a major involvement of the proximal chalaza and the integuments (Baker et al., 1997; Schneitz et al., 1997). A detailed comparison between wild-type and ovule mutants, *ino-5* and *sup-7*, 3D digital ovules provided evidence for two distinct processes that contribute to ovule curvature: kink formation in the ovule primordium and later bending of the elongating integuments.

4.5.1 Kink formation

Kink formation is an early event in curvature formation, leading to the repositioning of the nucellus towards the apex of the gynoecium and it is established in ovule primordia. The analysis showed that *INO* function is required for this process, as kink formation is not

established in *ino-5*. The data support the hypothesis that a small number of asymmetric oblique cell divisions in the stage 2-III posterior chalaza led to the characteristic early kink of the ovule primordium.

The results suggest that *SUP* is not required for kink formation as this feature is conserved in early-stage *sup-7* ovule, in which the reorientation of the nucellus is still achieved. However, an abnormal growth of the chalaza in *sup-7* mutant ovule was found. During *sup-7* development the anterior chalaza results to be reduced compared to wild-type ovules. Additionally, some aberrations are also highlighted in the posterior chalaza, which results higher in volume in *sup-7* compared to wild-type. Therefore, it appeared evident that *SUP* is not strictly required for kink formation, but its function become fundamental in the regulation of the integuments bending, since *sup-7* ovules show an aberrant shape.

4.5.2 Integuments bending

The establishment of the final step of curvature formation involves the integuments outgrowth and elongation. From the performed comparison of wild-type and ovule mutant emerged the involvement of *INO*, as well as for kink formation, in the integument bending. Regarding integument bending *ino* ovules are characterized by straight growth of the inner integument. However, the general parameters of the inner integument are not affected in *ino-5*. Therefore, the results suggest that the outer integument exert an influence on the inner integument, controlling its bending. The molecular and/or mechanical mechanisms through which the bending is imposed on the inner integument is still uncleared.

From the analysis of the cellular characteristic and growth pattern of *ino* ovules, it appeared evident that the outer integument has a central role for the morphogenesis of ovule curvature.

Studies on ovule diversity through the major clades of angiosperms and comparison with gymnosperms with curved ovules suggest that in angiosperms the presence of an outer integument is instrumental for ovule curvature (Doyle & Endress, 2000; Endress, 2011).

The analysis of *INO* expression pattern showed the presence of a frontal region, where the *INO* expression is absent, and no growth is observed throughout the development. Therefore, *INO* is a promoter of the outer integument asymmetric elongation. The analysis of *sup* mutant showed the importance of the asymmetric growth of the outer integument for the correct curvature formation. In the analyzed *sup* mutant ovule, the asymmetric growth of the outer integument is abolished, and the frontal region results to be interested by higher growth compared to wild-type. As already showed from previous studies, *SUP* is a negative regulation

of *INO* expression in the frontal region, corroborating the role of *INO* as a positive regulator of asymmetric growth of the outer integument (Balasubramanian & Schneitz, 2002; Meister et al., 2002). Future studies will address in more detail the interplay between genetics, cellular behavior, and tissue mechanics that underlies ovule curvature.

5 Conclusion

The present study showed the power of three-dimensional digital representation when investigating the morphogenetic process of an organ of complex architecture. To understand ovule morphogenesis and curvature formation, it is important to gain a quantitative understanding of the cellular growth patterns that generate this unique shape. The approach used in the study is based on the generation of 3D digital reconstruction of the ovule organ covering all the developmental stages, to obtain quantitative information on cellular characteristic and growth behavior.

The analysis of the 3D digital atlas of wild-type ovule development described the growth patterns that shape the organ, gaining information on *WUS* expression and highlighting the presence of two distinct subpopulation of cells in the central chalaza characterized by differential quantitative descriptors. Moreover, during this study a temporal framework of ovule development, estimating the duration of the different stages, have been successfully establishes. The temporal information has been employed to obtain tissue growth rate, representing a base for further studies and generation of growth models. The analysis was concentrated with detail in the characterization of integuments growth, highlighting the presence of regional growth patterns within the layers and the presence of differential growth between them. Although more studies are required, differential growth might contribute to the curvature and bending of the ovule.

In the context of ovule curvature, the analysis of the 3D digital atlas of mutant ovules defective in curvature such *ino* and *sup* suggested that ovule curvature is a multi-step process. An early on set is represent by the kink formation, with the involvement of the central region in ovule primordium, leading to the repositioning of the nucellus. A later step in curvature formation is represented by the integument outgrowth and elongation. Comparison of growth pattern and cellular parameters of wild-type and mutant ovules, suggested a central role of the outer integument in shaping the curvature, as already reported from evolutionary comparative studies. Additionally, this study evidenced that the outer integument imposes the bending to the inner integument, which appears to have a passive role in the curvature process.

Moreover, the comparison with *sup* mutant showed that the asymmetric growth of the outer integument is a crucial aspect in the formation of an anatropous ovule and that *INO* gene needs to be tightly regulated to allow the growth of the outer integument as hood-like structure.

The work generated an incredible amount of quantitative data that were interpreted to gain understanding in the morphogenetic process of ovule development and curvature formation.

However, morphogenesis is a complex process where different genetic, mechanical, and cellular processes are integrated in time and space within the tissues constituting the organ. Therefore, a successful strategy needs to integrate all these different aspects to obtain a comprehensive description. This work represents a first step in the buildup of a computational modeling strategy to model the growth of ovule and its curvature. The quantitative data generated in this work will be employed for the generation of a model of growth to understand the different contribution of ovule tissues and growth patterns to curvature and to test the proposed hypothesis. The establishment of a growing model will allow to test hypothesis but also to implement with further data the model itself and expand the understanding of the roles of different components in ovule morphogenesis. Further analysis will be concentrated into the role of hormones in integument outgrowth and elongation and into the investigation of stress patterns shaping the ovule.

6 References

List of Previous Publications

Tofanelli, R., Vijayan, A., Scholz, S., & Schneitz, K. (2019). Protocol for rapid clearing and staining of fixed Arabidopsis ovules for improved imaging by confocal laser scanning microscopy. *Plant Methods*, *15*, 120. https://doi.org/10.1186/s13007-019-0505-x

Vijayan, A., **Tofanelli, R.,** Strauss, S., Cerrone, L., Wolny, A., Strohmeier, J., Kreshuk, A., Hamprecht, F. A., Smith, R. S., & Schneitz, K. (2021). A digital 3D reference atlas reveals cellular growth patterns shaping the arabidopsis ovule. *ELife*, *10*, 1–38. https://doi.org/10.7554/eLife.63262

Wolny, A., Cerrone, L., Vijayan, A., **Tofanelli, R.**, Barro, A. V., Louveaux, M., Wenzl, C., Strauss, S., Wilson-Sánchez, D., Lymbouridou, R., Steigleder, S. S., Pape, C., Bailoni, A., Duran-Nebreda, S., Bassel, G. W., Lohmann, J. U., Tsiantis, M., Hamprecht, F. A., Schneitz, K., Kreshuk, A. (2020). Accurate and versatile 3D segmentation of plant tissues at cellular resolution. *ELife*, *9*. https://doi.org/10.7554/{eLife}.57613

Bibliography

Arnault, G., Vialette, A. C. M., Andres-Robin, A., Fogliani, B., Gateble, G., & Scutt, C. P. (2018). Evidence for the Extensive Conservation of Mechanisms of Ovule Integument Development Since the Most Recent Common Ancestor of Living Angiosperms. *Front Plant Sci*, *9*, 1352. https://doi.org/10.3389/fpls.2018.01352

Bailoni, A., Pape, C., Wolf, S., Beier, T., Kreshuk, A., & Hamprecht, F. A. (2019). A generalized framework for agglomerative clustering of signed graphs applied to instance segmentation. In *arxiv.org*. https://arxiv.org/abs/1906.11713

Bajon, C., Horlow, C., Motamayor, J. C., Sauvanet, A., & Robert, D. (1999). Megasporogenesis in Arabidopsis thaliana L.: an ultrastructural study. *Sexual Plant Reproduction*, *12*(2), 99–109. https://doi.org/10.1007/s004970050178

Baker, S. C., Robinson-Beers, K., Villanueva, J. M., Gaiser, J. C., & Gasser, C. S. (1997). Interactions Among Genes Regulating Ovule Development in Arabidopsis thaliana. *Genetics*, *145*, 1109–1124.

Balasubramanian, S., & Schneitz, K. (2000). NOZZLE regulates proximal-distal pattern formation, cell proliferation and early sporogenesis during ovule development in Arabidopsis thaliana. *Development*, *127*(19), 4227–4238.

Balasubramanian, S, & Schneitz, K. (2002). NOZZLE links proximal-distal and adaxial-abaxial pattern formation during ovule development in Arabidopsis thaliana. *Development*, *129*(18), 4291–4300. https://www.ncbi.nlm.nih.gov/pubmed/12183381

Balasubramanian, Sureshkumar, & Schneitz, K. (2002). NOZZLE links proximal-distal and adaxial-abaxial pattern formation during ovule development in Arabidopsis thaliana. *Development*, *129*(18), 4291–4300.

Barbier de Reuille, P., Routier-Kierzkowska, A. L., Kierzkowski, D., Bassel, G. W.,

Schupbach, T., Tauriello, G., Bajpai, N., Strauss, S., Weber, A., Kiss, A., Burian, A., Hofhuis, H., Sapala, A., Lipowczan, M., Heimlicher, M. B., Robinson, S., Bayer, E. M., Basler, K., Koumoutsakos, P., … Smith, R. S. (2015). MorphoGraphX: A platform for quantifying morphogenesis in 4D. *Elife*, *4*, 5864. https://doi.org/10.7554/eLife.05864

Baroux, C., & Autran, D. (2015). Chromatin dynamics during cellular differentiation in the female reproductive lineage of flowering plants. *Plant Journal*, *83*(1), 160–176. https://doi.org/10.1111/tpj.12890

Barro-Trastoy, D., Dolores Gomez, M., Tornero, P., & Perez-Amador, M. A. (2020). On the Way to Ovules: The Hormonal Regulation of Ovule Development. *Critical Reviews in Plant Sciences*, *39*(5), 431–456. https://doi.org/10.1080/07352689.2020.1820203

Bartrina, I., Otto, E., Strnad, M., Werner, T., & Schmülling, T. (2011). Cytokinin regulates the activity of reproductive meristems, flower organ size, ovule formation, and thus seed yield in Arabidopsis thaliana. *Plant Cell*, *23*(1), 69–80. https://doi.org/10.1105/tpc.110.079079

Bassel, G W. (2015). Accuracy in Quantitative 3D Image Analysis. *Plant Cell*, *27*(4), 950–953. https://doi.org/10.1105/tpc.114.135061

Bassel, G W. (2019). Multicellular Systems Biology: Quantifying Cellular Patterning and Function in Plant Organs Using Network Science. *Mol Plant*, *12*(6), 731–742. https://doi.org/10.1016/j.molp.2019.02.004

Bassel, G W, & Smith, R. S. (2016). Quantifying morphogenesis in plants in 4D. *Curr Opin Plant Biol*, *29*, 87–94. https://doi.org/10.1016/j.pbi.2015.11.005

Bassel, George W., Stamm, P., Mosca, G., De Reuille, P. B., Gibbs, D. J., Winter, R., Janka, A., Holdsworth, M. J., & Smith, R. S. (2014). Mechanical constraints imposed by 3D cellular geometry and arrangement modulate growth patterns in the Arabidopsis embryo. *Proceedings of the National Academy of Sciences of the United States of America*, *111*(23), 8685–8690. https://doi.org/10.1073/pnas.1404616111

Bassel, George W. (2018). Information processing and distributed computation in plant organs. *Trends in Plant Science*, *23*(11), 994–1005. https://doi.org/10.1016/j.tplants.2018.08.006

Becker, A. (2020). A molecular update on the origin of the carpel. *Current Opinion in Plant Biology*, *53*, 15–22. https://doi.org/https://doi.org/10.1016/j.pbi.2019.08.009

Bemer, M., Wolters-Arts, M., Grossniklaus, U., & Angenenta, G. C. (2008). The MADS domain protein DIANA acts together with AGAMOUS-LIKE80 to specify the central cell in Arabidopsis ovules. *Plant Cell*, *20*(8), 2088–2101. https://doi.org/10.1105/tpc.108.058958

Bencivenga, S, Simonini, S., Benkova, E., & Colombo, L. (2012). The transcription factors BEL1 and SPL are required for cytokinin and auxin signaling during ovule development in Arabidopsis. *Plant Cell*, *24*(7), 2886–2897. https://doi.org/10.1105/tpc.112.100164

Bencivenga, Stefano, Colombo, L., & Masiero, S. (2011). Cross talk between the sporophyte and the megagametophyte during ovule development. *Sexual Plant Reproduction*, *24*(2), 113–121. https://doi.org/10.1007/s00497-011-0162-3

Bencivenga, Stefano, Simonini, S., Benková, E., & Colombo, L. (2012). The Transcription Factors BEL1 and SPL Are Required for Cytokinin and Auxin Signaling During Ovule Development in Arabidopsis. *The Plant Cell*, *24*(7), 2886–2897. https://doi.org/10.1105/tpc.112.100164

Benkova, E., Michniewicz, M., Sauer, M., Teichmann, T., Seifertova, D., Jurgens, G., & Friml, J. (2003). Local, efflux-dependent auxin gradients as a common module for plant organ formation. *Cell*, *115*(5), 591–602. https://www.ncbi.nlm.nih.gov/pubmed/14651850

Benková, E., Michniewicz, M., Sauer, M., Teichmann, T., Seifertová, D., Jürgens, G., & Friml, J. (2003). Local, efflux-dependent auxin gradients as a common module for plant organ formation. *Cell*, *115*(5), 591–602. https://doi.org/10.1016/s0092-8674(03)00924-3

Bink, K., Walch, A., Feuchtinger, A., Eisenmann, H., Hutzler, P., Höfler, H., & Werner, M. (2001). {TO}-{PRO}-3 is an optimal fluorescent dye for nuclear conterstaining in dual-colour {FISH} on paraffin sections. *Histochemistry and Cell Biology*, *115*(4), 292–299.

Boudon, F., Chopard, J., Ali, O., Gilles, B., Hamant, O., Boudaoud, A., Traas, J., & Godin, C. (2015). A Computational Framework for 3D Mechanical Modeling of Plant Morphogenesis with Cellular Resolution. *PLoS Computational Biology*, *11*(1). https://doi.org/10.1371/journal.pcbi.1003950

Bowman, J. L. (2000). The YABBY gene family and abaxial cell fate. *Current Opinion in Plant Biology*, *3*(1), 17–22. https://doi.org/10.1016/S1369-5266(99)00035-7

Bowman, J. L., Baum, S. F., Eshed, Y., Putterill, J., & Alvarez, J. (1999). *Molecular Genetics of Gynoecium Development in Arabidopsis* (R. A. Pedersen & G. P. Schatten (eds.); Vol. 45, pp. 155–205). Academic Press. https://doi.org/https://doi.org/10.1016/S0070-2153(08)60316-6

Bowman, J. L., Eshed, Y., & Baum, S. F. (2002). Establishment of polarity in angiosperm lateral organs. *Trends in Genetics*, *18*(3), 134–141. https://doi.org/10.1016/S0168-9525(01)02601-4

Brambilla, V., Battaglia, R., Colombo, M., Masiero, S., Bencivenga, S., Kater, M. M., & Colombo, L. (2007). Genetic and Molecular Interactions between BELL1 and MADS Box Factors Support Ovule Development in Arabidopsis. *The Plant Cell*, *19*(8), 2544–2556. https://doi.org/10.1105/tpc.107.051797

Braybrook, S. A., & Jönsson, H. (2016). Shifting foundations: The mechanical cell wall and development. *Current Opinion in Plant Biology*, *29*, 115–120. https://doi.org/10.1016/j.pbi.2015.12.009

Brodland, G. W. (2015). How computational models can help unlock biological systems. In *Seminars in Cell and Developmental Biology* (Vols. 47–48, pp. 62–73). Elsevier Ltd. https://doi.org/10.1016/j.semcdb.2015.07.001

Caggiano, M. P., Yu, X., Bhatia, N., Larsson, A., Ram, H., Ohno, C. K., Sappl, P., Meyerowitz, E. M., Jonsson, H., & Heisler, M. G. (2017). Cell type boundaries organize plant development. *Elife*, *6*. https://doi.org/10.7554/eLife.27421

Cao, M., Chen, R., Li, P., Yu, Y., Zheng, R., Ge, D., Zheng, W., Wang, X., Gu, Y., Gelová, Z.,

Friml, J., Zhang, H., Liu, R., He, J., & Xu, T. (2019). {TMK1}-mediated auxin signalling regulates differential growth of the apical hook. *Nature*, *568*(7751), 240–243. https://doi.org/10.1038/s41586-019-1069-7

Cardarelli, M., & Cecchetti, V. (2014). Auxin polar transport in stamen formation and development: How many actors? *Frontiers in Plant Science*, *5*(JUL), 1–13. https://doi.org/10.3389/fpls.2014.00333

Ceccato, L., Masiero, S., Sinha Roy, D., Bencivenga, S., Roig-Villanova, I., Ditengou, F. A., Palme, K., Simon, R., & Colombo, L. (2013). Maternal control of PIN1 is required for female gametophyte development in Arabidopsis. *PLoS One*, *8*(6), e66148. https://doi.org/10.1371/journal.pone.0066148

Chaudhary, A., Gao, J., & Schneitz, K. (2018). The genetic control of ovule development. In *Reference module in life sciences*. Elsevier. https://doi.org/10.1016/B978-0-12-809633-8.20737-1

Chen, G.-H., Sun, J.-Y., Liu, M., Liu, J., & Yang, W.-C. (2014). SPOROCYTELESS Is a Novel Embryophyte-Specific Transcription Repressor that Interacts with TPL and TCP Proteins in Arabidopsis. *Journal of Genetics and Genomics*, *41*(12), 617–625. https://doi.org/https://doi.org/10.1016/j.jgg.2014.08.009

Chen, X., & Brodland, G. W. (2008). Multi-scale finite element modeling allows the mechanics of amphibian neurulation to be elucidated. *Physical Biology*, *5*(1), 15003. https://doi.org/10.1088/1478-3975/5/1/015003

Cheng, C.-Y., Mathews, D. E., Schaller, G. E., & Kieber, J. J. (2013). Cytokinin-dependent specification of the functional megaspore in the Arabidopsis female gametophyte. *The Plant Journal: For Cell and Molecular Biology*, *73*(6), 929–940. https://doi.org/10.1111/tpj.12084

Cheng, Y., Dai, X., & Zhao, Y. (2006). Auxin biosynthesis by the YUCCA flavin monooxygenases controls the formation of floral organs and vascular tissues in Arabidopsis. *Genes and Development*, *20*(13), 1790–1799. https://doi.org/10.1101/gad.1415106

Chevalier, D., Batoux, M., Fulton, L., Pfister, K., Yadav, R. K., Schellenberg, M., & Schneitz, K. (2005). {STRUBBELIG} defines a receptor kinase-mediated signaling pathway regulating organ development in Arabidopsis. *Proceedings of the National Academy of Sciences of the United States of America*, *102*(25), 9074–9079. https://doi.org/10.1073/pnas.0503526102

Chickarmane, V., Roeder, A. H., Tarr, P. T., Cunha, A., Tobin, C., & Meyerowitz, E. M. (2010). Computational morphodynamics: a modeling framework to understand plant growth. *Annu Rev Plant Biol*, *61*, 65–87. https://doi.org/10.1146/annurev-arplant-042809-112213

Christensen, C. A., King, E. J., Jordan, J. R., & Drews, G. N. (1997). Megagametogenesis in Arabidopsis wild type and the Gf mutant. *Sexual Plant Reproduction*, *10*(1), 49–64. https://doi.org/10.1007/s004970050067

Clough, S. J., & Bent, A. F. (1998). Floral dip: a simplified method for Agrobacterium-

mediated transformation of Arabidopsis thaliana. *The Plant Journal: For Cell and Molecular Biology*, *16*(6), 735–743. https://doi.org/10.1046/j.1365-313x.1998.00343.x

Coen, E., Kennaway, R., & Whitewoods, C. (2017). On genes and form. *Development (Cambridge)*, *144*(23), 4203–4213. https://doi.org/10.1242/dev.151910

Coen, E., & Rebocho, A. B. (2016). Resolving conflicts: modeling genetic control of plant morphogenesis. *Developmental Cell*, *38*(6), 579–583. https://doi.org/10.1016/j.devcel.2016.09.006

Coen, E. S., & Meyerowitz, E. M. (1991). The war of the whorls: genetic interactions controlling flower development. *Nature*, *353*(6339), 31–37. https://doi.org/10.1038/353031a0

Cucinotta, M., Colombo, L., & Roig-Villanova, I. (2014). Ovule development, a new model for lateral organ formation. *Frontiers in Plant Science*, *5*, 117. https://doi.org/10.3389/fpls.2014.00117

Cucinotta, M., Di Marzo, M., Guazzotti, A., de Folter, S., Kater, M. M., & Colombo, L. (2020). Gynoecium size and ovule number are interconnected traits that impact seed yield. *Journal of Experimental Botany*, *71*(9), 2479–2489. https://doi.org/10.1093/jxb/eraa050

Cucinotta, M., Manrique, S., Cuesta, C., Benkova, E., Novak, O., & Colombo, L. (2018). CUP-SHAPED COTYLEDON1 (CUC1) and CUC2 regulate cytokinin homeostasis to determine ovule number in Arabidopsis. *Journal of Experimental Botany*, *69*(21), 5169–5176. https://doi.org/10.1093/jxb/ery281

Dahmann, C., Oates, A. C., & Brand, M. (2011). Boundary formation and maintenance in tissue development. *Nature Reviews Genetics*, *12*(1), 43–55. https://doi.org/10.1038/nrg2902

de Reuille, P. B., Robinson, S., & Smith, R. S. (2014). Quantifying cell shape and gene expression in the shoot apical meristem using MorphoGraphX. *Methods Mol Biol*, *1080*, 121–134. https://doi.org/10.1007/978-1-62703-643-6_10

Debeaujon, I., Nesi, N., Perez, P., Devic, M., Grandjean, O., Caboche, M., & Lepiniec, L. (2003). Proanthocyanidin-accumulating cells in Arabidopsis testa: regulation of differentiation and role in seed development. *The Plant Cell*, *15*(11), 2514–2531. https://doi.org/10.1105/tpc.014043

Doyle, J. A., & Endress, P. K. (2000). Morphological phylogenetic analysis of basal angiosperms: Comparison and combination with molecular data. *International Journal of Plant Sciences*, *161*(6 SUPPL.). https://doi.org/10.1086/317578

Drews, G. N., & Koltunow, A. M. . (2011). The Female Gametophyte. *The Arabidopsis Book*, *9*, e0155. https://doi.org/10.1199/tab.0155

Du, F., Guan, C., & Jiao, Y. (2018). Molecular Mechanisms of Leaf Morphogenesis. *Molecular Plant*, *11*(9), 1117–1134. https://doi.org/10.1016/j.molp.2018.06.006

Dupuy, L., Mackenzie, J., & Haseloff, J. (2010). Coordination of plant cell division and expansion in a simple morphogenetic system. *Proceedings of the National Academy of Sciences of the United States of America*, *107*(6), 2711–2716.

https://doi.org/10.1073/pnas.0906322107

Durán-Figueroa, N., & Vielle-Calzada, J.-P. (2010). ARGONAUTE9-dependent silencing of transposable elements in pericentromeric regions of Arabidopsis. *Plant Signaling & Behavior*, *5*(11), 1476–1479. https://doi.org/10.1038/nature08828

Duran-Nebreda, S., & Bassel, G. W. (2017). Bridging Scales in Plant Biology Using Network Science. *Trends in Plant Science*, *22*(12), 1001–1003. https://doi.org/10.1016/j.tplants.2017.09.017

Elliott, R. C., Betzner, A. S., Huttner, E., Oakes, M. P., Tucker, W. Q., Gerentes, D., Perez, P., & Smyth, D. R. (1996). AINTEGUMENTA, an APETALA2-like gene of Arabidopsis with pleiotropic roles in ovule development and floral organ growth. *The Plant Cell*, *8*(2), 155–168. https://doi.org/10.1105/tpc.8.2.155

Emery, J. F., Floyd, S. K., Alvarez, J., Eshed, Y., Hawker, N. P., Izhaki, A., Baum, S. F., & Bowman, J. L. (2003). Radial Patterning of Arabidopsis Shoots by Class III HD-ZIP and KANADI Genes. *Current Biology*, *13*(20), 1768–1774. https://doi.org/10.1016/j.cub.2003.09.035

Endress, P. K., & Igersheim, A. (2000). Gynoecium structure and evolution in basal angiosperms. *International Journal of Plant Sciences*, *161*(6 SUPPL.). https://doi.org/10.1086/317572

Endress, P K. (2011). Angiosperm ovules: diversity, development, evolution. *Ann Bot*, *107*(9), 1465–1489. https://doi.org/10.1093/aob/mcr120

Endress, Peter K. (2011). Evolutionary diversification of the flowers in angiosperms. *American Journal of Botany*, *98*(3), 370–396. https://doi.org/10.3732/ajb.1000299

Eng, R. C., & Sampathkumar, A. (2018). Getting into shape: the mechanics behind plant morphogenesis. In *Current Opinion in Plant Biology* (Vol. 46, pp. 25–31). https://doi.org/10.1016/j.pbi.2018.07.002

Enugutti, B., Kirchhelle, C., Oelschner, M., Torres Ruiz, R. A., Schliebner, I., Leister, D., & Schneitz, K. (2012). Regulation of planar growth by the Arabidopsis {AGC} protein kinase {UNICORN}. *Proceedings of the National Academy of Sciences of the United States of America*, *109*(37), 15060–15065. https://doi.org/10.1073/pnas.1205089109

Enugutti, B., & Schneitz, K. (2013). Genetic analysis of ectopic growth suppression during planar growth of integuments mediated by the Arabidopsis AGC protein kinase UNICORN. *BMC Plant Biology*, *13*(1). https://doi.org/10.1186/1471-2229-13-2

Eshed, Y, Izhaki, A., Baum, S. F., Floyd, S. K., & Bowman, J. L. (2004). Asymmetric leaf development and blade expansion in Arabidopsis are mediated by KANADI and YABBY activities. *Development*, *131*(12), 2997–3006. https://doi.org/10.1242/dev.01186

Eshed, Yuval, Baum, S. F., Perea, J. V, & Bowman, J. L. (2001). Establishment of polarity in lateral organs of plants. *Current Biology*, *11*(16), 1251–1260. https://doi.org/https://doi.org/10.1016/S0960-9822(01)00392-X

Fernandez, R., Das, P., Mirabet, V., Moscardi, E., Traas, J., Verdeil, J. L., Malandain, G., &

Godin, C. (2010). Imaging plant growth in 4D: robust tissue reconstruction and lineaging at cell resolution. *Nat Methods*, *7*(7), 547–553. https://doi.org/10.1038/nmeth.1472

Florijn, R. J., Slats, J., Tanke, H. J., & Raap, A. K. (1995). Analysis of antifading reagents for fluorescence microscopy. *Cytometry*, *19*(2), 177–182. https://doi.org/10.1002/cyto.990190213

Fox, S., Southam, P., Pantin, F., Kennaway, R., Robinson, S., Castorina, G., Sanchez-Corrales, Y. E., Sablowski, R., Chan, J., Grieneisen, V., Maree, A. F. M., Bangham, J. A., & Coen, E. (2018). Spatiotemporal coordination of cell division and growth during organ morphogenesis. *PLoS Biol*, *16*(11), e2005952. https://doi.org/10.1371/journal.pbio.2005952

Fulton, L., Batoux, M., Vaddepalli, P., Yadav, R. K., Busch, W., Andersen, S. U., Jeong, S., Lohmann, J. U., & Schneitz, K. (2009). {DETORQUEO}, {QUIRKY}, and {ZERZAUST} represent novel components involved in organ development mediated by the receptor-like kinase {STRUBBELIG} in Arabidopsis thaliana. *{PLoS} Genetics*, *5*(1), e1000355. https://doi.org/10.1371/journal.pgen.1000355

Gaillochet, C., Daum, G., & Lohmann, J. U. (2015). O cell, where art thou? The mechanisms of shoot meristem patterning. *Current Opinion in Plant Biology*, *23*, 91–97. https://doi.org/10.1016/j.pbi.2014.11.002

Gaiser, J. C., Robinson-Beers, K., & Gasser, C. S. (1995a). The Arabidopsis superman gene mediates asymmetric growth of the outer integument of ovules. *Plant Cell*, *7*(3), 333–345. https://doi.org/10.1105/tpc.7.3.333

Gaiser, J. C., Robinson-Beers, K., & Gasser, C. S. (1995b). The Arabidopsis SUPERMAN Gene Mediates Asymmetric Growth of the Outer Integument of Ovules. *Plant Cell*, *7*(3), 333–345. https://doi.org/10.1105/tpc.7.3.333

Galbiati, F., Sinha Roy, D., Simonini, S., Cucinotta, M., Ceccato, L., Cuesta, C., Simaskova, M., Benkova, E., Kamiuchi, Y., Aida, M., Weijers, D., Simon, R., Masiero, S., & Colombo, L. (2013). An integrative model of the control of ovule primordia formation. *Plant Journal*, *76*(3), 446–455. https://doi.org/10.1111/tpj.12309

Gasser, C. S., Broadhvest, J., & Hauser, B. A. (1998). Genetic Analysis of Ovule Development. *Annual Review of Plant Physiology and Plant Molecular Biology*, *49*(1), 1–24. https://doi.org/10.1146/annurev.arplant.49.1.1

Gasser, Charles S, & Skinner, D. J. (2019). Development and evolution of the unique ovules of flowering plants. *Current Topics in Developmental Biology*, *131*, 373–399. https://doi.org/10.1016/bs.ctdb.2018.10.007

Geitmann, A., & Ortega, J. K. (2009). Mechanics and modeling of plant cell growth. *Trends Plant Sci*, *14*(9), 467–478. https://doi.org/10.1016/j.tplants.2009.07.006

Gifford, M. L., Dean, S., & Ingram, G. C. (2003). The Arabidopsis ACR4 gene plays a role in cell layer organisation during ovule integument and sepal margin development. *Development*, *130*(18), 4249–4258. https://doi.org/10.1242/dev.00634

Gifford, M. L., Robertson, F. C., Soares, D. C., & Ingram, G. C. (2005). Arabidopsis Crinkly4

function, internalization, and turnover are dependent on the extracellular crinkly repeat domain. *Plant Cell*, *17*(4), 1154–1166. https://doi.org/10.1105/tpc.104.029975

Gómez, J. F., Talle, B., & Wilson, Z. A. (2015). Anther and pollen development: A conserved developmental pathway. *Journal of Integrative Plant Biology*, *57*(11), 876–891. https://doi.org/10.1111/jipb.12425

Gomez, M D, Barro-Trastoy, D., Escoms, E., Saura-Sanchez, M., Sanchez, I., Briones-Moreno, A., Vera-Sirera, F., Carrera, E., Ripoll, J. J., Yanofsky, M. F., Lopez-Diaz, I., Alonso, J. M., & Perez-Amador, M. A. (2018). Gibberellins negatively modulate ovule number in plants. *Development*, *145*(13). https://doi.org/10.1242/dev.163865

Gomez, M D, Ventimilla, D., Sacristan, R., & Perez-Amador, M. A. (2016). Gibberellins Regulate Ovule Integument Development by Interfering with the Transcription Factor ATS. *Plant Physiol*, *172*(4), 2403–2415. https://doi.org/10.1104/pp.16.01231

Gomez, Maria Dolores, Barro-Trastoy, D., Fuster-Almunia, C., Tornero, P., Alonso, J. M., & Perez-Amador, M. A. (2020). Gibberellin-mediated RGA-LIKE1 degradation regulates embryo sac development in Arabidopsis. *Journal of Experimental Botany*, *71*(22), 7059–7072. https://doi.org/10.1093/jxb/eraa395

Gonçalves, B., Hasson, A., Belcram, K., Cortizo, M., Morin, H., Nikovics, K., Vialette-Guiraud, A., Takeda, S., Aida, M., Laufs, P., & Arnaud, N. (2015). A conserved role for CUP-SHAPED COTYLEDON genes during ovule development. *Plant Journal*, *83*(4), 732–742. https://doi.org/10.1111/tpj.12923

Green, A. A., Kennaway, J. R., Hanna, A. I., Bangham, J. A., & Coen, E. (2010). Genetic control of organ shape and tissue polarity. *{PLoS} Biology*, *8*(11), e1000537. https://doi.org/10.1371/journal.pbio.1000537

Groß-Hardt, R., Kägi, C., Baumann, N., Moore, J. M., Baskar, R., Gagliano, W. B., Jürgens, G., & Grossniklaus, U. (2007). LACHESIS restricts gametic cell fate in the female gametophyte of Arabidopsis. *PLoS Biology*, *5*(3), 0494–0500. https://doi.org/10.1371/journal.pbio.0050047

Groß-Hardt, R., Lenhard, M., & Laux, T. (2002). WUSCHEL signaling functions in interregional communication during Arabidopsis ovule development. *Genes and Development*, *16*(9), 1129–1138. https://doi.org/10.1101/gad.225202

Gross-Hardt, R, Lenhard, M., & Laux, T. (2002). WUSCHEL signaling functions in interregional communication during Arabidopsis ovule development. *Genes Dev*, *16*(9), 1129–1138. https://doi.org/10.1101/gad.225202

Gross-Hardt, Rita, Lenhard, M., & Laux, T. (2002). {WUSCHEL} signaling functions in interregional communication during Arabidopsis ovule development. *Genes \& Development*, *16*(9), 1129–1138. https://doi.org/10.1101/gad.225202

Grossniklaus, U., & Schneitz, K. (1998). The molecular and genetic basis of ovule and megagametophyte development. *Seminars in Cell and Developmental Biology*, *9*, 227–238.

Hamant, O., Heisler, M. G., Jonsson, H., Krupinski, P., Uyttewaal, M., Bokov, P., Corson, F.,

Sahlin, P., Boudaoud, A., Meyerowitz, E. M., Couder, Y., & Traas, J. (2008). Developmental patterning by mechanical signals in Arabidopsis. *Science*, *322*(5908), 1650–1655. https://doi.org/10.1126/science.1165594

Hashimoto, K., Miyashima, S., Sato-Nara, K., Yamada, T., & Nakajima, K. (2018). Functionally Diversified Members of the MIR165/6 Gene Family Regulate Ovule Morphogenesis in Arabidopsis thaliana. *Plant and Cell Physiology*, *59*(5), 1017–1026. https://doi.org/10.1093/pcp/pcy042

Hasson, A., Plessis, A., Blein, T., Adroher, B., Grigg, S., Tsiantis, M., Boudaoud, A., Damerval, C., & Laufs, P. (2011). Evolution and Diverse Roles of the CUP-SHAPED COTYLEDON Genes in Arabidopsis Leaf Development. *The Plant Cell*, *23*(1), 54–68. https://doi.org/10.1105/tpc.110.081448

Hater, F., Nakel, T., & Groß-Hardt, R. (2020). Reproductive Multitasking: The Female Gametophyte. *Annual Review of Plant Biology*, *71*, 517–546. https://doi.org/10.1146/annurev-arplant-081519-035943

Hejátko, J., Pernisová, M., Eneva, T., Palme, K., & Brzobohatý, B. (2003). The putative sensor histidine kinase CKI1 is involved in female gametophyte development in Arabidopsis. *Molecular Genetics and Genomics : MGG*, *269*(4), 443–453. https://doi.org/10.1007/s00438-003-0858-7

Hernández-Lagana, E., Rodríguez-Leal, D., Lúa, J., & Vielle-Calzada, J.-P. (2016). A Multigenic Network of ARGONAUTE4 Clade Members Controls Early Megaspore Formation in Arabidopsis. *Genetics*, *204*(3), 1045–1056. https://doi.org/10.1534/genetics.116.188151

Herr, J. M. (1995). The Origin of the Ovule. *American Journal of Botany*, *82*(4), 547–564.

Hervieux, N., Dumond, M., Sapala, A., Routier-Kierzkowska, A.-L., Kierzkowski, D., Roeder, A. H. K., Smith, R. S., Boudaoud, A., & Hamant, O. (2016). A mechanical feedback restricts sepal growth and shape in Arabidopsis. *Current Biology*, *26*, 1019–1028. https://doi.org/10.1016/j.cub.2016.03.004

Hiratsu, K., Ohta, M., Matsui, K., & Ohme-Takagi, M. (2002). The SUPERMAN protein is an active repressor whose carboxy-terminal repression domain is required for the development of normal flowers. *FEBS Letters*, *514*(2–3), 351–354. https://doi.org/10.1016/S0014-5793(02)02435-3

Hong, L., Dumond, M., Zhu, M., Tsugawa, S., Li, C. B., Boudaoud, A., Hamant, O., & Roeder, A. H. K. (2018a). Heterogeneity and Robustness in Plant Morphogenesis: From Cells to Organs. *Annu Rev Plant Biol*, *69*, 469–495. https://doi.org/10.1146/annurev-arplant-042817-040517

Hong, L., Dumond, M., Zhu, M., Tsugawa, S., Li, C. B., Boudaoud, A., Hamant, O., & Roeder, A. H. K. (2018b). Heterogeneity and Robustness in Plant Morphogenesis: From Cells to Organs. *Annu Rev Plant Biol*, *69*, 469–495. https://doi.org/10.1146/annurev-arplant-042817-040517

Huang, C., Wang, Z., Quinn, D., Suresh, S., & Hsia, K. J. (2018). Differential growth and shape formation in plant organs. *Proc Natl Acad Sci U S A*.

https://doi.org/10.1073/pnas.1811296115

Huang, H. Y., Jiang, W. B., Hu, Y. W., Wu, P., Zhu, J. Y., Liang, W. Q., Wang, Z. Y., & Lin, W. H. (2013). BR signal influences arabidopsis ovule and seed number through regulating related genes expression by BZR1. *Molecular Plant*, *6*(2), 456–469. https://doi.org/10.1093/mp/sss070

Ishida, T., Aida, M., Takada, S., & Tasaka, M. (2000). Involvement of CUP-SHAPED COTYLEDON genes in gynoecium and ovule development in Arabidopsis thaliana. *Plant & Cell Physiology*, *41*(1), 60–67. https://doi.org/10.1093/pcp/41.1.60

Jackson, M. D. B., Duran-Nebreda, S., Kierzkowski, D., Strauss, S., Xu, H., Landrein, B., Hamant, O., Smith, R. S., Johnston, I. G., & Bassel, G. W. (2019a). Global Topological Order Emerges through Local Mechanical Control of Cell Divisions in the Arabidopsis Shoot Apical Meristem. *Cell Systems*, *8*(1), 53-65.e3. https://doi.org/10.1016/j.cels.2018.12.009

Jackson, M. D. B., Duran-Nebreda, S., Kierzkowski, D., Strauss, S., Xu, H., Landrein, B., Hamant, O., Smith, R. S., Johnston, I. G., & Bassel, G. W. (2019b). Global Topological Order Emerges through Local Mechanical Control of Cell Divisions in the Arabidopsis Shoot Apical Meristem. *Cell Systems*, *8*(1), 53-65.e3. https://doi.org/10.1016/j.cels.2018.12.009

Jackson, M. D. B., Xu, H., Duran-Nebreda, S., Stamm, P., & Bassel, G. W. (2017). Topological analysis of multicellular complexity in the plant hypocotyl. *ELife*, *6*, 1–24. https://doi.org/10.7554/eLife.26023

Jenik, P. D., & Irish, V. F. (2000). Regulation of cell proliferation patterns by homeotic genes during Arabidopsis floral development. *Development*, *127*(6), 1267–1276. https://www.ncbi.nlm.nih.gov/pubmed/10683179

Jia, D., Chen, L. G., Yin, G., Yang, X., Gao, Z., Guo, Y., Sun, Y., & Tang, W. (2020). Brassinosteroids regulate outer ovule integument growth in part via the control of INNER NO OUTER by BRASSINOZOLE-RESISTANT family transcription factors. *Journal of Integrative Plant Biology*, *62*(8), 1093–1111. https://doi.org/10.1111/jipb.12915

Jönsson, H., & Krupinski, P. (2010). Modeling plant growth and pattern formation. *Current Opinion in Plant Biology*, *13*(1), 5–11. https://doi.org/10.1016/j.pbi.2009.10.002

Jonsson, K., Lathe, R. S., Kierzkowski, D., Routier-Kierzkowska, A. L., Hamant, O., & Bhalerao, R. P. (2021). Mechanochemical feedback mediates tissue bending required for seedling emergence. *Current Biology*, 1–11. https://doi.org/10.1016/j.cub.2020.12.016

Kelley, D R, Arreola, A., Gallagher, T. L., & Gasser, C. S. (2012). ETTIN (ARF3) physically interacts with KANADI proteins to form a functional complex essential for integument development and polarity determination in Arabidopsis. *Development*, *139*(6), 1105–1109. https://doi.org/10.1242/dev.067918

Kelley, D R, & Gasser, C. S. (2009). Ovule development: genetic trends and evolutionary considerations. *Sex Plant Reprod*, *22*(4), 229–234. https://doi.org/10.1007/s00497-009-0107-2

Kelley, Dior R., Skinner, D. J., & Gasser, C. S. (2009). Roles of polarity determinants in ovule development. *Plant Journal*, *57*(6), 1054–1064. https://doi.org/10.1111/j.1365-313X.2008.03752.x

Kennaway, R., Coen, E., Green, A., & Bangham, A. (2011). Generation of diverse biological forms through combinatorial interactions between tissue polarity and growth. *PLoS Comput Biol*, *7*(6), e1002071. https://doi.org/10.1371/journal.pcbi.1002071

Kerstetter, R. A., Bollman, K., Taylor, R. A., Bomblies, K., & Poethig, R. S. (2001). KANADI regulates organ polarity in Arabidopsis. *Nature*, *411*(6838), 706–709. https://doi.org/10.1038/35079629

Kierzkowski, D, Runions, A., Vuolo, F., Strauss, S., Lymbouridou, R., Routier-Kierzkowska, A. L., Wilson-Sanchez, D., Jenke, H., Galinha, C., Mosca, G., Zhang, Z., Canales, C., Dello Ioio, R., Huijser, P., Smith, R. S., & Tsiantis, M. (2019). A Growth-Based Framework for Leaf Shape Development and Diversity. *Cell*, *177*(6), 1405-1418 e17. https://doi.org/10.1016/j.cell.2019.05.011

Kierzkowski, Daniel, Runions, A., Vuolo, F., Strauss, S., Lymbouridou, R., Routier-Kierzkowska, A.-L., Wilson-Sánchez, D., Jenke, H., Galinha, C., Mosca, G., Zhang, Z., Canales, C., Dello Ioio, R., Huijser, P., Smith, R. S., & Tsiantis, M. (2019). A Growth-Based Framework for Leaf Shape Development and Diversity. *Cell*, *177*(6), 1405-1418.e17. https://doi.org/10.1016/j.cell.2019.05.011

Kirchhelle, C., Garcia-Gonzalez, D., Irani, N. G., Jérusalem, A., & Moore, I. (2019). Two mechanisms regulate directional cell growth in Arabidopsis lateral roots. *ELife*, *8*, 1–26. https://doi.org/10.7554/eLife.47988

Klucher, K. M., Chow, H., Reiser, L., & Fischer, R. L. (1996). The AINTEGUMENTA gene of arabidopsis required for ovule and female gametophyte development is related to the floral homeotic gene APETALA2. *Plant Cell*, *8*(2), 137–153. https://doi.org/10.1105/tpc.8.2.137

Koncz, C., & Schell, J. (1986). The promoter of TL-DNA gene 5 controls the tissue-specific expression of chimaeric genes carried by a novel type of Agrobacterium binary vector. *Molecular and General Genetics MGG*, *204*(3), 383–396. https://doi.org/10.1007/BF00331014

Kurihara, D., Mizuta, Y., Sato, Y., & Higashiyama, T. (2015). {ClearSee}: a rapid optical clearing reagent for whole-plant fluorescence imaging. *Development*, *142*(23), 4168–4179. https://doi.org/10.1242/dev.127613

Lampropoulos, A., Sutikovic, Z., Wenzl, C., Maegele, I., Lohmann, J. U., & Forner, J. (2013). {GreenGate}---a novel, versatile, and efficient cloning system for plant transgenesis. *Plos One*, *8*(12), e83043. https://doi.org/10.1371/journal.pone.0083043

Larsson, E., Vivian-Smith, A., Offringa, R., & Sundberg, E. (2017). Auxin Homeostasis in Arabidopsis Ovules Is Anther-Dependent at Maturation and Changes Dynamically upon Fertilization. *Front Plant Sci*, *8*, 1735. https://doi.org/10.3389/fpls.2017.01735

Lee, K. J. I., Bushell, C., Koide, Y., Fozard, J. A., Piao, C., Yu, M., Newman, J., Whitewoods, C., Avondo, J., Kennaway, R., Marée, A. F. M., Cui, M., & Coen, E. (2019). Shaping of

a three-dimensional carnivorous trap through modulation of a planar growth mechanism. *{PLoS} Biology*, *17*(10), e3000427. https://doi.org/10.1371/journal.pbio.3000427

Leon-Kloosterziel, K. M., Keijzer, C. J., & Koornneef, M. (1994). A Seed Shape Mutant of Arabidopsis That Is Affected in Integument Development. *Plant Cell*, *6*(3), 385–392. https://doi.org/10.1105/tpc.6.3.385

Liang, H., & Mahadevan, L. (2011). Growth, geometry, and mechanics of a blooming lily. *Proceedings of the National Academy of Sciences of the United States of America*, *108*(14), 5516–5521. https://doi.org/10.1073/pnas.1007808108

Lieber, D., Lora, J., Schrempp, S., Lenhard, M., & Laux, T. (2011). Arabidopsis {WIH1} and {WIH2} genes act in the transition from somatic to reproductive cell fate. *Current Biology*, *21*(12), 1009–1017. https://doi.org/10.1016/j.cub.2011.05.015

Lituiev, D. S., Krohn, N. G., Müller, B., Jackson, D., Hellriegel, B., Dresselhaus, T., & Grossniklaus, U. (2013). Theoretical and experimental evidence indicates that there is no detectable auxin gradient in the angiosperm female gametophyte. *Development (Cambridge)*, *140*(22), 4544–4553. https://doi.org/10.1242/dev.098301

Lockhart, J. A. (1965). An analysis of irreversible plant cell elongation. *Journal of Theoretical Biology*, *8*(2), 264–275. https://doi.org/https://doi.org/10.1016/0022-5193(65)90077-9

Lora, J., Herrero, M., Tucker, M. R., & Hormaza, J. I. (2017). The transition from somatic to germline identity shows conserved and specialized features during angiosperm evolution. *The New Phytologist*, *216*(2), 495–509. https://doi.org/10.1111/nph.14330

Lora, J., Yang, X., & Tucker, M. R. (2019). Establishing a framework for female germline initiation in the plant ovule. *Journal of Experimental Botany*, *70*(11), 2937–2949. https://doi.org/10.1093/jxb/erz212

Louveaux, M., Julien, J. D., Mirabet, V., Boudaoud, A., & Hamant, O. (2016). Cell division plane orientation based on tensile stress in Arabidopsis thaliana. *Proc Natl Acad Sci U S A*, *113*(30), E4294-303. https://doi.org/10.1073/pnas.1600677113

Martinez, G., & Köhler, C. (2017). Role of small RNAs in epigenetic reprogramming during plant sexual reproduction. *Current Opinion in Plant Biology*, *36*, 22–28. https://doi.org/10.1016/j.pbi.2016.12.006

Martínez, G., & Slotkin, R. K. (2012). Developmental relaxation of transposable element silencing in plants: functional or byproduct? *Current Opinion in Plant Biology*, *15*(5), 496–502. https://doi.org/https://doi.org/10.1016/j.pbi.2012.09.001

McAbee, J. M., Hill, T. A., Skinner, D. J., Izhaki, A., Hauser, B. A., Meister, R. J., Venugopala Reddy, G., Meyerowitz, E. M., Bowman, J. L., & Gasser, C. S. (2006). {ABERRANT} {TESTA} {SHAPE} encodes a {KANADI} family member, linking polarity determination to separation and growth of Arabidopsis ovule integuments. *The Plant Journal: For Cell and Molecular Biology*, *46*(3), 522–531. https://doi.org/10.1111/j.1365-{313X}.2006.02717.x

McConnell, J. R., Emery, J., Eshed, Y., Bao, N., Bowman, J., & Barton, M. K. (2001). Role of PHABULOSA and PHAVOLUTA in determining radial patterning in shoots. *Nature*,

411(6838), 709–713. https://doi.org/10.1038/35079635

Meister, R. J., Kotow, L. M., & Gasser, C. S. (2002). {SUPERMAN} attenuates positive {INNER} {NO} {OUTER} autoregulation to maintain polar development of Arabidopsis ovule outer integuments. *Development*, *129*(18), 4281–4289. https://www.ncbi.nlm.nih.gov/pubmed/12183380

Mendes, M. A., Petrella, R., Cucinotta, M., Vignati, E., Gatti, S., Pinto, S. C., Bird, D. C., Gregis, V., Dickinson, H., Tucker, M. R., & Colombo, L. (2020). The RNA-dependent DNA methylation pathway is required to restrict SPOROCYTELESS/NOZZLE expression to specify a single female germ cell precursor in Arabidopsis. *Development (Cambridge, England)*, *147*(23). https://doi.org/10.1242/dev.194274

Moll, C., Von Lyncker, L., Zimmermann, S., Kägi, C., Baumann, N., Twell, D., Grossniklaus, U., & Groß-Hardt, R. (2008). CLO/GFA1 and ATO are novel regulators of gametic cell fate in plants. *Plant Journal*, *56*(6), 913–921. https://doi.org/10.1111/j.1365-313X.2008.03650.x

Montenegro-Johnson, T. D., Stamm, P., Strauss, S., Topham, A. T., Tsagris, M., Wood, A. T. A., Smith, R. S., & Bassel, G. W. (2015). Digital single-cell analysis of plant organ development using 3dcellatlas^{open}. *Plant Cell*, *27*(4), 1018–1033. https://doi.org/10.1105/tpc.15.00175

Montenegro-Johnson, T., Strauss, S., Jackson, M. D. B., Walker, L., Smith, R. S., & Bassel, G. W. (2019a). 3DCellAtlas Meristem: A tool for the global cellular annotation of shoot apical meristems. *Plant Methods*, *15*(1), 1–9. https://doi.org/10.1186/s13007-019-0413-0

Montenegro-Johnson, T., Strauss, S., Jackson, M. D. B., Walker, L., Smith, R. S., & Bassel, G. W. (2019b). {3DCellAtlas} Meristem: a tool for the global cellular annotation of shoot apical meristems. *Plant Methods*, *15*, 33. https://doi.org/10.1186/s13007-019-0413-0

Murashige, T., & Skoog, F. (1962). A Revised Medium for Rapid Growth and Bio Assays with Tobacco Tissue Cultures. *Physiologia Plantarum*, *15*(3), 473–497. https://doi.org/https://doi.org/10.1111/j.1399-3054.1962.tb08052.x

Musielak, T. J., Schenkel, L., Kolb, M., Henschen, A., & Bayer, M. (2015). A simple and versatile cell wall staining protocol to study plant reproduction. *Plant Reproduction*, *28*(3–4), 161–169. https://doi.org/10.1007/s00497-015-0267-1

Nakajima, K. (2018). Be my baby: patterning toward plant germ cells. *Current Opinion in Plant Biology*, *41*, 110–115. https://doi.org/10.1016/j.pbi.2017.11.002

Nakayama, N., Smith, R. S., Mandel, T., Robinson, S., Kimura, S., Boudaoud, A., & Kuhlemeier, C. (2012). Mechanical regulation of auxin-mediated growth. *Curr Biol*, *22*(16), 1468–1476. https://doi.org/10.1016/j.cub.2012.06.050

Nonomura, K.-I. (2018). Small RNA pathways responsible for non-cell-autonomous regulation of plant reproduction. *Plant Reproduction*, *31*(1), 21–29. https://doi.org/10.1007/s00497-018-0321-x

Olmedo-Monfil, V., Durán-Figueroa, N., Arteaga-Vázquez, M., Demesa-Arévalo, E., Autran, D., Grimanelli, D., Slotkin, R. K., Martienssen, R. A., & Vielle-Calzada, J. P. (2010).

Control of female gamete formation by a small RNA pathway in Arabidopsis. *Nature*, *464*(7288), 628–632. https://doi.org/10.1038/nature08828

Pagnussat, Gabriela C, Alandete-Saez, M., Bowman, J. L., & Sundaresan, V. (2009). Auxin-dependent patterning and gamete specification in the Arabidopsis female gametophyte. *Science (New York, N.Y.)*, *324*(5935), 1684–1689. https://doi.org/10.1126/science.1167324

Pagnussat, Gabriela Carolina, Yu, H. J., & Sundaresan, V. (2007). Cell-fate switch of synergid to egg cell in Arabidopsis eostre mutant embryo sacs arises from misexpression of the BEL1-like homeodomain gene BLH1. *Plant Cell*, *19*(11), 3578–3592. https://doi.org/10.1105/tpc.107.054890

Pekker, I., Alvarez, J. P., & Eshed, Y. (2005). Auxin response factors mediate Arabidopsis organ asymmetry via modulation of KANADI activity. *Plant Cell*, *17*(11), 2899–2910. https://doi.org/10.1105/tpc.105.034876

Pinto, S. C., Mendes, M. A., Coimbra, S., & Tucker, M. R. (2019). Revisiting the Female Germline and Its Expanding Toolbox. *Trends in Plant Science*, *24*(5), 455–467. https://doi.org/https://doi.org/10.1016/j.tplants.2019.02.003

Pischke, M. S., Jones, L. G., Otsuga, D., Fernandez, D. E., Drews, G. N., & Sussman, M. R. (2002). An Arabidopsis histidine kinase is essential for megagametogenesis. *Proceedings of the National Academy of Sciences of the United States of America*, *99*(24), 15800–15805. https://doi.org/10.1073/pnas.232580499

Prigge, M. J., Otsuga, D., Alonso, J. M., Ecker, J. R., Drews, G. N., & Clark, S. E. (2005). Class III homeodomain-leucine zipper gene family members have overlapping, antagonistic, and distinct roles in Arabidopsis development. *Plant Cell*, *17*(1), 61–76. https://doi.org/10.1105/tpc.104.026161

Prusinkiewicz, P., & Rolland-Lagan, A. G. (2006). Modeling plant morphogenesis. *Current Opinion in Plant Biology*, *9*(1), 83–88. https://doi.org/10.1016/j.pbi.2005.11.015

Rabiger, D. S., & Drews, G. N. (2013). MYB64 and MYB119 Are Required for Cellularization and Differentiation during Female Gametogenesis in Arabidopsis thaliana. *PLoS Genetics*, *9*(9). https://doi.org/10.1371/journal.pgen.1003783

Rasmussen, C. G., & Bellinger, M. (2018). An overview of plant division-plane orientation. *New Phytologist*, *219*(2), 505–512. https://doi.org/10.1111/nph.15183

Ray, A., Lang, J. D., Golden, T., & Ray, S. (1996). Short Integument (Sin 1), a gene required for ovule development in Arabidopsis, also controls flowering time. *Development*, *122*(9), 2631–2638.

Raz, V., & Ecker, J. R. (1999). Regulation of differential growth in the apical hook of Arabidopsis. *Development*, *126*(16), 3661–3668. https://doi.org/10.1242/dev.126.16.3661

Rebocho, A. B., Southam, P., Kennaway, J. R., Bangham, J. A., & Coen, E. (2017). Generation of shape complexity through tissue conflict resolution. *ELife*, *6*. https://doi.org/10.7554/eLife.20156

Refahi, Y., Zardilis, A., Michelin, G., Wightman, R., Leggio, B., Legrand, J., Faure, E., Vachez, L., Armezzani, A., Risson, A.-E., Zhao, F., Das, P., Prunet, N., Meyerowitz, E. M., Godin, C., Malandain, G., Jönsson, H., & Traas, J. (2021). A multiscale analysis of early flower development in Arabidopsis provides an integrated view of molecular regulation and growth control. *Developmental Cell*, *56*(4), 540-556.e8. https://doi.org/https://doi.org/10.1016/j.devcel.2021.01.019

Reiser, L., Modrusan, Z., Margossian, L., Samach, A., Ohad, N., Haughn, G. W., & Fischer, R. L. (1995). The BELL1 gene encodes a homeodomain protein involved in pattern formation in the Arabidopsis ovule primordium. *Cell*, *83*(5), 735–742. https://doi.org/10.1016/0092-8674(95)90186-8

Robinson-Beers, K., Pruitt, R. E., & Gasser, C. S. (1992). Ovule development in wild-type Arabidopsis and two female-sterile mutants. *The Plant Cell*, *4*(10), 1237–1249. https://doi.org/10.1105/tpc.4.10.1237

Robinson, S., Burian, A., Couturier, E., Landrein, B., Louveaux, M., Neumann, E. D., Peaucelle, A., Weber, A., & Nakayama, N. (2013). Mechanical control of morphogenesis at the shoot apex. *Journal of Experimental Botany*, *64*(15), 4729–4744. https://doi.org/10.1093/jxb/ert199

Rodrigo-Peiris, T., Xu, X. M., Zhao, Q., Wang, H. J., & Meier, I. (2011). RanGAP is required for post-meiotic mitosis in female gametophyte development in Arabidopsis thaliana. *Journal of Experimental Botany*, *62*(8), 2705–2714. https://doi.org/10.1093/jxb/erq448

Roeder, A. H., Cunha, A., Burl, M. C., & Meyerowitz, E. M. (2012). A computational image analysis glossary for biologists. *Development*, *139*(17), 3071–3080. https://doi.org/10.1242/dev.076414

Roeder, A. H. K., Tarr, P. T., Tobin, C., Zhang, X., Chickarmane, V., Cunha, A., & Meyerowitz, E. M. (2011). Computational morphodynamics of plants: Integrating development over space and time. *Nature Reviews Molecular Cell Biology*, *12*(4), 265–273. https://doi.org/10.1038/nrm3079

Roeder, A. H. K., & Yanofsky, M. F. (2006). Fruit development in Arabidopsis. *The Arabidopsis Book / American Society of Plant Biologists*, *4*, e0075. https://doi.org/10.1199/tab.0075

Rojek, J., Tucker, M. R., Pinto, S. C., Rychłowski, M., Lichocka, M., Soukupova, H., Nowakowska, J., Bohdanowicz, J., Surmacz, G., & Gutkowska, M. (2021). Rab-dependent vesicular traffic affects female gametophyte development in Arabidopsis. *Journal of Experimental Botany*, *72*(2), 320–340. https://doi.org/10.1093/jxb/eraa430

Ronneberger, O., Fischer, P., & Brox, T. (2015). U-Net: Convolutional Networks for Biomedical Image Segmentation. In N. Navab, J. Hornegger, W. M. Wells, & A. F. Frangi (Eds.), *Medical Image Computing and Computer-Assisted Intervention ({MICCAI})* (Vol. 9351, pp. 234–241). Springer International Publishing. https://doi.org/10.1007/978-3-319-24574-4_28

Rudall, P. J. (2021). Evolution and patterning of the ovule in seed plants. *Biological Reviews*, *952*, 943–960. https://doi.org/10.1111/brv.12684

Sakai, H, Medrano, L. J., & Meyerowitz, E. M. (1995). Role of SUPERMAN in maintaining Arabidopsis floral whorl boundaries. *Nature*, *378*(6553), 199–203. https://doi.org/10.1038/378199a0

Sakai, Hajime, Medrano, L. J., & Meyerowitz, B. E. M. (1995). Floral Whorl Boundaries. *Nature*, 199–203.

Sambrook, J., Fritsch, E. F., & Maniatis, T. (1989). *Molecular cloning : a laboratory manual*. Cold Spring Harbor Laboratory.

Sampathkumar, A., Krupinski, P., Wightman, R., Milani, P., Berquand, A., Boudaoud, A., Hamant, O., Jönsson, H., & Meyerowitz, E. M. (2014). Subcellular and supracellular mechanical stress prescribes cytoskeleton behavior in Arabidopsis cotyledon pavement cells. *ELife*, *3*, e01967. https://doi.org/10.7554/{eLife}.01967

Sapala, A, Runions, A., & Smith, R. S. (2019). Mechanics, geometry and genetics of epidermal cell shape regulation: different pieces of the same puzzle. *Curr Opin Plant Biol*, *47*, 1–8. https://doi.org/10.1016/j.pbi.2018.07.017

Sapala, Aleksandra, Runions, A., Routier-Kierzkowska, A.-L., Das Gupta, M., Hong, L., Hofhuis, H., Verger, S., Mosca, G., Li, C.-B., Hay, A., Hamant, O., Roeder, A. H., Tsiantis, M., Prusinkiewicz, P., & Smith, R. S. (2018). Why plants make puzzle cells, and how their shape emerges. *ELife*, *7*. https://doi.org/10.7554/{eLife}.32794

Sapala, Aleksandra, Runions, A., & Smith, R. S. (2019). Mechanics, geometry and genetics of epidermal cell shape regulation: different pieces of the same puzzle. *Current Opinion in Plant Biology*, *47*, 1–8. https://doi.org/10.1016/j.pbi.2018.07.017

Satina, S., Blakeslee, A. F., & Avery, A. G. (1940). Demonstration of the three germ layers in the shoot apex of Datura by means of induced polyploidy in periclinal chimeras. *Am J Bot*, *27*, 895–905.

Savin, T., Kurpios, N. A., Shyer, A. E., Florescu, P., Liang, H., Mahadevan, L., & Tabin, C. J. (2011). On the growth and form of the gut. *Nature*, *476*(7358), 57–63. https://doi.org/10.1038/nature10277

Schiefthaler, U., Balasubramanian, S., Sieber, P., Chevalier, D., Wisman, E., & Schneitz, K. (1999). Molecular analysis of NOZZLE, a gene involved in pattern formation and early sporogenesis during sex organ development in Arabidopsis thaliana. *Proc Natl Acad Sci U S A*, *96*(20), 11664–11669. https://www.ncbi.nlm.nih.gov/pubmed/10500234

Schindelin, J., Arganda-Carreras, I., Frise, E., Kaynig, V., Longair, M., Pietzsch, T., Preibisch, S., Rueden, C., Saalfeld, S., Schmid, B., Tinevez, J.-Y., White, D. J., Hartenstein, V., Eliceiri, K., Tomancak, P., & Cardona, A. (2012). Fiji: an open-source platform for biological-image analysis. *Nature Methods*, *9*(7), 676–682. https://doi.org/10.1038/nmeth.2019

Schmidt, A., Schmid, M. W., & Grossniklaus, U. (2015). Plant germline formation: common concepts and developmental flexibility in sexual and asexual reproduction. *Development*, *142*(2), 229–241. https://doi.org/10.1242/dev.102103

Schmidt, A., Wuest, S. E., Vijverberg, K., Baroux, C., Kleen, D., & Grossniklaus, U. (2011).

Transcriptome analysis of the arabidopsis megaspore mother cell uncovers the importance of RNA helicases for plant germline development. *PLoS Biology*, *9*(9). https://doi.org/10.1371/journal.pbio.1001155

Schneitz, K. (1999). The molecular and genetic control of ovule development. *Curr Opin Plant Biol*, *2*(1), 13–17. https://www.ncbi.nlm.nih.gov/pubmed/10047571

Schneitz, K, Baker, S. C., Gasser, C. S., & Redweik, A. (1998a). Pattern formation and growth during floral organogenesis: HUELLENLOS and AINTEGUMENTA are required for the formation of the proximal region of the ovule primordium in Arabidopsis thaliana. *Development*, *125*(14), 2555–2563. https://www.ncbi.nlm.nih.gov/pubmed/9636071

Schneitz, K, Baker, S. C., Gasser, C. S., & Redweik, A. (1998b). Pattern formation and growth during floral organogenesis: HUELLENLOS and AINTEGUMENTA are required for the formation of the proximal region of the ovule primordium in Arabidopsis thaliana. *Development (Cambridge, England)*, *125*(14), 2555–2563.

Schneitz, Kay, Hulskamp, M., Kopczak, S. D., & Pruitt, R. E. (1997). Dissection of sexual organ ontogenesis: a genetic analysis of ovule development in Arabidopsis thaliana. *Development*, *124*(7), 1367–1376. https://www.ncbi.nlm.nih.gov/pubmed/9118807

Schneitz, Kay, Hülskamp, M., Kopczak, S. D., & Pruitt, R. E. (1997). Dissection of sexual organ ontogenesis: A genetic analysis of ovule development in Arabidopsis thaliana. *Development*, *124*(7), 1367–1376.

Schneitz, Kay, Hülskamp, M., & Pruitt, R. E. (1995a). Wild-type ovule development in Arabidopsis thaliana: a light microscope study of cleared whole-mount tissue.pdf. *The Plant Journal*, *7*(5), 631–749.

Schneitz, Kay, Hülskamp, M., & Pruitt, R. E. (1995b). Wild-type ovule development in Arabidopsis thaliana: a light microscope study of cleared whole-mount tissue. *The Plant Journal*. https://doi.org/10.1046/j.1365-313X.1995.07050731.x

Scholz, S., Ple\ssmann, J., Enugutti, B., Hüttl, R., Wassmer, K., & Schneitz, K. (2019). The {AGC} protein kinase {UNICORN} controls planar growth by attenuating {PDK1} in Arabidopsis thaliana. *{PLoS} Genetics*, *15*(2), e1007927. https://doi.org/10.1371/journal.pgen.1007927

She, W., & Baroux, C. (2015). Chromatin dynamics in pollen mother cells underpin a common scenario at the somatic-to-reproductive fate transition of both the male and female lineages in Arabidopsis. *Frontiers in Plant Science*, *6*(APR), 1–7. https://doi.org/10.3389/fpls.2015.00294

She, W., Grimanelli, D., Rutowicz, K., Whitehead, M. W. J., Puzio, M., Kotlinski, M., Jerzmanowski, A., & Baroux, C. (2013). Chromatin reprogramming during the somatic-to-reproductive cell fate transition in plants. *Development (Cambridge, England)*, *140*(19), 4008–4019. https://doi.org/10.1242/dev.095034

Shi, D. Q., & Yang, W. C. (2011). Ovule development in Arabidopsis: progress and challenge. *Curr Opin Plant Biol*, *14*(1), 74–80. https://doi.org/10.1016/j.pbi.2010.09.001

Shi, G., Herrera, F., Herendeen, P. S., Clark, E. G., & Crane, P. R. (2021). Mesozoic cupules

and the origin of the angiosperm second integument. *Nature*, *594*(7862), 223–226. https://doi.org/10.1038/s41586-021-03598-w

Sieber, P, Petrascheck, M., Barberis, A., & Schneitz, K. (2004). Organ polarity in Arabidopsis. NOZZLE physically interacts with members of the YABBY family. *Plant Physiol*, *135*(4), 2172–2185. https://doi.org/10.1104/pp.104.040154

Sieber, Patrick, Gheyselinck, J., Gross-Hardt, R., Laux, T., Grossniklaus, U., & Schneitz, K. (2004). Pattern formation during early ovule development in Arabidopsis thaliana. *Developmental Biology*, *273*(2), 321–334. https://doi.org/10.1016/j.ydbio.2004.05.037

Siegfried, K. R., Eshed, Y., Baum, S. F., Otsuga, D., Drews, G. N., & Bowman, J. L. (1999). Members of the YABBY gene family specify abaxial cell fate in Arabidopsis. *Development (Cambridge, England)*, *126*(18), 4117–4128.

Simon, M. K., Skinner, D. J., Gallagher, T. L., & Gasser, C. S. (2017). Integument development in Arabidopsis depends on interaction of {YABBY} protein {INNER} {NO} {OUTER} with coactivators and corepressors. *Genetics*, *207*(4), 1489–1500. https://doi.org/10.1534/genetics.117.300140

Simonini, S., Bencivenga, S., Trick, M., & Østergaard, L. (2017). Auxin-induced modulation of ETTIN activity orchestrates gene expression in arabidopsis. *Plant Cell*, *29*(8), 1864–1882. https://doi.org/10.1105/tpc.17.00389

Simonini, S., Deb, J., Moubayidin, L., Stephenson, P., Valluru, M., Freire-Rios, A., Sorefan, K., Weijers, D., Friml, J., & Østergaard, L. (2016). A noncanonical auxin-sensing mechanism is required for organ morphogenesis in Arabidopsis. *Genes & Development*, *30*(20), 2286–2296. https://doi.org/10.1101/gad.285361.116

Skinner, D. J., & Gasser, C. S. (2009). Expression-based discovery of candidate ovule development regulators through transcriptional profiling of ovule mutants. *BMC Plant Biology*, *9*. https://doi.org/10.1186/1471-2229-9-29

Smyth, D. R., Bowman, J. L., & Meyerowitz, E. M. (1990). Early flower development in Arabidopsis. *The Plant Cell*, *2*(8), 755–767. https://doi.org/10.1105/tpc.2.8.755

Sprunck, S., & Groß-Hardt, R. (2011). Nuclear behavior, cell polarity, and cell specification in the female gametophyte. *Sexual Plant Reproduction*, *24*(2), 123–136. https://doi.org/10.1007/s00497-011-0161-4

Stamm, P., Strauss, S., Montenegro-Johnson, T. D., Smith, R., & Bassel, G. W. (2017). In Silico Methods for Cell Annotation, Quantification of Gene Expression, and Cell Geometry at Single-Cell Resolution Using 3DCellAtlas. *Methods Mol Biol*, *1497*, 99–123. https://doi.org/10.1007/978-1-4939-6469-7_11

Stebbins, L. G. (1974). *Flowering Plants: Evolution Above the Species Level*. Harvard University Press.

Steffen, J. G., Kang, I. H., Macfarlane, J., & Drews, G. N. (2007). Identification of genes expressed in the Arabidopsis female gametophyte. *Plant Journal*, *51*(2), 281–292. https://doi.org/10.1111/j.1365-313X.2007.03137.x

Steffen, J. G., Kang, I. H., Portereiko, M. F., Lloyd, A., & Drews, G. N. (2008). AGL61 interacts with AGL80 and is required for central cell development in Arabidopsis. *Plant Physiology*, *148*(1), 259–268. https://doi.org/10.1104/pp.108.119404

Su, Z., Zhao, L., Zhao, Y., Li, S., Won, S. Y., Cai, H., Wang, L., Li, Z., Chen, P., Qin, Y., & Chen, X. (2017). The THO Complex Non-Cell-Autonomously Represses Female Germline Specification through the TAS3-ARF3 Module. *Current Biology*, *27*(11), 1597-1609.e2. https://doi.org/10.1016/j.cub.2017.05.021

Susaki, D., Suzuki, T., Maruyama, D., Ueda, M., Higashiyama, T., & Kurihara, D. (2021). Dynamics of the cell fate specifications during female gametophyte development in Arabidopsis. *PLoS Biology*, *19*(3), e3001123. https://doi.org/10.1371/journal.pbio.3001123

Tallinen, T., Chung, J. Y., Rousseau, F., Girard, N., Lefèvre, J., & Mahadevan, L. (2016). On the growth and form of cortical convolutions. *Nature Physics*, *12*(6), 588–593. https://doi.org/10.1038/nphys3632

Tedeschi, F., Rizzo, P., Rutten, T., Altschmied, L., & Bäumlein, H. (2017). RWP-RK domain-containing transcription factors control cell differentiation during female gametophyte development in Arabidopsis. *New Phytologist*, *213*(4), 1909–1924. https://doi.org/10.1111/nph.14293

Truernit, E., & Haseloff, J. (2008). Arabidopsis thaliana outer ovule integument morphogenesis: ectopic expression of KNAT1 reveals a compensation mechanism. *BMC Plant Biol*, *8*, 35. https://doi.org/10.1186/1471-2229-8-35

Tucker, M. R., Okada, T., Hu, Y., Scholefield, A., Taylor, J. M., & Koltunow, A. M. G. (2012). Somatic small {RNA} pathways promote the mitotic events of megagametogenesis during female reproductive development in Arabidopsis. *Development*, *139*(8), 1399–1404. https://doi.org/10.1242/dev.075390

Uyttewaal, M., Burian, A., Alim, K., Landrein, B., Borowska-Wykret, D., Dedieu, A., Peaucelle, A., Ludynia, M., Traas, J., Boudaoud, A., Kwiatkowska, D., & Hamant, O. (2012). Mechanical stress acts via katanin to amplify differences in growth rate between adjacent cells in Arabidopsis. *Cell*, *149*(2), 439–451. https://doi.org/10.1016/j.cell.2012.02.048

Valuchova, S., Mikulkova, P., Pecinkova, J., Klimova, J., Krumnikl, M., Bainar, P., Heckmann, S., Tomancak, P., & Riha, K. (2020). Imaging plant germline differentiation within Arabidopsis flowers by light sheet microscopy. *ELife*, *9*. https://doi.org/10.7554/eLife.52546

Van Hooijdonk, C. A., Glade, C. P., & Van Erp, P. E. (1994). {TO}-{PRO}-3 iodide: a novel {HeNe} laser-excitable {DNA} stain as an alternative for propidium iodide in multiparameter flow cytometry. *Cytometry*, *17*(2), 185–189. https://doi.org/10.1002/cyto.990170212

Villanueva, J. M., Broadhvest, J., Hauser, B. A., Meister, R. J., Schneitz, K., & Gasser, C. S. (1999a). INNER NO OUTER regulates abaxial-adaxial patterning in Arabidopsis ovules. *Genes and Development*, *13*(23), 3160–3169. https://doi.org/10.1101/gad.13.23.3160

Villanueva, J. M., Broadhvest, J., Hauser, B. A., Meister, R. J., Schneitz, K., & Gasser, C. S. (1999b). INNER NO OUTER regulates abaxial-adaxial patterning in Arabidopsis ovules. *Genes and Development*, *13*(23), 3160–3169. https://doi.org/10.1101/gad.13.23.3160

Vroemen, C. W., Mordhorst, A. P., Albrecht, C., Kwaaitaal, M. A. C. J., & de Vries, S. C. (2003). The CUP-SHAPED COTYLEDON3 gene is required for boundary and shoot meristem formation in Arabidopsis. *The Plant Cell*, *15*(7), 1563–1577. https://doi.org/10.1105/tpc.012203

Wang, Z.-P., Xing, H.-L., Dong, L., Zhang, H.-Y., Han, C.-Y., Wang, X.-C., & Chen, Q.-J. (2015). Egg cell-specific promoter-controlled {CRISPR}/Cas9 efficiently generates homozygous mutants for multiple target genes in Arabidopsis in a single generation. *Genome Biology*, *16*, 144. https://doi.org/10.1186/s13059-015-0715-0

Wei, B., Zhang, J., Pang, C., Yu, H., Guo, D., Jiang, H., Ding, M., Chen, Z., Tao, Q., Gu, H., Qu, L. J., & Qin, G. (2015). The molecular mechanism of sporocyteless/nozzle in controlling Arabidopsis ovule development. *Cell Res*, *25*(1), 121–134. https://doi.org/10.1038/cr.2014.145

Willis, L., Refahi, Y., Wightman, R., Landrein, B., Teles, J., Huang, K. C., Meyerowitz, E. M., & Jönsson, H. (2016). Cell size and growth regulation in the Arabidopsis thaliana apical stem cell niche. *Proceedings of the National Academy of Sciences of the United States of America*, *113*(51). https://doi.org/10.1073/pnas.1616768113

Wyczalkowski, M., Chen, Z., Filas, B., Varner, V., & Taber, L. (2012). Computational Models for Mechanics of Morphogenesis. *Birth Defects Research. Part C, Embryo Today : Reviews*, *96*, 132–152. https://doi.org/10.1002/bdrc.21013

Yoshida, S., Barbier de Reuille, P., Lane, B., Bassel, G. W., Prusinkiewicz, P., Smith, R. S., & Weijers, D. (2014). Genetic control of plant development by overriding a geometric division rule. *Dev Cell*, *29*(1), 75–87. https://doi.org/10.1016/j.devcel.2014.02.002

Yu, S.-X., Zhou, L.-W., Hu, L.-Q., Jiang, Y.-T., Zhang, Y.-J., Feng, S.-L., Jiao, Y., Xu, L., & Lin, W.-H. (2020). Asynchrony of ovule primordia initiation in Arabidopsis. *Development*. https://doi.org/10.1242/dev.196618

Yuan, L., Liu, Z., Song, X., Johnson, C., Yu, X., & Sundaresan, V. (2016). The CKI1 Histidine Kinase Specifies the Female Gametic Precursor of the Endosperm. *Developmental Cell*, *37*(1), 34–46. https://doi.org/10.1016/j.devcel.2016.03.009

Žádníková, P., & Simon, R. (2014). How boundaries control plant development. *Current Opinion in Plant Biology*, *17*(1), 116–125. https://doi.org/10.1016/j.pbi.2013.11.013

Žádníková, P., Wabnik, K., Abuzeineh, A., Gallemi, M., Van Der Straeten, D., Smith, R. S., Inzé, D., Friml, J., Prusinkiewicz, P., & Benková, E. (2016). A model of differential growth-guided apical hook formation in plants. *Plant Cell*, *28*(10), 2464–2477. https://doi.org/10.1105/tpc.15.00569

Zhao, X., Bramsiepe, J., Van Durme, M., Komaki, S., Prusicki, M. A., Maruyama, D., Forner, J., Medzihradszky, A., Wijnker, E., Harashima, H., Lu, Y., Schmidt, A., Guthörl, D., Logroño, R. S., Guan, Y., Pochon, G., Grossniklaus, U., Laux, T., Higashiyama, T., … Schnittger, A. (2017). {RETINOBLASTOMA} {RELATED1} mediates germline entry

in Arabidopsis. *Science*, *356*(6336). https://doi.org/10.1126/science.aaf6532

Zimmermann, W. (1952). Main results of the "Telome Theory." *The Palaeobotanist*, *1*, 456–470. https://doi.org/10.1007/BF03041744

Zürcher, E., Tavor-Deslex, D., Lituiev, D., Enkerli, K., Tarr, P. T., & Müller, B. (2013). A robust and sensitive synthetic sensor to monitor the transcriptional output of the cytokinin signaling network in planta. *Plant Physiology*, *161*(3), 1066–1075. https://doi.org/10.1104/pp.112.211763

7 Supplementary Data

Supplementary table 1 Ovule developmental stages.

Ovule stages	Ovule development		Flower development	
	Embryo sac and endosperm development	Sporophytic tissue development	Gynoecium development	Floral landmarks of corresponding floral stages
1. Early phase of ovule development				
1-I		Protrusions arise	Open cylinder	Locules appear in long stamens (floral stage 8)
1-II		Protrusions elongated	Cylinder constricted at apex	Petal primordia stalked at base (floral stage 9)
2. Megasporogenesis				
2-I	Megaspore mother cell enlarges		Cylinder closed	Petals level with short stamens (floral stage 10)
2-II		Inner integument initiates		
2-III		Outer integument initiates, chalazal nucellus divides		
2-IV	Meiosis	Chalazal nucellus enlarges	First immature papillar cells which do not cover all of the stigma yet, lateral vasculature visible as lighter strip	Filaments start to elongate, anthers green (floral stage 11)
2-V	Tetrad formation	Integuments extend toward the apex of the nucellus		
3. Megametogenesis				
3-I	Degenerating tetrad with mono-nuclear embryo sac	Outer integument envelops the nucellus and the inner integument, funiculus and the nucellus curve		
3-II	Two-nuclear embryo sac	Outer integument surrounds nucellus, micropylar end pointing more	Papillar cells small and covering all the stigma, style recognizable,	Petals level with long stamens, anthers turn

		than 90° away from funiculus, further differential growth of integuments	valves almost visible as distinct structures	yellow (flower stage 12)
3-III	Vacuole appears	Micropylar end points away about 90° from funiculus	Papillar cells grow longer	
3-IV	Four-nuclear embryo sac	Inner integument surrounds nucellus, endothelium differentiates	Valves more pronounced	
3-V	Eight-nuclear embryo sac, cellularization			
3-IV	Central cell nuclei fuse, antipodal cells degenerate	Additional cell layer initiated in inner integument	Well-extended papillar cells, prominent style and valves	
4. Postfertilization development				

Supplementary table 2 Primers used in this work.

Name	Sequence	Purpose
pINO_F1	5'-AACAGGTCTCAACCTCTG GAACTTTCATGGCGAGTCA-3'	Cloning INO promoter in pGGA000 entry vector
pINO_R1	5'-AACAGGTCTCTTGTTAGAGA GTGTGTGTGTACGATGAATGA-3'	
tINO_F1	5'-AACAGGTCTCACTGCTAACAAT TTGGGATATGAAAATTTA-3'	Cloning INO terminator in pGGE000 entry vector
tINO_R1	5'-AACAGGTCTCTTAGTCTCTCACA CCTGAAAATCAAAAGTTA-3'	
INO sgRNA	5'-ACCATCTATTTGATCTGCCG-3'	Generation of *ino* mutant through CRISPR-Cas9 system
INO_fw	5'- ATCATTCATCGTACACACACA -3'	Sequencing gINO
INO_rw	5'- AAAGGAGAAATCGCAAAACT -3'	
SUP sgRNA1	5'- GCCGTGCAAGAACTTCACCA -3'	Generation of *sup* mutant through CRISPR-Cas9 system
SUP sgRNA2	5'- TCCTCACCAAGATATAGGGC -3'	
SUP_fw	5'- TCTAGCATAGCCAAAAAGAAAG -3'	Sequencing gSUP
SUP_rw	5'- AATTGTGAACTTCGAATCCT -3'	

Supplementary table 3 Cells type labels.

Cell type	Morphological definition of cell type	Standardized cell type label
Radial organization of early stage ovule tissue		
L1	Outermost cell layer (epidermis).	L1
L2	First sub-epidermal cell layer.	L2
L3	Innermost cell layer.	L3
MMC	Single large L2 cell in distal end of nucellus, eventually undergoing meiosis, volume ≥ 350 μm^3.	mmc
Tissues organization of late stage ovule		
Nucellus	Distal region, harbors the mmc, proximally delineated by adaxial inner integument .	nu
Chalaza	Central region, flanked by the two integuments, distal end marked by adaxial inner integument, proximal end marked by abaxial outer integument, does not include epidermis.	ch
Anterior chalaza	Group chalazal cells, positioned at the anterior side, underlying the epidermal cells forming the frontal base of the hood-like structure generated by the epidermis-derived outer integument.	ac
Posterior chalaza	Group of proximal chalazal cells, positioned opposite to the cells of the anterior chalaza.	pc
Funiculus	Proximal region, stalk-like structure, carrying the vascular strand, distal end marked by chalaza, proximal end marked by placenta.	fu
Embryo sac	Haploid female gametophyte encompasses all stages up to but not including fertilization.	es
Integuments		
Abaxial outer integument	Outermost single cell layer of outer integument, entirely made of epidermal cells, proximal end marked by chalaza.	oi2
Adaxial outer integument	Innermost (dorsal) single cell layer of outer integument, proximal end marked by chalaza.	oi1
Abaxial inner integument	Outer (ventral) single cell layer of inner integument, entirely made of epidermal cells, proximal end marked by chalaza.	ii2

Adaxial inner integument	Inner (dorsal) single cell layer of inner integument, entirely made of epidermal cells, proximal end marked by chalaza.	ii1
Parenchymatic inner integument	Cell layer derived from adaxial inner integument, proximal end marked by chalaza.	ii1’
Integument coordinate system annotation		
Anterior	Anterior region of the integument layer.	Ant
Posterior	Posterior region of the integument layer.	Post
Proximal	Proximal half of the integument layer. Relative PD distance values form 0 to 50.	P
Distal	Distal half of the integument layer. Relative PD distance values form 50 to 100.	D
Negative oi2	Region of the outer integument placed behind the Bezier ring and characterized by relative PD distance negative values.	Neg oi2
Medio-lateral oi2	Medio-lateral region of the abaxial outer integument.	MED-LAT
Frontal oi2	Frontal region of the abaxial outer integument.	FRONT
Cell cycle		
M-phase	Mitotic figures (metaphase, anaphase).	M
Interphase	Cells in G0, S, or G2 phase.	I
Gene expression		
WUS expressing cells	Cells of pWUS::2xVenus-NLS reporting line showing fluorescently labeled nuclei. Cells expressing *WUS.*	WUS+
INO expressing cells	Cells of pINO::NLS-GFP reporting line showing fluorescently labeled nuclei. Cells expressing *INO*.	INO+

Supplementary table 4 Information on the datasets analyzed.

Dataset index	Dataset name	Purpose	N of ovules
1	Wild type dataset	3D digital atlas of WT ovule development	158
2	pWUS::2xVenus-NLS reporter line dataset	Analysis of *WUS* expression pattern	67
3	Ovule growth T0-T1 dataset	Analysis of ovule growth at two time points	94
4	*ino-5* dataset	3D digital atlas of *ino-5* ovule development	119
5	*sup-7* dataset	3D digital atlas of *sup-7* ovule development	55
6	pINO::NLS-GFP reporter line dataset	Analysis of *INO* expression pattern	56

Supplementary table 5 Correlation of pistil length with ovule stages.

		Ovules counted												
Pistil length (mm)	**N ovules counted**	1-I	1-II	2-I	2-II	2-III	2-IV	2-V	3-I	3-II	3-III	3-IV	3-V	3-VI
0.33	17	17	-	-	-	-	-	-	-	-	-	-	-	-
0.38	21	21	-	-	-	-	-	-	-	-	-	-	-	-
0.38	13	13	-	-	-	-	-	-	-	-	-	-	-	-
0.44	25	12	13	-	-	-	-	-	-	-	-	-	-	-
0.45	11	11	12	-	-	-	-	-	-	-	-	-	-	-
0.49	24	7	13	4	-	-	-	-	-	-	-	-	-	-
0.51	27	8	19	-	-	-	-	-	-	-	-	-	-	-
0.57	24	-	2	22	-	-	-	-	-	-	-	-	-	-
0.61	25	-	10	15	-	-	-	-	-	-	-	-	-	-
0.62	16	3	6	7	-	-	-	-	-	-	-	-	-	-
0.62	16	-	8	8	-	-	-	-	-	-	-	-	-	-
0.66	18	-	1	8	9	-	-	-	-	-	-	-	-	-
0.68	20	-	1	8	11	-	-	-	-	-	-	-	-	-
0.69	22	-	-	9	13	-	-	-	-	-	-	-	-	-
0.71	25	-	-	10	13	-	-	-	-	-	-	-	-	-
0.72	27	-	-	7	16	4	-	-	-	-	-	-	-	-
0.75	29	-	-	2	13	14	-	-	-	-	-	-	-	-
0.82	41	-	-	8	22	11	-	-	-	-	-	-	-	-
0.83	21	-	-	-	10	11	-	-	-	-	-	-	-	-
0.88	18	-	-	-	-	15	3	-	-	-	-	-	-	-
0.94	20	-	-	-	-	6	10	4	-	-	-	-	-	-
0.95	31	-	-	-	5	10	13	3	-	-	-	-	-	-

0.95	26	-	-	-	1	16	13	-	-	-	-	-	-	-
0.98	29	-	-	-	-	13	7	8	1	-	-	-	-	-
1.1	27	-	-	-	-	6	8	13		-	-	-	-	-
1.13	25	-	-	-	-	2	5	9	9	-	-	-	-	-
1.15	28	-	-	-	1	2	7	12	6	-	-	-	-	-
1.18	20	-	-	-	-	4	10	6	-	-	-	-	-	-
1.2	43	-	-	-	-	3	13	19	8	-	-	-	-	-
1.2	34	-	-	-	-	4	10	16	4	-	-	-	-	-
1.2	33	-	-	-	-	-	-	12	20	1	-	-	-	-
1.21	24	-	-	-	-	3	8	13	-	-	-	-	-	-
1.22	32	-	-	-	-	-	-	6	13	13	-	-	-	-
1.28	22	-	-	-	-	3	5	10	4	-	-	-	-	-
1.3	24	-	-	-	-	-	-	-	19	4	1	-	-	-
1.31	18	-	-	-	-	-	-	-	13	4	1	-	-	-
1.32	25	-	-	-	-	-	2	8	15	-	-	-	-	-
1.35	28	-	-	-	-	-	-	6	22	-	-	-	-	-
1.46	19	-	-	-	-	-	-	7	12	-	-	-	-	-
1.49	36	-	-	-	-	-	-	1	19	9	6	1	-	-
1.55	41	-	-	-	-	-	-	-	15	10	11	5	-	-
1.55	20	-	-	-	-	-	-	-	13	4	3	-	-	-
1.6	30	-	-	-	-	-	-	1	3	12	10	4	-	-
1.61	24	-	-	-	-	-	-	2	6	9	7	-	-	-
1.62	24	-	-	-	-	-	-	-	4	6	7	5	2	-
1.63	25	-	-	-	-	-	-	-	-	2	7	11	5	-
1.65	23	-	-	-	-	-	-	-	2	8	11	2	-	-
1.71	19	-	-	-	-	-	-	-	1	1	1	12	4	-
1.72	25	-	-	-	-	-	-	-	-	1	-	11	12	1

1.75	25	-	-	-	-	-	-	-	-	-	2	7	10	6
1.79	37	-	-	-	-	-	-	-	-	-	3	3	21	8
1.82	28	-	-	-	-	-	-	-	3	4	5	12	4	-
1.84	29	-	-	-	-	-	-	-	-	-	2	14	13	-
1.9	21	-	-	-	-	-	-	-	-	2	3	10	6	-
1.96	17	-	-	-	-	-	-	-	-	-	-	5	12	5
1.97	19	-	-	-	-	-	-	-	-	-	4	2	13	-
2.1	23	-	-	-	-	-	-	-	-	-	-	-	17	6
2.1	14	-	-	-	-	-	-	-	-	-	-	-	12	2
2.1	27	-	-	-	-	-	-	-	-	5	3	7	12	-
2.18	18	-	-	-	-	-	-	-	-	-	-	15	13	-
2.2	28	-	-	-	-	-	-	-	-	2	-	11	10	5
2.27	18	-	-	-	-	-	-	-	-	-	-	-	2	16
2.3	20	-	-	-	-	-	-	-	-	-	-	-	7	13
2.32	14	-	-	-	-	-	-	-	-	-	-	-	-	14

8 Acknowledgement

I would like to thank Prof. Dr. Kay Schneitz for giving me the opportunity to work in his group, in particular I am grateful for his supervision, support patience and motivation throughout the project development and research, feedback to improve my oral presentations and thesis writing.

I would also like to thank all the members of the Research Group Computational Morphodynamics for the great collaborations during the four years of the doctorate project. A big thanks goes to the MorphographX team and the PlantSeg team, their contribution was fundamental during the project.

I would like to thank past and present colleagues: Sebastian, Jin, Ajeet, Regina, Athul, Xia, Anne, Barbara, Rodion, Teejasvine and Katrin for the scientific feedback during lab meetings, the friendly talks and fun moments we shared.

I would like to thank Prof. Dr. Ramon Torres and the CALM unit for the technical support during the hours spent at the microscopes and for taking care of the imaging facility with great patience.

I would like to thank Susanna for the great help when comes to bureaucracy and for the great and always friendly company.

I would like to thank the bachelor students who worked in the project in particularly to Joanna and Natalie.

Last but not least, I would like to thank my family and friends from Italy and Germany: Kongy, Tita, Lia, Alfio, Julienne, Zazie, Giudi, Lucy, Azzu, Mel, Peppa, Liku, Camuzza, Fagio, Laura and family, Dirki and Linus for their support and constant encouragement.

To conclude, a special thanks to my beloved Julie, who supported me and was always there.